University of Sheffield

Understanding Controls on Dust Emission in the Gonghe Basin, China using Integrated Remote Sensing Data

Sihui Wen

PhD Thesis

Submitted in accordance with the requirements

for the degree of Doctor of Philosophy

Department of Geography

September 2023

Abstract

China contains some of the largest dust sources in the northern hemisphere and has a long-recorded history of Sand and Dust Storms (SDS). The Gonghe Basin is a known SDS source and transport corridor located at the northeast margin of the Qinghai Tibet Plateau (QTP) in China. In the Gonghe Basin SDS impacts on the management of infrastructure, energy security and critical local populations. However, inherent seasonal and diurnal variability in SDS from this and similar source regions, along with apparent spatial heterogeneity with dust sources, is poorly constrained in global and mesoscale models. Here we use an integrated remote sensing approach to identify and characterise SDS occurrence, determine climate drivers and map the landform signatures of SDS emission zones. To detect and quantify SDS occurrence [as Dust Storm Days; DSD], MODIS [2000-2022], mean Terra/Aqua AOD, AE, DOD data were used. Analysis revealed peak SDS seasons in DJF [DOD = 0.293 in Terra; 0.32 in Aqua]and MAM [DOD =0.332 in Terra; 0.385 in Aqua]. Typically, we recorded 19 DSD year^{-1} and the surface maximum daily wind speed in DSD is about 6.3 ms^{-1} vs 3.2 ms^{-1} in the non-DSD. SDS occurrence and intensity are strongly influenced by vegetation cover and Dust Uplift Potential (DUP) by controlling sediment availability [in DJF] and transport capability [in MAM]. Regional climate drivers, Westerlies [DJF] and East Asian Summer Monsoon (EASM) [JJA] have a weak positive influence on SDS occurrence.

Sub-daily analysis of SDS/DSD observed by MODIS was undertaken using hourly GEO-stationary Himawari-8 data (Visible and Near-infrared Radiometer (VNR) and AOT; 2019-2022). We derived SDS start time, duration, and associated DUP for each event. Results show that cloud effects limit the observing time window of Himawari-8 by 40%. We find that MODIS [Terra/Aqua] overpass times [02.30 - 05.30 UTC] missed the peak DUP [08.00 UTC] and SDS start time [05.30 - 10.00 UTC], highlighting significant bias in recorded MODIS DSD, where 34.6% of SDS start between 05.30 -10.00 UTC. These data allowed DSD/SDS events to be attributed to four key types: Haboob [4.6%], Haze [38.2%], Pre/Post Frontal systems [47.4%], and unidentified processes [9.8%].

For a subset of representative SDS, we mapped dust point sources (DPS) locations and used these to populate a Preferential Dust Source geomorphic scheme (PDS); Bullard et al., (2011), and Land Use and Land Cover (LULC) assessment. We find that 70% of the DPS were emitted from Aeolian Dunes (PDS class: 5a and 5b), compared to 23.2% originating from Alluvial Deposits (2c, 3c, and 3d) and 5.6% from ephemeral lakes (1b). The Gonghe Basin is therefore a unique Dust Source region that has an implicit link between sand transport and SDS, and HYSPLIT trajectories suggest a large down-wind zone of deposition, post-24h impact on the downwind cities (e.g., Gansu, Xian). The total dust mass was estimated for 14 SDSs is about 0.196-0.302 Tg. LULC data suggest that DPS from cultivated land accounts for 40% of low-relief alluvial (PDS class: 3c), contributing half of the dust sources [DJF]. We show that synergistic remote sensing at a range of space/time scales can be used to observe the process and climate drivers associated with SDS at the sub-basin scale. These data can be used to determine SDS controls and measurement bias at a scale that is valuable to modelling studies that aim to forecast SDS. Linking SDS observations with PDS *and* LULC landform schemes allows the quantification of factors that may control the location, frequency and magnitude of SDS, and could be directly relevant to agencies involved in the management and mitigation of SDSs in China.

Acknowledgement

I am incredibly grateful to my first supervisor, Robert Bryant, for sparking my passion for desert research and providing unwavering support, guidance, and inspiration throughout my Ph.D. studies. I also want to express my gratitude to Professors Mark Bateman and Wanyin Luo, my second and third supervisors, for their invaluable assistance with my doctoral thesis. Working with such a supportive and friendly team has been a dream come true. I am also deeply thankful to everyone in the Geography Department at the University of Sheffield who has contributed to helping me achieve my goals during my 5 years there.

The global pandemic has made everything more challenging. Planned conferences and fieldwork had to be cancelled, and the five months of living alone during lockdown took a toll on my mental well-being. This experience also made me more independent and stronger. I want to thank Rob for his moral support and assistance during this challenging period. Our socially distanced catch-up in the Weston, Botanical and Bole Hills parks was a delight.

I want to express my immense gratitude to all my friends who have been there for me through thick and thin. We shared wonderful moments together at festivals, enjoyed fun outdoor activities, went on day trips, and had great conversations over beers in the pub. These memories in Sheffield will always hold a special place in my heart. I would also like to give special thanks to Zeyi Jiang, Yu Wang, and Wei Huang for their unwavering support and love that has kept me going. Lastly, I want to thank my family (Mommy Zhangxia and Brother Siyuan) for always supporting my dreams and generously providing full financial support.

Table of Contents

List of Figures

List of Tables

List of Abbreviations

ADS	Active dust Source
AE	Angstrom Exponent
AHI	Advanced Himawari Imager
AOD	Aerosol Optical Depth
AOT	Aerosol property products aerosol optical thickness
BTD	brightness temperature difference
C	Cloud
CMWS	Cubed Maximum Wind Speed
CPO	cold pool outflows
CSD	Clear Sky Difference
CST	China Standard Time
D	Dust
DFJ	Winter (December, February and January)
DOD	Dust Optical Depth
DP	drift potential
DPS	Dust Point Source
DSD	Dust Storm Day
DUP	Dust Uplift Potential
EASM	East Asian Summer Monsoon
ERA-5	European Centre for Medium-Range Weather Forecasts (ECMWF) ReAnalysis v5
FCC	False Colour Composite
FO-AOT	the frequency of occurrence of the AOT
GEO	Geostationary Earth Orbits
GIOVANNI	Goddard Interactive Online Visualization ANd aNalysis Infrastructure
HR	High-Resolution
HR-LEO	High Spatial Resolution Low Earth Orbit
HYSPLIT	Hybrid Single-Particle Lagrangian Integrated Trajectory

JJA	Summer (June, July and August)
LD	Locally derived Dust
LEO	Low Earth Orbit
LEO-Mod	Moderate spatial Resolution Low Earth Orbit
LULC	Land Use and Land Cover
MAM	Spring (March, April, May)
MERRA-2	Modern-Era Retrospective Analysis for Research and Applications-version 2
MODIS	Moderate Resolution Imaging Spectroradiometer
N	No-Dust
NAO	North Atlantic Oscillation
NDVI	Normalized Difference Vegetation Index
NOAA	National Oceanic and Atmospheric Administration
PC	Partial Cloud
PDS	Preferential Dust Source
QTP	Qinghai Tibetan Plateau
RDP	Resultant Drift Potential
RH	Relative Humidity
RS	Remote Sensing
SDS	Sand and Dust Storm
SON	Autumn (September, October, and November)
SSA	Single Scattering-Albedo
TCI	True Colour Image
TD	Transport Dust
TWV	Threshold Wind Velocity
UTC	Coordinated Universal Time
VIIRS	Visible Infrared Imaging Radiometer Suite
VNR	Visible and Near-infrared Radiometer
WNW	West Northwest
WSW	West Southwest

1. Introduction

1.1 Significance and Rationale

Dust is a significant part of the Earth's climate system (Ravi et al., 2011). The interaction of dust with biogeochemical cycles and direct and indirect radiation forcing of the atmosphere plays an essential role in the land-atmosphere-ocean system (Saidou Chaibou et al., 2020; Kok et al., 2018; Chen et al., 2023). However, inherent seasonal and diurnal variability in Sand and Dust Storms (SDS) from source regions, along with apparent spatial heterogeneity with dust sources, is both poorly constrained in global and mesoscale models due to inexact source allocation and quantification (Vickery et al., 2013; Leung et al., 2023; Hassan et al., 2023).

Although we can constrain the drivers of SDS and some components of the dust cycle through meteorological observations (Baddock et al., 2015), it is clear that processes controlling the location and activity of dust source regions at the sub-basin scale are best observed using high temporal/spatial resolution remote sensing data. However, although remote sensing data can be used to capture surface erodibility heterogeneity in the sub-basin scale (von Holdt et al., 2019; Baddock et al., 2021), these observations often lack a close link (in space and time) to the climate mechanisms driving the SDS at the sub-basin scale. Thus, although these and similar approaches have been successful in deriving dust source and activation frequency understanding, very few studies exist globally at this scale (Baddock et al., 2016; Boloorani et al., 2023; Bakker et al., 2019). It is also clear that few of these studies have been able to observe dust plumes and events in a manner that is directly relevant to modelling studies (von Holt et al., 2019; Baddock et al., 2021).

In order to focus research efforts, Bullard et al (2009, 2008) proposed the use and application of a preferential dust source (PDS) geomorphic classification method. Where applied (e.g., Lee et al., 2012), it can be used to outline consistently (i.e., between dust sources) the dominant geomorphic type that makes up dust sources, a factor aimed at facilitating the global emission potential of surfaces and SDS processes occurring within source regions (Bullard et al., 2011; Chappell et al; 2023). However, most studies that have generated SDS inventories in this manner have challenges in accounting for significant bias (in space and time) in the fundamental detection and attribution of source locations. Although the recent availability of PlanetScope constellation remote sensing data (3 m resolution, global, daily coverage) provides an extraordinary opportunity to monitor SDS dynamics through remote sensing (Planet, 2017; Baddock et al., 2021), these data are still limited by fixed overpass times and occurrence of cloud. An opportunity does, however, exist to overcome sample bias by linking SDS observations derived from LEO data with simultaneous observations made by GEO satellite data (e.g., Schepanski et al., 2007 and 2009).

China contains some of the largest dust sources in the northern hemisphere and has a long-recorded history of SDS (Qiang et al., 2013; Chen et al., 2007; Zeng et al., 2011; Dong et al., 1993). However, our understanding of processes occurring in these source regions remains incomplete. Although aeolian features and geomorphological changes have been mapped in the Gonghe Basin (Dong et al., 2017a; Luo et al., 2019 a and b; Luo et al., 2020), knowledge about the importance of different land surface types in the dust cycle is lacking at the sub-basin scale. Understanding the relationship between SDS and landform types is crucial for comprehending the factors that influence the nature and magnitude of SDS, which hinders accurate modelling without proper dust source information. There is a lack of research in Asia which seeks to link SDS observations with a viable geomorphological scheme to quantify factors which may control the nature and magnitude of SDS (Bryant, 2013). The Gonghe Basin is located at the northeast margin of the Qinghai Tibet Plateau and is a hyper-arid and semi-arid climate area in China and is both a known source and transport corridor for emitted SDS in this region (Bi et al., 2017). The basin sits at an altitude of 3000 m, is dissected by the yellow river (Miao et al., 2010; Wang et al., 2012; Hu et al., 2013; Miao et al., 2016) and contains a diverse range of geomorphological units that are known to emit SDS (Dong *et al.*, 2017b). This location is sensitive to climate (Zhao et al., 2010; Gao et al., 2019) and is human-impacted (Zhang et al., 2007; Dong et al., 2010). Various meteorological mechanisms may lead to the different affected areas and duration of SDS at different times of day. Accurately identifying the spatial-temporal heterogeneity and meteorological characteristics of SDS is a prerequisite for accurate estimates of dust aerosol effects. This information is significant for the overall understanding of dust sources in China.

Chapter 1 - Introduction

The overall aim of this project is to use synergistic remote sensing and climate data sets to determine the factors controlling SDS within the Gonghe Basin at the sub-basin scale. This PhD focuses on addressing the research gaps and uncertainties surrounding how we determine the processes driving SDS from specific surfaces within landscapes. To achieve this, we will utilise a range of remote sensing [MODIS, Himawari-8, Sentinel-2, Planet, and Landsat], climate, and field data to quantify factors that control the nature and magnitude of SDS, improving the understanding and quantification of the complex spatial and temporal relationships among SDS factors, as well as the broader regional climate and human impacts. This thesis provides a basis for quantifying factors that may control the nature and magnitude of SDS and could be directly relevant to modelling studies for accurate estimates of dust aerosol effects. This information is significant for the overall understanding of dust sources in China. Specific 'Research Questions' and 'Research Objectives' in support of this aim are discussed in section 1.3.

1.2 Research Context

1.2.1 The Global dust Cycle: Climate Impacts and Hazards

Mineral dust aerosols are tiny soil particles (usually <100 µm in diameter) suspended in the atmosphere (Kok et al., 2023) that are mainly derived from source areas within arid and semi-arid regions where annual rainfall is deficient (<250 mm/year; Washington et al., 2003). The life cycle of mineral dust particles suspended in the atmosphere is commonly referred to as the atmospheric dust cycle (Schepanski, 2018). As shown in Figure 1.1, the dust cycle involves a range of processes on various spatial-temporal scales, as the wind blows, dust particles are emitted from the dust source and then suspended in the air, then transported over long distances [via a SDS] and deposited to other dust source area (Bullard et al., 2011; Bryant, 2013).

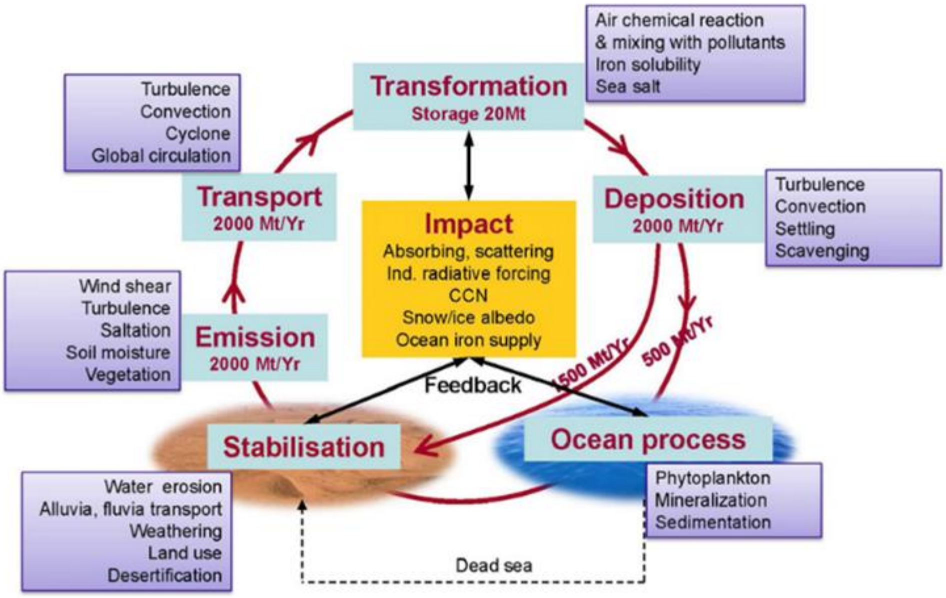

Figure 1.1 The dust cycle in the Earth System and the primary process in which dust plays an important role (Reproduced from Shao et al., 2011; Fig.2)

The interaction of dust cycles with biogeochemical cycles and direct and indirect radiation forcing of the atmosphere plays a vital role in the land-atmosphere-ocean system (Bryant, 2013). The emissions and deposits of dust are involved in a series of physical, chemical and biogeological processes that interact with the cycle of energy, carbon, and water (Ravi et al., 2011). Mineral aerosol can exert a primary impact on the energy balance of the Earth system through the absorption and scattering of radiation in the atmosphere and the modifications of the optical properties of clouds and snow/ice surfaces (Shao et al., 2011). However, dust also acts to disperse soil, which carries organic matter and iron and thereby contributes directly to the carbon cycle and ocean productivity and ocean-atmosphere CO_2 exchange (Ravi et al., 2011)

When mineral dust aerosol is in the respirable size (PM<10) it can cause health problems, including asthma, tracheitis, and pneumonia (Goudie, 2014). SDS have posed severe problems to downwind areas, causing house collapse, damaging power facilities, increasing traffic accident rates, affecting aviation safety, and even causing human and animal casualties (Terradellas et al., 2015).

The main dust sources areas were identified in deserts and semi-arid regions using filed and remote sensing data, including the Sahara Desert in Africa (Middleton and Goudie, 2001; Schepanski et al., 2007), the Middle East (Moridnejad et al., 2015; Gherboudj et al., 2017), Taklamakan Desert and Gobi Desert in East Asia (Cui et al., 2019; Chen et al., 2013; Wang et al., 2018), and parts of Australia (Baddock et al., 2009; Ginoux et al., 2012), and Americas (Baddock et al., 2011; Lee et al., 2012), see detail in Figure 1.2 from *Go et al., (2022).*

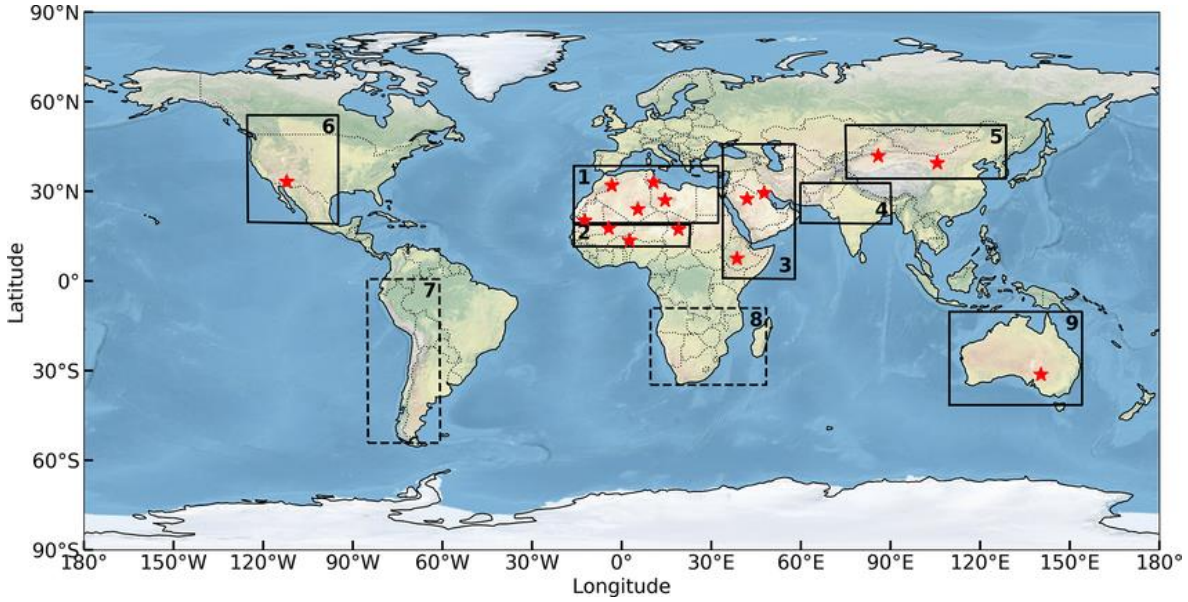

Figure 1.2 The main global dust-source regions: (1) northern Africa, (2) the Sahel, (3) East Africa and the Middle East, (4) Central Asia, (5) East Asia, (6) North America, (7) South America, (8) southern Africa, and (9) Australia. (Reproduced from Go et al., (2022); Figure 4)

The locus of dust activity in the dust belt shifts with the season caused by climate drivers, including North Africa to Middle East, southern Europe and East Asia (Yang et al., 2022). In North Africa, the winter SDS is most significant in the low latitudes and moves to the higher latitudes as the year progresses (Shi, et al., 2021). In the Middle East, activity peaks in the late spring and summer and is minimal in winter. The SDS activity extends to a peak in spring in Asia (Prospero et al., 2002). Yang et al. (2021) indicated that SDS paths' gradual movements are closely related to the northward movement of the Westerlies and monsoons over that region. Westerlies and Monsoon act on the SDS by influencing the climate conditions (Meng et al., 2020; Han et al., 2008; Lou et al., 2016).

1.2.2 Representation of the dust cycle in global climate models

Our understanding of the dust sources is primarily based on the information derived from a combination of dust field measurements (e.g., Webb et al., 2019), satellite and ground-based remote sensing (e.g., Prospero et al., 2002), and numerical models (e.g., Shao et al., 2011). These information sources are strongly skewed towards satellite and modelling outputs (Bryant, 2013), and results from the latter approach will be summarised here.

Dust models are able to represent the different components of the SDS cycle, including dust emission (e.g., Dust Observations for Models (DO4Models), Haustein et al., 2015), atmospheric transport (e.g., Hybrid Single Particle Lagrangian Integrated Trajectory Model (HYSPLIT), Gasso et al. 2010; Bao et al., 2023), and deposition process (Prospero et al.,2010). Global Model of Aerosol Processes (GLOMAP) is used in climate modelling to simulate the multi-component global aerosol (Mann et al., 2010). CMIP5 (Coupled Model Intercomparison Project Phase 5) models, such as HadGEM2-CC (Collins et al., 2011), calculated dust emission flux across different regions like North America and Australia (Taylor et al., 2012), showing remarkable progress in understanding the dust cycle. Kok et al. (2023) estimates a slight net cooling effect of dust aerosols on climate change, with a total effect of dust interactions on the global energy budget of Earth, the dust effective radiative effect being -0.2 ± 0.5 W m^{-2} (90% confidence interval), suggesting that dust net cools the climate. Kok et al. (2021a) concluded the relative contribution of each of the world's main dust source regions (Fig1.2) to the global dust cycle (Table 1.1).

Modelling of SDS from the 'Dust Belt' of the Sahara generated viable prediction results, primarily due to the fact that SDS for much of this region is only limited by transport capacity (windiness, Huneeus et al., 2011). Kim et al. (2017) notes that SDS from this region are closely correlated with 10-metre wind variability. In this hyper-arid location, seasonal soil moisture and vegetation variability are not significant inhibitors of SDS. Outside of the 'Dust Belt' models have to deal with a more complex suite of processes that can control SDS, such as soil texture, soil crusting, vegetation changes, and a range of human impacts (Kok et al., 2020).

Table 1.1 Constraints on the contribution of dust deposition from individual source regions to areas where dust deposition has significant effects, specifically the high-albedo regions of Antarctica, Greenland, and the Tibetan Plateau, along with the Amazon rainforest. Median values with 1 standard error interval. The coordinates of the Tibetan Plateau are between 26–40◦ N and 75–105◦ E, with elevation over 4000 m, including the Gonghe Basin. (Reproduced from Kok et al., 2021a; Table 2)

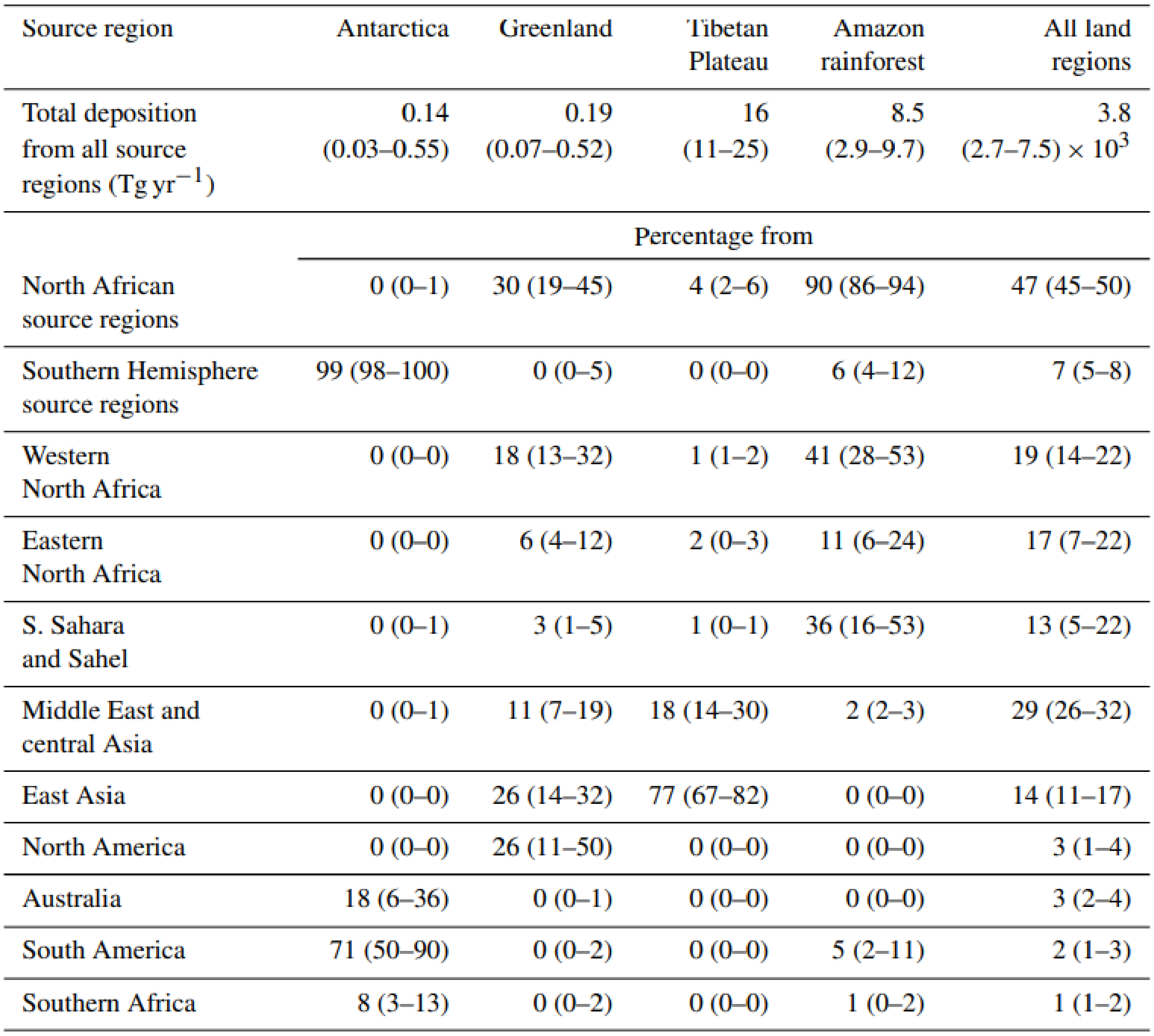

Source region	Antarctica	Greenland	Tibetan Plateau	Amazon rainforest	All land regions
Total deposition from all source regions (Tg yr^{-1})	0.14 (0.03–0.55)	0.19 (0.07–0.52)	16 (11–25)	8.5 (2.9–9.7)	3.8 (2.7–7.5) × 10^3
			Percentage from		
North African source regions	0 (0–1)	30 (19–45)	4 (2–6)	90 (86–94)	47 (45–50)
Southern Hemisphere source regions	99 (98–100)	0 (0–5)	0 (0–0)	6 (4–12)	7 (5–8)
Western North Africa	0 (0–0)	18 (13–32)	1 (1–2)	41 (28–53)	19 (14–22)
Eastern North Africa	0 (0–0)	6 (4–12)	2 (0–3)	11 (6–24)	17 (7–22)
S. Sahara and Sahel	0 (0–1)	3 (1–5)	1 (0–1)	36 (16–53)	13 (5–22)
Middle East and central Asia	0 (0–1)	11 (7–19)	18 (14–30)	2 (2–3)	29 (26–32)
East Asia	0 (0–0)	26 (14–32)	77 (67–82)	0 (0–0)	14 (11–17)
North America	0 (0–0)	26 (11–50)	0 (0–0)	0 (0–0)	3 (1–4)
Australia	18 (6–36)	0 (0–1)	0 (0–0)	0 (0–0)	3 (2–4)
South America	71 (50–90)	0 (0–2)	0 (0–0)	5 (2–11)	2 (1–3)
Southern Africa	8 (3–13)	0 (0–2)	0 (0–0)	1 (0–2)	1 (1–2)

However, most models oversimplify the processes and use unrealistic or qualitative input data. For example, Chappell et al. (2023) suggested that models overestimated SDS related to simplifying the Earth's land surface characteristics, not considering vegetation. Parajuli and Zender (2017) have studied how topography and hydrology affect SDS, singling out drainage areas and ephemeral lakes as key components. The main factors controlling the variable erodibility of surface erosion are (i) particle size, (ii) crusting level, (iii) soil moisture, and (iv) the formulas used to describe the relationship between wind speed and surface roughness (e.g., Boosted Regression Tree model, von Holdt et al., 2019)

However, the amount of global SDS is significantly different among various models, even in the same particle size range the difference is 4 or 5 times (Wu, Lin and Liu, 2020). Also, atmospheric models struggle to represent its spatial and temporal distribution accurately. These model errors are partially caused by fundamental difficulties in simulating SDS in coarse-resolution models and in accurately representing dust properties, e.g., size, shape, geochemistry and optical properties (Adebiyi and Kok, 2020). Adebiyi et al. (2023) found that coarse and super-coarse dust particles are transported farther than previously expected, which has implications for climate and air quality. Shi et al. (2016) note that most of the factors controlling SDS operate at scales below the landscape scale. Kok et al. (2021b) uses inverse modelling to improve the representation of the global dust cycle using observational constraints on dust properties and abundance, leading to better agreement with independent observations of dust optical depth (DAOD) and dust deposition. Leung et al. (2023) propose a new process-based and scale-aware desert SDS scheme for global climate models. They propose a straightforward methodology to rescale lower-resolution SDS simulations to match the spatial variability of higher-resolution simulations. Chappell et al. (2023) found that albedo-based SDS model (AEM) models showed strong spatial relations to the Dust Point Source (DPS). Inherent seasonal and diurnal variability in SDS from source regions and apparent spatial heterogeneity of dust sources remains poorly constrained in global and mesoscale models due to inexact source allocation and quantification (Vickeryet al., 2013; von Holdt et al., 2019; Bullard et al., 2011; Bryant, 2013; Haustein et al., 2015).

In this thesis, my work from regional, basin to sub-basin scale could help to characterise SDS processes better and also provide a more realistic basis for modelling efforts that are able to resolve scaling issues caused by inherent dust model simulation bias and spatial heterogeneity (Webb and Strong., 2011) and to improve the representation of dust in climate models.

1.2.3 Study Area: The Gonghe Basin in China

The Gonghe Basin is about 13,800 km^2 in area and is located on the northeast edge of the Tibet Plateau (TP, Figure 1.3). It is known as a significant dust source and transportation corridor in this region (Bi et al., 2017). The elevation of the Gonghe Basin is between 2400 to 3200 metres, and is cut by the Yellow River (Miao, Ni and Borthwick, 2010; Miao et al., 2016) and contains various known aeolian geomorphic units (Dong et al., 2017a), facilitating the eastward transport of SDS. Similar to other dust sources in North China, Sand and Dust Storms (SDS) occur mainly in the winter to early spring in the Gonghe Basin, between December and April (Bi et al., 2017; Dong et al., 2017b).

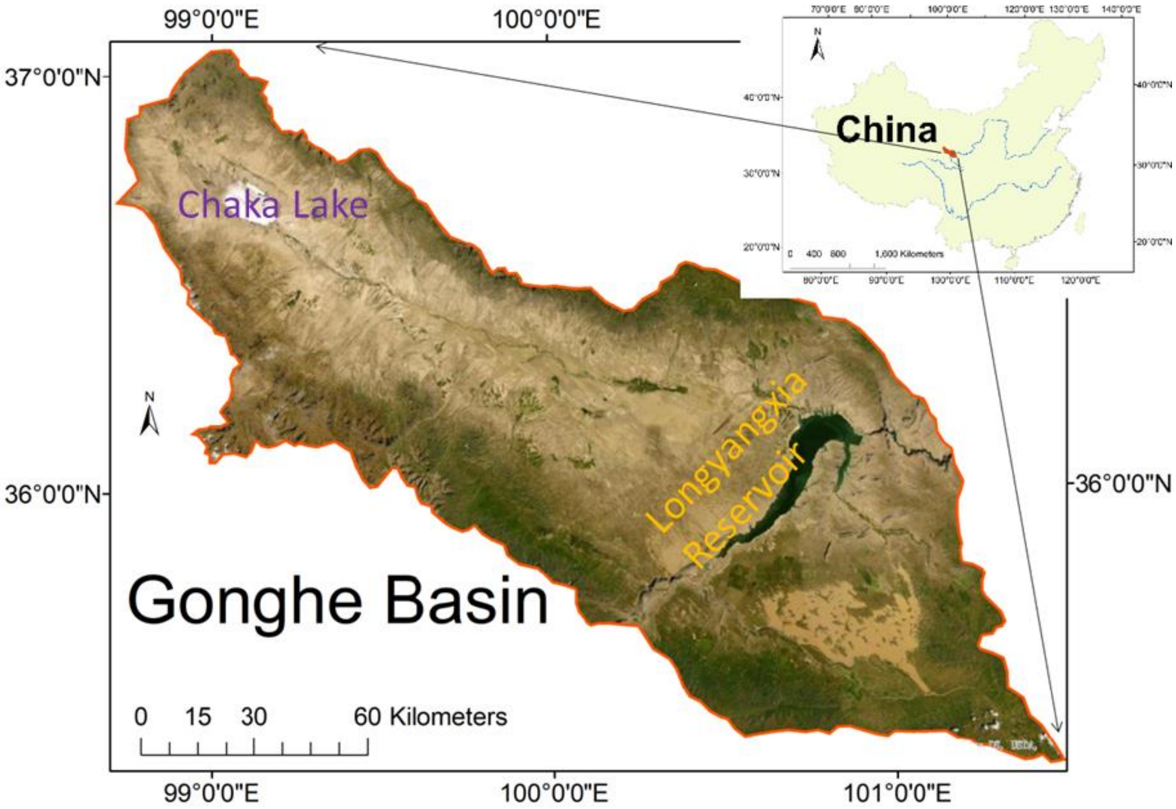

Figure 1.3 Research area of the Gonghe Basin and its relative position in China. The base map is derived from the Planet Monthly Basemap. Chaka Lake is a salt and ephemeral lake and Longyangxia Reservoir.

Wind environment is dominated by the Asian monsoon and westerlies during summer and winter in this region (An et al., 2012). The impact of the Westerlies during the spring and winter seasons leads to a heightened intensity of the sand drift potential (DP) and during summer and autumn, the winds of the East Asian Summer Monsoon (EASM) originating from the southeast contribute to a weakening of the Resultant Drift Potential (RDP) while not reversing the prevailing wind direction, which generally flows from the northwest (Dörwald et al. 2023). Thus, a westerly wind direction is typical of the year-round pattern of atmospheric circulation and transport across the basin (Xu et al., 2022). In the winter, due to mountain-blocking on the QTP, the high-level westerlies are generally divided into two zones, and jets generally move northward in summer (Schiemann et al., 2009). Wind velocity, magnitude and direction can vary significantly on a seasonal basis, impacting dust transport height, direction and duration (Zhao et al., 2010). The basin is highly sensitive to climatic change due to its high altitude and semi-arid climate (Qiang et al., 2016). Regarding climatic conditions, the mean annual precipitation in the Gonghe Basin is 280-350 mm (Qiang et al., 2013; Dong et al., 2017a), and up to 80% of the annual total rainfall occurs between May and September. Precipitation is closely related to the intensity of the EASM in this region (An et al., 2012). During the dry season between October to April, there is little precipitation due to the presence of the Mongolian high pressure and the downdraft system (Dong et al., 1993).

In terms of likely sources of dust within the Gonghe Basin, the landscape is dominated by shifting, semi-fixed and fixed sand dunes, ephemeral lakes, stone pavement and a range of alluvial surfaces (Liu et al., 2013; Dong et al., 1993), with sparse vegetation at the surface (Qian, Quan and Shi, 2002). Saltation and sand transport are apparent (some of the solitary dues are active), and aeolian deflation of surface sediments has caused enormous blowouts, which are thought to have been initiated in the Little Ice Age climate period (Luo et al., 2019a). Since the late Quaternary, fluctuation in the activity of lakes and aeolian sediments has developed in the Gonghe Basin, which provides an essential basis for understanding past climate change in the region (Dong et al., 1993). The basin began accumulating sediment during the early Miocene, at 20 Ma and lasted until the early Pleistocene to middle Pleistocene (7 Ma, Qiang et al., 2016). The extensive development of dunes in the basin follows the relative availability of sand sediment in this period (Zongyan et al., 2018). The basin structure has risen slowly, about 500 m relative to the Yellow River (Figure 1.4, reproduced from Luo et al., 2019b), caused by fault deformation in the late Pleistocene (7-12 Ma; Xu et al., 1984). An obvious eastern residual plain appeared after the incision of the Yellow River, exposing a set of fluvial sediments (extremely thick strata deposited in the early Quaternary; Ding, Zhao and Dong, 2010), which provide rich fine-grained materials for dust emissions and deposition (Luo et al., 2019b).

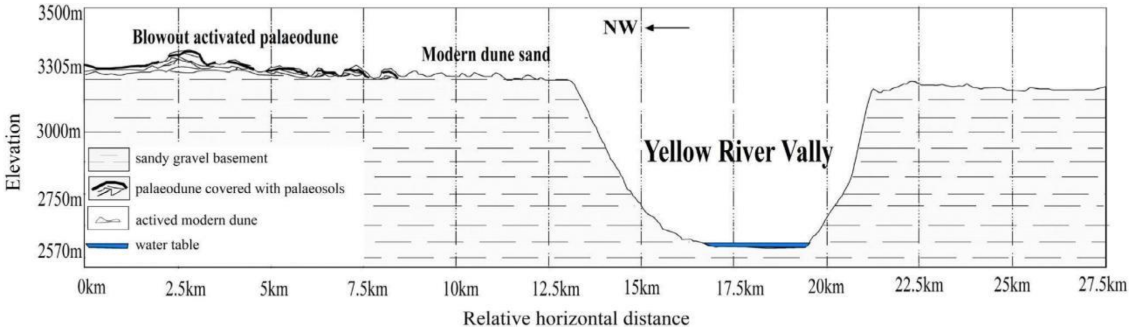

Figure 1.4 Landform profile of Yellow River, Gonghe Basin. (Reproduced from Luo et al., 2019b; Figure 2A).

As noted previously, the Gonghe Basin contains a significant surface cover of wind erodible materials, which can become available and transportable due to low precipitation and strong winds allied to the apparent impacts of ongoing land management. Dong *et al.* (2017) documents the size distribution, geochemistry and mineralogy of aeolian sediments in each basin of the Tibet Plateau influenced by local sources. The mean grain size of sediment within the Gonghe is about 0.125 mm (Dong et al., 1993), with a significant component of coarse silt and clay fractions.

1.2.4 Understanding long-term variability in SDS; Use of meteorological, LEO and contextual data

1.2.4.1 Known climate drivers for SDS: Asian Westerlies [AW] and the East Asia Summer Monsoon [EASM] since Quaternary and Holocene

Reviewing the environmental changes of the aeolian surface in the whole geological period helps understand the driving mechanisms of environmental change, the modern surface process and future environmental change trend in the semi-arid areas (Yang et al., 2011; Lancaster, 2022).

The mid-latitude Asian continent can be roughly divided into two distinct climatic regions: the monsoon-dominated south-eastern Asian region and the westerly belt-dominated arid Central Asian region (i.e. by north-western China and Central Asia; Huang *et al.*, 2013, Chen et al., 2019). The Gonghe Basin is in a sensitive semi-arid zone at the junction of these two atmospheric circulations (Figure 1.5). At the same time, Gonghe Basin is also an essential part of the desert-loess transition zone with a fragile landscape (Liu *et al.*, 2013). It is a region controlled by the EASM (wet) and influenced by westerly winds (dry) at the same time. The EASM circulation reaches the region in summer (JJA), while the westerly climate dominates in winter (DJF) (An et al., 2012). Cui et al. (2021) identified that AW winds are likely to be associated with climate change in the North East of the QTP (high altitude). Previous studies have shown that 700 hPa (~3000 m) is a threshold height for temperature and pressure contrasts between the east and west sides of the QTP. Below this threshold altitude, the winter monsoon strongly influences the wind field in winter, while the westerlies are the dominant wind regime above this height (An et al., 2012). Thus, the East Asian Winter Monsoon does not have a direct influence on the variability of the 10 m wind field in the north-eastern QTP (which includes the Gonghe Basin), where the westerly winds dominate in January, and the EASM dominates in July. The simulation results of PMIP2 show that the 10 m wind field and 600 hPa wind field during LGM are similar to those of modern times, so the review of LGM dust is of reference significance for modern dust environments and changes (An et al., 2012).

Aeolian activity in the Gonghe Basin was particularly significant in the Last Glacial Maximum (LGM) and early Holocene (Qiang et al., 2013); both loess and aeolian sand (sand sheets) formed in this period (Xu et al., 2022). LGM refers to the last glacial period closest to the present, with the ice sheet at its maximum extent (LGM, c. 31-16 Ka). An et al. (2012) applied a drill core from Qinghai Lake to show that this region was dominated by mid-latitude westerlies (32-20 Ka) during the LGM, and the intensity and variability of the westerlies were significantly greater than in the Holocene. Thus, the northeastern part of the Qinghai-Tibet Plateau was dominated by a dry and cold environment accompanied by windy weather. Then, the westerlies gradually weakened, accompanied by an intensification of the EASM from 20 ka onwards, especially after 11.5 ka. For example, high water levels in the Chacha Salt Lake within the Gonghe Basin could be used as evidence of intensified Asian summer winds between 17.2 and 11.4 ka, where EASM led to higher temperatures and melting glaciers, increasing water supply (Xingqi et al., 2008).

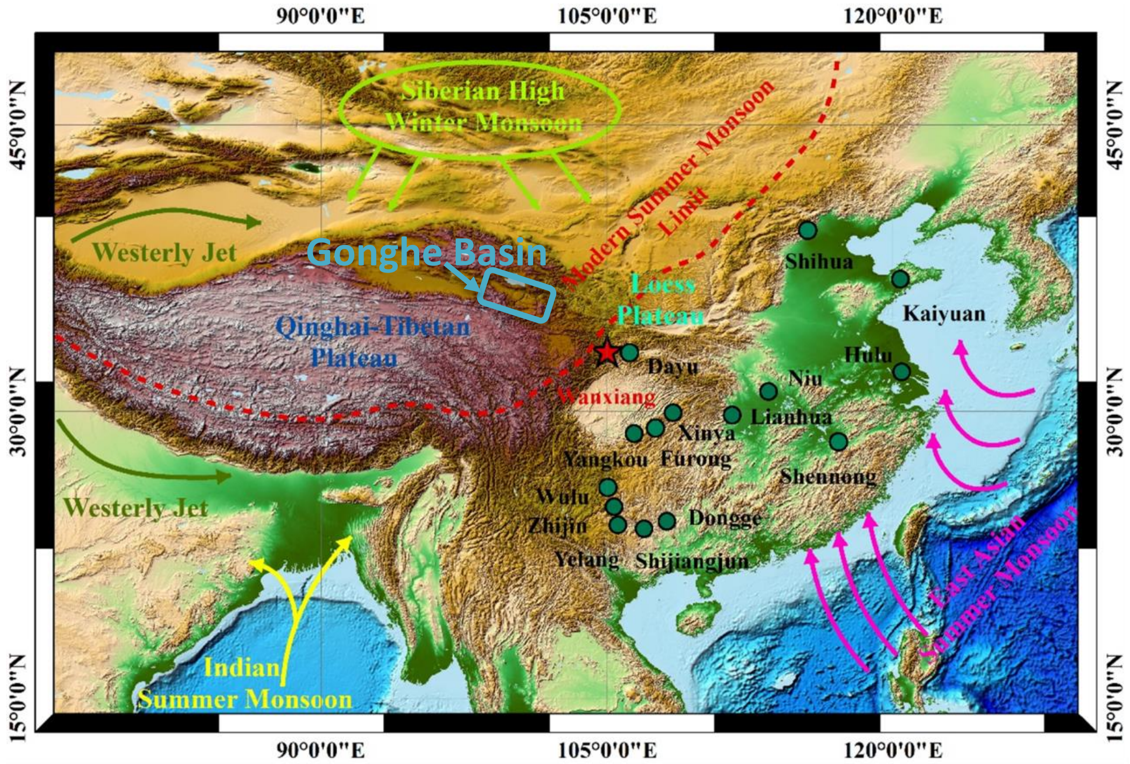

Figure 1.5 Westerly and Monsoon influenced Area in China, also indicated the location of the Gonghe Basin (Blue). The dashed red line illustrates the approximate northwestern extent of the modern summer monsoon (Reproduced from Jia et al., (2022); Figure 1). Arrows depict the Asian Monsoon (including East Asian Summer Monsoon (magenta) and Indian Summer Monsoon (solar yellow). Westerly (dark green) and winter monsoon (light green) are also marked on the map.

Surface aeolian geomorphic changes in the Gonghe Basin have been recorded by environmental records via thermoluminescence dating (e.g., Zeng et al., 2003) and lake sediment core reconstruction of the hydrological evolution from the Chaka Salt Lake (e.g., Xingqi et al., 2008). During the Late Pleistocene to Early Holocene (12-9 ka), the area was dominated by a dry thermal environment, with effective humidity (Evaporation-precipitation balance) maintained at low levels, accompanied by large amounts of aeolian sediments and sparse vegetation (Liu et al., 2020). Detailed Luminescence dating results from the basin also support the increased dune activity caused by low effective humidity in Gonghe Basin and its adjacent areas from the late glacial to early Holocene. The formation of saline lakes in the early Holocene suggests increased temperatures may have triggered high evaporation due to increased summer insolation (Xingqi et al., 2008). The Chaka Salt Lake closed its surface outflow, suggesting warm and dry conditions during the first half of the Holocene. At the same time, the winter monsoon forced by residual ice cover is consistent with a record of stronger winter winds in northwestern China (Liu et al., 2018; Qiang et al., 2010).

Since post 9-8 ka, there has been a significant increase in regional humidity, accompanied by sharp decreases in summer temperature and the East Asian winter Monsoon (EAWM) and increase in vegetation and soil development (Liu et al., 2020). The impact of the EASM in the region did not increase until about 8 ka (Dyke, 2004; Lu et al., 2013). The peak value of the EASM in northern China has a lag response of thousands of years in summer, and the high rainfall of the summer monsoon begins at about 8-7 Ka (Mason et al., 2009). Thus, the change from a humid climate to a dry climate, effective humidity in this region can be explained by the fluctuation of the intensity of the EASM (Liu et al., 2012; Xiao et al., 2002; Yang et al., 2012; Qiang et al., 2014).

It is also concluded that after 8 Ka, lower temperature and reduced evapotranspiration lead to the stability of aeolian sand, even the development of paleosol and increased vegetation. The dating results of aeolian sand sediments in the dune area of northern China also support the enhancement of the East Asian summer monsoon (EASM) during the middle Holocene, vegetation coverage and shrinking desert area (Zeng *et al.*, 2018). Aeolian sediment accumulation is associated with dry climatic conditions, whereas loess accumulation is a shift to more humid climatic conditions (Yu and Lai, 2014). Loess is a periglacial or aeolian (windborne) sediment composed largely of silt-size grains that are loosely cemented by calcium carbonate (Lehmkuhl et al., 2021). In the middle Holocene (9-4/3 Ka), aeolian sand was replaced by paleosols, which confirmed the optimal humid environment of the Gonghe Basin (Liu et al., 2020). During the Holocene, the desert area in Northwest China and central North China decreased by about 5% - 20% (Lu et al., 2013). Fixed ancient dunes and active dunes are the main dunes in the Gonghe, formed on the basin's surface during the Holocene dry periods 6 Ka and 3 Ka, respectively (Luo et al., 2019b).

In the late Holocene, the weakening of the EASM led to reduced precipitation and a significant decrease in effective humidity, accompanied by a decline in summer temperature, precipitation and vegetation coverage. The climate has tended to be relatively dry, accelerating the formation of higher salinity lakes in the Chaka Salt Lake (Xingqi et al., 2008). Accordingly, the loess was replaced by aeolian sand, and the peak value of intense dune activity appeared at about 3.5 Ka and 1.5 Ka. Specifically, Qiang et al. (2017) found a response of 5.3-4.8, 3.7-3.4, 2.8-2.3, 1.7, 1.3 Ka for the strengthening of the mid-latitude westerlies, with variations indicating a significant positive correlation between westerly jet and dune activity (Han et al., 2008). Meanwhile, a short humid interval of about 2-1Ka was present in the late Holocene, evidenced by the alternation of aeolian sentiment and paleo-losses in the Gonghe Basin (Stauch et al., 2018; Liu et al., 2020; Hu, Feng and Li, 2019). High drought periods coupled with high wind speed can lead to frequent cycling of aeolian sediments (Stauch et al., 2018).

Overall, the alternating effects of the EASM and Westerlies have played an essential role in determining atmospheric circulation patterns and SDS activity in the Gonghe Basin over a long period. An investigation of the northeast of TP during the Quaternary and Holocene provides the framework for understanding the aeolian environmental evolution of the Gonghe Basin. However, there is no agreement on the Holocene paleoclimate evolution of the Gonghe Basin. Further, to examine the westerlies and EASM on decadal timescales, we built the time-series of dust-related climate factors record from the Merra-2 model between 1980 to 2022 and focus on how regional dust activities responded to climate anomalies and westerlies and EASM.

1.2.4.2 Contemporary Factors Influencing SDS at the Regional Scale

- *Observations of SDS in the Past 50 Years*

Numerous studies have been conducted to explore the various potential driving factors of SDS. Surface conditions of the dust source and the wind velocity in the near-surface layer are generally recognised as the two main reasons causing variations in SDS's frequency and distribution (Liu et al., 2021). Both reasons are closely related to global climate change (An et al., 2018). Middleton (2019) suggested that most dust sources are associated with topographic lows characterised by deep alluvial deposits, playa and dunes. Although geomorphic conditions mainly control the spatial variation trend of dust flux and dust particle size, the monthly variation trend is mainly affected by climate (East and Sankey, 2020). Kang et al. (2016) determined that the decline of surface wind speed is part of the reason for the decrease of SDS through the analysis of the records of SDS by the surface meteorological stations on the QTP from 1961 to 2010. The uneven distribution of solar radiation on the earth's surface leads to the spatial difference in atmospheric temperature and pressure, forming a horizontal pressure gradient, and atmospheric flow produces winds of different intensities (Cui et al., 2018). Threshold friction velocity associated with SDS refers to the surface friction velocity above which soil erosion begins and which is determined by a combination of natural, e.g., precipitation, wind velocity, soil moisture, soil properties, vegetation and anthropogenic conditions (Foroutan et al., 2017). Zhao et al. (2006) used the Northern Aerosol Regional Climate Model to analyse the interannual variability of spring SDS from 1960 to 2003, and according to their findings, the impact of surface wind speed on dust production is more significant than that of precipitation and surface temperature in Asia. Dörwald et al. (2023) utilised the ERA-5 datasets to assess the sand drift potential (DP) and resultant drift potential (RDP) values in the Gonghe Basin covering the period from 1968 to 2019. Their findings indicate a notable decline in DP values from the north-western to the south-eastern regions, corresponding to the observed dune migration rates. The average dune migration rate is estimated at 7.3 m a^{-1}, with an overall reduction of -1.81 m a^{-1}. Additionally, the RDP values for the Gonghe Basin were calculated to be below 10 m^3 s^{-3}, exhibiting a spatial decrease from the northwest to the southeast, which aligns with the diminishing migration rates.

Precipitation reduces SDS by suppressing emissions when snow covers the potential dust source areas and increasing soil moisture when snow melts (Tanaka et al., 2011). In addition, precipitation reduces SDS in other seasons by affecting soil moisture and vegetation conditions in dust source regions (Lou et al., 2016). Han et al. (2009) used the observation data of SDSs and the Cloud-Aerosol Lidar and Infrared Pathfinder Satellite Observation (CALIPSO) satellite to explore the significant negative correlation between precipitation and dust aerosols in QTP. The effects of temperature on SDS are complex, with both positive and negative correlations existing simultaneously (Namdari et al., 2018; You et al., 2010). Several studies have shown that changes in relative humidity are the main factor influencing surface soil moisture, which in turn significantly impacts the threshold friction velocity (Cui et al., 2019). The climate in the source regions directly affects vegetation cover, which plays a crucial role in the wind erosion system. However, human activities also have similar effects on vegetation and other determinants of surface erodibility.

- *Possible Human Impacts on SDS Occurrence*

SDS is controlled by regional climate and has a long history of links to human activity and land use in northern China. Human activities appeared around 8 Ka (Miehe et al., 2014) in the Gonghe Basin. Huang et al. (2017) utilised pollen analysis of a sediment core obtained from Genggahai Lake, a shallow lake situated in the central region of Gonghe Basin, to assess the level of human influence on the local vegetation during the middle and late Holocene. The identification of Stella, a marker indicating the degree of grassland degradation caused by grazing activities, in the sediment samples from Gonggahai Lake indicates that the impact of livestock grazing on the degradation of grasslands commenced at approximately 4.7 ka. They concluded that heavy human grazing accelerated the process of grassland degradation at QTP from 3.6-3.0 ka and an even greater intensity by human settlement from 1.6 ka to the present. In terms of farming, Hou et al. (2018) present two significant phases in the Gonghe's environmental history. The first phase, known as the Middle Holocene Humid Phase (6300-5000 aBP), marks the introduction of primitive millet farming to the basin with increased humidity. The second phase, referred to as the Late Holocene Fluctuation Phase (3900-2900 aBP), witnessed a mean annual rainfall of approximately 240 mm and the development of a stable farming-pastoral economic pattern. Currently, Gonghe has an intricate composition of aerosols more pronounced caused by human activity, e.g., grazing, farming and cities.

Human activities via modified land use types and water usage influence wind erosion. Bi et al. (2017) found frequent SDSs and local anthropogenic emissions in the 2012 Spring contributed to dust aerosol fluxes from the Gobi Desert. Wang et al. (2018) estimated the contribution of anthropogenic dust columns in disturbed soil to the observed total dust. According to multi-satellite retrievals, in the total SDS in eastern China from 2007 to 2014, the contribution rate of anthropogenic dust in near desert areas was less than 9.2 %, but as high as 76.8 %. The investigation on the impact of land use on SDSs reveals that changes in land use, such as agricultural practices (Galloza et al., 2018), have a significant influence on relative humidity and groundwater runoff (Xi and Sokolik, 2016). Additionally, they affect surface soil moisture and threshold friction velocity (Ravi et al., 2004) while also exerting an influence on the seasonal variability of SDSs in northern China (Liu et al., 2021). Using the geographic detector model, Liu et al., (2021) identified strong winds and dry ground conditions as the main driving factors of SDSs in spring in northern China. In summer and autumn, human factors significantly impact SDSs. They found that the frost period and relative humidity in winter are the main factors affecting the occurrence of SDSs.

Wu et al. (2016) used Landsat images to identify the changes in the areas of lakes in the Gonghe Basin from 1953 to 2013. The results show that (i) From the 1950s to the 1980s, the total area of lakes (Lake Dalianhai, Lake Genggahai, and Lake Yindehai) in the Gonghe Basin decreased significantly. Mainly due to human activities, including the development of farmland in the context of the increasing population. The region's climate data also show a slight drying trend as the temperature rises slightly during this period. Several reservoirs were built simultaneously, so a considerable part of the runoff was redistributed to irrigate farmland, resulting in the lake's shrinkage. (ii) The cultivated land area and population size remained similar after 1990. Climatic factors (precipitation and temperature) mainly control the changes in the lake area. Lake expansion occurs in years with relatively high precipitation and relatively low temperature.

In summary, according to the dynamic dust theory of Bullard et al., (2011), human activities affect SDS by changing the availability and supply of fine dust particles. Specifically, human activities have changed the state of the surface, for example, heavy water use for agricultural irrigation has increased vegetation in some areas, transient lakes (Chaka Lake) have exposed more areas of sand with fine and corrosive particles, and livestock grazing has reactivated the stable surface (fixed dunes) to discharge dust.

1.2.4.3 Use of LEO Remote Sensing AOD & AE products for dust detection

The influence of atmospheric aerosols on solar and atmospheric radiation is significant in climate change (Myhre, 2009). However, the regional and global effects on climate are still uncertain because of their significant heterogeneity in temporal and spatial distribution (Pathak et al., 2012; Knippertz and Todd, 2012). The heterogeneity is caused by different types of aerosols, various sources, and their short residence time in the atmosphere (Mark, 1969; Schepanski, 2018). Remote sensing provides an opportunity for large-area retrieval and characteristic analysis of aerosols (e.g., Parajuli, Yang and Kocurek, 2014; Ginoux et al., 2010). Different methods have been proposed for different combinations of MODIS sensor bands to detect dust, for example, using thermal emissive bands that correspond to MODIS and VIIRS to detect dust (Madhavan, Sun, and Xiong, 2021); Normalized Difference Dust Index algorithm, uses a spectral ratio between reflectance and near-infrared bands of the MODIS sensor to detect dust (Qu et al., 2006); Dynamic threshold supported SDS monitoring method suitable for changing conditions (Proestakis et al., 2018); and Dark-Target Algorithm: This algorithm is used to detect dust aerosols over oceans (Zhou et al., 2020). Arid regions primarily attributed mineral dust in aerosol products, but elsewhere, other aerosols absorb and scatter light more efficiently. Aerosols can be classified into several types: (i) Biomass-burning aerosols from forest and grassland fires, (ii) urban/industrial aerosols from fossil fuel burning in densely populated urban/industrial areas, (iii) dust blown into the atmosphere from dryland, (iv) aerosols from ocean origin and (v) mixed aerosol (polluted dust) represents an optical mixture of coarse mode dust with fine mode aerosols (Badarinath et al., 2007; Gharibzadeh et al., 2018). While arid regions primarily contain mineral dust in their aerosol products, other areas exhibit a higher presence of aerosols that efficiently absorb and scatter light. Distinguishing dust particles from other aerosols relies on retrieving spectral optical properties. The Gonghe Basin, being both a significant natural dust source and a densely populated region, requires additional information to differentiate between dust particles and those originating from anthropogenic sources.

Gharibzadeh et al. (2018) explore that one of the most effective methods to identify aerosol types is drawing AOD versus AE. Aerosol Optical Depth (AOD) and Angstrom Exponent (AE) are the most critical dust retrieval parameters. AOD is an index used to quantify the concentration of aerosols in atmospheric vertical dispersion columns (Qin et al., 2018). The AE index (or called α) is another parameter used to infer aerosols' particle size and absorption characteristics, and AE curvature analysis can also be used to distinguish aerosol types (e.g., Wang, Zhang and Draxler, 2009). Generally, Dust presents a bimodal size distribution with fine mode (particle size < 1.0 µm) and coarse mode (particle size > 1 µm, Schuster, Dubovik and Holben, 2006). Depending on their size, smaller particles will expand rapidly due to condensation, while larger particles will fall due to their weight (Liou, 2002). Coarse mode particles, ‘dust’ is referred to when AOD > 0.25 and AE < 0.7 (Kaskaoutis et al., 2011).

The dust size distribution allocated depends on where the dust is generated from and how far the dust is transported (Maring et al., 2003; Mahowald et al., 2014). Cheng et al. (2006) investigated the correlations between AOD and AE and found that a higher AOD was associated with the occurrence of SDS. They also observed that the Angstrom exponent decreased as the AOD increased during high SDS in the Hunshan Dake desert. Similarly, Yu et al. (2015) examined the relationship between AOD 440 nm and AE(α) and found that an α value smaller than 0.80 was accompanied by an increase in AOD 440 nm at Lanzhou. In summer, autumn, and winter, the mean AE was greater than 0.80, indicating that fine particles were the main contributors to aerosols due to the frequent anthropogenic activities at the urban sites in Lanzhou. Similarly, Pathak et al. (2012) concluded that the contribution of five different aerosol types varied with seasons, and winter predominated with the fine aerosol. By contrast, Liu et al., (2021) observed that in Xinjiang, which is in the northwest of China, the highest seasonal AOD occurs during the spring, accompanied by the lowest AE, indicating that dust particles are dominant during spring.

1.2.5 Understanding Climate Drivers of SDS; Monitoring sub-daily SDS events using GEO data

1.2.5.1 Remote sensing of dust sources detection

Given the paucity of field observations, most recent paradigms in the understanding of the dust cycle have been derived via the use of remote sensing data (Bryant, 2013; Bakker et al., 2019). Since most dust sources reside in dryland (desert) areas where many of these sites are inaccessible and insufficient meteorological stations are allocated there, field-based measurements are significantly scarce (Sagintayev et al., 2012). Therefore, remote sensing data offer an opportunity to fill this gap and provide a continuous spatial and temporal context for the observation of dust, collection data, and generation of SDS inventories at regional scales (e.g., Vickery et al., 2013; Lee et al., 2012). Several researchers have used remote sensing data to identify the location of dust sources (e.g., Prospero et al., 2002; Bakker et al., 2019), and systematically determine the geochemical variability of landforms and dust sources (e.g., Baddock et al., 2009), as well as the variability of entrained and transported sediments (e.g., Mahowald et al., 2005). Figure 1.6 summarises the various spatial-temporal distributions of existing satellite systems for dust emission and transport studies (Figure from Baddock et al., 2021, Figure 4), and we will address each of these processes in turn.

Initial observation of the dust cycle using remote sensing involved the use of the Total Ozone Mapping Spectrometer (TOMS, Fig 1.6A) with a spatial resolution of 1 degree. These data were first used by Prospero et al. (2002) and Washington et al. (2003) and involved aggregation of a time series of atmospheric dust loading data in space/time to locate the principal dust source regions at a regional/global scale. Further studies using these data were able to highlight the intermittency and interannual variability of dust emission from key source areas at large scale (e.g., Mahowald et al., 2003). Subsequently, Ahmad et al. (2006) explored the synergistic use of TOMS and the Ozone Monitoring Instrument (OMI) to refine maps of dust distribution at higher resolution.

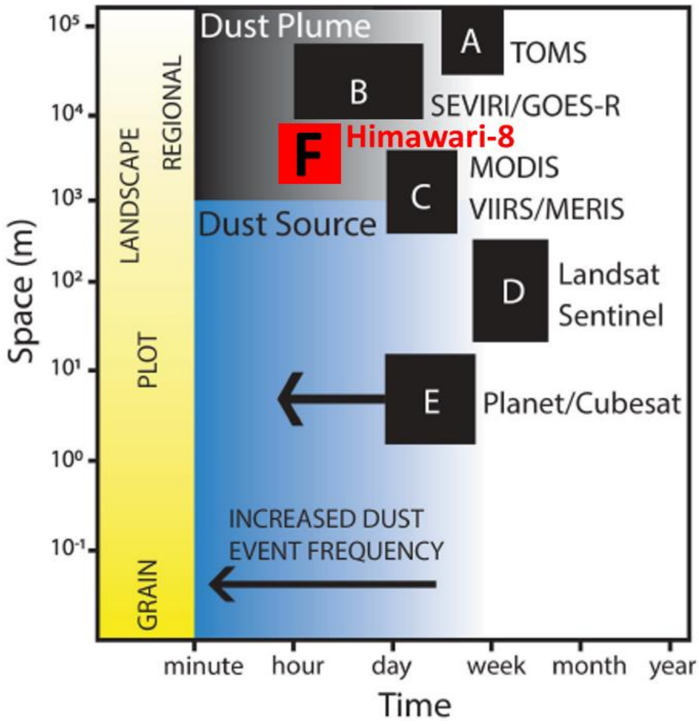

Figure 1.6 Time and spatial scales of dust emission and dust transport related to the monitoring/detection capabilities of existing satellite systems. (Reproduced from Baddock et al., 2021; Figure 4.)

Advances in the development and availability of remote sensing data between 2005-2015 also allowed workers to investigate the dust cycle at landscape scales where SDS could be initially linked to geomorphology and surface types (Bullard et al., 2008, 2011; Baddock, Bullard and Bryant, 2009). For example, the Moderate Resolution Imaging Spectroradiometer (MODIS, Fig 1.6C) sensor with sub-daily time sample, 0.25–1 km resolution and multispectral capability has enabled global and regional SDS chronologies to be mapped at the level of point dust sources over multiple years (e.g., Bullard et al., 2008; Walker et al., 2009; von Holdt, Eckardt and Wiggs, 2017).

Following on from this, quantitative dust products such as the MODIS deep blue aerosol optical depth (AOD) products allow daily mineral aerosol characterisation at 1 to 10 km resolution (e.g., Liu and Liu, 2015) via two aerosol parameters: (i) the aerosol optical depth, a measure of dust loading in the atmosphere (Kjeldsen et al., 2014); and (ii) the Angstrom exponent (AE), used (per wavelength) to describe the aerosol particle size distribution (Baddock et al., 2016). MODIS deep blue is especially useful for studying dust sources because the data can successfully retrieve dust even over bright deserts where many other satellite-based algorithms failed (Parajuli, Yang and Kocurek, 2014).

These moderate spatial resolution sensors (i.e., MODIS or VIIRS) identify that SDS is spatially localised. The limits of these data are that they only represent two overpass times in a day (10:30 or 13.30 local time), which means that SDSs can either be missed or tracked in transit, resulting in the number of dust storm days (DSD) and dust sources is either underestimated or poorly characterised (Schepanski et al., 2012). This problem highlights the importance of temporal sampling from higher-frequency data.

From 2010 onwards, geostationary (GEO) satellites (e.g., MSG-SEVIRI; Spinning Enhanced Visible and Infra-Red Imager, Fig 1.6 B) have been used extensively to detect SDS with a high temporal resolution every 15 minutes (e.g., Schepanski et al., 2012; Bakker et al., 2019). Hennen et al. (2019) found the higher temporal resolution GEO data observe more SDS, and compared to 60 min, the 15 min SEVIRI enables the observation of SDSs of shorter duration. SEVIRI has a moderate spatial resolution (c.3 km) but a high time sample (c. 15 minutes), allowing excellent detection of SDSs at the basin scale and similar source locations for dust location to MODIS (Murray et al., 2016). The widely used infrared RGB (red–green–blue) dust rendering scheme developed by Lensky and Rosenfeld (2008) for SEVIRI measurements to detect dust plumes. However, SEVIRI cannot quantify dust, another GEO data, Himawari-8 (Figure 1.6F), is a high-temporal satellite with 10-minute intervals of true-colour images and aerosol products that furnishes valuable insights into daytime SDS. Himawari-8 enables direct observation of dust source activation in sub-basin and sub-daily scale (She et al., 2018) and allows the monitoring of SDS processes, e.g., dust sources, emissions, and plumes. Also, the high temporal frequency GEO satellite demonstrates has the ability to constrain dust uplift timing, helping characterise meteorological processes (wind effect) in SDS in the sub-basin scale (e.g., Schepanski et al., 2009).

Landsat 8/9 and Sentinel-2 (Fig 1.6 D) are Earth monitoring missions launched by the Copernicus Programme and NASA. These data have been used to help map and interpret dust plume locations at the sub-basin and landform scale (e.g., von Holdt et al., 2017, 2019). The ability to use RS data to detect dust plumes and identify locations influenced by several factors, including radiative transfer characteristics of material releases, plume transport of ground or ocean surface radiative characteristics, the size and density of dust plumes (Baddock et al., 2009).

1.2.5.2 Meteorological Processes Leading to Dust Source Activation

The intensity of SDSs is mainly influenced by the surface winds generated by the prevailing weather system (Lu and Shao 2001). Sun et al., (2001) conclude that SDSs in China are associated with frontal systems and the height of Mongolian cyclonic depressions from an analysis of data on SDSs in China over the last 40 years. Frontal storms can be classified into prefrontal, and postfrontal and caused downwind dust transport called haze (Cao et al., 2018). The occurrences of Local Strong Sandstorms and haboobs are linked to severe convection weather processes, whether dry or moist convection in large-scale (Gu et al., 2021). Also, the undefined dust emissions process might link to human activity in the Gonghe Basin.

- (i) Haboob (Local Strong Sandstorms (LSS))

Haboobs are organised outflows of sinking air that blow dust plumes out of the source area. These dust plumes blown away by the storms then present a moving wall of dust that spans several miles and is thousands of feet high (Gu et al., 2021). Haboob are usually found in or near desert areas of the western United States and Africa (Raman et al., 2014). Haboobs in the United States occur mostly during the rainy season, followed by thunderstorms, whereas Habbob in China (or called Local Strong Sandstorms (LSS)), which are not seasonal, rarely accompanied by rain, are related to the relative humidity of the squall line formation related to the intrusion of cold air (Hu and Mitsuta, 1997). In China, LSS is caused by small- to medium-scale local intense convection, usually ranging from tens to hundreds of kilometres (Zhang and Li, 2003).

Strong winds caused by the intrusion of strong cold air masses have been widely recognised as the primary factor in the occurrence of SDSs. Evaporation of convective precipitation from deep, dry sub-cloud layers over desert areas may produce intense sinking air. As the cold air sinks, a large pool of cold air can form at the surface. When the cold air mass is strong enough, it can create a strong pressure gradient and promote atmospheric circulation. The subsequent unstable surface thermal stratification can facilitate the movement of updrafts, thereby enhancing their disturbance of the surface. The interaction between the radiative heating of dust and local atmospheric instability during the growth of a dry squall line may trigger the onset of LSS.

LSS events often occur in desert source and desert fringe areas such as Xinjiang, Gansu and Inner Mongolia in northwestern China, independent of differences in the physical properties of desert surface materials in different regions. The leading edge is a gust front that forms a wall of sand and dust storm front (He et al., 2020). During LSS events, the sky may be clear or cloudy. Visibility within the local SDS plume is less than 50 m. The boundaries of the sand wall are clearly discernible, and the cloud cover above is stable. When LSS occurs, the rising height of sand is not high, and the horizontal transport distance is short (Gu et al., 2021).

- (ii) Haze

Haze (or floating dust) is advected rather than locally emitted dust. Floating dust is the weakest of the three types of SDS events as defined by the Meteorological Observation Standard of the National Meteorological Administration of China (1979) and it is generally defined as a weather phenomenon where dust (<90 microns) is suspended in the lower troposphere with horizontal visibility less than 10 km. Haze mostly occurs when dust is transported by upper tropospheric air currents upwind or when a small amount of fine sand remains suspended in the air after a SDS has occurred (Wang et al., 2005). For example, Siyu Chen (2013) described an intense SDS event in the Taklamakan Desert with transport to the northern part of the Tibetan Plateau. SDSs are triggered by a strong cold front system approaching the Taklamakan while being influenced by the thermal action of the plateau and the weakening of the East Asian westerlies in July, thus facilitating the transport of dust from the Taklamakan to the Tibetan Plateau.

- (iii) Fontal System.

SDSs are caused by the passage of cold fronts, ranging from hundreds to thousands of kilometres (Filonchyk, 2022). In Australia, Baddock et al., (2015) found that when fronts move across the continent, the prefrontal northerly winds that precede them are usually strong enough to raise dust ahead of the front. The arrival of a front is usually associated with well-developed westerly winds, which can potentially entrain substantial amounts of dust. These westerly bands can raise dust along roughly north-south aligned extensions and are characterised by rolling SDSs often hundreds of kilometres long. This mechanism tends to produce the most significant SDSs in the Gonghe Basin (Jia et al., 2015). Finally, the post-frontal winds can also entrain dust if they are strong enough to exceed the threshold for suspended surface sediment. According to Adachi et al. (2007), the occurrence of a westerly wind within the cold sector of a cold frontal system in China results in the generation of SDS. This SDS is then propelled towards the cold front, where it subsequently divides into two primary flows that run parallel to the front. One of these flows moves towards the centre of the cyclone, while the other moves in the opposite direction. In the Gobi Desert of northern Gonghe, the presence of cold air, typically caused by Siberian and Mongolian cyclones, consistently sweeps through Mongolia and Inner Mongolia and extends southeast and northeast into areas such as Ningxia, Shaanxi, Shanxi, and Hebei Province (Wang et al., 2011).

- (iv) Unidentified Processes

Human activities increase SDSs mainly by increasing the exposure of soils to the atmosphere, thus creating a greater potential for wind erosion. Unidentified Processes occurs mainly during the transformation of wild landscapes into agricultural landscapes (Hooper and Marx, 2018). The unidentified processes are usually an independent event, with short-duration SDS triggered by human activity. It can be caused by anthropogenic mechanised operations related to grazing, agriculture, landscaping, and the solar industry. The mechanical unidentified processes cause fixed sand dunes to become active; Vegetation cover and soil stability are disrupted; Surface water levels are reduced by agricultural watering, etc (Micklin, 2007).

1.2.6 Understanding Controls on SDS; linking observed SDS plumes to a geomorphological framework

1.2.6.1 Controls on SDS in source areas

The presence of non-erodible roughness elements, such as vegetation, plays a significant role in determining the susceptibility of a landscape to wind erosion (Webb & Strong, 2011). These elements not only affect the wind erodibility of the landscape but also influence the erodibility of its soils. Consequently, the scale of a wind-erodible area can vary depending on changes in roughness elements, such as alterations in vegetation cover due to growth, senescence, or harvesting, as well as shifts in wind strength and direction (Chappell et al., 2010). These changes can occur over seasonal, interannual and longer-term cycles (e.g., where climate drivers such as ENSO are key). As Figure 1.7 suggests, the wind-erodible component of a landscape is, therefore, likely to vary naturally in both space and time. By inference, human activities can also impact and amplify these changes (Bryant, 2013).

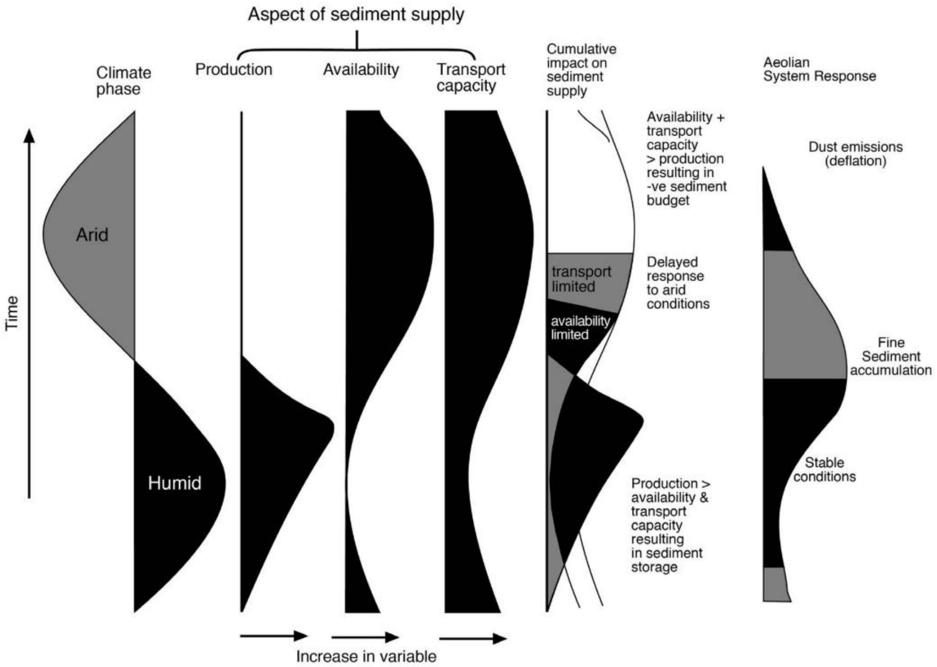

Figure 1.7 Model of the impact of humid-arid phases on the fine sediment production/ availability and transport and the response of the aeolian system (Reproduced from Bullard et al., 2011; Fig.1)

Within this context, SDSs are primarily driven by saltation, which is itself is constrained by a combination of vegetation, mechanical disturbance and geomorphology (including surface soil properties: particle size distribution, soil moisture, and roughness; Shao et al., 2011; Ravi et al., 2011). The controls on wind erodibility and SDSs from soils vary in space and time. Webb and Strong (2011) provide a context for the spatial scales at which these controls operate (Figure 1.8), working from the **grain scale** $<10^{-2}$ m, to a **plot (sub-basin) scale** 10^{1} m, **landscape** (basin) 10^{3} m and **regional scale** $>10^{4}$ m. Figure 1.8 also highlights how human activities, such as Agriculture, grazing, and industry, can influence sediment supply and availability via changes to surface hydrology and land usage (e.g., Webb and Strong, 2011). Agricultural areas often allow sediment to become available during unvegetated, dry seasons (e.g., Lee et al., 2012). However, Figure 1.8 is a conceptual model of fine sediment production/availability and transport and the response of the aeolian system. Until recently, the SDS dynamics have not been quantified or well understood (Galloza et al., 2018). Equally, where coarse-resolution remote sensing data have been used to detect SDSs at the basin scale, the processes driving dust uplift have only been inferred (Webb & Strong, 2011), so even in these cases, the SDS process has yet to be constrained.

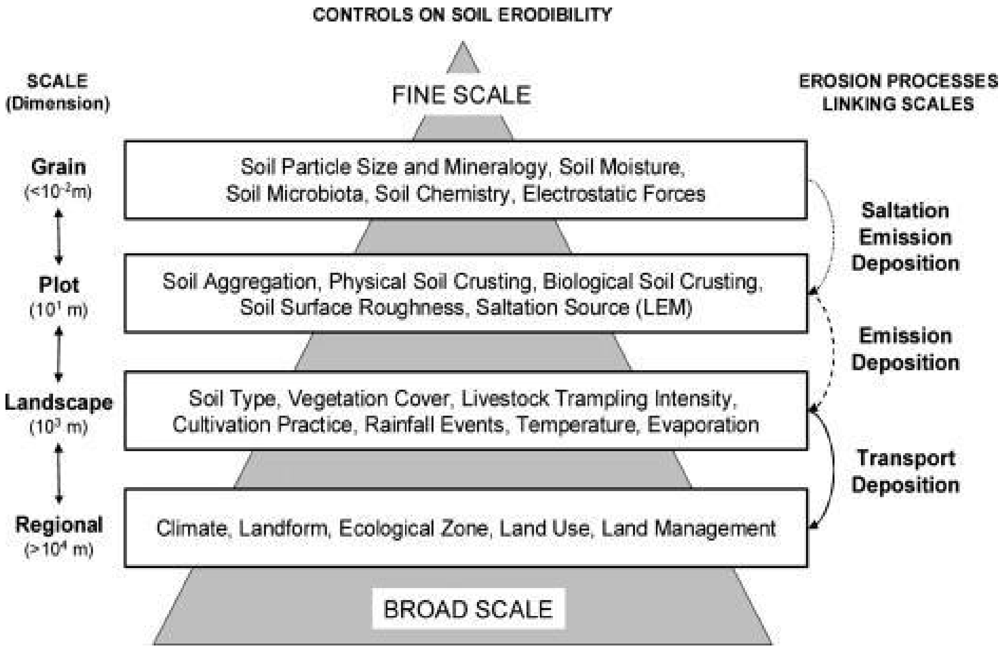

Figure 1.8 Controls on soil erodibility at different spatial scales with erosion process connect the scale. (Reproduced from Webb and Strong, 2011, Fig 2)

Controls on the SDS processes operate at plot scales, which are likely to be preferentially linked to specific geomorphology and surface types (Bullard et al., 2008; 2011). However, Webb and Pierre (2018) suggest that the ability to quantify the impact of Land Use and Land Cover (LULC) changes on wind erosion has been limited by using moderate-resolution data and low-precision landform classifications. One way of overcoming these difficulties is using newly available high spatial/temporal data (e.g., Planet and Sentinel-2), which have become available since 2017. Thus, we will focus on the sub-basin scale to explore controls on the emission processes.

1.2.6.2 New opportunities for observing SDS at the sub-basin scale

Based on Webb and Strong (2011) and Haustein et al. (2015) studies on the spatial-temporal scale of emissions, Baddock et al. (2021) refer to a ‘scale limit’ (c. 10-metre and <1 day) that provides the highest spatial and temporal resolution RS data for capture surface erodibility heterogeneity. As Figure 1.6 shows, most current dust remote sensing samples did not meet the spatial limitation scale (10 m) and time (daily or hourly) requirement for SDS emission processes. Recently, ‘CubeSats’ miniaturised and multi-platform satellite constellations were developed (CubeSats, 2023). PlanetScope (Fig 1.6 E) sensor is one such novel CubeSats constellation, with an extremely high spatial resolution (3-5 metres) daily, and the processed data, images in four bands (Red, Green, Blue, and Near-Infrared), available for download within a short time (<24 hours). PlanetScope offers a valuable tempo-spatial limiting balance in using remote sensing to observe dust. Baddock et al. (2021) conducted a case study demonstrating PlanetScope has extraordinary dust plume capture ability, found numerous discrete point sources than MODIS and visualisation plumes in detail consistent with the field measurement in the Chihuahuan Desert, Mexico.

The recent study by Baddock et al. (2021) highlights the capability of PlanetScope, which provides highly detailed spatial images, to accurately capture the spatial variability of emissions in the MODIS single class. This is particularly valuable in accounting for the variations in emission potential that can be observed in the field (e.g., von Holdt et al., 2019; Cui et al., 2019). The dynamism of dust source regions in space and time and the associated magnitude and frequency of SDS that we can measure have led to the conceptualisation of three different modes of operation for dust sources at the sub-basin scale: (i) **transport**

capacity limited (TCL), where erodible sediment is available, but wind strength is too low to entrain particles, (ii) **supply-limited (SL**) or called exhaustion where restricted by whether the region has suitable erodible sediment (i.e. an area running out of fine sediment cannot emit dust) and (iii) **availability-limited (AL**), where suitable sediment is available, but erodibility is restricted by other components in the landscape (Bullard et al., 2011). It is necessary to consider both natural and human-induced spatial and temporal emission dynamics to directly link these dust source modes to a geomorphological context at the sub-basin scale. PlanetScope will enable daily monitoring dust emission and track dust plumes back from specific land surfaces to quantify controls on (i) dust source points, (ii) geomorphic thresholds of emission, and (iii) temporal limits on dust uplift.

1.2.6.3 HR-LEO Images Dust Detection & Enhancement Methods

To observe the SDS process using remote sensing data, a wide range of methods have been developed for various sensor types. For example, Baddock et al. (2009) successfully applied MODIS aerosol data to identify dust source locations in Australia, and they compare five principal approaches in detecting dust, including un-processed False Colour Composite (FCC), brightness temperature difference (BTD), and three dust algorithm methods. The BTD approach was found to be the most consistently reliable method for source detection in the Lake Eyre basin, and all other techniques were seen to be influenced by dust mineralogy or ground surface reflectance (Baddock et al., 2009). These authors also noted that version-1 MODIS Deep Blue algorithms (Hsu et al., 2004) struggled to detect suspended dust over bright desert surfaces.

To reduce 'bright background' effects, Clear Sky Difference (CSD) has been used to boost the signal noise of the dust plumes (Tramutoli et al., 2010). The Clear Sky Difference (CSD) method refers to an enhancement of atmospheric signals in satellite channel radiances by subtraction of the contribution of the underlying surface (Miller, 2016). Murray et al. (2016) combined CSD methods with a false colour rendering approach on SEVIRI on solar reflectance and near-infrared channels. Using DSD's single-band image to subtract the clear sky images, we can calculate the CSD image and then with selected channel combinations to enhance transient dust signals in FCC imagery (Figure 1.9, Murray et al., 2016), which improve the contrast between land surface features and allow the easier tracing dust plumes back to the first point of dust occurrence (Dust Points Source (DPS); Lensky and Rosenfeld, 2008). However, MODIS and SEVIRI have a moderate spatial resolution (0.5-3 km), the sensors struggle to detect small dust plumes, and source location accuracy is generally at the 1-5 km scale (Baddock et al., 2021).

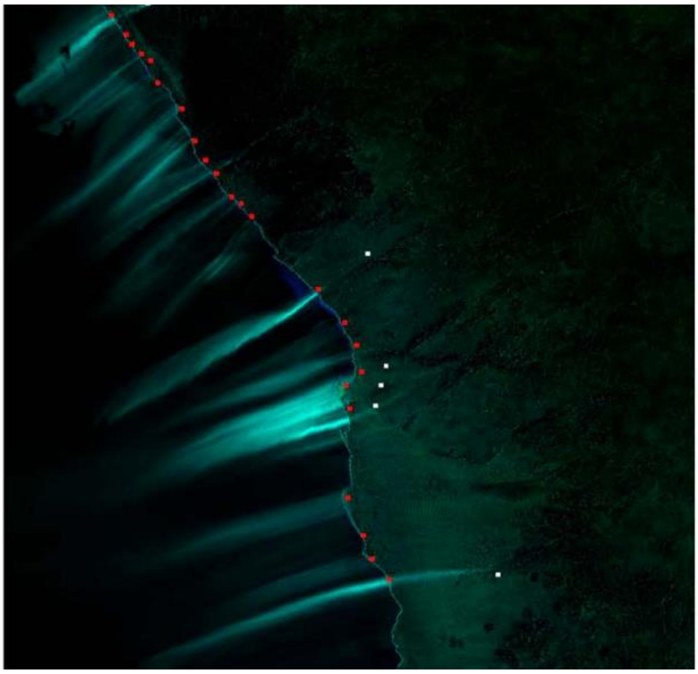

Figure 1.9 Dust plumes identified by SEVIRI CSD imagery in South Africa (Reproduced from Murray et al. 2016; Fig.10)

Tracking the location of dust sources and the up-wind termination of dust plumes is not straightforward (Baddock et al., 2009), and a range of manual, subjective approaches have been used to map active emission locations in a range of locations (Sinclair and LeGrand, 2019; Hennen, 2017). Because of the complexity and variability of the dust plume signal in space/time, automated dust detection algorithms struggle to provide a reliable alternative to manual dust plume detection approaches (Shi et al., 2020).

In this project, a range of tried and tested dust source detection techniques were used a version of the modified (CSD) approach (Murrey et al., 2016) allied to FCC enhancement (Baddock et al., 2009). In this case, however, these approaches will be applied to high-resolution Sentinel-2 (10-metre) and PlanetScope (3-metre) data to uncover the site of SDS in the Gonghe Basin in China.

1.2.6.4 A geomorphological classification: Preferential dust source (PDS)

Recent studies (Sweeney et al., 2016 a and b) have aimed to establish a connection between the prevailing geomorphic type and operational mode of dust sources in various regions. To achieve this, they gathered more than 500 individual dust flux measurements from eight common desert landforms in southern California, utilizing the PI-SWERL (Portable In Situ Wind Erosion Lab). Sweeney et al. (2011) discovered that the primary sources of dust are dry washes, dunes, and playa margins, while crusted playas and desert pavements produce lower emissions in eastern Mojave Desert, USA. The significant differences in emission rates are attributed to local variations in soil texture and the presence of surface crusts. The largest emitters of dust various in different regions, for example, Wang et al., (2006) proposing that SDS originates mainly from Gobi (gravel) deserts formed in the piedmont alluvial fans of the Kunlun, Qilian, and Helan mountains. Conversely, the northern Gurbantunggut and eastern Taklimakan regions exhibit lower SDS. Nevertheless, very little is known about why some seasons are more active dust sources than other seasons and why SDSs from certain landforms and human-active areas. Bullard et al. (2008) proposed a preferential dust source (PDS) geomorphic classification method aimed at facilitating the global emission potential of surfaces and dust processes occurring within source regions (Bullard et al., 2011). The PDS scheme is focused on the primary need to improve dust source characterisation within dust models (e.g., Chihuahuan Desert; Baddock et al., 2011). As such, it includes a simple classification of surface properties and their known susceptibility to wind erosion (Baddock et al., 2016). The PDS scheme directly shows that different geomorphologic units have different susceptibilities to SDS (Figure 1.10) and known operation within the modes of dust source operation (i.e., SL, TCL and AL). This scheme has been evaluated via fieldwork at several active dust source regions, e.g., the Chihuahuan Desert and North Africa. Thus, we expand the PDS sampling approach to China, one of the leading dust source regions worldwide (Wang et al., 2018), to fill the geomorphology classification research gap in Asia (Bryant, 2013; Cui et al., 2019).

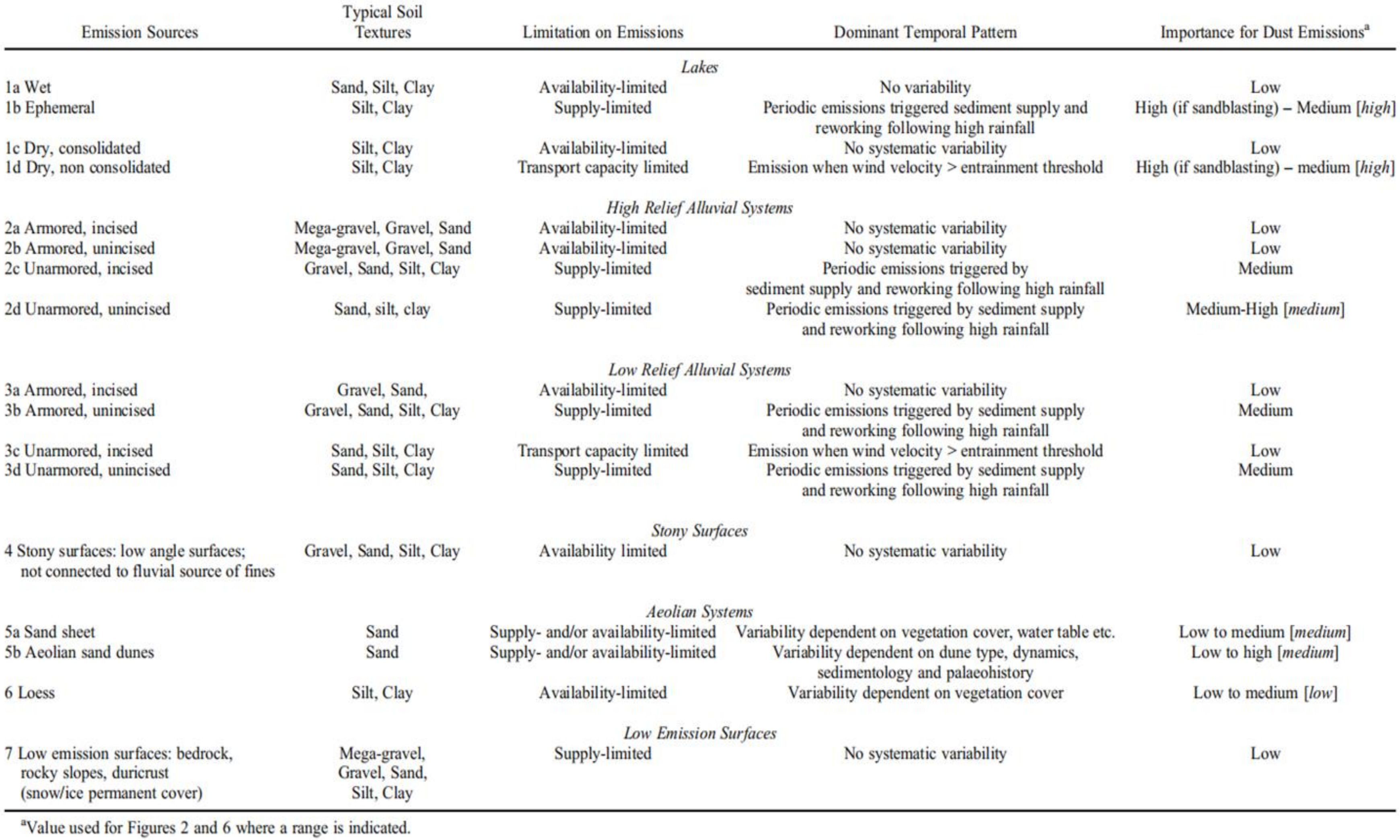

Emission Sources	Typical Soil Textures	Limitation on Emissions	Dominant Temporal Pattern	Importance for Dust Emissions[a]
		Lakes		
1a Wet	Sand, Silt, Clay	Availability-limited	No variability	Low
1b Ephemeral	Silt, Clay	Supply-limited	Periodic emissions triggered sediment supply and reworking following high rainfall	High (if sandblasting) – Medium [*high*]
1c Dry, consolidated	Silt, Clay	Availability-limited	No systematic variability	Low
1d Dry, non consolidated	Silt, Clay	Transport capacity limited	Emission when wind velocity > entrainment threshold	High (if sandblasting) – medium [*high*]
		High Relief Alluvial Systems		
2a Armored, incised	Mega-gravel, Gravel, Sand	Availability-limited	No systematic variability	Low
2b Armored, unincised	Mega-gravel, Gravel, Sand	Availability-limited	No systematic variability	Low
2c Unarmored, incised	Gravel, Sand, Silt, Clay	Supply-limited	Periodic emissions triggered by sediment supply and reworking following high rainfall	Medium
2d Unarmored, unincised	Sand, silt, clay	Supply-limited	Periodic emissions triggered by sediment supply and reworking following high rainfall	Medium-High [*medium*]
		Low Relief Alluvial Systems		
3a Armored, incised	Gravel, Sand,	Availability-limited	No systematic variability	Low
3b Armored, unincised	Gravel, Sand, Silt, Clay	Supply-limited	Periodic emissions triggered by sediment supply and reworking following high rainfall	Medium
3c Unarmored, incised	Sand, Silt, Clay	Transport capacity limited	Emission when wind velocity > entrainment threshold	Low
3d Unarmored, unincised	Sand, Silt, Clay	Supply-limited	Periodic emissions triggered by sediment supply and reworking following high rainfall	Medium
		Stony Surfaces		
4 Stony surfaces: low angle surfaces; not connected to fluvial source of fines	Gravel, Sand, Silt, Clay	Availability limited	No systematic variability	Low
		Aeolian Systems		
5a Sand sheet	Sand	Supply- and/or availability-limited	Variability dependent on vegetation cover, water table etc.	Low to medium [*medium*]
5b Aeolian sand dunes	Sand	Supply- and/or availability-limited	Variability dependent on dune type, dynamics, sedimentology and palaeohistory	Low to high [*medium*]
6 Loess	Silt, Clay	Availability-limited	Variability dependent on vegetation cover	Low to medium [*low*]
		Low Emission Surfaces		
7 Low emission surfaces: bedrock, rocky slopes, duricrust (snow/ice permanent cover)	Mega-gravel, Gravel, Sand, Silt, Clay	Supply-limited	No systematic variability	Low

[a] Value used for Figures 2 and 6 where a range is indicated.

Figure 1.10 Identification of Surface Geomorphologies and Their Contribution to SDSs in Space and Time (Reproduced from Bullard et al., 2011; Table 2)

1.3 Research aim, questions, and objectives

The literature review has pointed out multiple research gaps with regards to our understanding of the spatial heterogeneity with dust sources. Overall, inherent seasonal and diurnal variability in SDS from source regions, along with apparent spatial heterogeneity with dust sources, is both poorly constrained in global and mesoscale models due to inexact source allocation and quantification. Accurately identifying the spatial-temporal heterogeneity and meteorological characteristics of SDS is a prerequisite for accurate estimates of dust aerosol effects. Given the remote and harsh nature of the Gonghe Basin, synergistic remote sensing data are used to implement existing and novel methodologies to study SDS at greater spatial and temporal scales than previously accomplished. (i) Regional scale, how EASM and Westerlies affect climate change and SDSs is unknown in this region. It is important to know the chronology of dust and climate conditions, linking both can gain insights into drivers that caused aeolian activity in the past, which provides a better understanding of the controls on SDS. (ii) Processes controlling the location and activity of dust source regions at the basin and sub-basin scale are best observed using high temporal/spatial resolution remote sensing data. However, although remote sensing data can be used to capture surface erodibility heterogeneity in the sub-basin scale, these observations often lack a close link (in space and time) to the climate mechanisms driving the SDS at the basin scale. It is also clear that few of these studies have been able to observe dust plumes and events in a manner that is directly relevant to modelling studies. (iii) Sub-basin scale, understanding the relationship between SDS and landform types is crucial for comprehending the factors that influence the nature and magnitude of SDS, which hinders accurate modelling without proper dust source information. There is a lack of research in Asia, which seeks to link SDS observations with a viable geomorphological scheme to quantify factors which may control the nature and magnitude of SDS. The following three empirical Chapters will aim to investigate these topics in further detail.

THESIS AIM: Understanding Controls on Dust Emission from Remote Sensing in the Gonghe Basin, China

CHAPTER 2 [REGIONAL SCALE] A season and interannual chronology and drivers of SDS in the Gonghe Basin [2000-2022]

Q2.1: When do SDS occur in the Gonghe Basin?

[O2.1]: Use a time series of moderate resolution remote sensing data (MODIS AOD/AE) data to determine dust properties and dust detection protocols for the Gonghe Basin, and generate a time series of Dust Storm Days [DSD]

[O2.2]: To use a time series of moderate resolution remote sensing data (MODIS Deep Blue) to build an overview chronology of quantitative dust loading (AOD/DOD) for the Gonghe Basin

Q2.2: What are the potential drivers on the basin and regional scale?

[O2.3]: Use gridded climate and bioclimate data (e.g., ERA 5, Merra-2), hosted via GIOVANNI modelling climate data, and daily meteorological station data to determine wind fields, DUP and annual/seasonal variability in climate metrics from 1980 to 2022.

[O2.4]: Time-series analysis and cross-correlation identify how wind velocity, DUP, rainfall, and other factors [e.g., human activity] influence dust uplift [as determined by O1/O2].

CHAPTER 3 [BASIN SCALE] Understanding controls on SDS in the Gonghe Basin using GEO data [2019-2022]

Q3.1: Can SDS from the Gonghe Basin be detected in GEO data, and at what time of day is dust emitted?

[O3.1]: Build a sub-daily [10 hr/10 min] dust observation/detection time series [dust, cloud, no dust, etc.] for four years (2019-2022) using GEO data.

[O3.2]: Compare daily, monthly annual GEO dust chronologies with LEO observations [Chapter2]

Q3.2: To what extent do meteorological events and climate data explain sub-daily SDSs?

[O3.3]: Identify local/regional meteorological mechanisms associated regarding SDSs.

[O3.4]: Investigate relationships between climate variables for known SDS events at the sub-daily scale.

Q3.3: What links exist between sub-daily records of SDS and quantitative GEO AOD chronologies?

[O3.5]: Mapped Frontal SDS's Active Dust Source (ADS) area in Morning and Afternoon

Chapter 4 [SUB-BASIN SCALE] Use of High-Resolution Low Earth Orbit [LEO] data for Dust Point Source [DPS] detection and derivation of Preferential Dust Source [PDS] and Land Cover/Use Characteristics.

Q4.1: Where are the dust point sources [DPS] within the Gonghe Basin at the sub-basin scale, and what is the PDS/ LULC signature of those DPS?

[O4.1]: Develop a Dust Point Source [DPS] detection protocol for PlanetScope, Sentinel 2 and Landsat 8/9.

[O4.2]: Derive PDS and Land Cover/Use [LULC] Maps for the Gonghe Basin.

Q4.2: What are the properties of observed SDSs at the sub-basin scale?

[O4.3]: Use DPS data to derive PDS and LULC signatures for SDSs in the Gonghe Basin.

[O4.4]: Measure dust loadings for observed plumes emanating from the Gonghe Basin.

[O4.5]: Determine the bulk trajectory of SDSs emanating from known DPS.

1.4 Thesis Structure

The remainder of this thesis contains a literature review in Chapter 1, three key research Chapters 2, 3, and 4. Discussion and significant conclusions are presented in Chapters 5 and 6. The key research chapters are structured as manuscripts, each containing its introduction, data, methods, results, discussion, and conclusion. However, please note that aspects of the literature review in this chapter (e.g., sections 1.2.4, 1.2.5, and 1.2.6), also contain some of the background information that underpins Chapters 2, 3 and 4.

2. A seasonal and interannual chronology of drivers of SDS in the Gonghe Basin [2000-2022]

2.1 Introduction

The mineral dust cycle has become a core theme of Earth System Science, and many dust studies are based on an interest in its interaction with climate (Liu et al., 2021). China is one of the largest dust sources in the Northern Hemisphere and has a long history of SDS, transportation and deposition (Qiang et al., 2013; Chen et al., 2007; Zeng et al., 2011; Dong et al., 1993). The Qinghai Tibet Plateau (QTP) seems to be a key component in the North China dust system. Almost 60% of the QTP is classed as arid or semi-arid, and the region has low annual precipitation (less than 500 mm), strong winds and a sensitive ecological environment (Han et al., 2009), contributing to the existence of dust source in this region (Qiang et al., 2007). The northeast QTP altitude is about 4000 metres above sea level, including Qinghai Lake, Gonghe and Qaidam basins. Gonghe is the most important part of the fragile landscape zone and agro-pastoral ecotone in Northwest China (Yang et al., 2019). In addition, the region is located at the triple intersection of the Asian summer and winter monsoon and the westerly belt. This fragile natural ecology and hydrothermal sensitivity region is related to climate change (Zhao et al., 2010; Gao et al., 2019) and human impacts (Zhang et al., 2007; Dong et al., 2010). However, our understanding of dust processes and specific dust source processes in this region remains incomplete.

Determining the climate factors controlling SDS in arid regions is important for understanding the control of Sand and Dust Storms (SDS) frequency and intensity (Modarres, 2021). Globally, previous research has examined the connections between SDS, climate, and ground surface conditions. The prevailing factor driving dust processes has been identified as wind speed (Wu et al., 2022). Multiple studies have indicated that the occurrence of SDSs tends to increase with higher wind speeds (Liu et al., 2022; Jiang et al., 2023; Liu et al., 2021). Jugder et al. (2011) found that the frequency of strong winds played a role in the variation of dust days in the Gobi Desert region. SDS exhibits a consistent negative correlation with precipitation due to the positive impact of enhanced soil moisture and vegetation growth (Aili, Oanh, & Abuduwaili, 2016). The arid climate and unique terrain are important conditions for sediment deposition (Tian et al., 2020). Gonghe has a long history of aeolian processes, and sediments are closely related to the paleogeographic environment. Paleosol profiles in the Gonghe Basin have also been used to trace the changes in Quaternary and Holocene aeolian sediments and show multiple active sand formation stages during this period (Gao et al., 1993). However, how EASM and Westerlies affect climate change and SDSs is unknown in this region. It is important to know the chronology of dust and climate conditions, linking both can gain insights into drivers caused aeolian activity in the past, which provide a better understanding of the controls on SDS.

Satellite instruments contain retrieved aerosol properties data, enabling the identification of natural sources in arid and semiarid regions. One commonly used remote sensing measurement platform is the Moderate-Resolution Imaging Spectrometer (MODIS, Gkikas et al., 2021), which has been widely used in atmospheric aerosol research since 2002, providing daily global aerosol retrieval. The Deep Blue (DB) algorithm was developed by Hsu et al. (2004), using multiple radiances in MODIS measured 412 nm channel. This algorithm is specifically designed for retrieving aerosols over bright surfaces such as deserts and arid lands. Given the strong relationship between aerosol optical depth (AOD) and Angstrom exponent (AE) indexes and retrieval wavelength, researchers often utilise satellite data and aerosol optical properties to infer aerosol types and source characteristics in different seasons (Yu et al., 2015; Kumar et al., 2014). For instance, Proestakis et al. (2018) identified an AOD threshold of 0.2 for distinguishing dust (AOD>=0.2) and non-dust (AOD<0.2) over the Tibet Plateau and Taklamakan. Kaskaoutis et al. (2011) addressed the complexity of aerosol composition in areas affected by human activities and proposed a clustering method to differentiate various aerosol types based on physical interpretability. By considering the typical spectral variation of dust optical properties, it becomes possible to identify dust sources using these satellite products. The criterion for dust aerosols is an AOD value greater than 0.25 and an AE value less than 0.7 (Sreekanth, 2014b; Kumar et al., 2015). Pu and Ginoux (2016) utilised the Dust Optical Depth (DOD) method in MODIS developed by Ginoux et al. (2010) to effectively sample coarse-mode dust particles (Gui et al., 2022). Furthermore, Ginoux et al. (2012) established a base criterion of daily annual mean DOD> 0.2 for detecting SDSs.

Chapter 2 - A seasonal and interannual chronology of drivers of SDS

2.1.1 Chapter Aims and Objectives

Chapter 2 Research Aim: [REGIONAL SCALE] A season and interannual chronology and drivers of SDS in the Gonghe Basin [2000-2022]

This chapter characterises the seasonal dust variability in the Gonghe Basin from 2000 to 2022. Gridded level 2 MODIS Terra and Aqua Deep Blue products provide Aerosol Optical Depth [AOD], Angstrom Exponent [AE] and single scattering-albedo [SSA], and Normalized Difference Vegetation Index [NDVI] data. Three definitions to distinguish dust from other aerosol species in the Gonghe Basin: (i) P2021 method, AOD > 0.2; (ii) K2011 method, AOD> 0.25 and AE <0.7; (iii) P&G2016 method, calculated as DOD > 0.2. In addition, Merra-2 reanalysis data and ERA investigate a range of climate and environmental factors related to the dust cycle, including (i) precipitation, (ii) wind speed, (iii) temperature, (iv) soil moisture, and (v) relative humidity and snow cover. To further understand how these climate factors either drive or influence variations in dust occurrence, we also include an assessment of regional-scale variability in known climate drivers such as Westerlies and East Asian Summer Monsoon [EASM] and consider the human impact related to grazing, agriculture and landscaping.

Q2.1: When do SDS occur in the Gonghe Basin?

[O2.1]: Use a time series of moderate resolution remote sensing data (MODIS AOD/AE) data to determine dust properties and dust detection protocols for the Gonghe Basin, and generate a time series of Dust Storm Days [DSD]

[O2.1]: To use a time series of moderate resolution remote sensing data (MODIS Deep Blue) to build an overview chronology of quantitative dust loading (AOD/DOD) for the Gonghe Basin

Q2.2: What are the potential drivers on the basin and regional scale?

[O2.3]: Use gridded climate and bioclimate data (e.g., ERA 5, Merra-2), hosted via GIOVANNI modelling climate data, and daily meteorological station data to determine wind fields, DUP and annual/seasonal variability in climate metrics from 1980 to 2022.

[O2.4]: Time-series analysis and cross-correlation identify how wind velocity, DUP, rainfall, and other factors [e.g., Human activity] influence dust uplift [as determined by O1/O2].

2.2 Data and Methods

2.2.1 Data

To uncover controls on SDSs at the basin scale and build the climate context of the Gonghe Basin, we used weather station and MERRA-2 and ERA5 reanalysis climate data and LEO RS data in the research. In Table 1, each parameter data was described by its type, name, units, temporal-spatial resolution, data time frame, and data download web sources. According to the previous literature review, in the Gonghe Basin, seven parameters that contributed to SDS were chosen. The dust-related climate factors include Normalised Difference Vegetation Index (NDVI), precipitation, surface soil wetness, relative humidity, temperature, snow cover and wind velocity. The aerosol dust will be represented by Aerosol Optical Depth (AOD), Angstrom Exponent (AE) index and Dust Optical Depth, which are selected from three dust definition methods.

2.2.1.1 LEO Remote Sensing Data

Moderate Resolution Imaging Spectroradiometer (MODIS) instrument operating onboard Terra (overpass time: 10.30 a.m. local time) satellite from 2000 and Aqua (overpass time: 1.30 p.m. local time) satellite from 2002 are used in this study (Crosson et al., 2012). The atmospheric aerosol parameters were retrieved by the Deep Blue (DB) algorithm (Hsu et al., 2004), which was developed initially for retrieving over the bright surface (desert/arid land). The MODIS products, including Aerosol Optical Depth (AOD) and Angstrom Exponent wavelength index (AE), are considered to define 'DUST' from aerosol and answer the research question of when dust occurs and how much dust (AOD) was emitted from the Gonghe Basin. Here, we choose MODIS for Terra and Aqua satellite data, spatial resolution 1° x 1°, temporal resolution monthly and daily for AOD at 550 nm (DB, Land-only) and AE at 0.412-0.47 micron (DB, Land-only). The data plot in time-series during 2000-2022, and the value is area-averaged (Research Area coordination range: North 37.13°, West 98.65°, South 35.28°, East 101.56°) in Goddard Interactive Online Visualization ANd aNalysis Infrastructure (GIOVANNI) website which are developed by NASA's Goddard Earth Sciences Data and Information Services Centre and supports user visualising, analysing earth science data (Berrick et al., 2008). Aerosol data details are shown in Table 2.1.

Table 2.1 Chapter-2Data description, including parameter name, data name, plot type, data units, data source, temporal and spatial resolution, data begin, and end date and data download web information.

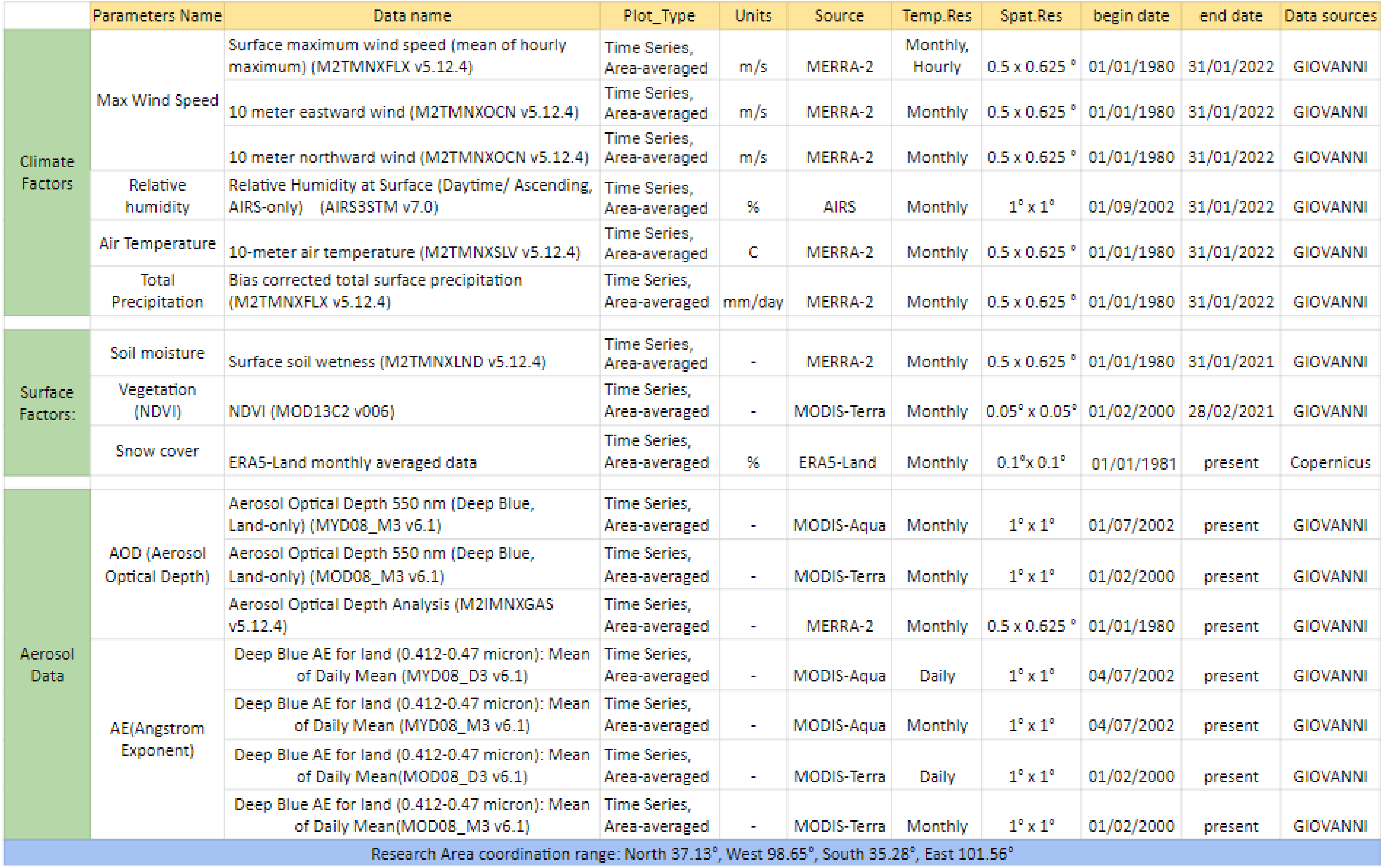

	Parameters Name	Data name	Plot_Type	Units	Source	Temp.Res	Spat.Res	begin date	end date	Data sources
Climate Factors	Max Wind Speed	Surface maximum wind speed (mean of hourly maximum) (M2TMNXFLX v5.12.4)	Time Series, Area-averaged	m/s	MERRA-2	Monthly, Hourly	0.5 x 0.625 °	01/01/1980	31/01/2022	GIOVANNI
		10 meter eastward wind (M2TMNXOCN v5.12.4)	Time Series, Area-averaged	m/s	MERRA-2	Monthly	0.5 x 0.625 °	01/01/1980	31/01/2022	GIOVANNI
		10 meter northward wind (M2TMNXOCN v5.12.4)	Time Series, Area-averaged	m/s	MERRA-2	Monthly	0.5 x 0.625 °	01/01/1980	31/01/2022	GIOVANNI
	Relative humidity	Relative Humidity at Surface (Daytime/ Ascending, AIRS-only) (AIRS3STM v7.0)	Time Series, Area-averaged	%	AIRS	Monthly	1° x 1°	01/09/2002	31/01/2022	GIOVANNI
	Air Temperature	10-meter air temperature (M2TMNXSLV v5.12.4)	Time Series, Area-averaged	C	MERRA-2	Monthly	0.5 x 0.625 °	01/01/1980	31/01/2022	GIOVANNI
	Total Precipitation	Bias corrected total surface precipitation (M2TMNXFLX v5.12.4)	Time Series, Area-averaged	mm/day	MERRA-2	Monthly	0.5 x 0.625 °	01/01/1980	31/01/2022	GIOVANNI
Surface Factors:	Soil moisture	Surface soil wetness (M2TMNXLND v5.12.4)	Time Series, Area-averaged	-	MERRA-2	Monthly	0.5 x 0.625 °	01/01/1980	31/01/2021	GIOVANNI
	Vegetation (NDVI)	NDVI (MOD13C2 v006)	Time Series, Area-averaged	-	MODIS-Terra	Monthly	0.05° x 0.05°	01/02/2000	28/02/2021	GIOVANNI
	Snow cover	ERA5-Land monthly averaged data	Time Series, Area-averaged	%	ERA5-Land	Monthly	0.1°x 0.1°	01/01/1981	present	Copernicus
Aerosol Data	AOD (Aerosol Optical Depth)	Aerosol Optical Depth 550 nm (Deep Blue, Land-only) (MYD08_M3 v6.1)	Time Series, Area-averaged	-	MODIS-Aqua	Monthly	1° x 1°	01/07/2002	present	GIOVANNI
		Aerosol Optical Depth 550 nm (Deep Blue, Land-only) (MOD08_M3 v6.1)	Time Series, Area-averaged	-	MODIS-Terra	Monthly	1° x 1°	01/02/2000	present	GIOVANNI
		Aerosol Optical Depth Analysis (M2IMNXGAS v5.12.4)	Time Series, Area-averaged	-	MERRA-2	Monthly	0.5 x 0.625 °	01/01/1980	present	GIOVANNI
	AE(Angstrom Exponent)	Deep Blue AE for land (0.412-0.47 micron): Mean of Daily Mean (MYD08_D3 v6.1)	Time Series, Area-averaged	-	MODIS-Aqua	Daily	1° x 1°	04/07/2002	present	GIOVANNI
		Deep Blue AE for land (0.412-0.47 micron): Mean of Daily Mean (MYD08_M3 v6.1)	Time Series, Area-averaged	-	MODIS-Aqua	Monthly	1° x 1°	04/07/2002	present	GIOVANNI
		Deep Blue AE for land (0.412-0.47 micron): Mean of Daily Mean(MOD08_D3 v6.1)	Time Series, Area-averaged	-	MODIS-Terra	Daily	1° x 1°	01/02/2000	present	GIOVANNI
		Deep Blue AE for land (0.412-0.47 micron): Mean of Daily Mean(MOD08_M3 v6.1)	Time Series, Area-averaged	-	MODIS-Terra	Monthly	1° x 1°	01/02/2000	present	GIOVANNI
Research Area coordination range: North 37.13°, West 98.65°, South 35.28°, East 101.56°										

2.2.1.2 Gridded Vegetation and Reanalysis Climate Data

To build the climate context of the Gonghe Basin and answer the second question, we are using reanalysis data in this project. The climate factors data mainly from the Modern-Era Retrospective Analysis for Research and Applications-version 2 (MERRA-2) datasets, including surface max wind speed, Relative humidity, 10-metre air temperature, Total precipitation, Surface soil moisture, and Vegetation (NDVI) from MODIS-Terra satellite, and snow cover provided by European Centre for Medium-Range Weather Forecasts (ECMWF) reanalysis v5 (ERA-5) Land produced from the GIOVANNI. The data was plotted in a time-series from 1980 to 2022, and the parameter value is area-averaged (same range as the Remote Sensing dataset).

Specifically, daily surface maximum wind speed data is transferred from the hourly max wind speed data. Then, Cubed Maximum Wind Speed (CMWS) data was applied. Because surface winds are highly variable, they may not represent the appropriate changes in the observations. Also, the energy content of the wind varies with the cube (the third power) of the average wind speed. Pearce and Walker (2005) suggested that wind power (cubed wind) can better represent wind speed in the statistic calculation. Wind Rose used hourly average wind speed data from Merra-2 and average to daily level.

NDVI is one of the most commonly used vegetation indices, and it measures vegetation activity on the land surface (Gao et al., 2022). NDVI values are between - 1 and 1; with higher vegetation coverage, the NDVI value will be close to 1, while a value greater than 0.5 generally indicates dense vegetation (Lee and Kim, 2012). Vegetation conditions between morning and afternoon are nearly the same, so we prioritise the use of the NDVI dataset from MODIS-Terra. Terra provides a longer time-series of data and tends to be less affected by clouds than Aqua, as Terra's morning orbit leads to more cloudless observations (Lyapustin et al., 2014). Snow cover using percentage % units represents the coverage of the whole study area.

2.2.1.3 Meteorological Station Data

The Gonghe meteorological station is a national station with a relatively long climate data record (from 1961 to now) and is the nearest meteorological station to the Gonghe Basin dune fields. The Gonghe Met Station is located in the middle of the basin (Figure 2.1). Its latitude is 36° 9' 33" N, Longitude 100° 22' 9" E, and Altitude is about 3200 metre above sea level. The

Gonghe Met station provides some climate data daily, such as max and average wind speed, wind direction, relative humidity, precipitation, temperature, but without visibility information.

Figure 2.1 A red star on the map highlights the Gonghe Meteorological Station.

2.2.2 Extracting a SDS Signal from the MODIS Time-series

Although dust aerosols are the main contributors to AOD in Northwest China, such as Taklimakan, Gobi Desert, and QTP, other aerosol types (e.g., urban Industrial, biomass and mix particles) can make notable contributions (Ridley et al., 2016). It is, therefore, necessary to consider specific methods for the extraction of SDS from satellite-retrieved to ensure that most of the AOD are influenced by mineral dust. Here, we use three approaches to determine the occurrence of 'Dust Aerosol' in space and time: (i) use of a fixed AOD threshold [whereby exceedance is linked to specific periods of dust emission and transport]; (ii) use of a clustering technique whereby AOD and AE are used together to characterise aerosol properties and types (including dust), using standard model assumptions; (iii) we use an existing algorithm which combines AOD, single scattering albedo(ω) and AE(α) to determine a quantitative Dust Optical Depth [DOD]. To explore the range of outputs and quality of data that these approaches can generate, we apply these methods to the same daily-level MODIS Terra and Aqua datasets (see Table 2.1).

2.2.2.1 P2021Dust Definition: Threshold-based approach

Baddock et al. (2009) and Jafari and Malekian (2015) suggest that, as a baseline approach, the application of a simple threshold-based method can be used to differentiate SDSs from a time series of AOD data. However, these authors also note that it is difficult to impose a single, fixed threshold to identify the SDSs. Therefore, this research optimised dust detection by testing a range of thresholds derived from the literature (e.g., Ginoux, Garbuzov and Hsu, 2010; Nobakht, Shahgedanova and White, 2021; Proestakis et al., 2018). According to the comparison, Proestakis et al. (2018) identified an AOD threshold of 0.2 for distinguishing dust (AOD>=0.2) and non-dust (AOD<0.2) over the QTP and Taklamakan. Thus, according to research, the first dust definition method applies to MODIS Terra and Aqua datasets.

The number of Dust Storm Days (DSD) refers to calculating the number of 'Dust' Storm days detected by RS AOD products. For example, we use AOD>0.2 as a threshold to distinguish dust from aerosol; the day's AOD over 0.2 is DSD in P2021's definition.

2.2.2.2 K2011 Dust Definition — Multiple clustering techniques

The use of a combination of AOD and AE data is one of the most effective ways to determine aerosol types in the atmosphere. Accordingly, several methods based on aerosol optical and physical characteristics have been used to classify species in space/time (Muneer et al., 2004; Bibi et al., 2016). Also, Gharibzadeh et al. (2018) proposed the classification of several common aerosol types from these data, including dust, urban industrial, biomass burning, and mixed aerosols and they uses cluster analysis to discriminate several types of aerosols and sort datasets into several clusters using predefined aerosol constraints (Appendix A). Cluster analysis is a statistical tool for grouping extensive data sets into several categories (Omar et al., 2005). In this study, cluster analysis approach does not make any assumptions about the presence or geographical locations of desert dust sources for grouping air mass types.

Scatter plots of AOD-AE graphs used the Kaskaoutis et al. (2011) method [Termed here: K2011] to distinguish several types of aerosols by determining physically interpretable cluster sources. Data sources are daily MODIS Aqua and Terra Deep Blue AOD and AE products from 2000 to 2022. To limit AOD observation to larger particles, the criterion of AE < 0.7 was applied, and the value is based on the inverse relationship between AE and dust particle size. Sreekanth (2014b) and Kumar et al. (2015) defined particles with a small Angstrom wavelength index ($\alpha < 0.7$) as dust aerosols. Thus, in the K2011 dust definition, we classify dust when AOD > 0.25 and AE < 0.7.

2.2.2.3 P&G2016 Dust Definition —Dust Optical Depth

Dust Optical Depth (DOD) refers to the cylindrical optical depth generated by the extinction of mineral particles. Ginoux et al. (2010) created the DOD method and applied it to the newly released MODIS Collection 6 aerosol product (Pu and Ginoux, 2016). DOD is one of the critical factors to control the interaction between dust and radiation. DOD only represents the effective sampling of coarse-mode particles of dust (Gui et al., 2022).

In order to separate dust from other aerosols, we use the single scattering albedo [SSA] and AE index (α). The value of the Angstrom index is also a qualitative indicator of aerosol particle size (Angstrom, 1929); the value of $\alpha <= 1$ indicates that the particle size distribution is composed of coarse model aerosols (radii >=0.5 μm) usually associated with dust and sea salt (Schuster, et al., 2006). Due to dust property absorption of solar radiation, setting single-scattering albedo (SSA) values less than 1 at a wavelength of 470 nm to differentiate land DOD dust from the ocean scattering aerosols such as sea salt.

We calculate the daily DOD according to the algorithm (Eq1, Fig 2.2), which is a continuous function relating the AE to fine-mode AOD built by Anderson et al. (2005; their Eq. 5) and it is used to extract dust from fine particles. Same with Pu and Ginoux (2018), data derived from MODIS Dark Blue aerosol product, which includes AOD and single scattering albedo (ω) and AE(α) from 2000 to 2022. Then, we used Ginoux et al. (2012) to identify the daily annual mean DOD> 0.2 as our base to detect SDSs.

$$\mathrm{DOD} = \mathrm{AOD} * (0.98 - 0.5089\alpha + 0.0512\alpha^2) \text{ if } (\omega < 1) \qquad \text{[Eq.1]}$$

Figure 2.2 Calculating DOD based on AOD, AE, and single-scattering albedo (Pu and Ginoux, 2018, reproduced from Eq 1)

2.2.3 Quantifying SDS Occurrence in the Gonghe Basin [2002-2022]

To quantify the occurrence of SDSs statistically in the MODIS time series, we divided our evaluation system into two parts: (i) The frequency of SDSs as determined by counting the number of DSD in which the occurrence of 'Dust Aerosol' is flagged in the daily MODIS time series via each of our methods and denoted Dust Storm Days (DSD); (ii) The magnitude of 'dust occurrence' - determined by the calculation of AOD/AE per DSD via a time-averaged monthly boxplot.

Based on daily MODIS Terra and Aqua datasets with aerosol products (AOD, AE, and DOD) and three DSD definition approaches (P2021, K2011, and P&G2016), we distinguish the Dust and non-Dust day, respectively. In order to provide a statistical baseline for comparison with climatological metrics, the boxplots generated here chart the number of DSD per month over the last 20 years [2002-2022]. The AOD and AE value was extracted from the date defined as a DSD. The AOD boxplot for each month shows the SDS magnitude, exploring the high-intensity SDSs months.

Chapter 2 - A seasonal and interannual chronology of drivers of SDS

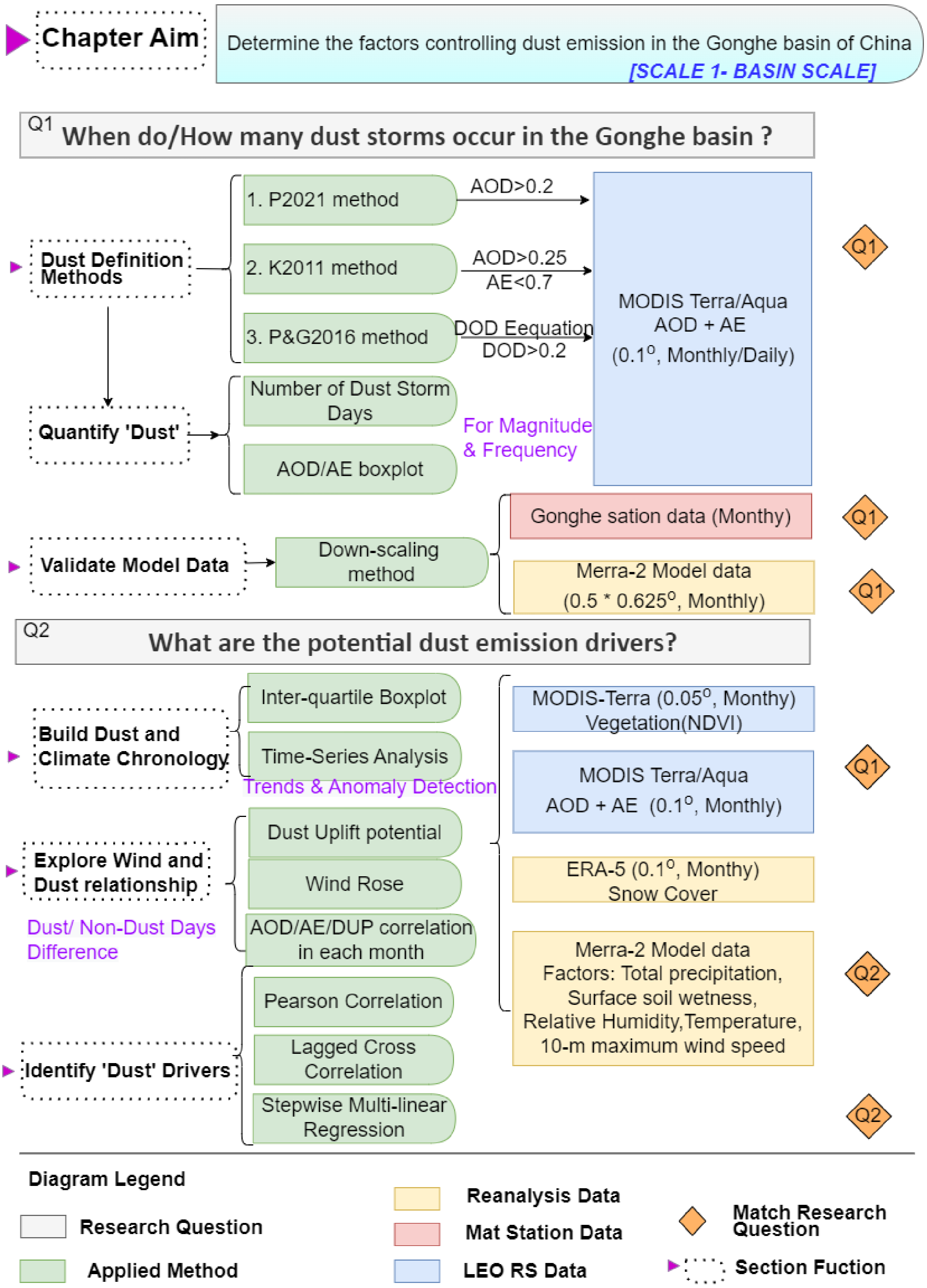

Figure 2.3 The research data, methods, and workflow for relevant research questions and objectives addressed in Chapter 2

2.2.4 Building a climate chronology via statistical analysis

2.2.4.1 Validating Merra-2 model by meteorological data using a down-scaling method

A Pearson correlation was run to determine the relationship between Merra-2 model and weather station data for monthly total precipitation from 2010-2014. There was a strong, positive correlation between the model and station data, which was statistically significant (Table 2.2, r=0.909, p<0.001). The statistical value means the Merra-2 model data from GIOVANNI show an excellent performance representing the actual weather conditions in the Gonghe Basin. However, Merra-2 AOD data display relatively gentle periodic changes over seasons and have less variability than MODIS. In fact, Baddock et al. (2009) indicate that remote sensing data may be affected by cloud cover and bypass time, which explains why MODIS has apparent seasonality. Also, this correlation analysis selected time range and type of data, e.g., total precipitation, is limited by weather station data’s availability, for future work suggesting repeat the correlation check on MERRA-2 wind speed.

Table 2.2 The monthly total precipitation correlation, data derived from the Gonghe weather station and Merra-2 model in 2010-2014. The N means sample number is 132.

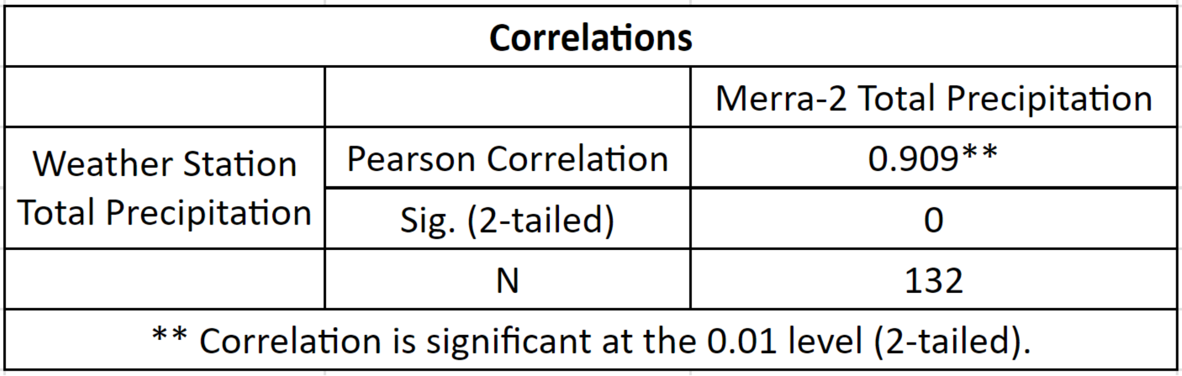

Correlations

		Merra-2 Total Precipitation
Weather Station Total Precipitation	Pearson Correlation	0.909**
	Sig. (2-tailed)	0
	N	132

** Correlation is significant at the 0.01 level (2-tailed).

2.2.4.2 Wind Rose and Dust Uplift Potential (DUP)

To determine wind speed and direction, it is necessary to calculate the u and v components of wind. The u component of wind aligns with the x-axis (longitude), with positive values denoting a westerly flow and negative values indicating wind comes from the east, so is an easterly flow. Similarly, the v component of wind aligns with the y-axis (latitude), with positive values representing a southerly and negative values representing a northerly flow. The Wind Rose approach utilized hourly average wind speed data obtained from Merra-2 and aggregated them to a daily level. Wind speed and direction were then calculated using the u and v components, employing the following formulas. The u and v components were averaged separately daily. The resulting average speed and direction were calculated using the Pythagorean Theorem and the "arctan(u/v)" function, respectively (Eq2, Fig 2.4).

$$\text{Wind speed: } \mathrm{sqrt}(u^2 + v^2)$$
$$\text{Wind direction: } \mathrm{atan2}(-u, -v) * (180/pi) + 180$$

[Eq. 2]

Figure 2.4 The wind speed and direction calculation from the u and v components is performed with reference to true north, where a direction of 0 degrees corresponds to north, 90 degrees to east, 180 degrees to south, and 270 degrees to west.

To better evaluate the wind velocity and dust relationship, we also used Dust Uplift Potential. An hourly surface maximum wind speed data was used in the Gonghe Basin from January 1, 1980, to December 31, 2022, to investigate the monthly and seasonal cycles of high wind speeds and Dust Uplift Potential (DUP). Marsham et al. (2011) proposed an equation to quantify and calculate parameterised dust uplift, which isolates the role of meteorology from that of the land surface. Then, Zhou et al. (2019) developed the equation for the condition S_t>=S, then the DUP =0 (Eq3, Fig 2.5). In this study, the Threshold Wind Velocity (TWV), denoted as 'St' is defined as the minimum wind speed required to initiate wind erosion at a height of 10 meters above the surface. The TWV is influenced by both atmospheric and surface conditions (Shinoda et al., 2010). The TWV was treated as a constant value specific to the Gonghe Basin, with a value of 6 ms^{-1} at the surface, derived from simulated erosion thresholds proposed by Laurent et al. (2005) for northern China.

$$\mathrm{DUP} = S^3 (1 + S_t/S) (1 - S_t^2/S^2) \quad \text{for } S > S_t \text{ and 0 otherwise}$$

[Eq.3]

Figure 2.5 Calculating DUP based on S=10 metre maximum wind speed and S_t=TWV, (Zhou et al., 2019), reproduced from Eq 1.

2.2.4.3 Climate and Bioclimate Time-series

BoxPlot used to show distribution changes of individual climate factors over 12 months from 1980 to 2022 (Brey et al., 2020). We processed the original time-series data downloaded from GIOVANNI into the data format with the month as abscissa and year as ordinate and generated a boxplot in MATLAB software. The interquartile range (IQR) is a measure between the upper and lower quartile of the dataset – i.e., the difference between the upper 75% and 25%. Observing the outliers of boxplot is useful to identify the extreme conditions, for example, the outliers of AOD dust boxplot shows the extraordinary SDS identified with very high AOD value.

This time series study is based on datasets downloaded from the GIOVANNI website from 1980-2022, and it builds the climate chronology of the Gonghe Basin. To identify and evaluate the trends and periodicity of those dust-related climate factors, a time-series analysis was conducted in MATLAB. The time series comprises three components: observed, trend, and anomaly (Krasnov et al., 2016). A time series is a set of repeated measurements of the same phenomenon, taken sequentially over time. The trends show persistent changes over a relatively long period, with an overall increase or decrease in the series. For analysis of trend differences in two decades, appropriate statistical tests such as the Mann-Whitney test were performed.

Anomaly detection helps understand which factors influence SDS on the basin scale (Bryant et al., 2007). Anomaly detection is discovering the data greater than three sigmas (± 3σ). The three-sigma rule (or 3σ rule) refers to the fact that approx. 99.7% of values fall within 3σ of the mean. The connection between dust dynamics and climatic variables can be established through the identification of anomalous patterns in a temporal sequence. For example, Mahowald et al. (2003) revealed a correlation between variations in the monthly average Total Ozone Mapping Spectrometer (TOMS) Aerosol Index (AI) anomalies and changes in aerosol concentration levels.

Pearson correlation coefficient and lagged cross-correlation were also calculated. We correlated the time-series monthly climate and surface variables with dust optical depth from 1980 to 2022. The data satisfy the assumption of continuous variables and linear relationships, so Pearson's correlation was used to measure the strength and direction of the relationship between two variables (Boloorani et al., 2020). Also, the p-value of Pearson's for evaluating value was computed as statistically significant and the standard deviation to evaluate the performance of the data.

Cross-correlation is a valuable tool for exploring climate lag impacts by quantifying the strength and delay of climatic interactions. It is commonly used in climatology to gain insights into interaction mechanisms between different climatological processes. Lagged cross-correlations refer to the dependence of two-time series on each other by considering different delay times (days, weeks, or months), depending on the research objectives, and then calculating the correlation coefficient in different lag times (Roustaei et al., 2021). The investigation involved examining the correlation between 24 months of leads and lags (both forward and backward) within time-series data sets to determine the potential lag effects of regional climate factors and dust emission on various climate drivers. If the data is periodic, there will be an oscillation in the correlation coefficients with lag, and values change from positive to negative (and vice versa). It is expected that the correlation coefficients will exhibit positive values and large magnitudes when the two series are in phase, while negative values and large magnitudes will be observed when the two series are out of phase, with peaks aligning with troughs. Plotting the correlation coefficients against the lag makes it possible to identify periodicities in the original time series. If the data exhibits periodic behaviour, there will be a noticeable oscillation in the correlation coefficients as the lag varies. Specifically, positive correlation coefficients with large magnitudes will indicate that the two series are in phase, whereas negative correlation coefficients with large magnitudes will indicate that the two series are out of phase, with peaks aligning with troughs.

2.2.4.4 Identifying Candidate SDS Drivers

In identifying candidate drivers of the SDS, correlation serves as a measure of the strength of the linear relationship between pairs of variables. On the other hand, regression analysis provides a mathematical expression of the relationship, describing how the factors involved impact each other. To better explore the relationship between factors, we removed the seasonal cycle first, and then stepwise multiple linear regression (Eq4, Fig 2.6) was conducted. The stepwise linear regression model is meant to explain the likelihood of SDS on a regional scale and quantitatively analyse the impact of various physical parameters on dust to assess the dynamic mechanism of these climate variables affecting the Gonghe dust activity (Yu et al., 2015).

$$Y = a + b_1X_1 + b_2X_2... + bnXn \qquad \text{[Eq.4]}$$

Fig 2.6 Multiple linear regression model

Where Y is the seasonally averaged DOD (Dust Optical Depth), a is the constant in the model; b_i is the linear regression coefficient that is estimated using the least squares method, representing the phase contribution rate of each influencing factor of the DOD, and X_i (i = 0,1,2..., n) are the predictors that regulate Gonghe Basin dust activity. To minimise the multicollinearity among climate variables, the prediction variables were first selected through stepwise regression (Ausati and Amanollahi, 2016). Stepwise regression is a technique employed in statistical modelling to systematically determine the inclusion or exclusion of independent variables within a regression model by iteratively assessing their statistical significance (Comrie and Glueck, 2007).

2.3 Results

Dust properties will be divided into dust frequency and magnitude. Each part has three dust definitions: P2021, K2011 and P&G2016.

2.3.1 [O1] Dust event frequency (Number of DSD) in the Gonghe Basin

Figure 2.7 presents the number of DSD aggregated per month from MODIS-Terra and Aqua satellites separately via the three occurrence definitions. P2021's results are different from K2011 and P&G2016's methods; the number of DSD in P2021's dust definition (Figure 2.7 A and D) is 3 times higher than others (Figure 2.7 B, C, E, F), especially in March and April, and this suggests that the simple definition of dust occurrence via threshold may include other aerosol species. Specifically, the scatter plot of AOD vs. AE from K2011 methods can be used to differentiate several types of aerosols (Appendix A). There are three main aerosol types in the Gonghe Basin atmosphere: (i) Mixed aerosol, (ii) Dust and (iii) Urban and industrial aerosol. A clean atmosphere was not found, and the MODIS-Aqua satellite found only one biomass event in spring over the last 20 years. The K2011 definition dust dataset is visualised in Appendix A in the box named ‘DUST’. Each type of aerosol contributes differently in the four seasons. Urban industrial aerosol is dominated throughout the year, and it contributes to over 97% of the total aerosol in summer and autumn. Besides, dust particle concentrations were high in spring (10-20% of days), winter (4-8% of days) and low in summer and autumn (less than 3%). Mixed aerosols are found in 4 seasons in the atmosphere but only account for about 0.5-2.4% of total aerosol (Appendix A). Overall, P2021 detected the number of DSD is about 48 DSD year^{-1}, whereas K2011 and P&G2016 only have about 14 DSD year^{-1} and 19 DSD year^{-1}, respectively. But March and April have obviously frequent SDS in all definitions, about 5-10 number of DSD. Figure 2.7 shows that SDS mainly occur from November to April. Thus, based on these initial definitions of dust occurrence, it can be suggested that a typical dust season in this Basin typically takes place in the winter and spring periods.

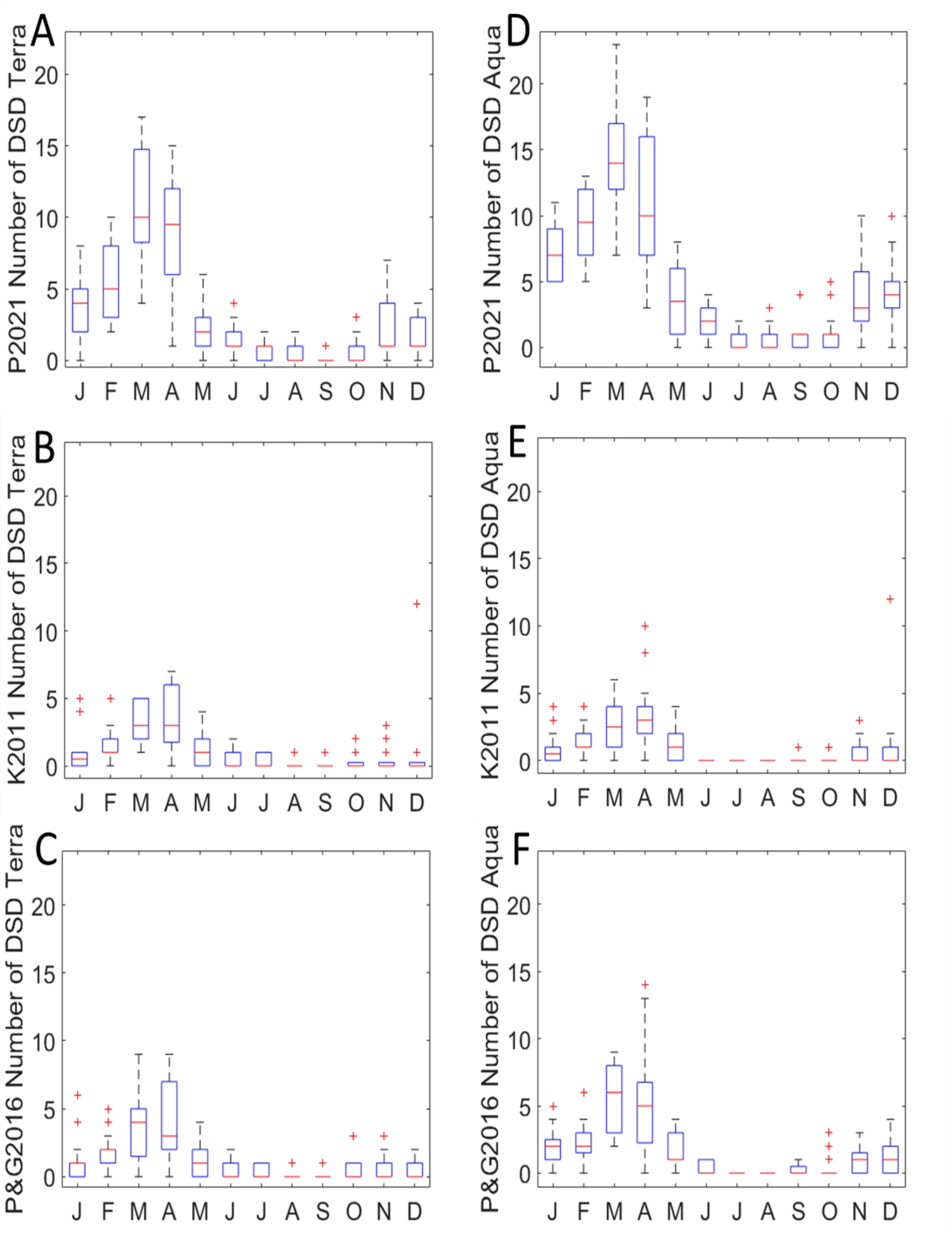

Figure 2.7 Average monthly Number of Dust Storm Days (DSD) by three kinds of dust definition in the Gonghe Basin from 2000-2022. A) Dust Definition-P2021, data from MODIS-Terra; B) Dust Definition-K2011, data from MODIS-Terra; C) Dust Definition: P&G2016, data from MODIS-Terra; D) Dust Definition-P2021, data from MODIS-Aqua; E) Dust Definition: K2011, data from MODIS-Aqua; F) Dust Definition: P&G2016, data from MODIS-Aqua. Between the top and bottom line, '_' means 99% and 1% percentile value; the 'red line in the blue box' means the mean value; the blue box shows the interquartile range.

Figure 2.8 shows Time-series graphs of the number of DSD per month from 2000-2022 via each definition. Although, generally, the dust cycle reaches its peak in the spring months, the number of DSD in this period can be seen to fluctuate significantly on an inter-annual basis. Generally, the K2011 and P&G2016 methods generate a similar time-series, showing a comparable magnitude of DSD and similar inter-annual trends. However, the P&G2016 method was able to detect that the DSD is slightly higher than K2011's DSD. In addition, Among the three dust definitions, the calculated DSD from Terra (10.30 CST or 02.30 UTC) is lower than that from Aqua (13.30 CST or 05.30 UTC) in most years, which suggests either higher dust detection or occurrence in the afternoon than morning.

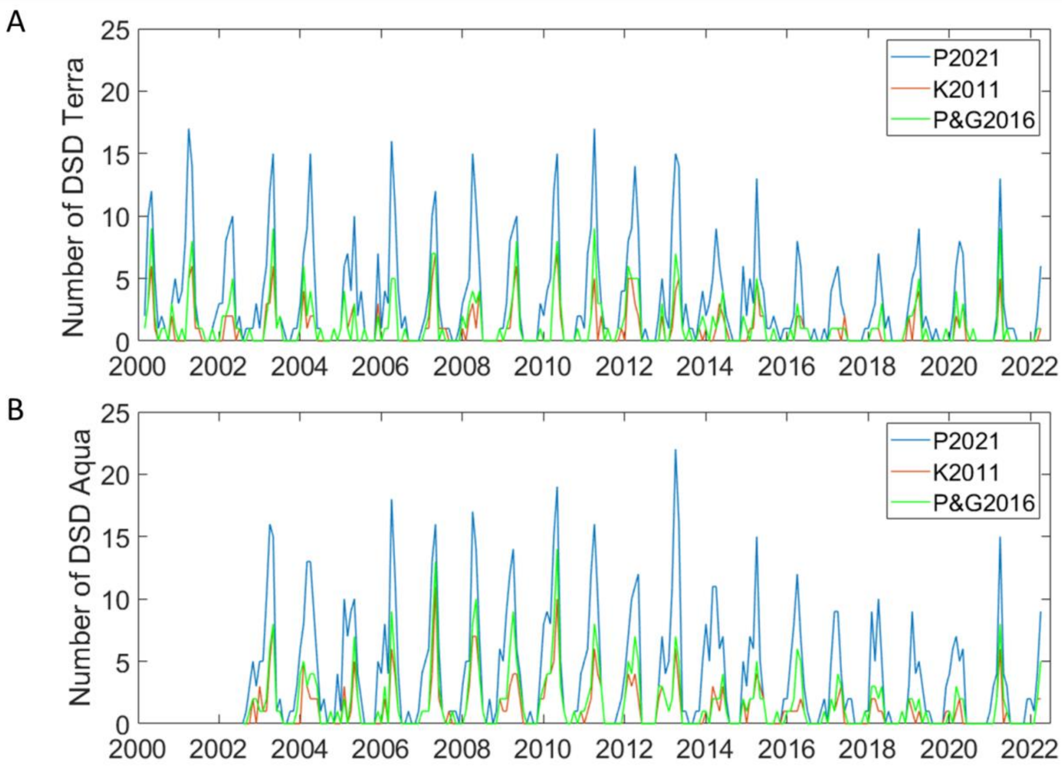

Figure 2.8 Time-series Number of Dust Storm Days (DSD) by three kinds of dust definition in the Gonghe Basin from 2000-2022. A) Data from MODIS-Terra, B)Data from MODIS-Aqua. The blue line is the P2021 method, the orange line indicates the K2011 Method and the Green line is the P&G2016 method.

2.3.2 [O2] SDS magnitude and mode in the Gonghe Basin

The monthly median AOD value from the P2021 method (~0.3, in Figure 2.9 A&B) is lower than AOD from the K2011 method (~0.5, in Figure 2.9 C&D). P&G2016 AOD boxplot represents a similar dust cycle with K2011, whereby AOD values have high variability during spring. The findings imply that the magnitudes of SDSs filtered through the K2011 and P&G2016 methods are more substantial compared to those derived from the P2021 method.

Overall, the dust loading (AOD value) increased since October and reached a peak in April, then dropped the value in June; during the summer period (June, July, and August) nearly no SDSs. The boxplot is much higher during March to May. An apparent seasonal variation suggests dust loading levels are different from other seasons. Spring is the period with the highest frequency and intensity of sandstorms in the basin. The AOD boxplot is comparatively lower in October, December, January, and February, which suggests dust loading has a high level of agreement with DSD frequency within those months. Winter has a relatively small and similar amount of dust loading. During Summer and early autumn, from June to September, nearly no dust loading. Only been 7 DSD with relatively high AOD were found in June in K2011 methods (Fig 2.9 C) and P&G2016 (Fig 2.10 D) from the MODIS-Terra datasetvover the last 22 years. The AOD outliers mainly occur between Feb and May and the value ranges from 0.5-2 (Figure 2.10), corresponding to potential significant SDSs during 2000-2022 under the climate background.

Angstrom Exponent (AE) is valuable to determine particle size, broadly if AE > 0.7 fine mode aerosol; if AE < 0.7 coarse mode aerosol. There is an obvious particle size difference between AE boxplots for the three definition groups (Figure 2.10); the P2021 boxplot is comparatively tall, the K2011 boxplot is comparatively short, and the P&G2016 boxplot is in the middle. Using the K2011 definition, we exclude the data with AE values > 0.7 (Figure 2.10 C&D), and the selected SDSs are therefore confined to a coarse mode. Whereas P2021 definition datasets display dust particle size various distributed in different months, a coarse mode in April and May, and fine dust mode from November to March (Figure 2.10 B). As for P&G2016, the medians are all at a similar level except for summer, lower than 0.75 is the coarse mode. AE November boxplots are uneven in size and the median varies between the two satellites. Aqua Satellite [PM] detected particle size and dust loading are typically bigger than Terra [AM] value, supporting the hypothesis that more dust [events] either occur or are detected in the Gonghe Basin afternoon.

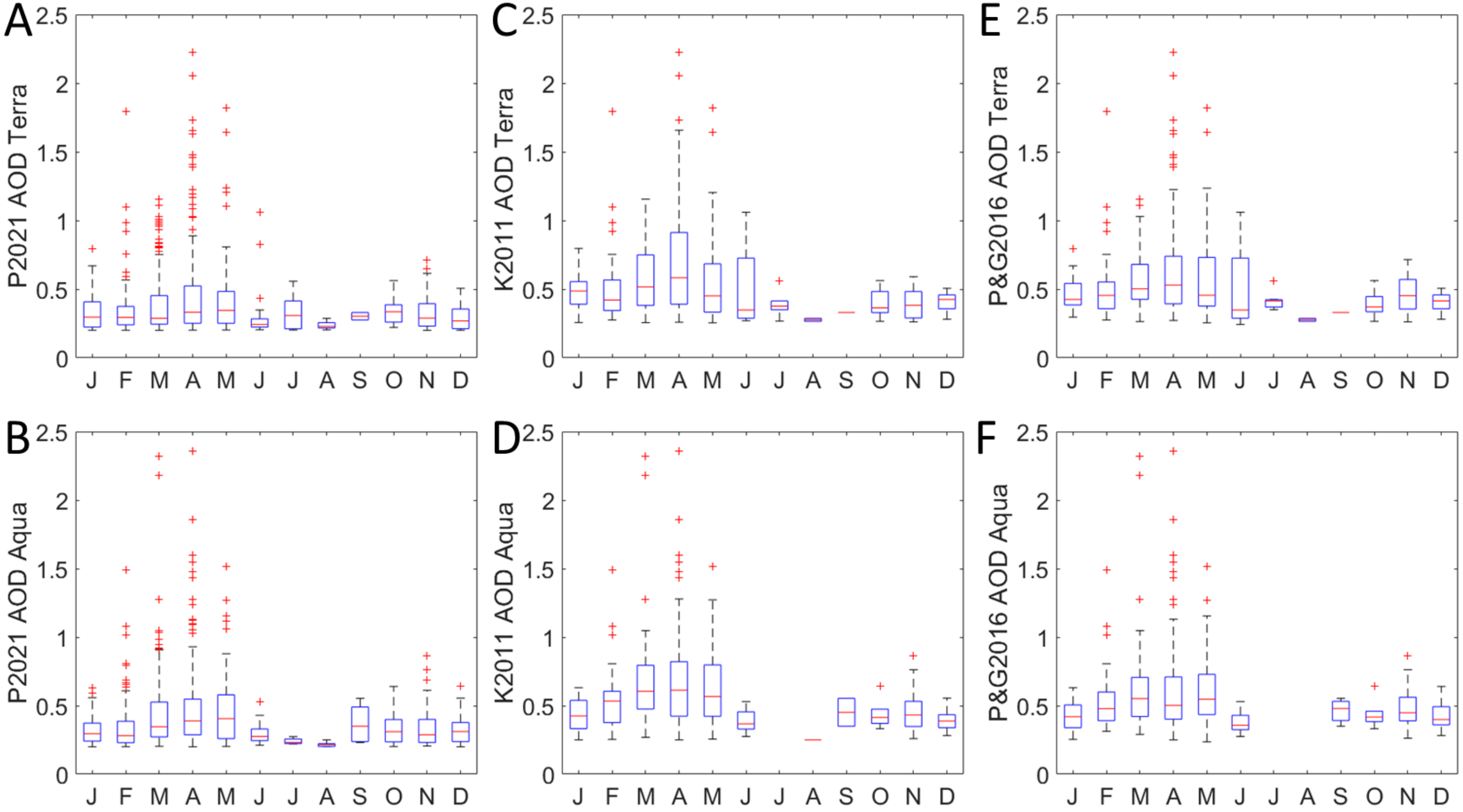

Figure 2.9 AOD monthly boxplot from three dust definition methods, data from MODIS-Terra (Up) and MODIS-Aqua (Bottom) over the Gonghe Basin 2000–2022. A) P2021 AOD Terra; B) P2021 AOD Aqua; C) K2011 AOD Terra; D) K2011 AOD Aqua; E) P&G2016 AOD Terra; F) P&G2016 AOD Aqua.

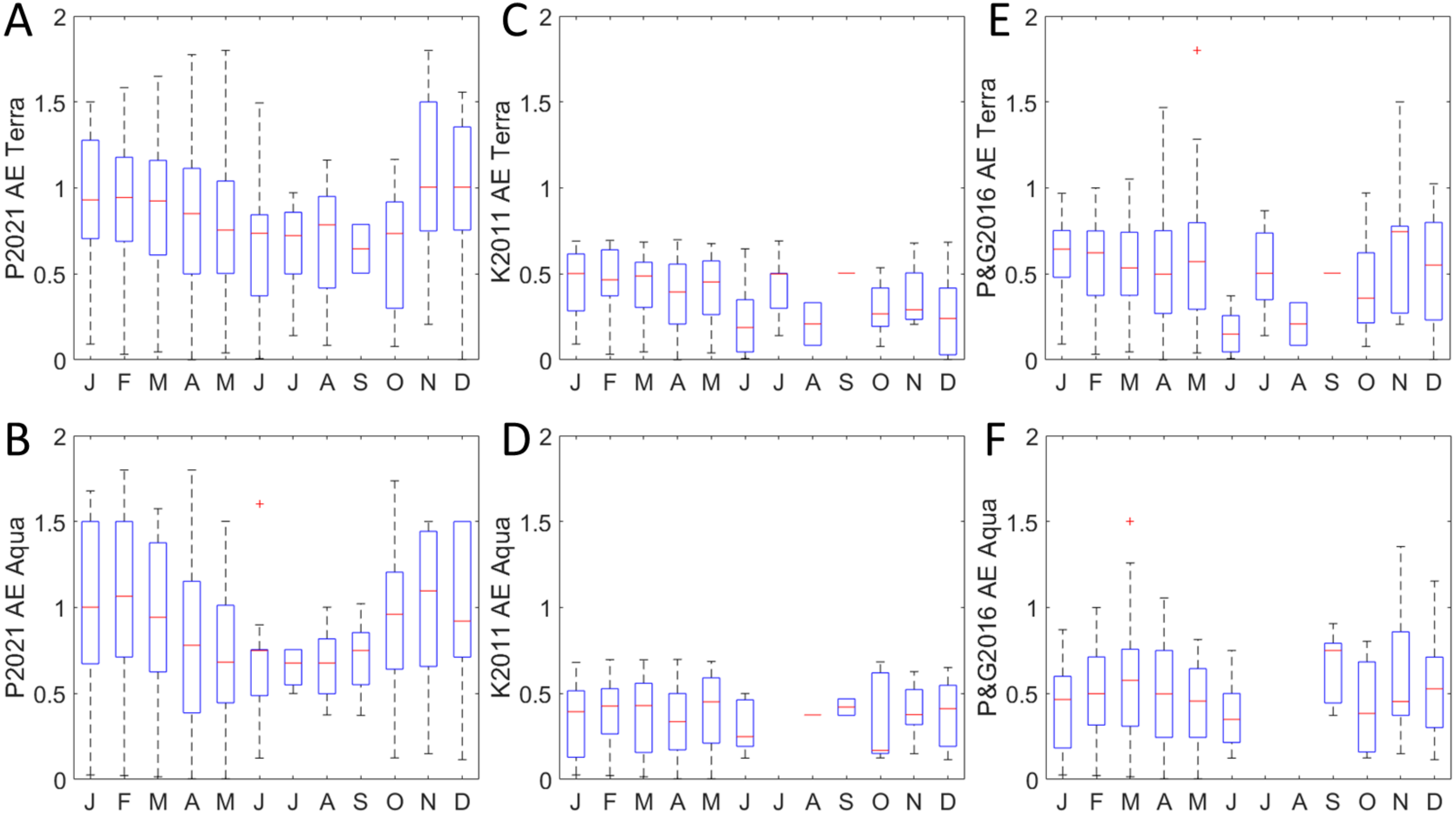

Figure 2.10 AE monthly boxplot from three dust definition methods, data from MODIS-Terra (Up) and MODIS-Aqua (Bottom) over the Gonghe Basin 2000–2022. A) P2021 AE Terra; B) P2021 AE Aqua; C) K2011 AE Terra; D) K2011 AE Aqua; E) P&G2016 AE Terra; F) P&G2016 AE Aqua.

2.3.3 [O3] Climate and Surface Properties

The box plots of dust-related climate parameters show apparent seasonality. The precipitation (Fig 2.11 A) is mainly concentrated from May to September in the Gonghe Basin. In summer, the total monthly rainfall is 75 mm month^{-1}. In July, the maximum total rainfall exceeds 100 mm month^{-1}, with almost no precipitation in this area from November to March. Similar fluctuation curves are shown in air temperature (Fig 2.11 B) and NDVI (Fig 2.11 C). The monthly averaged air temperature continuously rises from the lowest -12°C in January to the peak at 12°C in July and then decreases to the minus temperature in winter (Fig 2.11 B). In addition, the blue area of the box plot is tiny, indicating no noticeable difference in each month's average temperature every year. In summer, the vegetation index NDVI is significantly higher than in other seasons (Fig 2.11 C). In August, the vegetation coverage in the Gonghe Basin reaches a peak of about 0.4, followed by autumn, the monthly average NDVI decreases from 0.38 to 0.17, and the NDVI in winter drops to 0.12. The vegetation growth cycle starts in May, and the vegetation coverage period starts from May to October. The changes in rainfall and temperature in the Gonghe Basin are also reflected in the apparent seasonal and interannual fluctuations of vegetation greening. The average value of soil wetness (Fig 2.11 D) fluctuates gently each month, but the lowest and highest values change significantly. The soil humidity from May to October is generally higher than that from November to April; after the consistent lowest rainfall on the ground in winter, March and April are the months with the lowest soil humidity. Similar seasonal fluctuations also occur in Relative Humidity (RH, Fig 2.11 E). From May to October, the average relative humidity is greater than 47% and gradually decreases to about 30% by March next year.

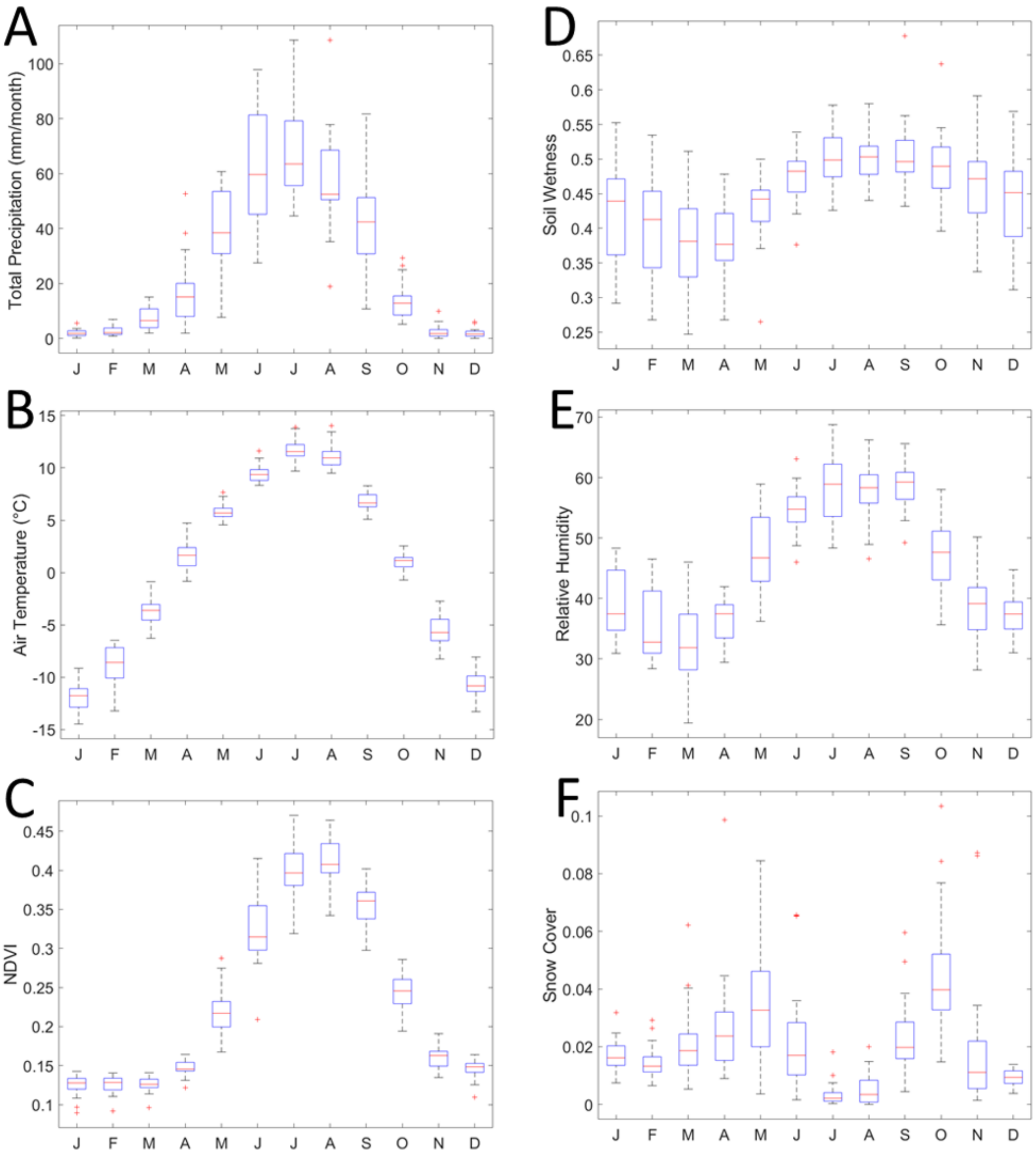

Figure 2.11 The boxplot of climate factors during 1980-2022 in the Gonghe Basin in China. A) Total Precipitation; B) Air Temperature; C) NDVI; D) Soil wetness; E) Relative Humidity; F) Snow Cover from the Merra-2 model monthly dataset.

Wind is characterised by high intensity and frequency in winter and early spring. Figure 2.12 A shows the number of DSD with wind speed over 6 ms^{-1}, which mainly occurs in early Spring (March, April) and Winter (December, January, and February), accounting for 66% of the total number of windy days. The frequency of wind speeds above 6 ms^{-1} (the Threshold Wind Velocity, TWV) exhibited clear seasonal variability and the dust season (winter 54.2%, spring 50.9%) is much higher than that in the non-dust season (summer 11.8%, autumn 24.1%,

Appendix B). The percentage of wind speeds exceeding the TWV was 35.1%. It indicates that about 128 days per year, wind erosion might occur in the Gonghe Basin.

Similarly, the Dust Uplift Potential (DUP) distribution with a clear seasonal cycle is shown in Fig 2.12 B. The DUP in spring and winter controlled most of the total variability of DUP (83.7%), with some outliers in May and November. Based on Figures 2.12 B and 2.7, although December has a similar amount of DUP to April, the number of DSD in April is much higher than in December. This suggests that the high-frequency and intensity wind does not always accompany high-frequency SDSs. Wind was identified as a significant driver; then relationships between AOD, AE, and wind were explored to understand the source of the material.

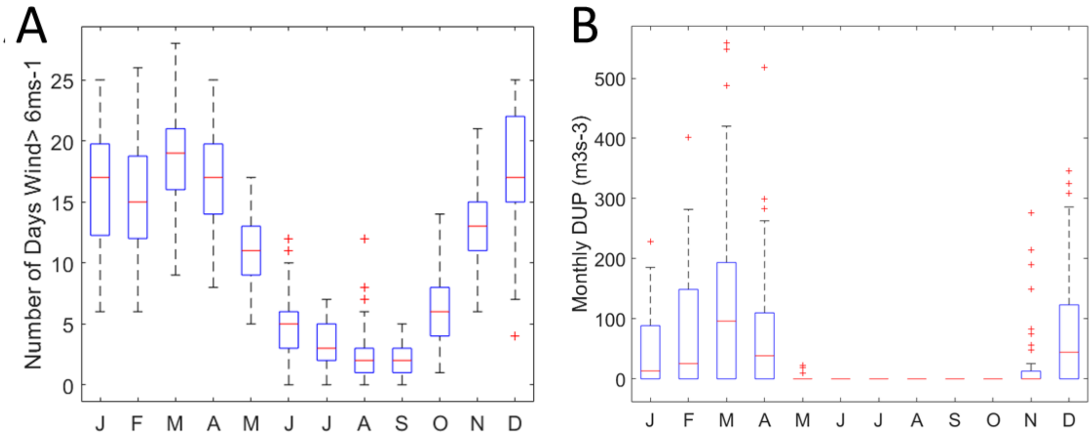

Figure 2.12 A) The number of days wind speed over 6 ms^{-1} *in each month using daily data; B) The boxplot of DUP using monthly data, during 1980-2022.*

2.3.4 [O4] Climate and Dust Relations

2.3.4.1 Inter-annual variability from 1980 to 2022

Time series are constructed to outline the role of climate and surface variables on SDS. This time-series graph (Fig 2.13, 2.14 and 2.15) shows an evident inter-annual variability and clear seasonality. As for the dates starting from 1980, we divided the time to 1980-2000 and 2000-2022 to discover the trends and changes. The monthly wind speed decreased from 8.46 ms^{-1}

in 1980 to 6.49 ms^{-1} in 2022, with a decline rate of 0.49 ms^{-1} per decade (Fig 2.13 D). By contrast, increasing trends were shown in temperature (Fig 2.13 A) and NDVI (Fig 2.13 B) in the observation period. Total precipitation (Fig 2.13 B) represented a falling trend from 1980-2000 and then rose from 2000-2022. Similarly, soil wetness (Fig 2.13 C) also shows the same trend as rainfall. SDSs are characterised by P&G 2016 DOD and show an overall declining trend since the 2000s (Figure 2.14 C&D).

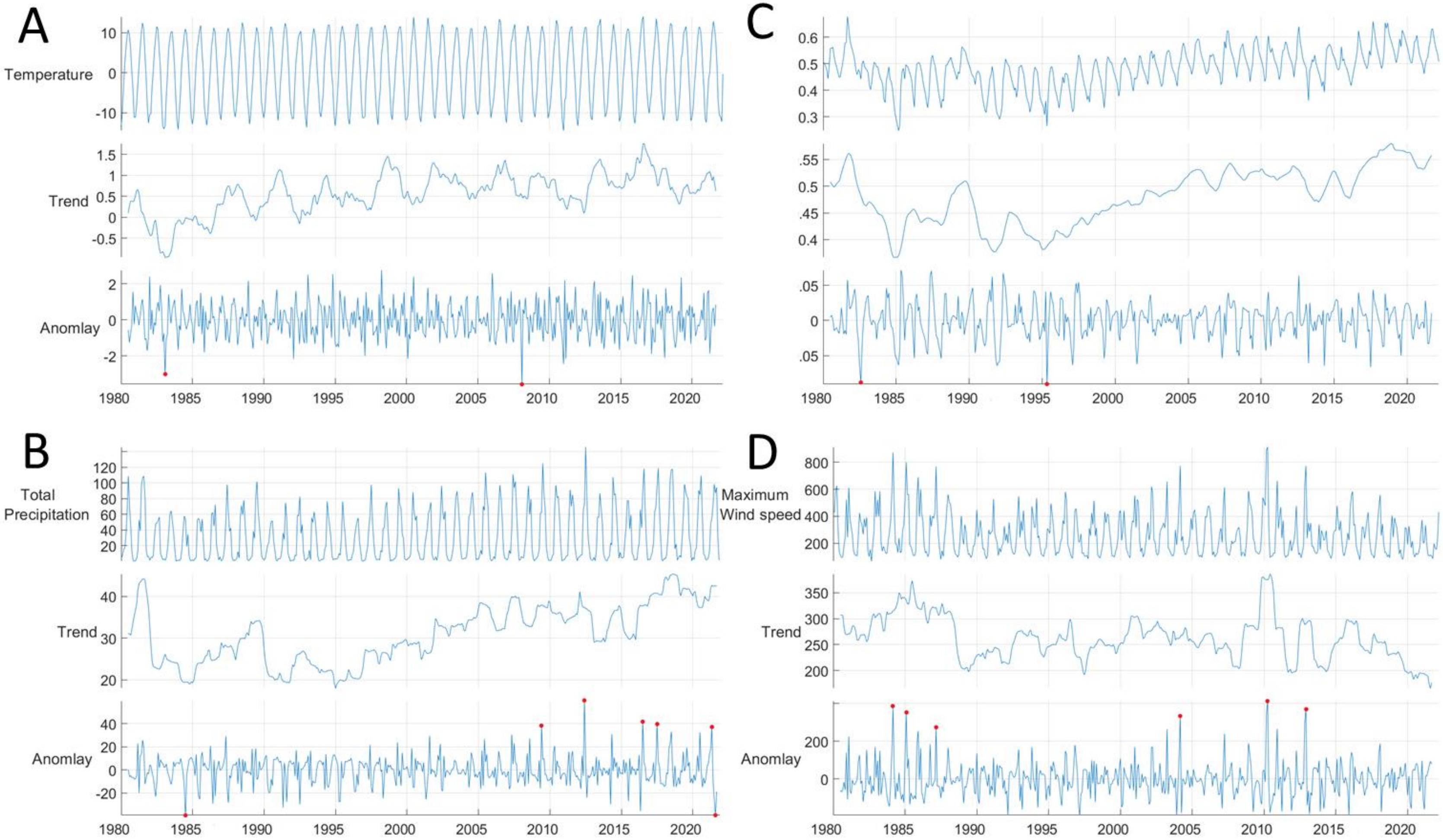

Figure 2.13 Time series of observations for the Gonghe Basin. A) Air Temperature; B) Total Precipitation; C) Soil wetness; D) Surface Maximum wind speed cubed from Merra-2 data in 1980-2022. The red points are the anomaly months, which are over ± 3σ. (Detail analysis of Anomalies in Appendix E)

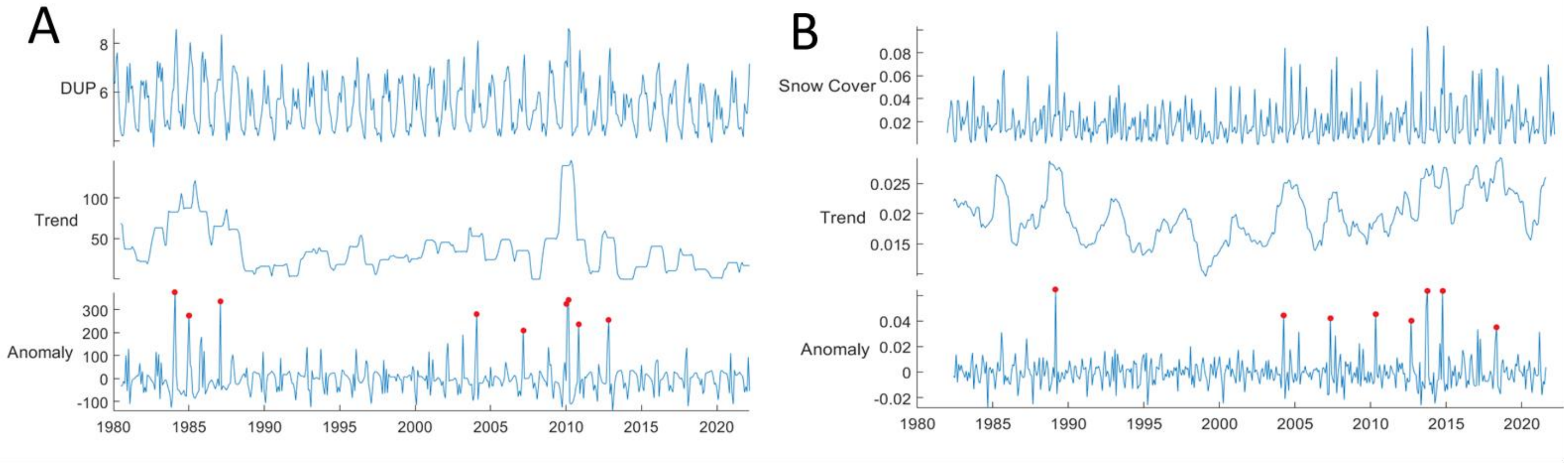

Figure 2.14 Time series of observations for the Gonghe Basin. A) Dust Uplift Potential (m^3s^{-3}); B) Snow Cover (% of the Gonghe Basin) from Merra-2 data in 1980-2022. The red points are the anomaly months, which are over ± 3σ. (Detail analysis of Anomalies in Appendix E)

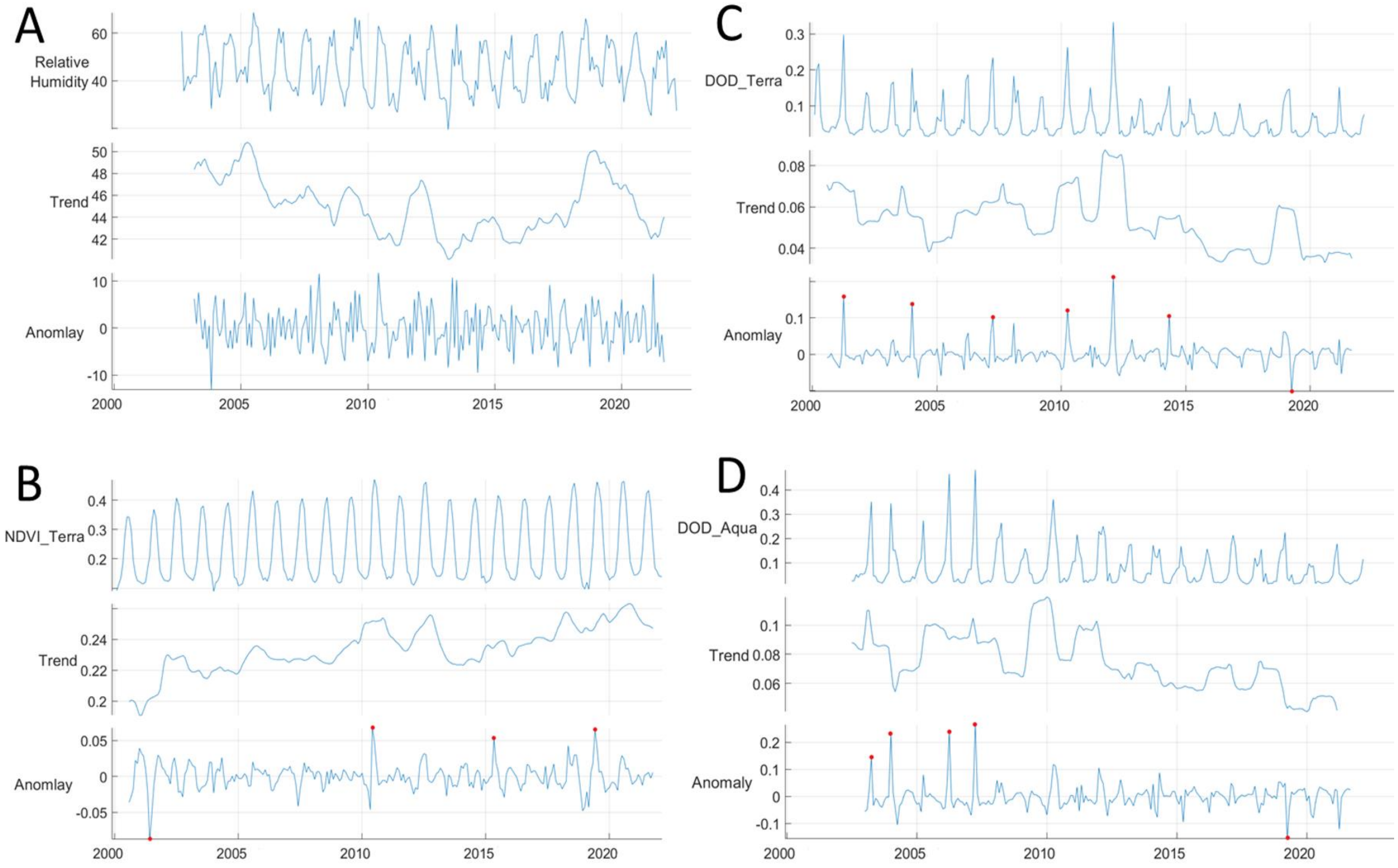

Figure 2.15 Time series of observations for the Gonghe Basin. The data was derived from A) Relative Humidity; B) NDVI from MODIS-Terra; C) Dust Optical Depth (DOD) from MODIS-Terra; and D) DOD MODIS-Aqua in the period of 2000-2022. The red points are the anomaly months, which are over ± 3σ. (Detail analysis of Anomalies in Appendix E)

2.3.4.2 Correlation

Using the Pearson correlation coefficient analysis shows that dust loading (DOD index) from MODIS Aqua & Terra has a moderate negative correlation with DUP, NDVI, Precipitation, surface soil wetness, relative humidity and temperature, and a strong positive relation with cube maximum wind speed in Table 2.3. The monthly total precipitation and surface soil wetness have a moderate ($r=0.453$) statistically significant ($p<0.001$) positive association. Besides, the factors, including temperature, NDVI, relative humidity, and rainfall ($r>0.8$) are significantly correlated with each other and moderately correlated with wind speed (about $r=0.5$).

The North Atlantic Oscillation (NAO) index can be considered an indicator of the strength of the westerly winds, and a positive NAO phase can enhance the strength of the westerly flow over the QTP. A weak negative correlation was found between Westerlies and temperature, rainfall, soil moisture, RH, and NDVI, and a positive correlation with wind and DOD. Besides, EASM correlated weakly negatively with temperature and rainfall. Thus, the Westerlies and EASM have a negative impact on temperature and rainfall, and the Westerlies have a weak positive influence on wind speed and SDS.

*Table 2.3 The Person correlation between 12 climate factors between 1980 to 2022 Monthly data in the Gonghe Basin in China. The aerosol product wavelength is AOD 550 nm and AE 440 nm. **. Correlation is significant at the 0.01 level (2-tailed). *. Correlation is significant at the 0.05 level (2-tailed). Grey highlights the non-statistically significant correlation results.*

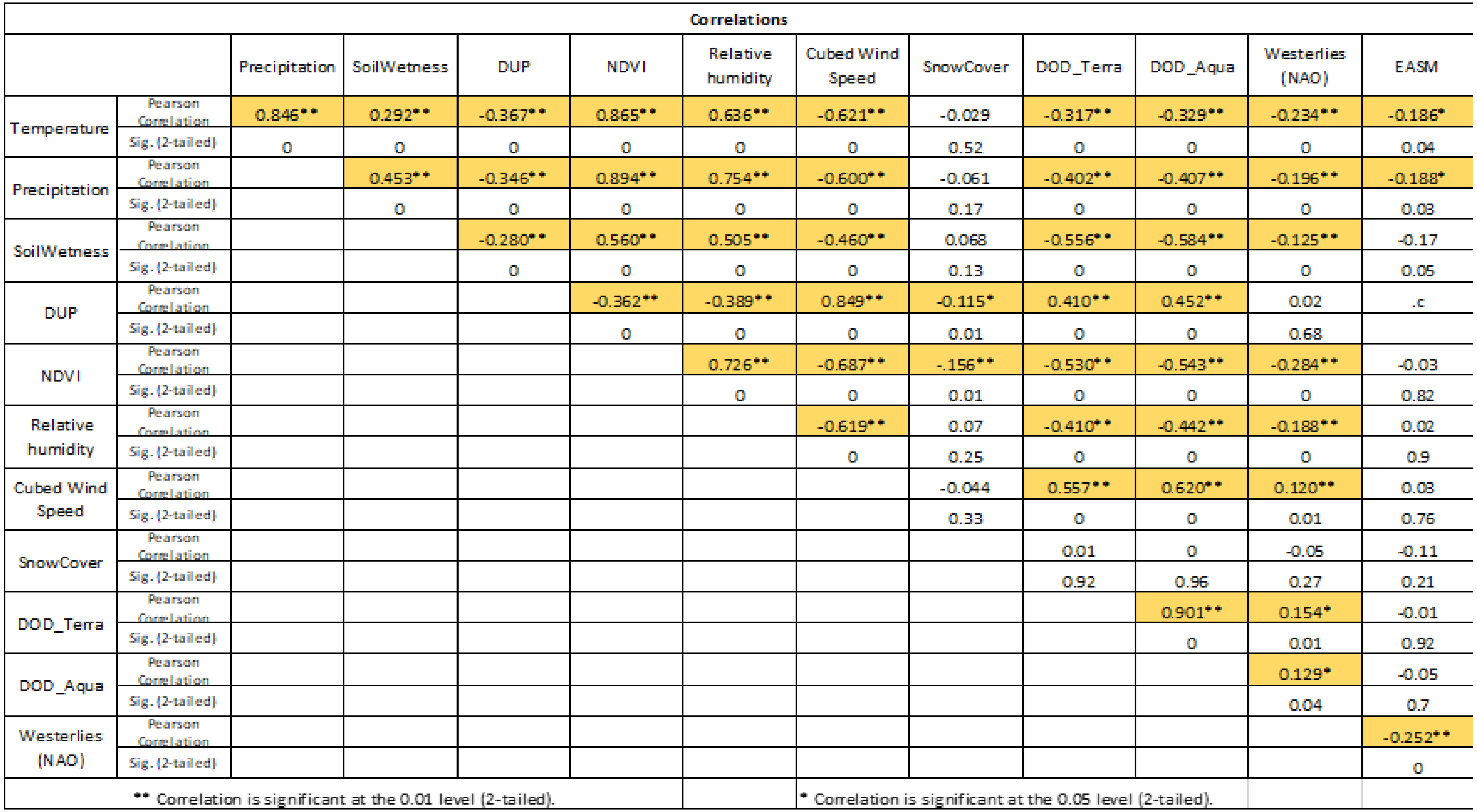

Correlations												
		Precipitation	SoilWetness	DUP	NDVI	Relative humidity	Cubed Wind Speed	SnowCover	DOD_Terra	DOD_Aqua	Westerlies (NAO)	EASM
Temperature	Pearson Correlation	0.846**	0.292**	-0.367**	0.865**	0.636**	-0.621**	-0.029	-0.317**	-0.329**	-0.234**	-0.186*
	Sig. (2-tailed)	0	0	0	0	0	0	0.52	0	0	0	0.04
Precipitation	Pearson Correlation		0.453**	-0.346**	0.894**	0.754**	-0.600**	-0.061	-0.402**	-0.407**	-0.196**	-0.188*
	Sig. (2-tailed)		0	0	0	0	0	0.17	0	0	0	0.03
SoilWetness	Pearson Correlation			-0.280**	0.560**	0.505**	-0.460**	0.068	-0.556**	-0.584**	-0.125**	-0.17
	Sig. (2-tailed)			0	0	0	0	0.13	0	0	0	0.05
DUP	Pearson Correlation				-0.362**	-0.389**	0.849**	-0.115*	0.410**	0.452**	0.02	.c
	Sig. (2-tailed)				0	0	0	0.01	0	0	0.68	
NDVI	Pearson Correlation					0.726**	-0.687**	-.156**	-0.530**	-0.543**	-0.284**	-0.03
	Sig. (2-tailed)					0	0	0.01	0	0	0	0.82
Relative humidity	Pearson Correlation						-0.619**	0.07	-0.410**	-0.442**	-0.188**	0.02
	Sig. (2-tailed)						0	0.25	0	0	0	0.9
Cubed Wind Speed	Pearson Correlation							-0.044	0.557**	0.620**	0.120**	0.03
	Sig. (2-tailed)							0.33	0	0	0.01	0.76
SnowCover	Pearson Correlation								0.01	0	-0.05	-0.11
	Sig. (2-tailed)								0.92	0.96	0.27	0.21
DOD_Terra	Pearson Correlation									0.901**	0.154*	-0.01
	Sig. (2-tailed)									0	0.01	0.92
DOD_Aqua	Pearson Correlation										0.129*	-0.05
	Sig. (2-tailed)										0.04	0.7
Westerlies (NAO)	Pearson Correlation											-0.252**
	Sig. (2-tailed)											0

** Correlation is significant at the 0.01 level (2-tailed).

* Correlation is significant at the 0.05 level (2-tailed).

2.3.4.3 Lags Correlation

The impact of temperature and rainfall on dust in the previous three months is more significant than that in the current month. DOD from Terra and Aqua correlation value with other variables is similar. The cross-correlation between temperature and DOD was significantly negative (R cc (lag -3~0) = -0.41 to -0.45; $p<0.05$, Fig 2.16 B and H). Similarly, NDVI and rainfall lead to DOD (lag -3~0). The strongest cross-correlations between NAO (Westerlies) and DOD were observed with a four-month lag (R cc(lag4) = -0.32; $p<0.05$) and 11-month lag (R cc (lag 1) = - 0.22; $p<0.05$), respectively (Fig 2.16 C and I). Also, Fig 2.16 A showed a significant cross-correlation between DUP and DOD in zero time offset with a correlation value of 0.41. This indicates that the variations of DUP may interact with the DOD without time lag in monthly time scales. Moreover, the cross-correlation between EASM and DOD was found to be predominantly significant (R cc(lag0) = + 0.18; $p<0.05$). In addition, the highest cross-correlation value was found at lag month -9, 3, 15 (R cc = - 0.62; $p<0.05$; Fig 2.16 F). Thus, EASM exhibits a lagged impact on DOD.

The cross-correlation analysis revealed a significant relationship between wind and the North Atlantic Oscillation (NAO), with lags of 5 to 9 months and 11 to 14 months. The highest correlation value was observed at a lag of 6 months (R cc(lag6) = -0.28; $p<0.05$, Fig 2.17 B). Similarly, the lagged NAO values were found to be positively correlated with the NAO (Fig 2.17 A), indicating that above-average wind values are likely to follow above-average values of the Westerlies by approximately 6 months. On the other hand, NDVI, temperature, and rainfall exhibited significant negative correlations with NAO at zero-month lag (R cc(lag0)； $p<0.05$, Fig 2.17 C, D, E). The analysis did not find a significant cross-correlation between snow cover and NAO during the study period. Fig 2.17 H depicts the significant positive cross-correlations between wind speed and the East Asian Summer Monsoon (EASM) within the pre 8-12 months.

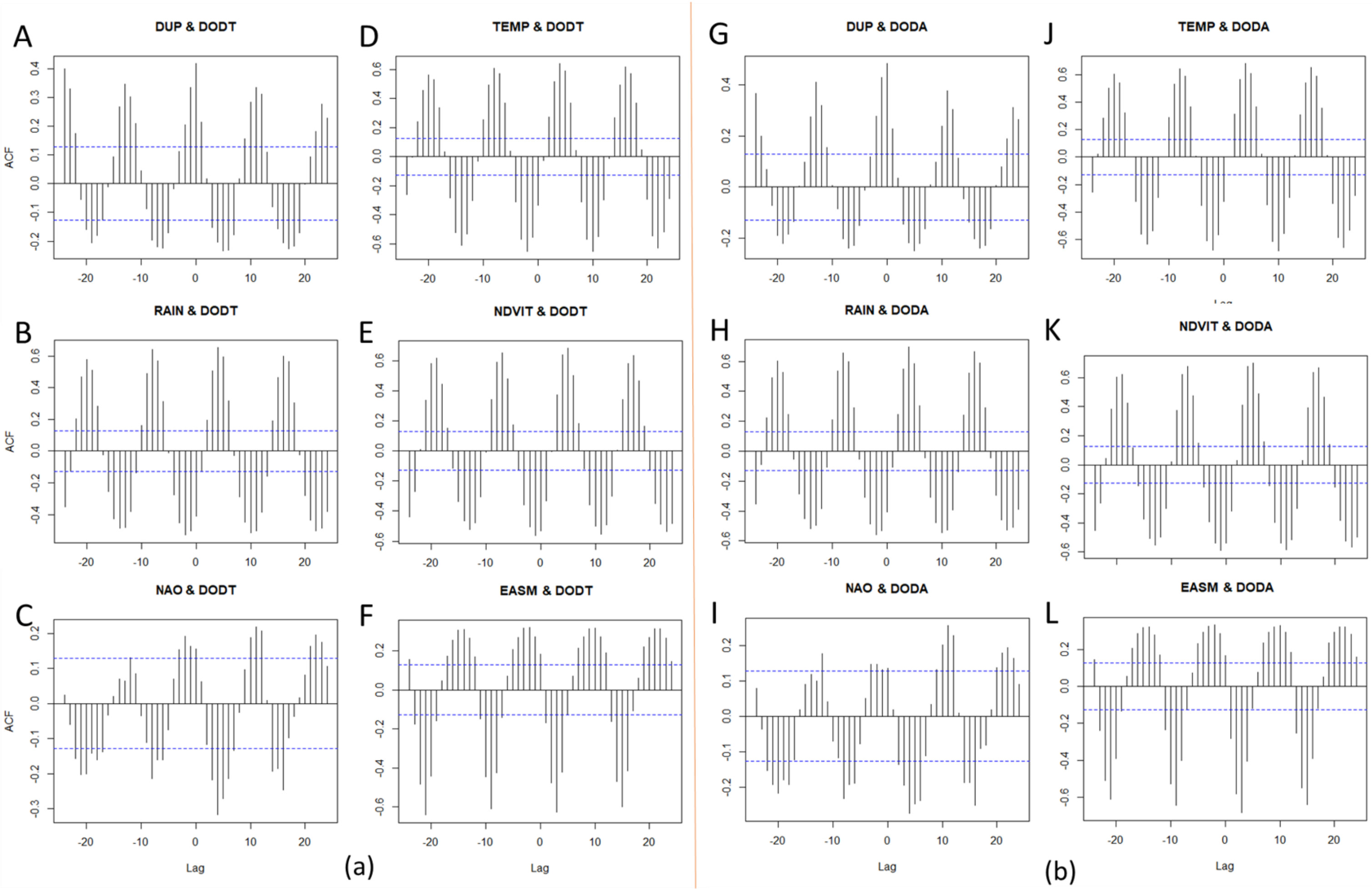

Figure 2.16 Lagged Corelation between climate and dust factors. DOD from Terra (a), DOD from Aqua(b) Lag correlation with DUP (A&G), Rainfall (B&H), Westerlies (NAO, C&I), Temperature (D&J), NDVI (E&K) and EASM (F&L). The X-axis is lagging months, and the Y-axis is the correlation value. The blue dashed lines represent an approximate confidence interval, by default a 95% interval. On both sides of the two blue lines, p<0.05, the value is statistically significant.

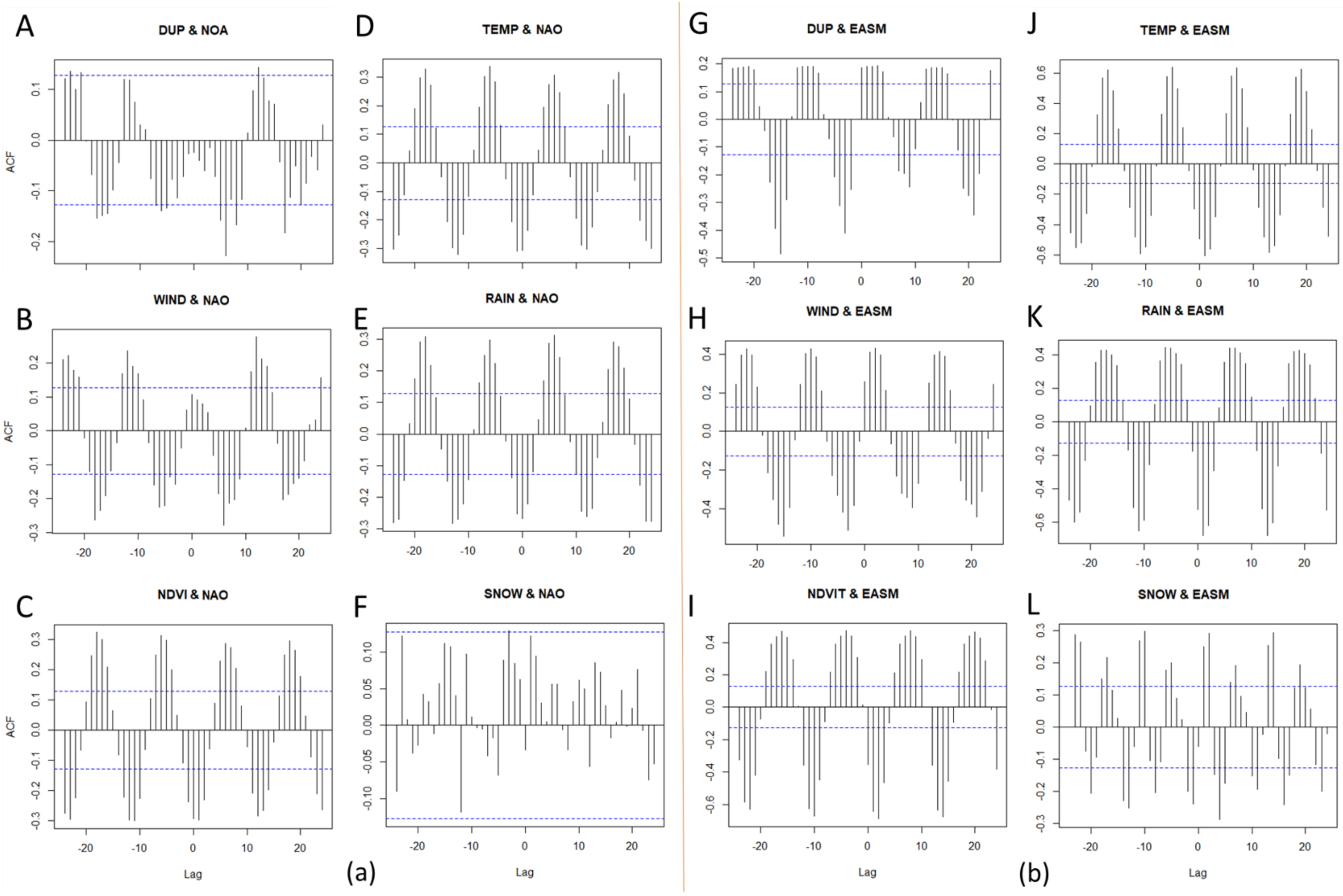

Figure 2.17 Westerlies (NAO, a), EASM Index (b) Lag correlation with DUP (A&G), Wind speed (B&H), NDVI (C&I), Temperature (D&J), Rainfall (E&K) and Snow Cover (F&L). The X-axis is lagging months, and the Y-axis is the correlation value.

2.3.4.4 Linear Regression

The dust prediction model for Gonghe Basin can be expressed by the following linear regression equation:

y(DOD-Terra) = 0.123 - 0.012*Temperature + 0.0001*DUP - 0.235*NDVI - 0.506*Snow Cover

y(DOD-Aqua) = 0.206 - 0.012*Temperature + 0.0004*DUP - 0.564*NDVI

Table 2.4 Stepwise Linear regression model. DOD-Terra and DOD-Aqua as independent variables separately

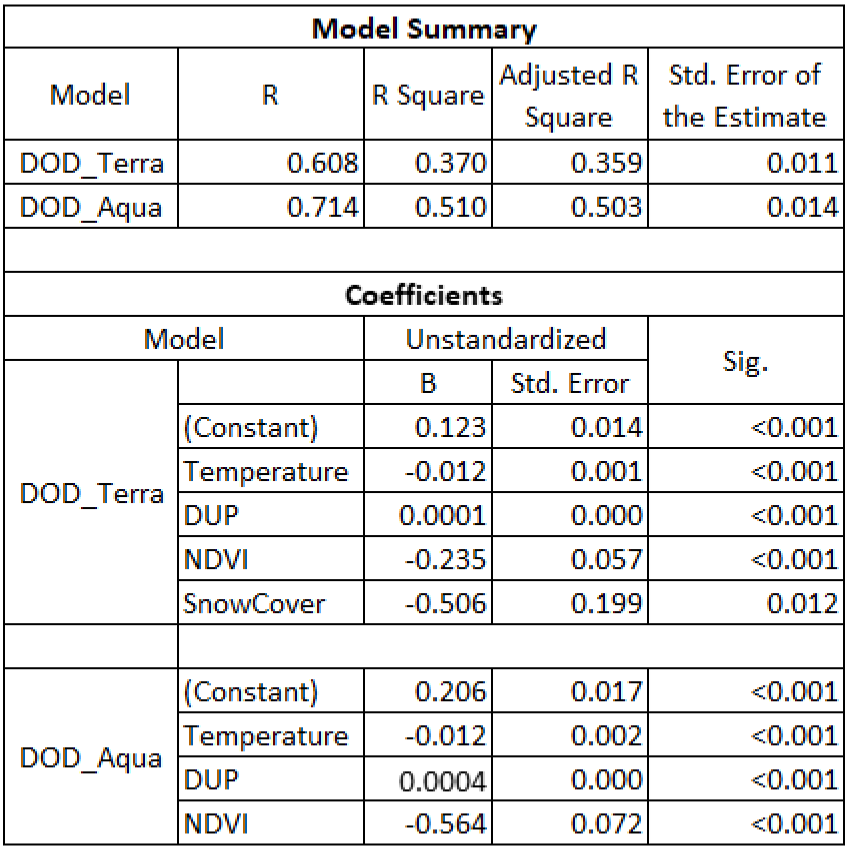

Model Summary

Model	R	R Square	Adjusted R Square	Std. Error of the Estimate
DOD_Terra	0.608	0.370	0.359	0.011
DOD_Aqua	0.714	0.510	0.503	0.014

Coefficients

Model		Unstandardized		Sig.
		B	Std. Error	
DOD_Terra	(Constant)	0.123	0.014	<0.001
	Temperature	-0.012	0.001	<0.001
	DUP	0.0001	0.000	<0.001
	NDVI	-0.235	0.057	<0.001
	SnowCover	-0.506	0.199	0.012
DOD_Aqua	(Constant)	0.206	0.017	<0.001
	Temperature	-0.012	0.002	<0.001
	DUP	0.0004	0.000	<0.001
	NDVI	-0.564	0.072	<0.001

Table 2.4 demonstrates that the stepwise multi-linear regression model correctly predicts DOD-Terra accuracy is 37% and the DOD-Aqua is 51% after removal of the seasonal cycle. DUP has a positive coefficient with DOD, which indicates that the DUP increases the probability of SDS. NDVI plays an essential role in preventing SDS due to their high negative B values of -0.235 and -0.564, respectively, in the DOD-Terra and DOD-Aqua equations. Also, temperature and snow cover which only for MODIS Terra DOD reduce SDSs.

2.3.5 Wind Difference in Dust and Non-Dust days

While the prevailing wind direction in Gonghe is from the west regardless of the conditions, the surface maximum wind speed is between 0–15 ms^{-1} during SDS events and 0–10 ms^{-1} during non-dust days with lots of outliers (Figure 2.18, Left). The sample size ‘n’ from MODIS Terra and Aquan and using different method was labelled. The number of non-Dusty day far exceeds the number of Dust day. The average wind speed on dust days from the three methods is about 5.6 ms$^{-1,}$ and the average wind speed on non-dust days is about 3.7 ms^{-1}. SDS in the afternoon has a higher wind speed than in the morning. The overall wind speed ranges from Aqua is larger than Terra, and the mean wind speed from Aqua at 5.7 ms^{-1} is higher than that from Terra at 5.3 ms^{-1}. Mann-Whitney Test difference between Dust and Non-Dust in each dataset, all $p<0.01$.

Overall, the Gonghe Basin's daily wind rose was shown in Figure 2.19 from 2000-2022, and the wind mainly from the West, also from WNW (West Northwest) and WSW (West Southwest) direction, and other directions with shallow wind speed. In dust days, wind from West and WNW and over 40%, 48%, and 48.5% of days wind speed over 6 ms^{-1} in P2021, K2011 and P&G2016 dust definition, respectively. Whereas, in non-dust days, wind mainly from West and WSW and more than 85%, 81%, and 81.7% of days speed lower than 6 ms^{-1} in P2021, K2011 and P&G2016 dust definition, respectively. MODIS Aqua accounts for a higher proportion than Terra in the wind speed range of 6-15 ms^{-1}.

P2021 daily DUP boxplot range from Terra and Aqua is similar (Fig 2.18 G&J), whereas K2011 and P&G2016 definition DUP from Aqua (Fig 2.18 H&K) is obviously higher than DUP from Terra (Fig 2.18 I&L), which suggests that afternoon (Aqua) is more likely to eject dust from the basin than morning (Terra) and the dust emission wind mechanism is different from a different time of day.

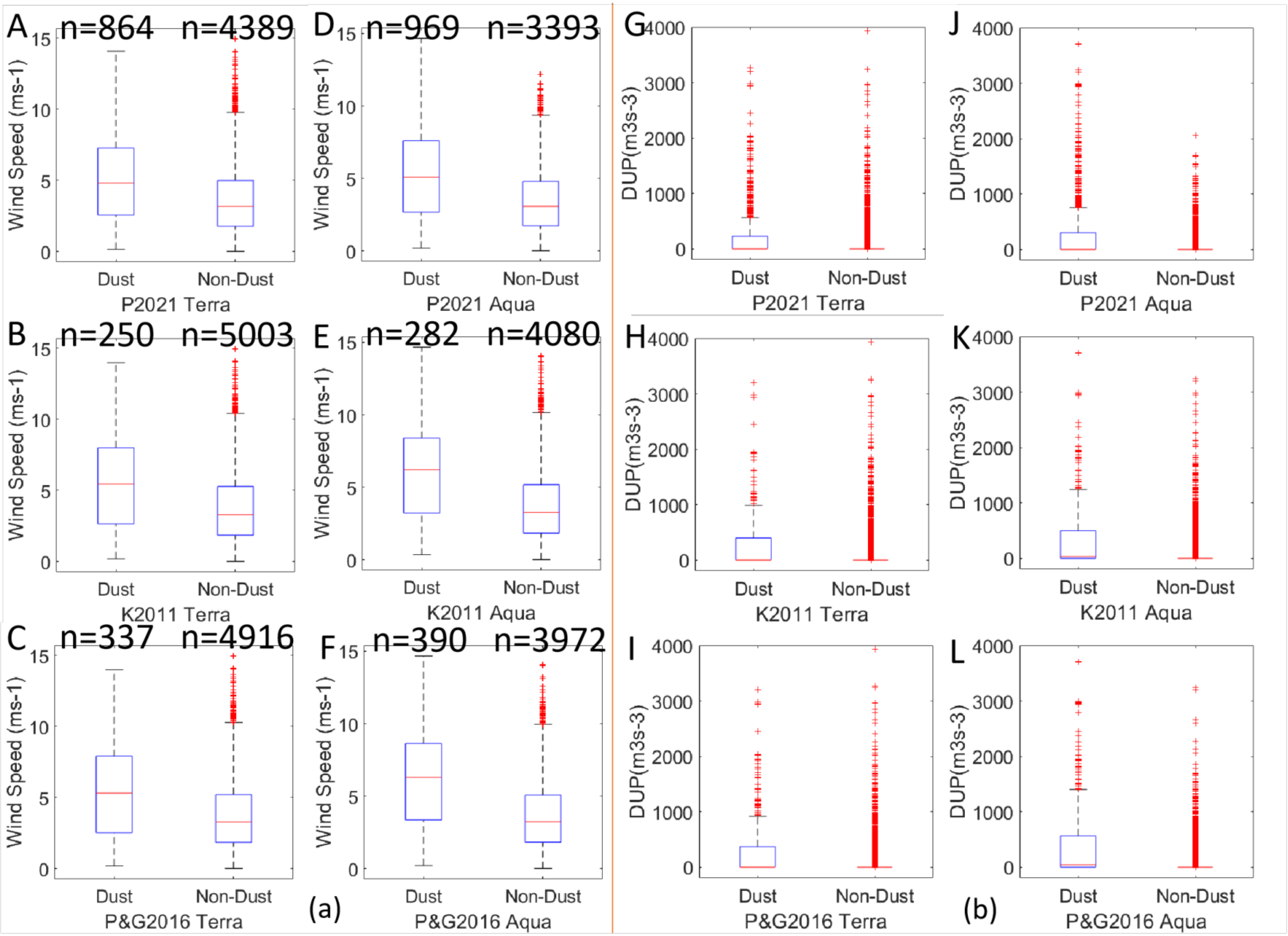

Figure 2.18 Daily Wind speed (a) and DUP (b) from DSD and non-DSD by three kinds of dust definition in the Gonghe Basin, data from MODIS-Terra (Left), MODIS-Aqua (Right) during 2000-2022. Dust Definition-P2021 DSD (A&D) and Non-DSD (G&J); Dust Definition-K2011 DSD (B&E) and Non-DSD (H&K); Dust Definition-P&G2016 DSD (C&F) and Non-DSD (I&L). n is sample size.

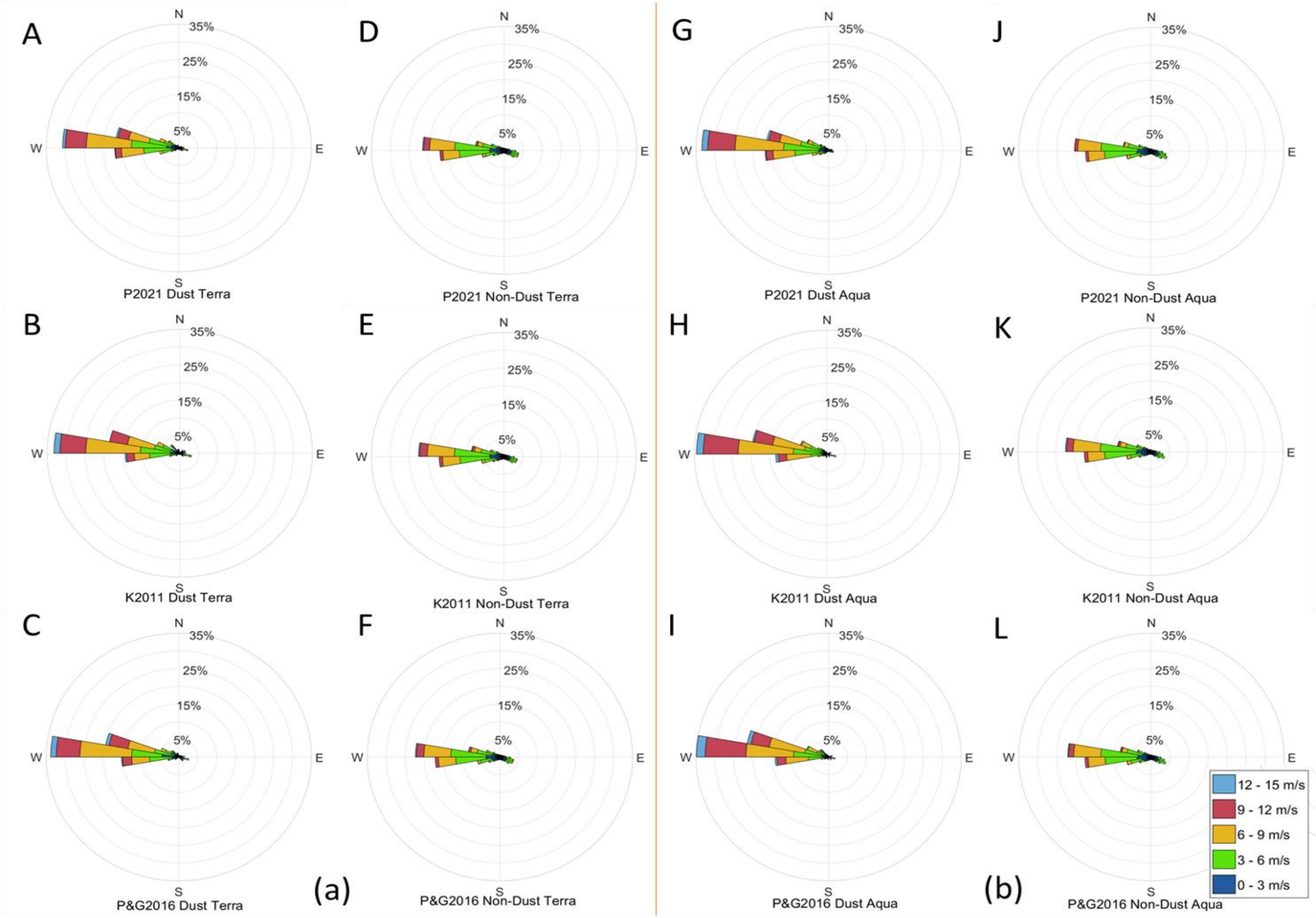

Figure 2.19 Daily Wind Rose from DSD and non-DSD by three kinds of dust definition in the Gonghe Basin, data from MODIS-Terra (a), MODIS-Aqua (b) during 2000-2022. Dust Definition-P2021 DSD (A&D) and Non-DSD (G&J); Dust Definition-K2011 DSD (B&E) and Non-DSD (H&K); Dust Definition-P&G2016 DSD (C&F) and Non-DSD (I&L). 29

2.4 Discussion

2.4.1 Sand and Dust Storms (SDS)

2.4.1.1 SDS definition method and datasets

K2011 and P&G2016 methods detected a smaller number of DSD than the P2021 approach. Different dust definition methods that explore dust seasonality are biassed. The K2011 approach is able to capture around 38% of DSD identified by the P2021 between 2002 to 2022 (Figure 2.6). The significant disparity in DSD count between P2021 and the K2011 approach for the Gonghe Basin is due to the K2011 not only using AOD>0.2 aerosol group but also AE index to subclassify dust (in K2011 dust datasets, Figure 2.11, AE<0.7) and urban aerosol (AE>0.7). P2021's AE boxplot shows the Gonghe Basin dominated by a fine mode, which means more transport dust to the basin than direct from within the basin itself. But, Chen Zongyan (2018) argue that the Gonghe Basin is a dust source area with various aeolian landforms, indicating the limitation of the P2021 method in the human-influenced urban area. Gharibzadeh et al. (2018) suggested that the influence of local human activities leads to a high concentration of fine aerosols. The threshold AOD over 0.2 might include too much urban aerosol.

The DSD calculated by the P&G2016 method using Dust Optical Depth (DOD) differs from the K2011 method. However, the dust frequency in each month from the two methods is similar to Y. Liu et al. (2020) results in Wuwei and Zhangye areas, about 9-16 DSD year^{-1}, which suggests that K2011 and P&G2016 dust definition approaches are more reliable than the P2021 method.

Dust activity showed a clear diurnal pattern with low frequency and magnitude in the morning and higher in the afternoon. The different kinds of winds primarily drive the morning and afternoon dust activity in the Gonghe Basin. Increasing wind speed during the morning is due to Low-Level jets (Li et al., 2020) and the results of SDSs. The afternoon SDSs are related to cold pool outflow, a typical springtime SDS mechanism (Li et al., 2022).

Besides, comparing wind speed from DSD and non-DSD groups, the DSD wind speed average is about 7.3 ms^{-1} higher than the non-DSD upper quarter of 6.7 ms^{-1}. Wind speed within the DSD group varies from 3 ms^{-1} to 14 ms^{-1}; the box and outlier show two dust mechanisms, the cold pool outflow and frontal wind were identified in northern China (Li et al., 2022). By contrast, wind speed within the non-DSD group also has high values, but no SDS might show that the wind is not the only SDS control. Other climate and surface dust drivers in the following sections.

2.4.1.2 Dust in the Gonghe Basin

From the SDS frequency aspect, SDS mainly happens in spring (MAM) and winter (DJF) in the Gonghe Basin. Dust Uplift Potential (DUP) shows a strong seasonal cycle and more than 84% of annual DUPs occur in summer and winter. SDS is significantly less in summer and autumn. It is in agreement with the results of dust across the QTP of China (Xu et al., 2020).

From the dust intensity aspect, maximum AOD values occur in the spring and winter. The highest monthly mean AOD values occurred in April, and TVW ($8ms^{-1}$) of 29%, which suggests the highest DUP when the surface is the most erodible, leading to intense wind erosion events during this period.

2.4.1.3 Other insights from these data: Transport or advected dust

The Angstrom Exponent (AE) is utilised to assess the relationship between aerosol optical depth and wavelength. AE serves as an effective indicator for determining the size distribution of fine particles. The hypothesis is that coarse aerosol particles deposit quicker than fine particles, so the various AE distribution may indicate SDSs from local sources or longer distance transport.

To distinguish whether dust is emitting from the basin or transported to the basin, we correlate AE, AOD, and CMWS (Cubed Maximum Wind Speed, Appendix D). When the wind speed rises, the AOD value increases, and AE decreases, so coarser particles are emitted. Based on our assumptions, dust is more likely to be derived from the local basin when SDSs have a high AOD value and low AE. The results suggest that locally derived SDSs happen in spring, and transported dust is more likely to occur in November in the Gonghe Basin.

2.4.2 Controls on SDS in basin scale

2.4.2.1 SDS response to climate change

The factors' correlation suggests that the dust emission is primarily controlled by surface wind and surface conditions (e.g., soil moisture, land cover type, vegetation, snow cover and soil size distribution). The climate and surface factors that controlled SDS are discussed below.

- Temperature and RH

Temperature reduction increases dust activity by reducing air relative humidity. Findings show SDSs mainly occurred in low-temperature conditions in winter (average -10.5°C) and spring (average 1.1°C), and haboobs happened several times during the dust seasons. Haboob describes sandstorms generated by cold pool outflows [CPO] in arid or semi-arid regions (Gu et al., 2021). Considering the difference in air density, which is affected by temperature and humidity, cold or dry air is heavier than warm or humid air when humidity or temperature are the same, respectively (Walker, 2010; Namdari et al., 2018). Thus, high-density cold air flow contains more energy to eject dust sediment during winter and spring when humidity and temperature are all at the lowest level of the year.

On the contrary, the increase in temperature will lead to a reduction in dust activity through three mechanisms: (i) promoting increased vegetation coverage by increasing precipitation and temperature; (ii) reducing wind speed by weakening the temperature gradient of the Qinghai Tibet Plateau (You et al., 2010); and (iii) increasing surface soil moisture through precipitation, resulting in an increase in the threshold wind speed required for SDSs.

- Soil Moisture

Haustein et al. (2015) explored that soil moisture plays a crucial role in controlling the model's shear velocity and SDS threshold. Soil moisture is a crucial constraint, especially in the crust state. Increasing temperatures accompanied by high precipitation will raise the surface soil moisture and help control SDSs. Soil Wetness is lower than 40% during March and April, and the low-level soil wetness leads to low cohesion of soil particles, so the threshold friction speed decreases, resulting in increased SDS.

- Precipitation

Precipitation is another critical factor leading to dust activities. Precipitation significantly influences the basin vegetation growth in the semi-arid Gonghe Basin, and rainfall affects the water level of Longyangxia Lake and the soil moisture level of the basin. The lakes' water level and groundwater level influence local SDS in the Gonghe Basin by fine particle availability from the ephemeral Lake.

- NDVI

The reduction in SDSs is partly due to increased vegetation cover. High rainfall carries abundant water vapour, leading to a simultaneous increase in surface moisture and relative humidity in the basin. At the same time, the warmer environment promotes vegetation growth, reducing SDSs (lower DOD values). Both processes contribute to a reduction in SDS events in the Gonghe Basin. For example, Bao et al. (2021) concludes that the number of DSD in spring in east-central Inner Mongolia is significantly correlated with the interannual variability of NDVI. An increase in vegetation cover can suppress the occurrence of SDSs, while deterioration of vegetation can lead to frequent SDSs.

The direct or lag influence and extent of vegetation on sandstorms vary in different areas of China. (i) Zou and Zhai (2004) demonstrated that the negative correlation between the previous summer NDVI and spring SDSs was more significant than the negative correlation between spring NDVI and dust, particularly in northeast China. (ii) In this research, we found a directly moderate negative correlation between NDVI and dust, and 3-month earlier temperature and precipitation have a more significant lag impact on SDS. (iii) In the desert areas of northwest China, where vegetation is absent or very sparse, the variation in SDSs does not seem to be related to vegetation, e.g., the Taklamakan Desert, the Batangilin Desert, and the Tengger Desert (Zou and Zhai, 2004).

- Wind Speed

Wind speed is the main controller of local SDSs in spring and it plays a role in transporting dust to the basin in winter. Same to the conclusion of Guan et al., (2017) that sand-blowing wind speed mainly occurs in spring and winter, coinciding with the sandstorm season in northern China. Nevertheless, this research goes further to characterise how the wind plays a role in SDSs in spring and winter.

The number of DSD frequencies is consistent with sand blowing wind speed frequency in spring. March and April account for more than 50% of the annual sandstorms, indicating that local SDSs make a more significant contribution. Also, Appendix D identify wind speed mainly correlated with dust AOD and AE values in March and April. The spring weather conditions are characterised by high wind speed, low vegetation coverage, and low soil moisture, which is suitable for SDS from the basin. In addition, vegetation cover has an impact on wind speed. Increased vegetation can enhance surface roughness, increasing the threshold for wind erosion (Zhang et al., 2017) and attenuating surface wind speed (Vautard et al., 2010).

Xu et al., (2020) pointed out that the frequent sandstorms in the Qaidam Basin are one of the factors causing the occurrence of sandstorms on the Tibet Plateau in winter. Based on our results (Appendix D) increased wind speed raises AE and AOD values, considering the dust particles might have been transported by high-speed wind from the Qaidam basin to the Gonghe Basin in December. However, In January, only 35.3% of DUP was caused by 9 ms^{-1} wind speed, suggesting that wind speed is not the constraint factor during winter.

- Anomaly Situation

Based on the DUST anomaly detection, it was found that (i) CMWS anomaly and DOD_ Aqua anomaly was significantly correlated ($r=0.313$; $p< 0.01$; Appendix E); (ii) Low vegetation NDVI coverage is related to low rainfall, which significantly affects the DOD value (dust loading level) of the following spring; (iii) NDVI affected by high temperature in early spring can immediately reduce the dust uplift by high vegetation coverage. The occurrence of SDSs is primarily influenced by wind speed in regions and time periods characterized by low NDVI values. Generally, elevated temperatures and increased precipitation contribute to enhanced vegetation activity through heightened plant photosynthesis (Piao et al., 2014). The factors temperature, precipitation, RH, and soil wetness influence SDS by affecting vegetation growth, the presence of non-erodible harsh elements (e.g., vegetation).

Compared with the typical climate circumstance, these two situations will increase SDSs. (i) During the spring, high wind speed over 2σ contributes to more locally derived SDSs. (ii) Drought and cold conditions caused less vegetation coverage in summer, resulting in more SDSs in the following winter, especially in January and February. Therefore, these results confirm the impact of climate factors on SDS and provide an important further understanding of the interannual fluctuation of SDSs in the Gonghe Basin, which may affect our understanding of other similar regional sources.

The predominant wind direction on dusty days in the Gonghe Basin is northwest, and SDSs are detected by MODIS satellites, consisting mainly of SDSs from the Gonghe Basin and dust transport from the Taklamakan Desert and the Qaidam Basin. Compared with the Ntwetwe Pan where no direct sediment available (Bryant et al., 2007), and Sahara where dust source is only controlled by wind and has no human impact (Middleton, 2019). Gonghe Basin is a dust source and transport zone and is limited by sediment availability and wind, also influenced by human activity. It reflects the complexity of SDSs in northwest China.

2.4.2.2 Landform changes response to Human Activities

Two types of human activities have contributed to desert greening in different types of desert areas in China: oasis expansion and desertification control measures (Liu and Xin, 2021). Oasis expansion is mainly in the form of farmland expansion. The increased green area is mainly distributed on the edge of the Qaidam Basin Desert, Badan Jilin Desert and Tengger Desert (Wang, Gao and Yu, 2019). Since 2000, China has implemented desert greening through national projects, such as the sandstorm source control project and the construction of the Three North Shelterbelt System (Tao, 2014). In the east of the Gonghe Basin, Guinan County, the area of desertification increased by 1094 km^2 from 1976 to 1996, then decreased by 122 km^2 during 1996-2006 (Feng, Y. et al., 2008). Guinan managed 217 km^2 desertification， including completing 14 km^2 of artificial grass planting and 23 km^2 fixed sand dune, and the specific measures include artificial afforestation, engineering sand fixation, and mountain closure for afforestation (Jianjun, 2017).

Besides, human activities have had a negative impact on vegetation, and the construction of dams and other activities may be related to the increased incidence of sandstorms. For example, the land use change in the central part of the Gonghe Basin is caused by the rapid expansion of construction land, which has a negative impact on the local vegetation (Wang et al., 2020). Boloorani et al. (2021) showed that the construction of the Ilisu dam in Turkey reduced the discharge of the lower Tigris and Euphrates rivers, leading to more widespread droughts and triggering SDSs over a wider area. In addition, overgrazing and cross-country driving will lead to severe soil degradation, which is considered an important additional factor for emitting dust (Duniway et al., 2019).

The alteration of aeolian landforms is intricately linked to both natural and anthropogenic factors. Yu-han (2021) asserts that variations in aeolian landform patterns in the Gonghe Basin are adversely affected by temperature and wind speed. During the expansion phase from 1989 to 2005, the aeolian area increased by 817 km^2. Subsequently, with the rise in temperatures, fluctuations in wind speed intensified, while precipitation remained relatively stable, reducing aeolian landforms by an area of 2412 km^2 between 2015 and 2019. The reactivation of fossil dunes and ancient sediments provides a huge source of sediments for SDSs. Li et al. (2016) found a link between fossil dune reactivation and livestock disturbance, which triggered blowout formation. Tracks left by vehicles may also lead to the development of blowouts. Livestock/vehicle breaks the crust, then the fossil sand is exposed to the wind, which then forms an eject. In summary, the contraction of the aeolian landforms area was slightly larger than the expansion and desertification project helped to green desert and fixed dunes in Gonghe Basin for the last 40 years.

2.4.3 Controls on SDS on a regional scale: Westerlies & EASM

The interannual and spatial variations of DUST over the Tibet Plateau are closely related to the interannual variations of westerly and monsoon circulation intensity. The wind field 10 metres above the Qinghai Lake in January is dominated by the westerly belt and the EASM in July, according to NCEP/NCAR reanalysis of current climate data in the Qinghai Lake area (An et al., 2012). Previous studies have shown that 700 hPa (about 3000 m) is the critical value of the temperature and pressure difference between the east and west sides of the Tibet Plateau. Below this critical height, the winter monsoon (related to the Siberian shallow high) has a significant impact on the winter wind field. In contrast, the westerly is the dominant wind system above this threshold height. Thus, the westerlies dominate the Qinghai Lake area in winter, while the shallow winter monsoon system prevails only in the low-altitude areas of the Middle East of China. The westerlies have a great impact on the northern part of the North Qinghai Tibet Plateau, like the Gonghe Basin and the Hexi Corridor, from March to May. During the transitional period of winter and spring, the westerlies fluctuate obviously, leading to frequent invasion of cold air from north to south, and accompanied by the abundant free-soil sediment in those areas, SDSs are the most frequent during this period.

During the study period, EASM showed a fluctuating downward trend, while the westerly index NAO/AO showed a fluctuating upward trend. Due to the influence of the EASM, the annual precipitation in the Gonghe Basin is concentrated in the summer months (June, July and August), with obvious seasonality. Cui et al. (2021) showed that although the Asian monsoon made a significant contribution in summer, the precipitation change in the Tibetan Plateau was mainly controlled by the westerly belt. Summer NAO has a significant impact on the interannual variation of summer precipitation in QTP. The stronger NAO increases the water transport in the QTP region, leading to an increase in precipitation. In addition, EOF analysis shows that the main spatial patterns of summer precipitation show opposite characteristics in the south and north of QTP (Wang et al., 2017). The intensity of the EASM circulation may lead to drought/flood, cold/warm events, and gale weather in northern China (Qian et al., 2002).

Han et al. (2008) conducted a study on the dust source area of the QTP and observed monthly and interannual northward shifts of the dust source area from the QTP to Mongolia. They found that these shifts were influenced by the westerly jet. The authors also noted that the Arctic Oscillation (AO) has displayed an increasing trend since 1980, which has resulted in a weakening of the westerly wind in the middle latitude of Asia. This weakening has subsequently caused a decrease in wind speed in the Gonghe Basin ($r = -0.17$). Additionally, Han et al. (2008) discovered that strengthening the AO has led to increased temperatures in the middle and high latitudes of Asia, resulting in more drought in these regions. The movement of the polar vortex towards the polar region from East Asia has weakened the Siberian High and the Aleutian Low, creating a shallow trough in East Asia (Wu, 2002). Consequently, the westerly jet has been observed to shift northward earlier than usual and then retreat to the south, causing the westerly jet to stagnate in the region. As a result, the SDS activity in the QTP has shown a gradual weakening trend, while it has increased in northern Mongolia. Han et al. (2008) also established a significant positive correlation between the westerly jet and dune activities.

2.4.4 Trends over the last 20 years

In the past 20 years, there has been a trend of warming and increased drought in the Gonghe Basin (Figure 2.13 A and B). Since the 2000s, with the increase in total precipitation, wind speed, RH, and DOD value [which represent SDSs] show a decreasing trend, while the value of NDVI gradually increases (Table 2.3). Similarly, soil wetness and temperature also show the same trend as NDVI (Figure 2.15 B). The maximum wind downward trend in the Gonghe Basin (Figure 2.14A) is consistent with the apparent downward trend of wind speed in Northern China (Chen et al., 2013; Shi et al., 2015). Numerous studies have documented a global decline in land wind speed, particularly at mid-latitudes (Azorin-Molina et al., 2016; Zhang et al., 2019). This decrease in wind speed has played a role in mitigating soil wind erosion in northern China (IPCC, 2013). For instance, Zhang et al. (2018) estimated that wind speed variability accounted for 41% of the reduction in wind erosion in Inner Mongolia from 1990 to 2015. Indeed, multiple studies have demonstrated a significant decrease in the frequency of SDSs in northern China over the past few decades (Zhang et al., 2019; Li et al., 2018), which could be attributed to the substantial decline in wind erosion.

Against the backdrop of a substantial reduction in SDSs in northern China over the last decades (Kang et al., 2016), the unexpected two significant SDS events in the central-eastern plateau of Inner Mongolia in March 2021 were triggered by the production of a powerful Mongolian cyclone and a cold high-pressure system at the surface (Yin et al., 2022). The events have raised potential concerns about whether such extreme SDS events will be frequent in the future or whether climate change will cause dune reactivation. There is no consensus on whether the SDSs in northern China will increase or decrease in the future. Some studies show that the frequency of SDSs in northern China may continue to decline in the future (Li et al., 2022; Liu et al., 2020). Using climate models, Li et al. (2022) estimates that the frequency of SDSs driven by Mongolian cyclones will decrease with global warming from 2020 to 2100. Besides, Liu et al. (2020) attributed the reduction in SDSs to a weakening of the prevailing westerlies in the future, increased precipitation, and a higher leaf area index. On the other hand, the IPCC report in 2013 predicts that arid or semi-arid areas of the Earth will experience increased dryness in the next century, indicating that SDS activities will become more frequent and intense in the future (Luo et al., 2019a). When the temperature transitions from cold to warm, the thawing of permafrost can lead to loosen surface conditions, contributing to a greater amount of erodible soil sediments and consequently resulting in more frequent SDS (Feng et al., 2023). Also, with the increase in temperature and precipitation, evaporation will further increase so that higher temperatures may lead to drought (Dai, Zhao and Chen, 2018). Vegetation coverage may be reduced in drier and hotter conditions and then exacerbate desertification processes, providing erodible surface conditions for SDSs (Duniway et al., 2019).

Feng et al. (2023) present a theoretical framework illustrating the potential mechanism of SDS changes in the northeastern QTP. Their findings suggest that SDS exhibits greater intensity under warm-dry conditions, particularly during the Late Holocene, when natural factors are dominant. Surprisingly, these findings contradict our observations, which indicate a decline in SDS and wind speed over the past two decades despite a warming trend. Considering human activities, ecological protection projects have been conducted in the Gonghe in the last decades, planting vegetation and fixed shifting dunes on the land surface, for example, the Three-North Shelterbelt Project (Li et al., 2012), the Natural Forest Conservation Program (Cao et al., 2010). With increasing precipitation and temperature may have partially improved the effectiveness of these programs. This implies that the impacts of natural processes and anthropogenic factors on global warming may have different effects. Drawing on the results of this research chapter, the Gonghe Basin is expected to witness a decreased occurrence of SDS in the future.

2.5 Conclusions

In this chapter the climatology of SDS in the Gonghe Basin is characterised by using synergistic moderate space/time resolution MODIS satellite data and associated climate and contextual data from 1980 to 2022. The main conclusions in relation to the initial research questions and objectives were as follows:

Q2.1: When do SDS occur in the Gonghe Basin?

[O2.1]: Use a time series of moderate resolution remote sensing data (MODIS AOD/AE) data to determine dust properties and dust detection protocols for the Gonghe Basin, and generate a time series of Dust Storm Days [DSD]

- Regarding dust definition/detection methods, the K2011 and P&G2016 methods were able to derive a more accurate and reliable suite of SDS data than the P2021 method. It is clear that local human activities lead to a high concentration of fine aerosols in all seasons. So, the P2021 approach threshold AOD over 0.2 might include too much urban aerosol. The DSD calculated by the P&G2016 method using Dust Optical Depth (DOD) differs from the K2011 method. However, the dust frequency in each month from the two methods is similar to other research in this region, which suggests that the K2011 and P&G2016 dust define approaches are more reliable than the P2021 method. P2021 detected the number of DSD is about 48 DSD year^{-1}, whereas K2011 and P&G2016 only have about 14 DSD year^{-1} and 19 DSD year^{-1}, respectively.

[O2.2]: To use a time series of moderate resolution remote sensing data (MODIS Deep Blue) to build an overview chronology of quantitative dust loading (AOD/DOD) for the Gonghe Basin

- Based on the number of DSD, the typical SDS seasons are winter and spring in the Gonghe Basin. Here, the mean dust AOD value increased from October (0.3) and reached its peak in April (0.7), then dropped in July (no data); during the summer period where few SDS events were detected. Similarly, analysis of Dust Uplift Potential (DUP) verifies that spring and winter controlled most of the magnitude of DUP (83.7%). SDS activity showed a clear diurnal pattern with low frequency in the morning [MODIS-Terra] and higher in the afternoon [MODIS-Aqua]. Different wind mechanisms primarily drive the morning and afternoon SDS activity in the Gonghe Basin. Increasing wind speed during the morning is likely due to Low-Level Jets. The afternoon SDS are more likely related to cold pool outflows and convection, a typical springtime SDS mechanism. DUP explains much of the SDS occurrence in spring, and it plays a role in transporting dust to the basin in winter. Dust particles might have been transported by high-speed wind from the Qaidam Basin to the Gonghe Basin in December. Qaidam Basin is one of active dust source in the northern China and located in the upper wind and north-west of the Gonghe Basin. Based on the assumptions used, coarse aerosol particles deposit more quickly than fine particles. When we detect dust suspended over the basin, with the wind speed and AOD value rising, if AE<=0.75, the coarser particles are emitted from the Gonge basin; if AE>0.75, fine dust particles are transported from other dust sources. In December, increased wind speed raised AE and AOD values, considering that dust particles are more likely to be transported by high-speed wind from the Qaidam basin to the Gonghe Basin.

- Analysis revealed peak SDS seasons in DJF [mean DOD = 0.293 in Terra; 0.32 in Aqua]and MAM [mean DOD =0.332 in Terra; 0.385 in Aqua]. Typically, we recorded 19 DSD year^{-1} and the Wind speed in DSD is about 6.3 ms^{-1}, higher than that in the non-DSD 3.2 ms^{-1}.

Q2.2: What are the potential drivers on the basin and regional scale?

[O2.3]: Use gridded climate and bioclimate data (e.g., ERA 5, Merra-2), hosted via GIOVANNI modelling climate data, and daily meteorological station data to determine wind fields, DUP and annual/seasonal variability in climate metrics from 1980 to 2022.

- In spring, rising temperatures cause frozen soil and snow to melt, and the weather system over East Asia is highly unstable, resulting in strong high-frequency winds. In addition, due to higher temperatures, less precipitation, and increased evaporation, the Gonghe Basin experienced the driest climate of the year in spring. The bare and loose surface provides a rich source of sand and dust for sandstorms. High-temperature boost vegetation in early spring can immediately reduce the dust uplift by high vegetation coverage. The frequency of SDSs is dominated by wind speed in areas and months where NDVI is low. SDSs mainly occur in March and April, accounting for more than 50% of the DSD. In spring, approximately 32% of the time, wind speeds exceed 7 ms^{-1}, but it contributes 63% of DUP. Previous studies by Cowie et al. (2015) and Bergametti et al. (2017) have also indicated that wind speeds range from 2~5 ms^{-1} above the threshold leading to most SDS. However, in Gonghe, where the surface is susceptible to erosion, wind speeds only surpassing 6 ms^{-1} will trigger most SDS.
- Besides, wind speed, rainfall, soil wetness, and vegetation greening time and coverage have very close control over SDSs in the Gonghe Basin. Summer is the warmest season with the most rainfall. During summer and early autumn, high vegetation coverage and shallow wind speed result in low SDSs. The increase in temperature will lead to the reduction of dust activity in three ways: (i) Promote the increase of vegetation coverage by increasing precipitation and temperature; (ii) Reduce wind speed by

weakening the temperature gradient of the Qinghai Tibet Plateau; (iii) Increasing the soil moisture of the surface through precipitation. Summer and Autumn seasons see dust controlled by Availability-limited and Transport-limited factors. The formation history of the Gonghe Basin contains abundant soil sediments, so the basin is not supply-limited.

- Soil moisture is a crucial constraint, restricting dust in the crust state or frozen state, but low-level soil wetness leads to low cohesion of soil particles. Hence, the threshold friction speed decreases, resulting in increased SDS. The average air temperature is about -10°C in winter, and the frozen soil and snow cover constrain soil availability, resulting in reduced SDS. Thus, the number of DSD in winter is lower than that in spring at the Gonghe Basin can be explained by relatively lower wind speed and frozen soil.
- The Westerlies and EASM directly have a negative impact on climate change and a weak positive influence on the SDS in the Gonghe Basin. The westerlies dominate the 10-metre wind field in January and the EASM in July. Westerlies have a lag impact on temperature and wind after 12 months, and EASM has a lag effect on NDVI after half a year.

[O2.4] Time-series analysis and cross-correlation identify how wind velocity, DUP, rainfall, and other factors [e.g., Human activity] influence dust uplift [as determined by O1/O2].

- A decline in SDS and wind speed has been observed over the past two decades despite a warming trend. The Gonghe Basin became warmer and dryer. DUP, RH, and DOD [= SDS] show a decreasing trend, while NDVI, rainfall, soil wetness, and temperature display a gradually increasing trend. The frequency of SDS has declined over the last two decades, related to the reduction trend in DUP, which helped to mitigate soil wind erosion. Ecological protection projects have been conducted to plant vegetation and fix shifting dunes, reducing the erodibility of the land surface. With increasing precipitation and temperature may have partially improved the effectiveness of these programs. The Gonghe Basin is expected to witness a decreased occurrence of SDS in the future.

3. Understanding controls on SDS in the Gonghe Basin using GEO data [2019-2022]

3.1 Introduction

Characterising SDS activity, meteorological processes, and sources is a prerequisite for accurate estimates of dust aerosol effects and for understanding the conditions under which SDSs are controlled. The Gonghe Basin is a well-known source and transport corridor for SDSs in the region (Qi et al., 2021; Luo et al., 2019a; Dong et al., 2017b). The climate background is complex, influenced by Westerlies and the East Asian Summer Monsoon. Gonghe only has one meteorological station, making it challenging to locate and track dust transport. Thus, using remote sensing (RS) is suitable for large-scale, constant monitoring of dust activity. Sand and Dust Storms (SDS) in northern China mainly occur in winter and early spring (Park et al., 2014; She et al., 2018), and their paths gradually move from south to north, which is closely related to the northward movement of the westerlies over the QTP in this period (Fang et al., 2004). Cold fronts in China may have a significant impact on air quality along their transport pathways. However, there is no research to study the processes and triggered weather systems over the Gonghe Basin.

Several approaches and RS datasets for dust source determination have been developed (e.g., Baddock et al., 2009; Nobakht, 2021; Schepanski et al., 2009; Yumimoto et al., 2019). Lei and Wang (2014) characterised SDS into four classes (e.g., cold front, cyclogenesis) based on the prevailing weather conditions associated with SDS detected in MODIS, which is a Low Earth Orbit (LEO) satellite. SDS range in duration from a few minutes and hours to several days and influences synoptic-scale, mesoscale and regional area (Li et al., 2021) and from a single-day near local-noon sample, cannot usually be adequately resolved (Schepanski et al., 2009). LEO results are helpful but limited to the instantaneous observations at a fixed slot. Geostationary Earth Orbits (GEO) with high temporal resolution might be a better choice for SDS detection (Shi et al., 2023). Hennen et al. (2019) used 'Dust Red/Green/Blue (RGB)' product derived from the Spinning Enhanced Visible and Infrared Imager (SEVIRI) with different temporal resolutions to monitor SDSs in the Middle East and Schepanski et al. (2007) inferences on possible meteorological processes responsible for SDS observed from SEVIRI. Himawari-8 has a higher observation frequency (once every 10 min, covering the entire Asia-Oceania region) and more aerosol detection channels than conventional geostationary satellites to capture the temporal evolution of SDSs (Tie Dai, 2019). However, there are biases between the number of DSD observed from LEO and GEO, but no one has yet compared how bias between LEO and GEO datasets are propagated.

Recently, it has been shown that various meteorological mechanisms may lead to dust mobilisation at different times of day (Schepanski et al., 2009). For example, Caton Harrison et al. (2021) studied the relationship between dust activation and meteorological systems in the Sahara during summer. Dust sources are activated by frequent Cold Pool Outflow in early summer, which follows a diurnal cycle and peaks at 1700 - 1900 UTC. Also, the affected area, duration, and surface wind speed of different SDS vary under each type of weather system (Shao et al., 2002). Therefore, it is crucial to accurately identify the spatial and temporal heterogeneity and meteorological characteristics of dust source activation. In this Chapter, the Himawari-8 Visible Infrared Radiometer Advanced Himawari Imager (AHI) is expected to retrieve highly accurate aerosol datasets, allowing work at the scale of meteorological observations and thereby linking a chance to make observations of dust to climate phenomena (From Regional to Basin Scales).

3.1.1 Chapter Aims and Objectives

Chapter 3 Research Aim: [BASIN SCALE] Understanding controls on SDS in the Gonghe Basin using GEO data [2019-2022]

This study will build a chronology of sub-daily dust source activation using GEO data and determine climate drivers. To understand the weather systems that control SDSs, the start time was recorded for SDS using coincident satellite data with GEO and LEO orbital characteristics. The GEO and LEO dust detectability is compared, and characteristic weather systems are associated with four distinct types of SDS, and a comparison of Locally derived Dust (LD) and Transport Dust (TD) differences in sub-daily wind speed (Dust drivers). Finally, based on the Himawari-8 AOT dataset, mapped dust source hotspots in the Gonghe Basin.

Q3.1: Can SDS from the Gonghe Basin be detected in GEO data, and at what time of day is dust emitted?

[O3.1]: Build a sub-daily [10 hr/10 min] dust observation/detection time series [dust, cloud, no dust, etc.] for four years (2019-2022) using GEO data.

[O3.2]: Compare daily, monthly annual GEO dust chronologies with LEO observations [Chapter2]

Q3.2: To what extent do meteorological events and climate data explain sub-daily SDSs?

[O3.3]: Identify local/regional meteorological mechanisms associated with SDS.

[O3.4]: Investigate relationships between climate variables for known SDS at the sub-daily scale.

Q3.3: What links exist between sub-daily records of SDS and quantitative GEO AOD chronologies.

[O3.5]: Mapped Frontal SDS’s Active Dust Source (ADS) area in Morning and Afternoon

3.2. Data and Method

3.2.1 Data

LEO satellites used in this chapter are MODIS-Terra, MODIS-Aqua (Description in Chapter 2) and VIIRS. NOAA's Joint Polar Satellite System (JPSS) provides global observations with two satellites currently flying in the fleet: the NOAA/NASA Suomi National Polar Orbit Partnership (Suomi NPP) satellite, NOAA-20 (formerly known as JPSS-1). The satellites carry instruments that can be used for dust studies, including the Visible Infrared Imaging Radiometer Suite (VIIRS) and the Ozone Mapping and Profiler Suite (OMPS) (NOAA, 2022). In addition, NOAA-20 carries instruments to measure the Earth's energy balance. JPSS satellites orbit the Earth from pole to pole, crossing the equator approximately 14 times per day in afternoon orbits, providing comprehensive global coverage twice daily. Both VIIRS satellites are in afternoon orbits (~1:30 p.m. local equator crossing time), with NOAA-20 a half orbit or about 50 minutes ahead of SNPP (2.20 p.m.) (Wu et al., 2018).

Table 3.1. Remote Sensing Data

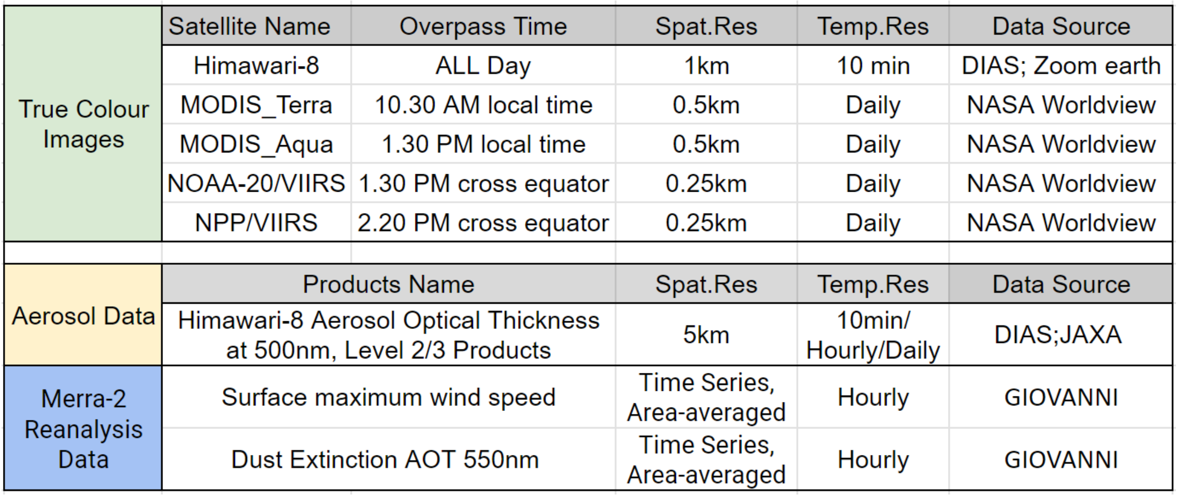

	Satellite Name	Overpass Time	Spat.Res	Temp.Res	Data Source
True Colour Images	Himawari-8	ALL Day	1km	10 min	DIAS; Zoom earth
	MODIS_Terra	10.30 AM local time	0.5km	Daily	NASA Worldview
	MODIS_Aqua	1.30 PM local time	0.5km	Daily	NASA Worldview
	NOAA-20/VIIRS	1.30 PM cross equator	0.25km	Daily	NASA Worldview
	NPP/VIIRS	2.20 PM cross equator	0.25km	Daily	NASA Worldview

	Products Name	Spat.Res	Temp.Res	Data Source
Aerosol Data	Himawari-8 Aerosol Optical Thickness at 500nm, Level 2/3 Products	5km	10min/ Hourly/Daily	DIAS;JAXA
Merra-2 Reanalysis Data	Surface maximum wind speed	Time Series, Area-averaged	Hourly	GIOVANNI
	Dust Extinction AOT 550nm	Time Series, Area-averaged	Hourly	GIOVANNI

Himawari-8 Visible and Near-infrared Radiometer (VNR) and aerosol property products aerosol optical thickness (AOT) were used in this chapter. Himawari-8 is a high-temporal satellite that furnishes valuable insights into daytime SDS (Table 3.1). Its capability to produce true-colour images at intervals of 10 minutes enables direct observation of dust source activation. It is an ideal instrument for studying related emission processes - as opposed to other satellite products such as MODIS, VIIRS, and PlanetScope, typically based on retrievals at a single time of day. Additionally, Himawari-8 yields quantitative indexes for Aerosol Optical Thickness and Angstrom Exponent, providing a reliable representation of atmospheric dust loading. This study uses the Himawari data downloaded from the Data Integration and Analysis System (DIAS) by the University of Tokyo. In this chapter, we applied Himawari-8 10-minutes/hourly/daily images over the Gonghe Basin. Besides, the surface maximum wind speed hourly data was collected from Merra-2, which was used to link meteorological mechanisms associated regarding SDS. Preferential dust sources (PDS) of the Gonghe Basin are used to understand how geomorphology controls SDS (PDS Map Analysis in Chapter 4). The data process workflow of Chapter 3, shown in Figure 3.1, matches each Objective and Result.

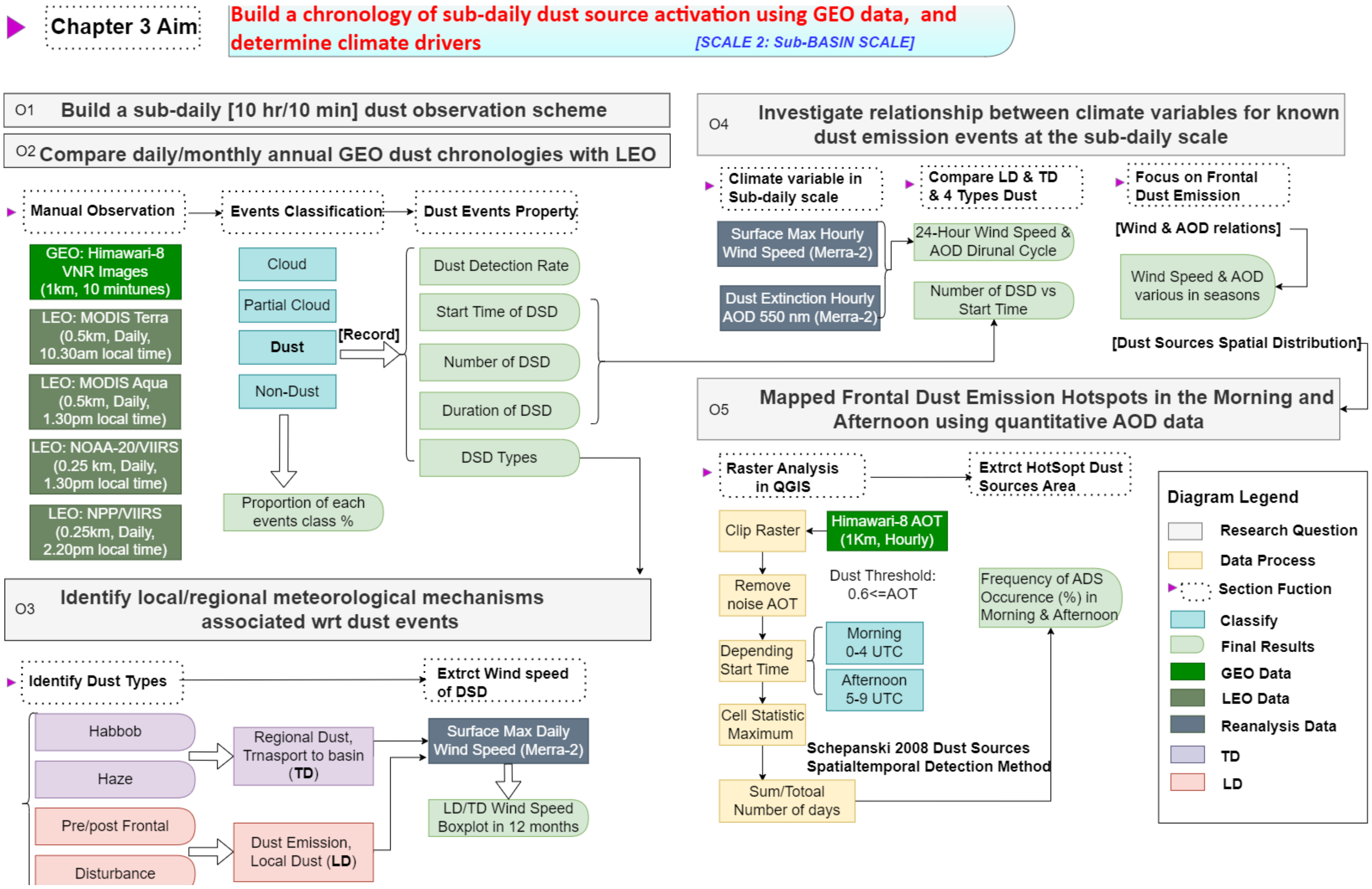

Figure 3.1. Methods and Workflows for Chapter 3, incorporating key research questions and objectives

3.2.2 GEO and LEO Observation of SDS [Plume, Source]

According to (Baddock, et al., 2021), SDS vary in different time scales and spatial (Fig 3.2). In terms of time, SDSs can be seasonal and short in duration, and the advection of material can vary through a typical diurnal cycle. As for space, SDS can also vary significantly in scale, height, and transport density/type of material.

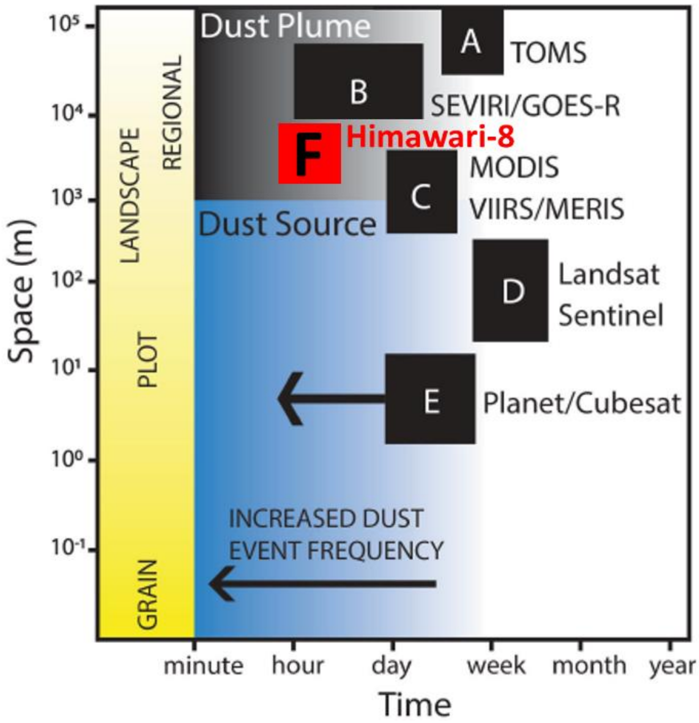

Figure 3.2 Time and spatial scales of dust emission and dust transport, related to the monitoring/detection capabilities of existing satellite systems (Figure derived from Baddock et al., 2021, Figure 4; Reused from Figure 1.6)

In comparing Active Dust Source retrieval capabilities, time resolution is crucial. In Hennen et al., (2019), they use SEVIRI, another high temporal resolution GEO data, to compare the difference between using 15 vs. 30 vs. 60 min data to observe dust. Figure 3.3 A&B shows that the higher temporal resolution data observe more ADS, and the more frequent dust occurs in the season (JULY), in the morning (06.00 -11.45), the more significant the difference in the number of SAMPLE observations at different times. Also, the difference in the number of DSD observed in different time samples was even more significant in the season (JULY) and time (06.00-11.45 am) when dust occurred most frequently. Compared to 60 min, the 15-minute data enables the observation of SDSs of shorter duration. This is why 10 min Himawari is used, it observes dust in sub-basin and sub-daily scale (Fig 3.2); it allows the monitoring of

SDS processes, e.g., dust sources, emissions, and plumes. GEO-stationary satellites have a higher observation frequency to capture the temporal evolution of SDSs.

As for the advantages of different aspects of dust detection: GEO Himawari-8 VIS data = dust event observation (best option for integration with meteorological data); LEO = lower detection rate but higher resolution; LEO/CubeSat = best data capture for dust source activity [but low sample].

Although LEO data was used to build up an annual cycle (in Chapter 2), this may be biased. Knowing how biassed and how many SDSs LEO is missing is worth exploring. Human shape recognition and decision-making capabilities currently surpass automated methods for detecting DPS (Chappell et al., 2023). I conduct manual monitoring of the daily conditions in the Gonghe Basin using three types of satellites: (i) Geostationary Earth Orbit (GEO) satellite, namely Himawari-8; (ii) Low Earth Orbit (LEO) satellites including MODIS-Terra, MODIS-Aqua, NPP VIIRS, NOAA-20 VIIRS; and (iii) High Spatial Resolution (HR-LEO) satellites such as PlanetScop, Sentinel-2, and Landsat-8 from 2019 to 2022. Each day is categorised into four classes based on the situation list provided: Dust, Cloud, Partial Cloud, and No Dust.

(i) If there was 'dust’, record it as 'Dust'(D) regardless of whether it is Partial Cloud cover or clear sky (No-Dust) at other times in the day. If there is no dust, then the day is classified according to the following conditions:

(ii) If most or all of the daytime period, the basin is entirely covered by thick clouds, obscuring the basin, the day should be classified as Cloud (C);

(iii) If clouds exist part of the day or cover more than half of the basin, day to be classified as Partial Cloud (PC);

(iv) Day to be classified as No-Dust (N) if the sky is clear all day or only a few clouds pass by, and no observed dust occurs in the day.

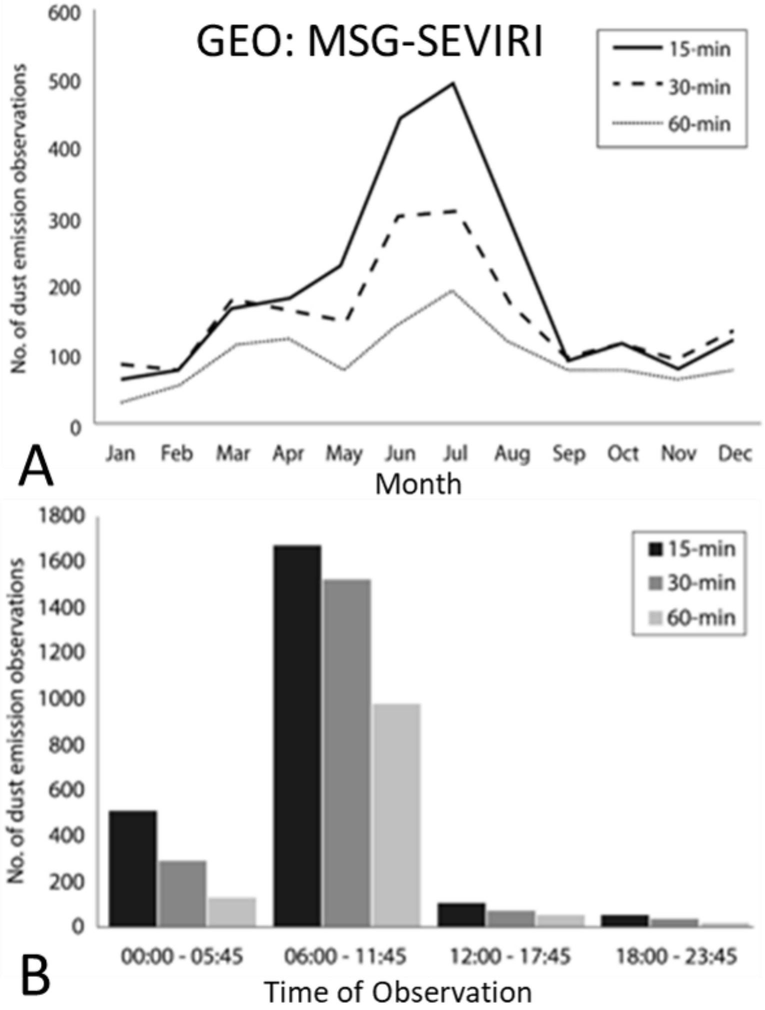

Figure 3.3 SEVIRI identified SDS events from 'Dust RGB' data with 15-min, 30-min, and 60-min temporal resolution in 2006 in the Middle East recorded (Figure derived from Hennen et al., 2019. Figure 3 and Figure 6)

To build a sub-daily [10 hr/10 min] dust observation scheme, furthermore detailed information was compiled on the days classified as 'Dust' (or SDS), including the date, start time, duration, and event type (Haboob, Haze, Frontal). A visual analysis of 10-minute VNR images of Himawari-8 from 2019-2022 was performed. The resolution of the images is 10 minutes so that the dust plume and its evolution can be easily identified. The visible band True Colour Image limited data are available during the 10-hour daylight period. Based on local time, the 10-hour daytime was divided into morning (00.00 - 04.00 UTC) and afternoon (05.00 - 09.00 UTC). Once the dust plume is detected by manual observation, the 10-minute time-series images allow for following the plume backwards to the time of its first appearance. Due to the low resolution of 1 km, the location of the sand source cannot be accurately recorded using visual inspection, and then calculating the frequency of occurrence of the AOT

(FO-AOT), FO-AOT > 16% define as Active Dust Source (ADS) area. Then, the LEO and GEO detection rate of SDS was compared for the Gonghe Basin from 2019-2022. Also, based on Himawari-8 observation, the proportion of PC/C/N/D and the number of DSD were measured.

3.2.3 Meteorological Processes at the Gonghe Basin

Surface wind speed and friction velocity, which are determined by surface conditions, are crucial factors in regulating SDS. SDSs vary in size, duration, and intensity, and the prevailing meteorological conditions play a vital role in determining the differences between SDSs (Shao et al., 2002). Temperature ranges can vary between haboob and frontal dust events. For haboob, temperatures may drop by about 7°C, with the range typically ranging from 3°C to 13°C (Miller, et al., 2008). Frontal dust events caused by moving thunderstorm cell fronts may also experience temperature fluctuations, depending on the specific weather conditions and dynamics involved. These characteristics can also aid in identifying SDSs, and when combined with the prevailing weather systems, can be used to classify them. A study conducted in the western United States (Lei and Wang, 2014) also supports this classification based on meteorological evidence. Therefore, the classification of SDS is based on the phenological and meteorological characteristics of SDS. Characteristics of dust from Himawari-8 10 min time-series observation were grouped, and prevailing weather systems (surface wind speed) were used to identify SDS and the exploration of mechanism in the Gonghe Basin.

To explore the mechanisms that control SDSs and to study the differences in seasonal and diurnal influences on SDS, it is first necessary to understand the meteorology of the study area. The Gonghe Basin is both a transport zone and dust source, and we Identify regional (TD) and local (LD) meteorological mechanisms associated with regard to SDS.

There are four types of climatology system led SDS. To better define the identifiable characteristics of SDS and to clarify the Himawari-8 dust type identification method, a typical SDS was chosen to represent each type of SDS separately, and Figure 3.4 shows the True Colour Himawari-8 Images of these SDS and its corresponding weather systems. Qualitative differences in each type of SDS can be obtained based on the images of airborne dust and the trajectory of the weather system after its movement [The detailed description of each class is seen in Section 1.2.5.2]. (i) Haboob; (ii) Dust Advection (Haze/Floating dust); (iii) Pre/Post-frontal emission; (iv) Local disturbance (or unidentified processes). Haboob and haze are regional SDSs that Transport Dust (TD) particles from the upper basin. Pre/Post-frontal systems lead to SDS, and Disturbance caused isolated dust plumes were Locally derived Dust (LD) from the Gonghe Basin. Appendix L lists detailed information on recorded SDS during 2019-2022.

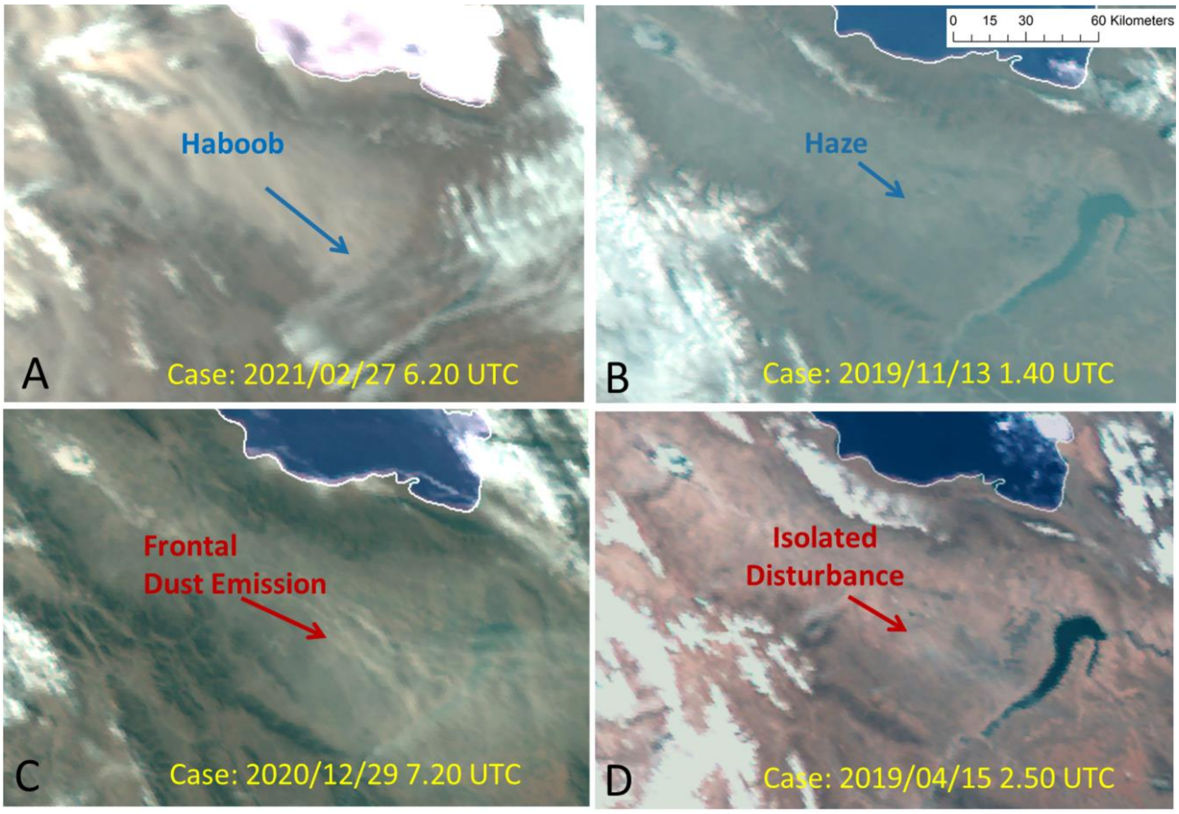

Figure 3.4 Four Types of SDSs with a case example respectively. A) Haboob; B) Haze; C) Pre/postfrontal; D) Unidentified processes (or called *Disturbance)*

3.2.3.1 Characteristic Sand and Dust Storms and Wind Speed

Daily variations of wind speed and SDS quantified by AOD index were analysed to understand further the characteristics of the 4 types of climatology and the links to the intense surface wind speeds that cause SDS. In the Gonghe Basin region, where there is only one meteorological surface station, differences in the relative position of the station (upwind, downwind of dust sources) detected the SDS start timing, dust loading level, and wind speed that may differ from the actual. Therefore, Area-Averaged AOD and surface maximum wind speed hourly data from the Merra-2 reanalysis dataset were used. With global coverage and high temporal resolution, the reanalysed aerosol products could be an essential tool for studying the diurnal cycle of dust (and wind) if they capture a large extent of the observed diurnal dust variability shown in satellite retrievals. For those SDS events identified from Himawari-8 during 2019-2022, we examined their diurnal variability by 24-hour wind speed and AOD data (00.00-23.00 CST) of SDS event.

To investigate the effect of surface winds generated by prevailing weather systems on the intensity of SDS, we compared the differences in wind speeds on the day of LD and TD for 12 months from 2019 to 2022. First, the wind speed data of each DSD were extracted from the daily max wind speed datasets according to the dates corresponding to the occurrence of LD and TD in the 4 years. Second, the wind speed datasets of LD and TD were created separately and refined to 12 months. Explored the distribution of LD and TD for 12 months using boxplot statistics.

To explore the active time difference by comparing the number of DSD for LD and TD in the morning and afternoon. Also, the next section only focuses on LD to understand Active Dust Source (ADS) distribution, using the scatter plot to explore the relationship between wind speed and ADS time.

3.2.5 Himawari-8 AOT Derived ADS Frequency Map in Morning and Afternoon

The dust sources within the study were determined by applying a combined version of the "back-tracking" and "Frequency" methods introduced by Schepanski et al. (2007 and 2009). They used high-temporal satellite-based data SEVIRI to gain information on the diurnal cycle of SDS. However, SEVIRI does not provide a quantitative index of atmospheric dust burden to apply the "Frequency" method. Schepanski's approaches based on the SEVIRI data were modified and applied to the Himawari-8 data. Himawari-8 datasets have high temporal (10 min) and relatively high spatial resolution (1 km) True colour Images and have quantitative detection AOT products (10 min, 2 km). Aerosol Optical Thickness expresses the quantity of light removed from a beam by scattering or absorption during its path through the atmosphere. In addition, Hennen et al., (2019) found that the high temporal data sample (15 minutes, SEVIRI) reduces the effect of overlapping plumes by allowing the observer to "backtrack" the evolution of the plume through successive images up to the first observation point.

Firstly, the "backtracking" method allows visual tracking of dust plume patterns back to their origin by examining continuous images during dust movement and transport events to observe and localise dust source activation. Then, the "Frequency" method was used to calculate the Active Dust Source (ADS) using Himawari-8 AOT data. AOT identifies dust source areas by using the frequency of occurrence of AOT (FO-AOT) values, where FO-AOT of high value was recognised as ADS areas. The frequency of source activation events was calculated for each grid cell. Specifically, once the dust plume was detected by manual observation, the most eligible AOT image corresponding to the +- 1-hour interval was extracted from the recorded START time. This location was eventually marked on 1◦ × 1◦ as the active dust source map.

Regarding Himawari-8 AHI products, AOT value greater than 0.6 indicates medium to high dust loading (Wang et al., 2020). AHI AOT product, like Chapter 2 MODIS datasets, defines a fine-dominated model (e.g., urban-industrial and biomass burning) when the Angstrom Exponent (α) is greater than 1.2, and a coarse-dominated model (dust) when α is less than 0.6. The threshold of 0.6 for AOT and α to remove fine aerosol particles, which is background noise for dust detection. The DPS is automatically identified and traced back to the pixel in the scene where the dust signal first appeared by time-series AOT images (+-1 Hour of start time). A high AOT pixel represents the location of the ADS, and each cell can only be tagged once per day by the 'cell count' function of QGIS. Unless a SDS is identified as two separate events during visual observation, the two events are counted separately. Repeating the ADS tagging method daily, an active dust source location dataset has been compiled for LD covering 2019 to 2022 only. The frequency of occurrence of the AOT (FO-AOT) was obtained from the total number of AOT (> o.6, from Himawari-8) per grid cell and divided by the total number of DSD. It is important to note that it is impossible to accurately identify dust sources under thick and wide clouds or optically thick dust layers. Consequently, this map characterizing dust sources underestimates the FO-AOT under cloud conditions. FO-AOT was analysed for the Pre/post-Frontal SDS in the morning and afternoon and identified the Active Dust Source (ADS) when FO-AOT was over 16%.

3.3 Results

3.3.1 Himawari-8 Daytime Observation Scheme

SDS events observed from GEO and LEO data were manually recorded and with the start time based on GEO satellite Himawari-8 VNR Images. Himawari-8 VNR covers the daytime period, 08.00 - 17.00 China Standard Time (CST), and it observes dust every 10 min and LEO overpass the basin in the noon and early afternoon (e.g., MODIS -Terra 10.30 am, MOIDS_Aqua 1.30 pm Local Time). The number of DSD was calculated for different times of day from 2019-2022 (Fig 3.5 A). To better understand how much dust-related information was missed and to explore the dust mechanism difference based on different climatology at different times of day, daytime was divided into the morning (08.00 - 12.00 CST) and afternoon (13.00 - 17.00 CST). Overall, 55% of SDSs start in the morning in the Gonghe Basin. Secondly, SDS detection rates from different GEO and LEO satellite was compared. The assumption is that GEO has the capability to see all RS-detectable SDSs in the daytime, so the GEO detection rate is 100%, whereas the LEO satellite detection rate is less than 40%, and CubeSat dust detection rate is even lower because its early overpass time (Fig 3.5 B).

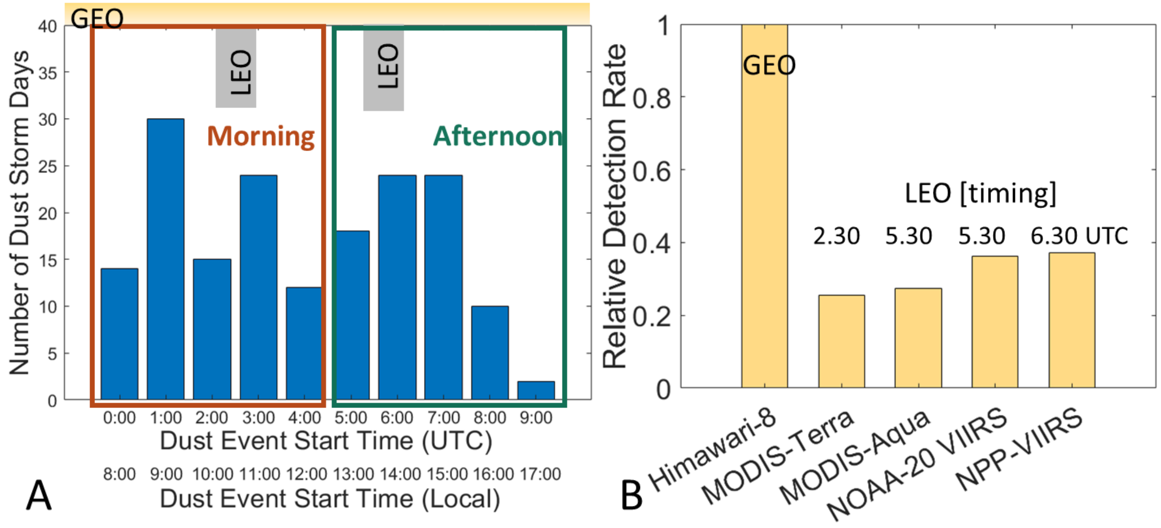

Figure 3.5 A) Number of Dust Storm Day (DSD) start at different times of day (UTC, CST), in relation to GEO and LEO observation time window; B) DSD relative detection rate of Himawari-8; MODIS-Terra, MODIS-Aqua, NOAA-20 VIIRS and NPP-VIIRS and its overpass time.

Regarding cloud effects on GEO Himawari-8 dust observations, the stacked bar Fig 3.6A below illustrates the proportion of different categories of events recorded in 2019, 2020, 2021 and

2022. The cloud and partial cloud account for a similar amount, totalling about 60% of the time effects by cloud cover in a year. Only 40% of the Himawari-8 (VNR) Images over Gonghe Basin are available to observe dust activation. Due to the Cloud effects, using Himawari-8 discovered the dust mechanism was limited by 40% of no cloud period.

The next section of the research concerned the various proportions of events in 12 months, as the chance to observe SDSs depends on whether there are non-cloud-covered images. As shown in Figure 3.6 B, SDSs mainly happened from November to May, and the proportion of DSD in November and December is especially high during 2019-2022, about 25% and 27%, respectively. At the same time, the 'No dust' proportion of these two months is also the highest of another month; thus, the number of DSD in November and December might be skewed by the low amount of cloud cover situation (35% and 25%) when dust cannot be observed from Himawari-8. Also, January has 50% of days classified as PC or C, which is lower than other months' average cloud proportion is about 60%.

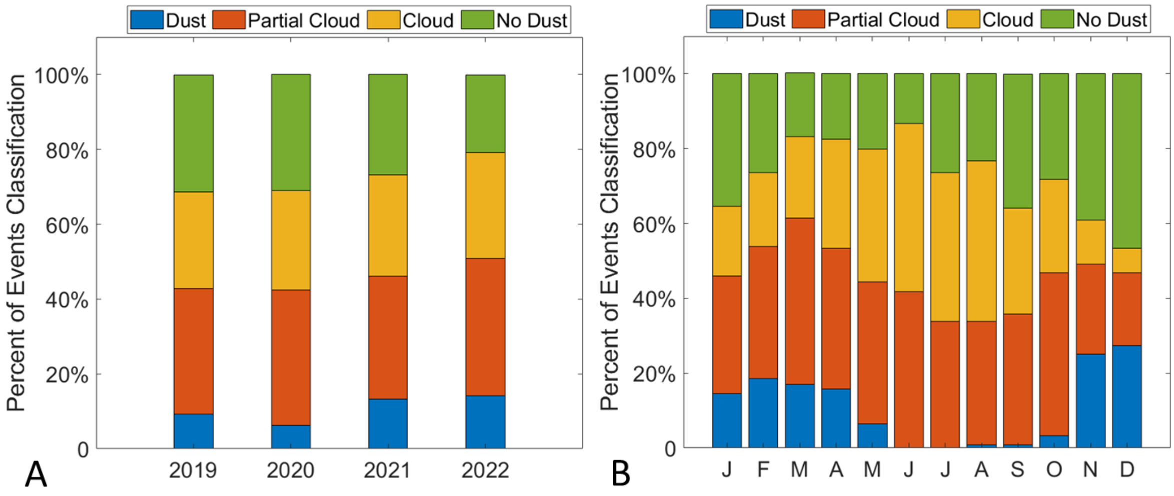

Figure 3.6 A) Percentage of 4 Events Classification in 2019-2022 separately; B) Percentage of 4 Events Classification in different times of year during 2019-2022, in the Gonghe Basin, China.

3.3.2 Classification of different SDSs types

Number of DSD for 4 types of SDS at different times of year during 2019-2022 shown in Figure 3.7. Pre/post-frontal and Haze are the two main dust types over the Gonghe Basin, accounting for about 80% of DSD. Haboob happens in most dust months and is more likely to occur in May but not January. *U*nidentified processes (or called *Disturbance)* lead SDSs were not found in February and March.

LD occurs from October to May, and TD occurs except in June and July. For August and September, only one SDS, which was Haze over 4 years. October has four events classified as two types of events. SDSs rarely happen from June to October. Approximately 43% of the total number of DSD is TD during 2019-2022. TD may include LD emission, but we cannot see it from Himawari-8. Higher frequency of LD than TD in Winter.

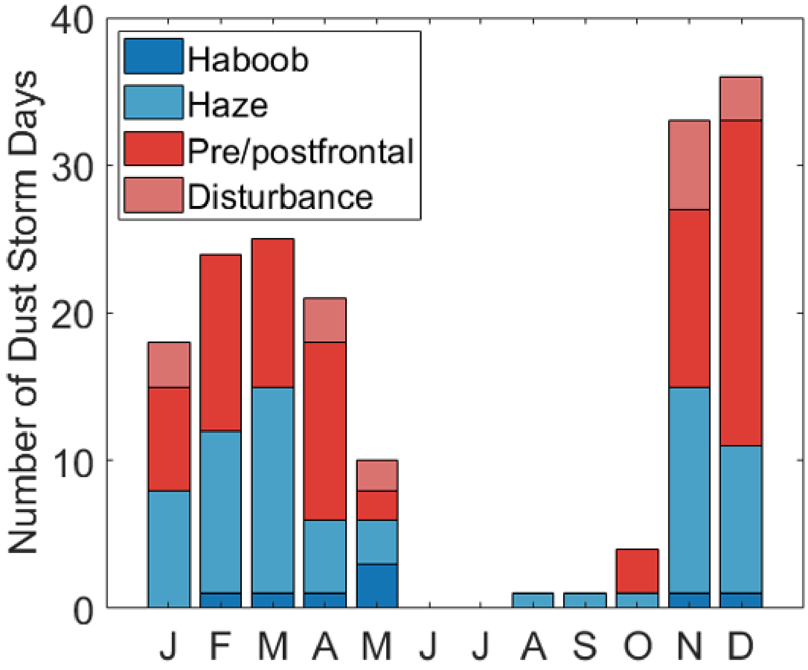

Figure 3.7 Number of Dust Storm Day (DSD) of Four types of SDSs in different times of year, in 2019-2022.

LD Emission is above the 6 ms^{-1} DUP threshold throughout the year, whereas the TD events can occur below the threshold, suggesting the advection through the basin coming from upwind (Figure 3.8). The median daily maximum wind speed of LD is higher than TD. The difference between LD and TD median wind speed is significant in January and December, and it is similar in May and November. Boxes represent the daily maximum wind speed's Interquartile Range (IQR). High wind speeds in LD were concentrated in March and April, with IQRs reaching 9-11 ms^{-1}, while IQRs in LD ranged from 6-10 in other months, except for some events below 6 ms^{-1} in May. TD's median wind speed is lower than 5 ms^{-1} in January and December, and it is higher at about 7-8.1 ms^{-1} in other months, which validates the results that we recorded TD may include LD emission, but we cannot see it from Himawari-8. Comparing the LD and TD boxplots for December, the LD is above the DUP threshold of 6 ms^{-}

^{1}, while the TD IQR is below the DUP value, which means that we can distinguish well between TD and LD using Himawari-8 in December.

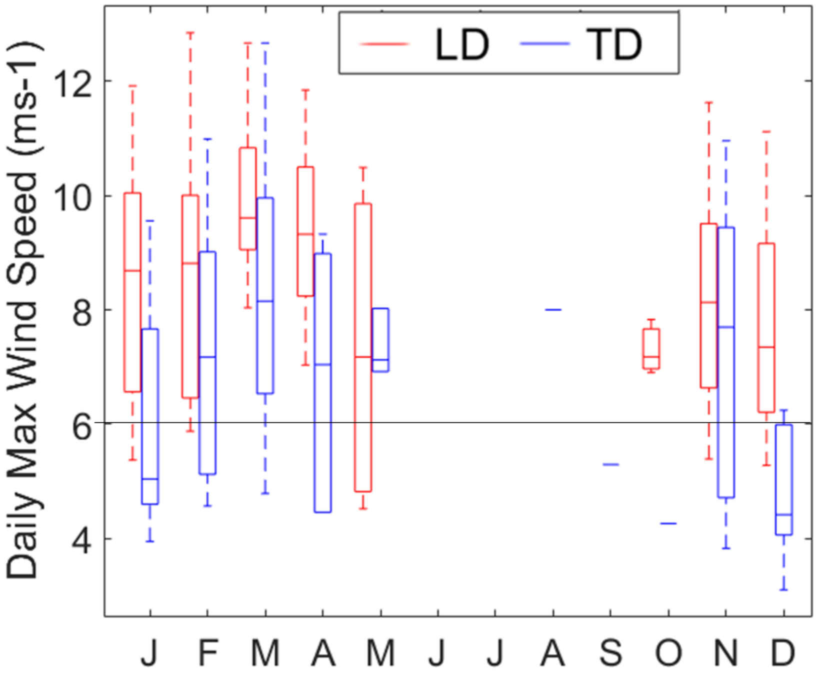

Figure 3.8 Compare Locally derived Dust (LD) and Transport Dust (TD)*'s Daily surface maximum wind speeds at different times of year, in 2019-2022.*

3.3.3 Dust Source Activation Timing

As shown in Figure 3.9, TD is more likely to start in the morning, and LD is more likely in the afternoon. Most of the TD was observed from the early morning at 01.00 UTC, and most of the LD occurred from 03.00 to 08.00 UTC in the afternoon. LD emissions are relatively low at 00.00 - 02.00 and 09.00 UTC, and TDs occur less during 04.00 - 09.00 UTC. SDSs that occur in AM are more likely to be recorded in LEO and GEO. Approximately 31% and TD = 5%, and these events will be undetected by LEO. SDS occur earlier and will have a longer duration. Due to Himawari-8 VNR 10min-temporal images only allowing observations of the daytime period, the earliest dust starting time is local sunrise time, and dust ending time usually be sunset time.

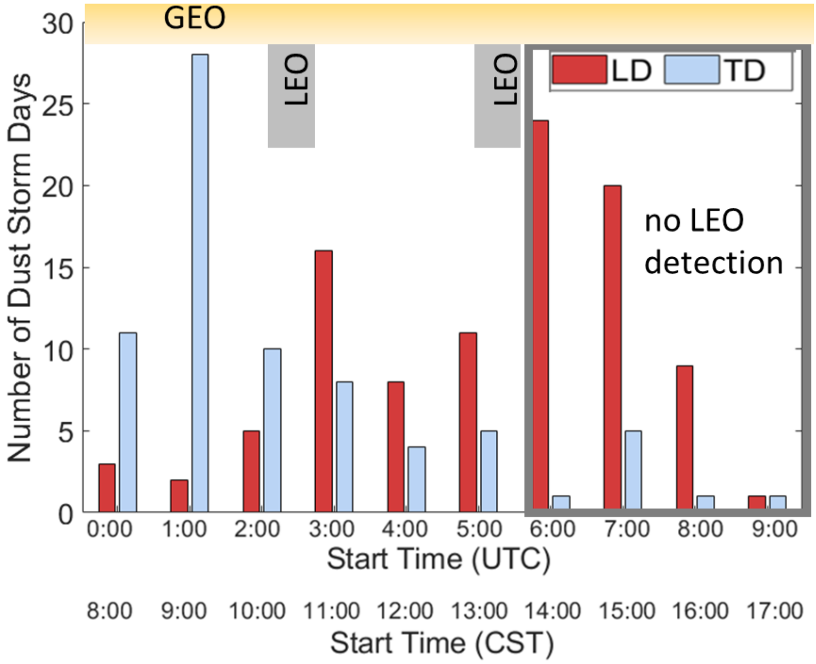

Figure 3.9 Number of DSD from Locally derived SDS (LD) and Transport SDS (TD) *occurring at different times of day, in relation to the monitoring capability of GEO and LEO satellites.*

Figure 3.10 illustrates scatter plots for the four SDS types, including their start times (UTC) and the distribution of the daily maximum wind speeds for the day. Habbob can start at any time during the day with daily maximum wind speeds ranging from 4.4 to 10.5 ms^{-1}. 84% of Haze occurs in the morning (00.00 - 04.00 UTC) with a wind speed of 4-12 ms^{-1}, and after 04.00 UTC the wind speed is higher. Morning high-frequency of Haze and wind speed related to pre-day/night SDSs from far-away upper wind regions. By contrast, In the afternoon, the wind speed of haze transport SDSs is higher than 5.8 ms^{-1}. The haze wind speed tends to differ in the time of day, indicating that TD may include LD emission, especially in the afternoon.

Pre/post-frontal ocurred from morning to afternoon, 94% of Frontal Dust is above the 6ms^{-1} DUP threshold, and the lowest wind speed is over 5.3 ms^{-1}. Wind speeds for disturbance-induced dust were low, with 59% of events having wind speeds below 6 ms^{-1} and a concentration of events occurring between 02.00 and 06.00 UTC. Disturbance Dust can occur below the threshold associated with human disturbance, e.g., agriculture and mining.

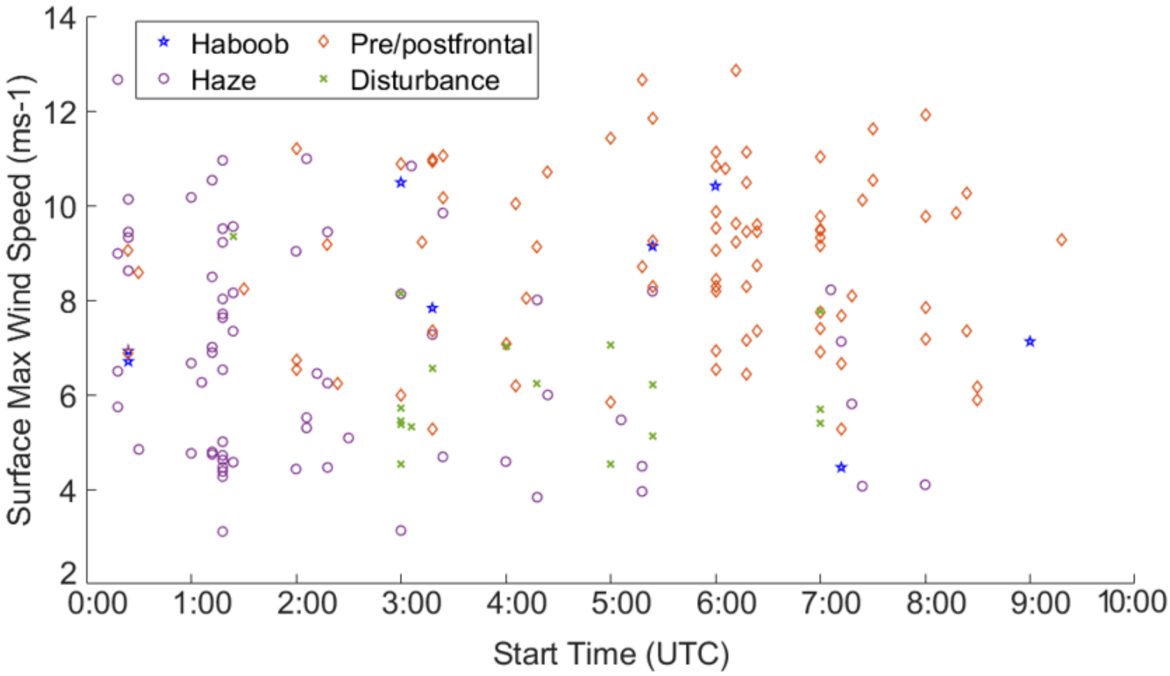

Figure 3.10 Four Types of SDSs and its start time vs. daily surface max wind speed.

Both LD and TD show a clear diurnal cycle in Figure 3.11. The wind speed gradually increases from 00.00 (CST), peaks at 15.00 or 16.00 (CST), and then gradually decreases during the night. The overall wind speed of the LD boxplot is higher than that of the TD boxplot, especially during the daytime period from 08.00 to 17.00 (CST), where the wind speed varies widely, and this is also the period (Orange Range) that can be observed with Himawari-8. It is especially obvious that in the afternoon, more than 3/4 of the LD days are concentrated with high wind speeds of 8 ms^{-1} in the 12.00 - 17.00 CST period. Winds of more than 6 ms^{-1} persist until 20.00 CST, which confirms our observation that high wind speeds accompanying LD tend to occur in the afternoon.

Different types of SDS have different diurnal variations in wind speed and the time to reach the highest value (Figure 3.12 A). Although LD and TD show similar trends, LD is much higher than TD over time and significantly higher during the afternoon (after 05.00 UTC). Haze and Frontal are the main meteorological drivers of Gonghe Basin dust transport and emissions, respectively.

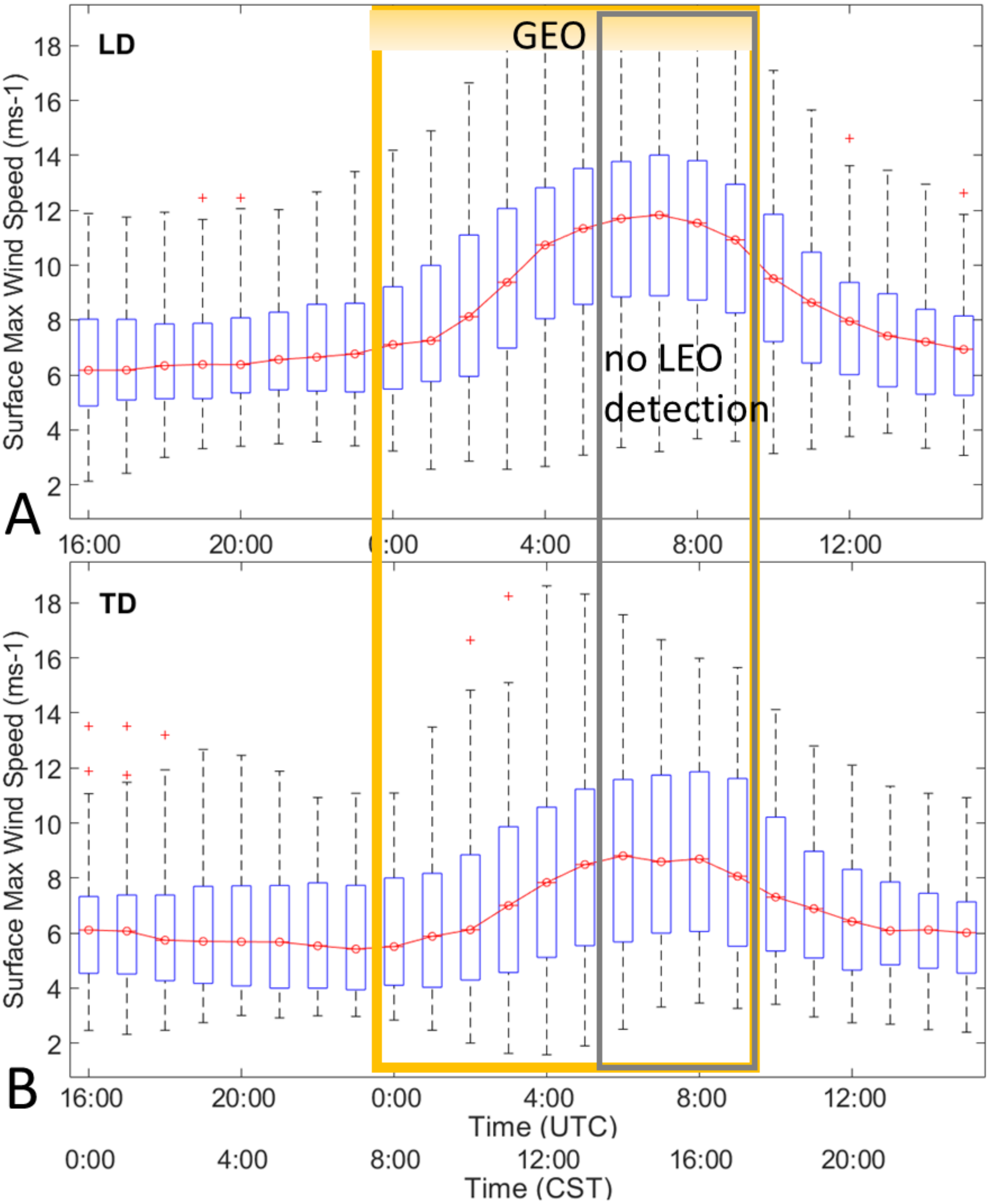

Figure 3.11 A) Locally derived Dust (LD) *24-hour (00.00 - 23.00 CST) surface max wind speeds (ms^{-1}) and its median value line (red); B)* Transport Dust (TD) *24-hour surface max wind speeds boxplot, 2019-2022.*

(i) The Green dot-dash line represents the wind speed of Disturbance, which is the lowest during 09.00 - 23.00 CST, and the wind speed is over 6 ms^{-1} at 11.00 - 18.00 CST, which is a time window for emitting dust. (ii) The highest red star line is pre/postfrontal caused SDS, wind speed increased since 00.00 CST (6.3 ms^{-1}) and reached its highest at 16.00 CST at about 12.9 ms^{-1}, until 20.00 CST wind speed was still over 8 ms^{-1}. (iii) Haboob climatology is the high wind speed period from 12.00 - 23.00 CST, and it reaches the highest wind speed at 16.00 CST at 10.76 ms^{-1}. (iv) As for Haze, the median of wind speed boxplot is over 6 ms^{-1} during daytime (10.00 - 20.00 CST), highest in 13.00 CST at 8.48 $ms^{-1,}$ and it is relatively low during the night (20.00 - 09.00 CST). Wind speed over DUP during the daytime might cause SDS, but we cannot observe from Himawari-8. Rating 4 types of System Wind Peak Time: Haze<Disturbance <Frontal<Haboob.

Figure 3.12 B illustrates that the Frontal system wind speed varies in different seasons and impacts SDS timing. In the GEO observation daytime, the Spring wind speed increased earlier and was significantly higher than in Autumn and Winter. During 04.00-24.00 CST, wind speed over DUP threshold 6 ms^{-1} in three seasons. Wind Speed: Spring> Autumn> Winter.

In Appendix F, the distribution of the start time of Frontal SDS changes in different months is shown. It is found that the amount of dust during 00.00 - 05.00 UTC is relatively stable in months, and the considerable difference in the amount of dust between months is mainly in the afternoon between 05.00 - 09.00 UTC. Especially in April, November, and December, a large number of SDS started at 05.00 - 07.30 UTC, which matches the Fontal Cycle wind speed reach peaked at this period (Fig 3.12 B). The high Frontal wind controls SDS in winter and spring, and SDS occurs most during the afternoon.

The hourly AOD dust loading from Merra-2 datasets was extracted for each hour of the day based on the recorded SDS (Appendix K). The LD dust AOT boxplot range is lower and smaller than TD, and LD has more outliers, which represent severe SDSs with high AOD dust loading levels. Pre/postfrontal and Disturbance-caused SDS (LD) were not detected very well by MERRA-2. The AOT products derived from the Himawari-8 satellite exhibit limitations in effectively identifying LD over the Gonghe Basin. Although Merra-2 and Himawari-8 underestimated very high aerosol loadings of LD, the satellite sensor was effective in observing LD SDS/plumes from True Colour Images.

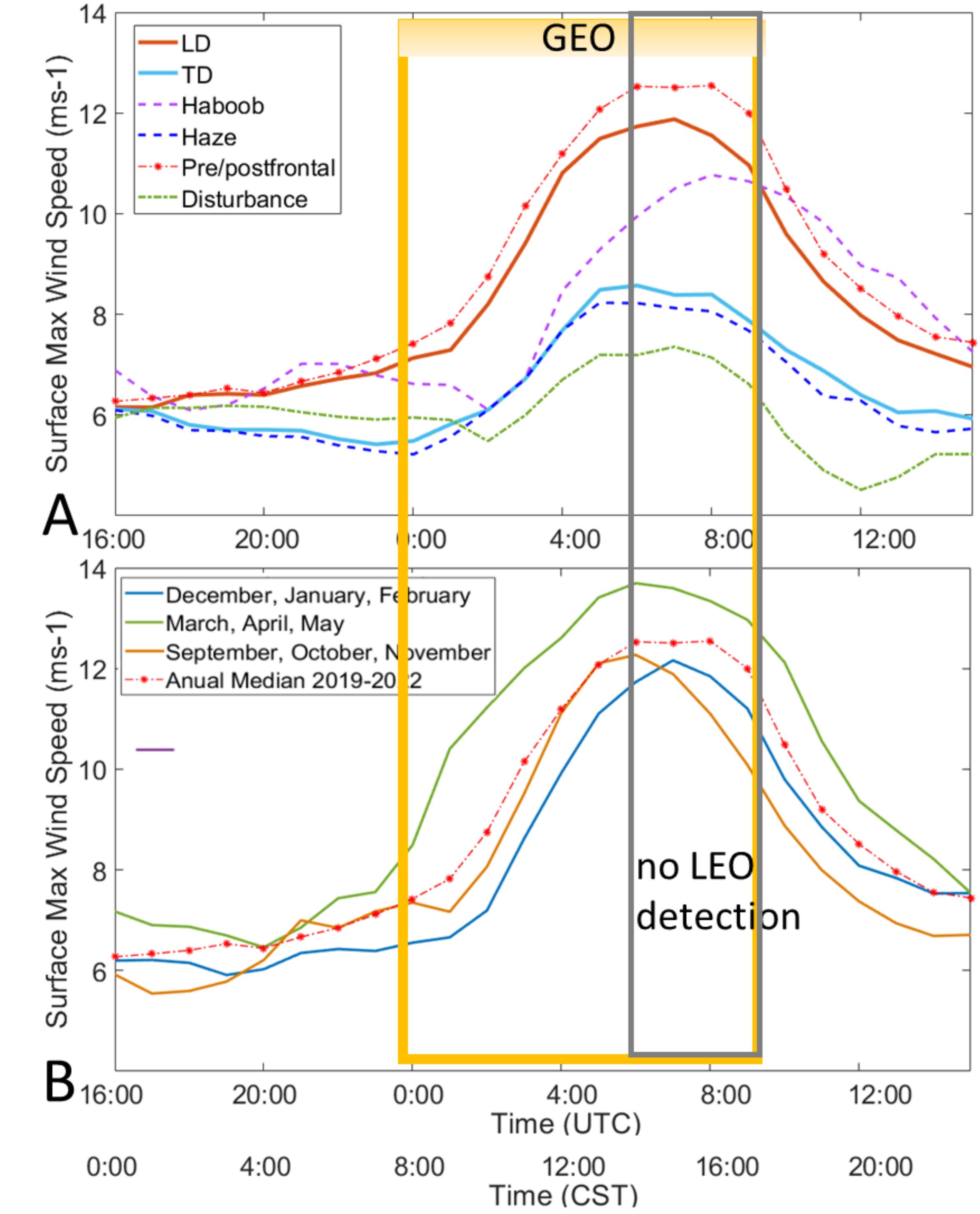

Figure 3.12 A) Median value of Surface max wind speeds vary at different times of day (24h) for the Locally derived Dust (LD), Transport Dust (TD) *and 4 types of SDSs. B) Median value of Merra-2 hourly surface max wind speeds (ms−1) for the large frontal in seasons DJF (December, January, February), MAM (March, April, and May), and SON (September, October, and November) during 2019-2022, at the Gonghe Basin, China.*

Figure 3.13 shows the median of 24-hour basin averaged AOD dust loading affected by SDS. The group characteristics (range of AOD) of each type of SDS are clearly different. Haboob, caused by strong winds, is the most severe type. SDS associated with cold fronts transport dust to the basin (Haze)'s AOD is higher than the AOD of Pre/postfrontal led SDS from the Gonghe Basin. By contrast, *U*nidentified processes (or called *Disturbance)* caused SDS AOD is relatively weak. The strength of the weather system mainly influences differences in intensity between individual events or groups at the time.

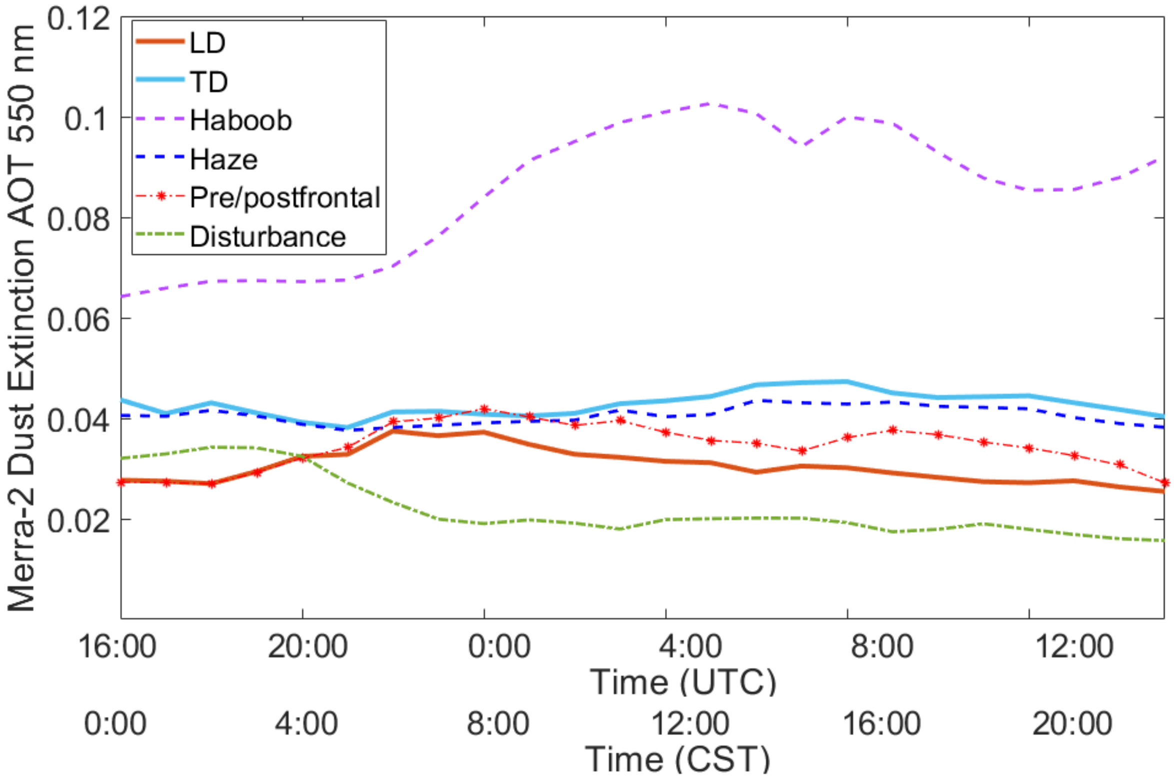

Figure 3.13 Median of Dust Extinction AOT 550 nm varies at different times of day (24h) for the Locally derived Dust (LD), Transport Dust (TD) *and 4 types of SDSs.*

3.3.4 Characteristics of ADS Areas and Using Quantitative AOD Data

To discover the basin dust plume source locations, the following study focuses on frontal SDS in the Gonghe Basin. Spatially, Active Dust Sources (ADS) are defined as those where the frequency of occurrence of the AOT (FO-AOT) is over 16% (Figure 3.14). Morning has fewer SDS events (n=19) but a higher FO-AOT (marked dark red FO-AOD>20%, in the Figure 3.14 A), and afternoon has more SDS events (n=49) but a lower FO-AOT (marked orange and red FO-AOD 12-20%, in the Figure 3.14 B). ADS in the morning has a wider distribution range and a larger number than ADS in the afternoon, and morning ADS contains more areas with FO-AOT exceeding 20%. There are four ADS zone in the morning and three in the afternoon.

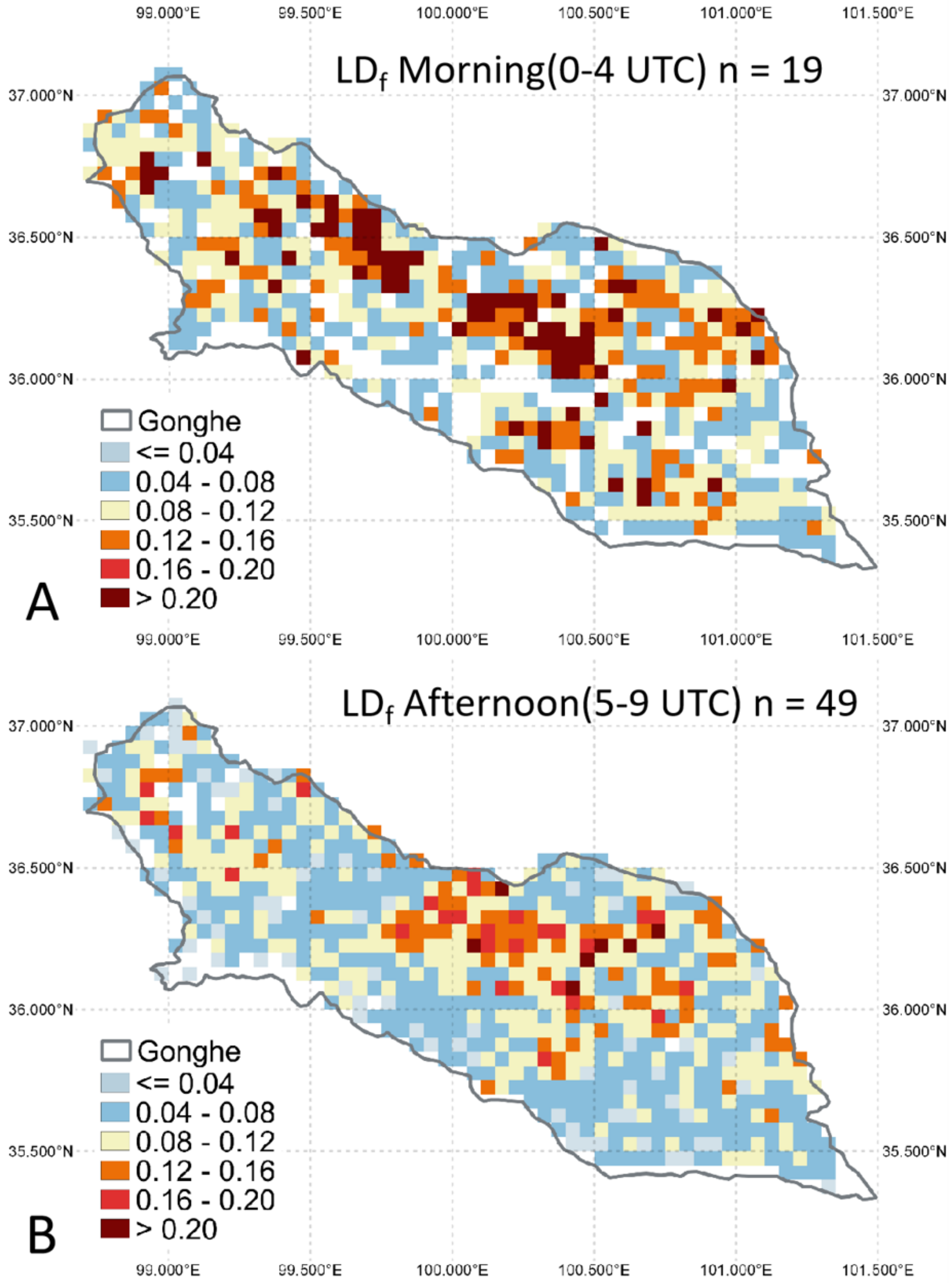

Figure 3.14 SDS Frequency of Occurrence of the AOT (FO-AOT) Map in the morning (00.00-04.00 UTC) and afternoon (05.00 - 09.00 UTC). LDf = Frequency Data uses AOD > 0.6 at the time [+- 1 hr] of Pre/postfrontal caused SDSs [2019-2022], LDf pixel value of 1 = AOD > 0.6 [+- 1 hr] of all recorded Frontal.

3.4. Discussion

3.4.1 Remote Sensing of SDSs detection

3.4.1.1 GEO and LEO detection rate Difference

In presenting dust sources derived from Himawari-8 images, we show how the high temporal resolution is capable of direct observation of SDS from sources and transport to the downwind area. Every 10-minute image allows us to tack back to the origin of SDS areas precisely. It highlights the details of the emission process that can be explored from GEO Himawari-8, including dust type, emission start time, duration, and prevailing wind weather. The continuous and short interval of GEO data demonstrates the ability to provide a complete view of the SDS process in the daytime, achieving insight into the temporal heterogeneity of emissions far beyond that revealed by the LEO satellite. The impact of increasing temporal resolution on the number and spatial distribution of observed SDS.

- Number of DSD Difference

An example case on 2019 October 8, compare the True Colour images (TCI) and Aerosol index from LEO and GEO, respectively. As for the TCI in Appendix E and G, dust plumes were observed from MODIS-Terra, MODIS Aqua, NOAA-VIIRS, NPP-VIIRS, and Himawari-8 images in different times of that day, but the distortion of RS images in the Gonghe Basin is different, and the stages of SDS in RS images are different. MODIS observes QTP from a lower orbit. In contrast, the orbital height of the Himawari-8 AHI operating in geostationary orbits is much higher than that of MODIS, but QTP is located at the edge of the Himawari-8 satellite's full disk image, so Gonghe Basin has greater geometric deformation.

Based on Himawari-8 (GEO), 173 SDSs from 2019-2022 were manually detected, compared with GEO, the LEO detection rate is 40% of GEO, and CubeSat data is about 15% of GEO. It reveals that (i) the lower the satellite revisit time, the lower the probability of RS capturing SDSs (Naeger et al., 2015); (ii) the early overpass time of LEO missing about 35% of SDSs which occur after 05.00 (UTC), these will be undetected by LEO; (iii) Temporal resolution is key when identifying small-scale SDS. In terms of time, SDSs can be seasonal and short in duration, and the advection of material can vary. Comparing the SDS detection rate from GEO and LEO in the morning, the detection rate of LEO is still lower due to some of the SDSs caused by human disturbance. These might have only a short duration and small plumes unable to be captured by LEO. It reflects the role of high temporal resolution RS TCI in exploring SDS.

- Dust Spatial Distribution

Due to the different temporal availability of dust products (AOT), the accuracy in linking the atmospheric dust burden to a source location varies. An example shown in Appendix H and J, GEO and LEO’s AOT products detected ADS areas located in different places. Due to LEO's temporary resolution once a day, there is a 6-hour lag between the SDSs starting in the morning and the flyover time of LEO satellites. When the dust plume detected in low Earth orbit has already spread downwind of the source area (Schepanski et al., 2012). In the Example Case, the Location of MODIS-Terra AOD in the morning is more upwind than the AOD pixel in MODIS-Aqua and NPP-VIIRS. Also, dust location varies more obviously during dust starts emitting 4 hours (05.00 - 08.00 UTC) in Appendix J, the high AOD pixel (Blue) moves to the downwind area through time. The shift in source area location is not only caused by the downwind transport of dust during the time between emission onset (morning) and detection (midday) but can also be influenced by a combination of atmospheric dynamics and boundary layer mixing, which was shown by Schepanski et al. (2012) to lead to a local overestimation of the dust plume in the OMI AI product, resulting in displaced dust sources. Similar findings from Tie Dai (2019) comparing AOT observations from AERONET, MODIS, and Himawari-8 confirm that the hourly aerosol assimilation from Himawari-8 can generate more accurate hourly aerosol analysis. In addition, biomass burning generated aerosols, particularly in urban/industrial areas between November and March, resulting in DeepBlue AOT ultimately increasing the aerosol burden in the Gonghe region.

- Timing of Events

Jin et al., (2019) found that the Himawari-8 satellite could observe SDS in detail at a very early stage, whereas ground-based stations are often far from the dust source area and have a lag in their observation of SDS. For example, on 4 May 2017 in North China, the nearest station Bayannur, measured severe PM10 one hour after Himawari-8 captured dust. Thus, early observations of the SDS by Himawari-8 may complement the accuracy of LEO/Station on the onset of SDS.

This study suggests that sub-daily temporal resolution Himawari-8 satellite products are suitable for observing the SDS process with the most remarkable time accuracy. Whereas other LEO RS data detect dust in transport (Dust Plumes/ Advection). In addition, the interannual variability in the number of ADS may not be captured in daily data alone due to the predominance of downwind transport from dust source regions. The total dust flux from many small dust sources (Ephemeral Lake, Chaka) may be comparable to that of a few strong dust sources, sources not captured in True Colour Images in LEO/GEO due to the basin background being desert hard to observe dust.

3.4.1.2 Cloud effects on dust observation

Himawari-8 reveals that about 60% of days are covered by cloud or partial cloud in the Gonghe Basin, indicating that RS-detected dust loading in this region is underestimated. It is well known that high cloud cover is typical for Tibet Plateau in high altitude Dust sources. Due to the mountain effect, water condenses from the air at higher elevations and forms clouds, which often blanket tall peaks and hide them altogether (Chris Deziel, 2018). Also, the daily variation of highland cloud cover links convection and precipitation processes.

We found that winter cloud cover is lowest at about 30%. These results are consistent with other cloud cover studies conducted over QTP (Wang et al., 2020). Qianrong (2021) confirmed that the maximum cloud over QTP occurs in spring and summer, with Total Cloud Cover gradually increasing from January to July and decreasing from August to December. According to Shang et al. (2018), the diurnal cycle of clouds over the QTP exhibits an increasing trend throughout the day based on hourly cloud data from the Himawari-8 satellite. The minimum and maximum cloud cover were observed at 10.00 and 18. 00 (CST). This finding explains why there are often partial clouds in the afternoon that cover the Gonghe Basin. Additionally, Schepanski et al. (2012) discovered that sub-pixel cloud pollution can negatively impact the accuracy of passive satellite aerosol remote sensing. Cloud pollution tends to introduce a positive bias in aerosol optical depth and a negative bias in aerosol Angstrom index, which is a measure of particle size. This is because clouds have higher reflectivity and lower spectral dependence due to the presence of more large-sized particles. Furthermore, Jin et al. (2019) suggested that the high aerosol optical depth values obtained from satellite inversion of Himawari-8 could not be verified by AERONET observations and might be attributed to the presence of cloud scenes. In this study, the AOT retrieved by Himawari-8 sometimes showed quite high values in the area next to the cloud cover region. However, based on Himawari-8 TCI, we did not observe dust plumes exist in this region, so the high values of AOT may also come from retrieval errors in a partially clouded scene.

3.4.2 CPO and Front System

The meteorological conditions that can cause SDS are described in this section. SDS caused by different weather systems exhibit different intensities and identifiable characteristics. Four types in the Gonghe Basin include Haboob, Haze **[TD]**, Pre/post-Frontal and Disturbance **[LD].** Two dust types (Haze and Frontal) associated with cold fronts are the primary mechanisms for GH transport and ejected dust.

- **Haboob (Local Strong Sandstorms (LSS))**

The rarest and most clearly distinguishable system at Gonghe is haboob (or called (Local Strong Sandstorms (LSS)), which may occur in February, March, April, May, November, and December when is low precipitation periods, with onset times spanning from 00.00 - 09.00 UTC. A similar conclusion comes from Zhaolin (2021), who suggests that LSS in deserts in China often occurs most frequently in relatively dry seasons, and LSS occurs suddenly in tens of minutes during the late afternoon and before dusk in deserts in China.

Haboob occurrences are all attributed to strong, dry or wet convecting weather processes. LSS is always followed by dry squalls, and the interaction of radiative heating of dust in the near-surface mixed layer with upper mesoscale anticyclonic air masses (cold pools outflow) is an essential process leading to LSS (He et al., 2020). Whereas Vukovic et al. (2014) observed that haboobs in America are often followed by wet squalls. This interaction is attributed to the radiative heating of dust near the ground and upper mesoscale anticyclonic air masses, critical processes leading to the formation of LSS. In the afternoon, the desert experiences a significant temperature gradient vertically, which induces strong convection and contributes to the development of local SDSs (He et al., 2020). When dry squall lines form, the combination of atmospheric weather conditions, such as cold fronts or an upper air trough passage, along with local atmospheric instability, triggers the emergence of LSS (He et al., 2020).

The occurrence of Haboob in the Gonghe Basin during 2019-2022 has been a rarity, with only eight documented cases observed by Himawari-8. Surprisingly, no academic papers have been found that specifically mention the presence of Haboob in this basin. Anisimov et al. (2018) suggest that scattered surface observation networks are prevalent in sparsely populated desert areas and that Haboob is often obscured by satellite images of upper clouds (Allen et al., 2015), thus making it difficult to observe Haboob type events.

- **Haze (Floating Dust）**

Haze, or floating dust, is a dusty weather phenomenon in which dust aerosol particles are uniformly suspended in the atmosphere, and it is advected from the upper region or remains in the air after local SDS (Jin and He, 2023). Haze is characterised by a high frequency of occurrence throughout the year except in June and July at Gonghe. Pi et al. (2017) found that one of the reasons for the high frequency of floating SDSs in Chinese deserts is the steep topographic environment. The Tianshan Mountains, the Kunlun Mountains, the Qinghai-Tibet Plateau and the Pamir Mountains confine the atmospheric circulation of airborne particles to the interior of the Tarim Basin. Similarly, the high mountains on both sides of the Gonghe Basin also restrict floating dust transportation. Shao et al. (2003) also reported a high frequency and long duration of suspended dust caused by topographic features and atmospheric circulation restrictions.

Jia et al. (2015) confirm that the Taklamakan and Gurbantunggut deserts, which are dust sources in the northern part of the QTP, and their SDSs are triggered by the formation and development of strong cold front systems. Meanwhile, they found that dust aerosols from the Taklamakan, Gurbantungut, or Badan Jaran deserts are easily transported to or across the Tibetan Plateau, then the downwind region is the Gonghe Basin located at the northeastern edge of the QTP. Cao et al. (2018) describe five major dust propagation pathways in China, including the sources and transport pathway of Haze in Gonghe (light green arrow in Fig 3.15). In Qinghai Province, the Qaidam Basin is bordered by the Qilian Mountains and Aljinshan to the north and the Kunlun Mountains to the south. When westerly winds from Xinjiang Province flow into Qinghai, Haze moves into the downwind region of the Qaidam Desert, i.e., the Gonghe Basin (Qiang et al., 2007). Thus, fine aerosol particles suspended in the lower troposphere of the basin are caused by cold front systems in the upper wind dust sources region and transport dust to the Gonghe Basin. Chen et al. (2013) further explains the process of dust movement from Taklamakan to QTP. The levels of the turbulent mixing phenomena over the QTP exhibit the lowest magnitudes during the morning and reach the highest levels in the late afternoon. Turbulent mixing plays a key role in transporting dust flux from the near-surface layer to the upper boundary layer. Besides, the stronger thermal effect on the QTP in the afternoon contributes to stronger convergence, leading to dust transport from TD to QTP. Conversely, cooling of the QTP surface during the night and early morning leads to wind and dust flow forward to the south and north.

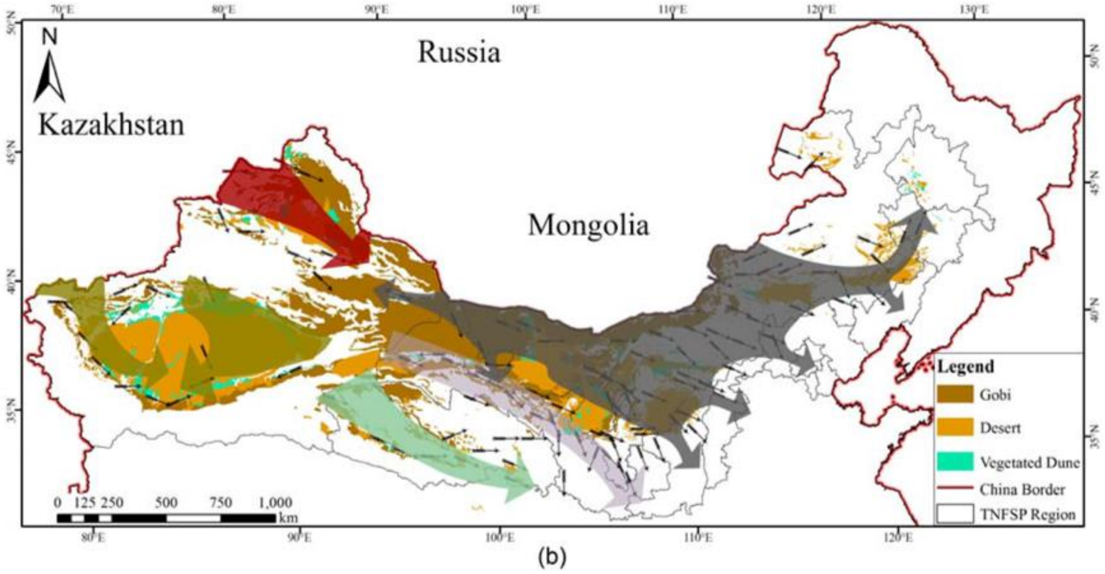

Fig 3.15 Five major transportation routes of SDSs in North China, reproduced from Cao et al.(2018), Figure 7b. (i) Grey Arrow is SDS caused by cold airflows from northern Asia (usually Siberian and Mongolian cyclones) transport over Mongolia and inner Mongolia; (ii) Dark Green Arrow is SDS caused by Westerly winds crossing the Pamir Plateau and arriving in the Tarim Basin then back due to the blocked by the Tianshan Mountains; (iii) Red Arrow is SDS caused by westerlies from Central Asia dominate Northern Xinjiang; (iv) Purple Arrow is westerlies from Xinjiang separate to two SDS routes one in Gansu; and (v) Light Green Arrow is other in Qinghai (transport cross the Gonghe Basin).

- **Pre/post-frontal**

Strong surface winds behind the coil front produced SDS that erupted throughout Winter and Spring in the AOI. A similar conclusion is drawn from Sun et al. (2001), where strong surface frontal winds associated with a Mongolian cyclone swept southeast across the Gobi Desert and the northern boundary of the Tibetan Plateau in spring. Zhang et al. (2022) suggested that the southward pressure of a cold front from Western Siberia is the main weather system triggering SDS in the northwest. Frontal systems, including pre and post-frontal events, both occur in the Gonghe Basin. The post-frontal SDS was observed when a cloud front overpassed the basin in the morning, followed by strong winds that triggered SDS. In the prefrontal SDS, dust covered a large area from Gonghe, lying in front of or below cloud masses associated with a frontal system.

The seasonal variability of SDS depends on the seasonality of the atmospheric circulation patterns of frontal development. This points to the important role of the LLJ in the ADS of these areas. Knippertz (2014) suggested that many generic meteorological phenomena can be identified and classified in many dust source regions on Earth. For example, mobile synoptic-scale systems, such as anticyclones, cyclones, and cold fronts, typically occur in late winter and spring. This matches up to Gonghe Basin. The seasonal cycle in the distribution of frontal dust amounts shows similar seasonal characteristics to the LLJ (Frontal), higher in winter and spring (highest in December and April). These processes can be locally modified according to the topography and are often characterised by a distinct diurnal cycle. The QTP is a prominent geographical feature that forms a physical barrier to circulation in this region (Li et al., 2019), affecting the interaction between wind and dust.

Chen et al. (2021) reported the presence of a Low-Level Barrier Jet (LLBJ) on the northeastern slope of the Qinghai-Tibetan Plateau, which triggered the occurrence of an SDS. They found that the establishment of the LLBJ can be attributed mainly to the movement of high-momentum air, which descended towards the southeast at a mid-level and collided with the northern slope of the QTP. This collision led to an acceleration of a geostrophic flow as a result of geostrophic adjustment. LLBJ intensity and SDSs are modulated by the radiative forcing of dust. Dust radiative forcing is mainly governed by dust-radiation interactions. Daytime, the dust-radiation forcing warms the upper dust layer and cools the lower layers of the main DPS area. Dust enhances wind speeds within the entire boundary layer from daytime to evening. The airflow from western China and the Tarim Basin first enters the Hexi Corridor and then flows into the Gonghe. The Hexi Corridor is located in the southwestern Gobi Desert parallel to the northeastern slope of the QTP (i.e., Gonghe Basin).

Liu et al. (2014) confirmed that the Low-Level Jet (LLJ) is distributed east of the QTP, including Gonghe. Synoptic-scale low-pressure systems are consistently observed on the southwest of the LLJ, while large-scale high-pressure systems are on its northeast. The pressure gradient between these contrasting systems results in raised air currents. Notably, the LLJs present comparable horizontal structures and synoptic configurations at QTP, Africa, and South America (Hong-Bo, 2012). Similarly, LLJ caused by strong frontal systems leads to SDS at the Hexi Corridor in spring (Tang et al., 2004). At daytime, the high-momentum air at LLJ moves downward, enhancing surface wind speeds and dust ejected from the surface, peaking in the early afternoon with a strong diurnal signature (Chen et al., 2021). Similar diurnal features also occur at Gonghe, with strong surface wind induced SDSs in the afternoon.

- **Unidentified processes (or called Disturbance)**

Pye (2015) suggested that cultivating desert or marginal soils contributes to the frequent occurrence of SDSs in semi-arid regions. Cao et al. (2018) proposed that regional SDS in China mainly occur in spring and winter and that regional SDS are caused by weather-scale weather (e.g., the passage of cold fronts). Other SDS occur frequently in the desert during summer and autumn in China. Those undefined process might be in the form of LSS or small dust storms.

3.4.3 Events timing and Wind (Based on Merra-2 Reanalysis hourly data)

3.4.3.1 Wind speed difference

The presence of strong wind speeds is the leading cause of SDSs. The surface maximum wind speed on Dust Storm Day (DSD) shows a clear diurnal cycle, and LD surface maximum wind speed is higher than that of TD. The LD wind speed median line of the boxplot is higher than DUP throughout the day, and TD is relatively low from 12.00 - 00.00 UTC, indicating the importance of the high near-surface wind speed required for LD to produce SDSs. This confirms the conclusion of Cowie et al. (2014) that all atmospheric processes forcing dust movement must produce wind speeds over local threshold velocities depending on surface roughness length, soil structure, and vegetation when dust emits from the basin (LD).

Surface winds in dust source areas exhibit a diurnal cycle and seasonal differences associated with a stratified diurnal cycle at different heights (Fiedler, et al., 2016). When high-momentum air at high layers is convectively mixed with low-momentum air from near the surface. The reduction in vertical transport of momentum air results in the slowest near-surface winds at night. In addition, changes in pressure gradient forces associated with mesoscale and weather-scale systems can also produce extreme wind speeds.

3.4.3.2 Pre/post-frontal surface Winds

Frontal associated SDS mainly occurs (62%) in the afternoon 05.00 - 09.00 (UTC), which is consistent with the apparent diurnal cycle of frontal near-surface winds. This suggests that the relationship between frontal and stronger surface wind speed drivers is an important mechanism for SDSs in the Gonghe Basin. Based on 701 meteorological stations data during 1954-2000, Wang et al. (2005) found that the daily variation in SDS occurrence in northern China was significant, with SDS occurring mostly in the afternoon. Tindan et al. (2023) used IASI DOD products from Laboratoire de Météorologie Dynamique, as well as ground-based observations from LISA sites and AERONET, and they also confirmed the diurnal difference in SDS occurrence. DOD daytime values are higher than nighttime values in the Taklamakan Desert, possibly related to the stronger wind speeds during the daytime and the more SDSs.

An example of Frontal lead SDS is shown in Appendix G-J (A case on 8 October 2022). Under the influence of high pressure, the front moved southeastward and the airflow collided with the mountains formatting LLJ which dominates the weather conditions in the Gonghe. The strong cold advection behind the front and the effective downward transfer of momentum air caused high winds at the surface with surface maximum wind speeds exceeding 10.6 ms^{-1}. A strong post-frontal SDS appeared behind the cold front. Dust particles were confined to the area behind, and the highest dust loading occurred near the cold front. Suspended dust particles gradually move forward to the southeast in the following hours (shown in Appendix H and J Satellite Aerosol Products), corresponding to the southeastward shift of the cold front and the strong northwest wind state.

3.4.4 Spatiotemporal Dust Source Characteristics Inferred From GEO Satellite (Himawari-8) Observations

3.4.4.1 Active dust sources Frequency caused by Pre/post-Frontal

Morning has fewer SDS events but a higher FO-AOT, and afternoon has more SDS events but a lower FO-AOT (Figure 3.14). This is caused by the following reasons. (i) Frontal SDS emitted more dust on a larger scale in the morning and mixed haze transport from the upper wind source region. (ii) The dust is more readily detectable as AOD (it may take time for dust to reach an altitude whereby it can impact AOD) in the morning, and 33% frontal associated SDSs occurs after 07.00 (UTC). (iii) Downwind Movement. Impacts of co-incident TD from other upper wind dust sources, e.g., Taklamakan Desert, Qaidam Basin and suspended in the local Gonghe atmosphere in the morning;

FO-AOT derived from frontal dust is higher in the morning, caused by mixed haze transport from the upper region. Due to statistical methods, stationary or persistent dust plumes are considered more than one day. Dust particles (haze) that remain stationary over topographic basins or accumulate along ridges or valleys significantly increase the frequency of local occurrences in the morning. Ultimately, maps of ADS areas are used as input masks for some SDS models, and the ADS areas covers specify potential SDS areas or increase the dust emission fluxes in these areas. However, limiting dust emissions to inaccurate dust sources or increasing dust fluxes in areas of non-dominant dust sources can lead to an overestimation of local atmospheric dust loads. Thus, dust feedback on radiation-related parameters such as temperature, atmospheric stability, and cloud physics requires it to be aligned, potentially leading to a misrepresentation of atmospheric conditions.

The detecbility of AOD aerosol inversion algorithm from RS satellites various across different altitudes and surface types, as the afternoon FO-AOT associated with frontal dust tends to be lower. Regarding space, SDSs can also vary significantly in scale, height, and the density/type of material in transport. Frontal-induced SDS more frequently occurs in the late afternoon, but the dust is more readily detectable as AOD in the morning. It may take time for dust to reach an altitude, whereby it can be recognised by an optical depth sensor. Zhang et al., (2019) indicate that the AHI aerosol retrieval algorithm tends to underestimate the atmospheric aerosol load on land. Underestimation may be due to inaccurate characterization of surface reflectance in the AHI sol inversion algorithm, especially on bright surfaces (high reflectivity). Aerosols typically exhibit stronger absorption characteristics than scattering characteristics on bright surfaces, especially when the aerosol load is low. If a higher surface dependency value is used for inversion, the partial radiation contributed by aerosols observed by satellites will be mistaken for the surface, resulting in lower AOD.

Chaka Lake is an ADS area (Figure 1.3). However, Chaka Lake is hard to observe manually from satellites due to the basin/dust background having the same colour, causing the SDSs to be missing and underestimating the number of DSD and dust loading level over the Gonghe Basin. Himawari-8 AOT products are good at detecting ephemeral lake dust sources, and the MODIS AOD dataset also highlights SDS from Chaka Lake.

3.4.4.2 Controls on dust sources activation

Bullard et al. (2011) propose three states for limiting SDS, **Transport Capacity Limited** (TCL), **Supply-Limited** (SL), and **Availability-Limited** (AL), in this chapter, we use GEO data to understand the controls on SDS at the basin level.

- **Transport Capacity Limited**

Number of DSD at different times of year and day shows a clear dust annual/ cycle in the Gonghe Basin. Wind speed variation at different times of the year and day relate to 4 types of SDS mechanism. For example, wind speed changes match LLJ seasonal and diurnal cycle (Fajber et al., 2014) and have higher wind speeds in the afternoon in winter and spring. Du et al. (2022) conducted a study on the impact of lower temperatures and lower air pressure on SDS in the QTP. The researchers discovered that the primary cause of the heightened intensity of SDSs during winter and early spring was air density. This period experiences the lowest temperatures, particularly in February, and higher air pressure compared to other seasons, resulting in increased air density and wind speed. The higher-density airflow possesses a greater viscosity coefficient and can generate stronger shear stress. Consequently, SDS is more prevalent in the Gonghe Basin during winter and early spring.

- **Supply-Limited**

In Gonghe Basin, Quaternary deposits of sand dunes and fluvial terraces provide sufficient erodible sediment. The fluvial system includes Chaka Lake, Longyangxia River and many tributaries providing fine sediment and related to active dust sources in the Gonghe Basin. Feuerstein and Schepanski (2018) suggest that an important source type is sediment accumulated by surface water runoff, known as alluvial sediment. Recently, satellite remote sensing products have enabled the monitoring of global surface water variations for lakes and reservoirs (Tortini et al., 2020). For example, Ginoux et al., (2012) analysed dust sources globally using a comparison of MODIS Deep Blue Dust products with surface geomorphology. Moreover, the study revealed that 20% of emissions originated from vegetated surfaces, predominantly desert scrub and agricultural land. Anthropogenic dust sources are influenced by land use and temporary water bodies, which are interconnected with the hydrological cycle. Climate change and human activities also influence emissions, as indicated by previous studies (Gill, 1996; Muhs et al., 2014; Webb and Pierre, 2018).

- **Availability-Limited**

Xu et al. (2020) found that sand dune systems can have other stable states co-existing in the semi-arid region of northern China: a vegetated stable state and a bare active state. In the range between activation and stability thresholds, dunes in the activated and stable states can coexist. However, there are occasionally sharp temporal changes between these contrasting states. For example, a dune with stable vegetation can transition to an active state caused by reduced precipitation and will not stabilise again unless precipitation rises to a level much higher than the initial threshold required for dune activation. In the semi-arid regions of northern China, extreme weather, fire, and local human-induced disturbances including grazing, farming, and recently revegetation and desertification programs, may activate site-specific sand dunes (Miao et al., 2016). By contrast, Liu et al. (2021) concluded that the desertification programs decreased the sandy desertification of North China by about 73000 km^2 during 2010-2018. Several programs have been implemented to address these issues, including the Three Norths Shelterbelt Project, the Conversion of Cropland to Forest or Grassland Program, and the Water and Soil Conservation Program (Xue et al., 2013). Han et al. (2015) further explores anthropogenic factors such as population change and increased land cultivation, which have significant implications for the direct desertification change, improvement, or expansion of desert areas.

On the other hand, once the dunes are stabilised by vegetation, an increase in wind cannot easily mobilise them because the vegetation increases surface roughness, reduces sand transport and covers the surface from wind erosion (Xu et al., 2020). Another sediment supply-limited scenario in the QTP is Snow Cover. For example, there were no SDSs in 2020 November because the snow covered the Gonghe Basin, also considering snow melting also resulted in higher soil moisture causing frozen soil, thus, the soil surface is covered by snow and a formed ice crust. The QTP situated at an elevation of 4000 m above sea level, is globally recognized as the World's Third Pole (Orsolini et al., 2019). Moreover, QTP exhibits analogous characteristics to other high-latitude regions. Bullard et al., (2016) suggest that at high latitudes, factors such as low temperature, humidity, strong winds and permafrost can influence SDSs. Meinander et al., (2022) showed that climate change can lead to a reduction in snow cover duration and an increase in the intensity and frequency of droughts and heat waves at high latitudes. Under heatwave and drought conditions, when the ground is unfrozen and snow-free at high latitudes, it causes ground conditions that are conducive to SDSs and greater susceptibility to wind erosion, thus increasing the probability of SDS.

3.5. Conclusion

Q3.1: Can SDS from the Gonghe Basin be detected in GEO data, and at what time of day is dust emitted?

O3.1: Build a sub-daily [10 hr/10 min] dust observation/detection time series [dust, cloud, no dust etc.] for four years (2019-2022) using GEO data

- The Gonghe Basin is cloudy, but lots of SDS events (and associated dust emissions) were detected. About 60% of the time the Gonghe Basin is covered by cloud or partial cloud because it is located in QTP at a high altitude.
- Due to the cloud effects, the use of the Himawari-8 observing time window is limited to 40% of the year. The 10 min high-temporal Himawari-8 satellite covers the daytime period at (00.00 - 09.00 UTC, or 08.00 - 17.00 CST), and 55% of SDS start in the morning in the Gonghe Basin.
- SDS mainly happened from November to May. Winter has the lowest cloud cover and the highest number of DSD detections from RS, indicating that RS-detected dust loading in this region is underestimated.

O3.2: Compare daily, monthly annual GEO dust chronologies with LEO observations [Chapter 2]

- GEO data has the capability to see all RS-detectable SDS in the daytime, so the GEO SDS detection rate is 100% in the absence of cloud whereas the daily LEO daily satellite products only observe morning SDS (before 05.00 UTC), so the detection rate reduces to less than 40%. TD is more likely to start in the morning, and LD is more likely in the afternoon. SDS occurring in morning means they are more likely to be recorded in LEO and GEO. Approximately 31% LD and 5% TD were missed by LEO, and these SDS events will be undetected by LEO.

- The continuous and short interval of GEO (Himawari-8) data demonstrates the ability to provide a complete view of the SDS emission process in the daytime, including SDS type, emission start time, duration, and prevailing wind conditions. Here, GEO data achieved insight into the temporal heterogeneity of emissions far beyond that revealed by the LEO satellite, increasing temporal resolution on the number and spatial distribution of observed SDS. Temporal resolution is key when identifying small-scale SDS. Himawari-8 allows us to work at the scale of meteorological observations, and thereby link observations of dust to climate phenomena. Whereas other LEO RS data detect dust in transport (dust advection).

Q3.2: To what extent do meteorological events and climate data explain sub-daily SDSs?

O3.3: Identify local/regional meteorological mechanisms associated wrt SDSs.

- Based on the prevailing weather systems and their physical conditions associated with SDS, we found that the spatial and temporal characteristics of each type of SDS show significant diversity.
- Dust activity in Gonghe can be divided into four typical types. (i) Haboob SDS caused by convection are the most intense, with dust walls developing rapidly and producing the highest levels of SDSs. (ii) Haze has the longest duration and occurs frequently due to the high number of dust sources in the upwind region, including the Taklamakan Desert, the Qaidam Basin, and the surrounding mountains that confine the atmospheric circulation of airborne particles to the interior of the basin. (iii) The clear dust plumes of frontal-induced SDS on RS, indicate rapid and intense emissions and the largest influence area. (iv) Disturbance-induced SDS shows lower (or undetectable) airborne dust and has the shortest duration and smallest area of impact. Pre/postfrontal and Haze are the two main dust types from November to May over the Gonghe Basin, accounting for about 80% of DSD.

Haboobs occur infrequently during the dusty months, and Disturbances do not lead to SDSs in February and March.

- Haboob and haze are regional SDSs that transport dust particles from the upper basin (TD). Large and small Pre/Postfrontal systems lead to SDS and observed dust plumes derived from the local basin (LD) over the basin. LD is a likely record of SDS from the Gonghe Basin. Haze and Haboob (TD) are regional SDSs transported from the upper basin. TD may include LD emission because the morning has high AOT values and TD has high wind speed, but we cannot see it from Himawari-8. Higher frequency of LD to TD in Winter. LD Emission is above the 6 ms^{-1} DUP threshold throughout the year, whereas the TD events can occur below the threshold, suggesting the advection through the basin coming from upwind. The wind speed of the LD is higher than TD, and both LD and TD show a clear diurnal cycle. The wind speed reaches peaks at 16.00 (CST), and then gradually decreases during the night. During the daytime period from 8.00 to 17.00 (CST), the LD and TD wind speeds differ widely, confirming high wind speeds accompanying LD tend to occur in the afternoon.

- These data allowed DSD/SDS events to be attributed to four key types: Haboob [4.6 %], Haze [38.2 %], Pre/Post Frontal systems [47.4 %], and unidentified processes (or called Disturbance) [9.8 %].

O4: Investigate relationships between climate variables for known SDS events at the sub-daily scale

- Morning has fewer SDS events but a higher FO-AOT, and afternoon has more SDS events but a lower FO-AOT. Frontal SDS emitted more dust on a larger scale in the morning and also mixed haze transport from the upper wind source region. Frontal-induced SDS more frequently occurs in the late afternoon, but the dust is more readily detectable as AOD in the morning. It may take time for the dust to reach an altitude, whereby it can be recognised by an optical depth sensor. There is a time gap between Himawari-8 TCI recognition of dust and AOD detecting dust, causing some SDSs to be missing from AOD detection. The spatial offset caused by the movement of dust downwind is evident and related to the timing of sensor-captured SDS. Himawari-8 could capture SDS from the source but also capture SDS transport downwind, causing some misdetection of ADS location.

- Within the Gonghe Basin, the presence of Quaternary aeolian deposits and a fluvial system ensures an ample supply of sediment that is prone to erosion. The fluvial system includes Chaka Lake, Longyangxia River, and many tributaries providing fine sediment and related to active dust sources in the Gonghe Basin. The presence of strong wind speeds is the main driver of SDSs. Wind speed variation at different times of the year and day relate to 4 types of SDS mechanism. In winter and early spring, lower temperatures and higher air pressure than other months on the QTP, result in higher air density and wind speed. Higher-density airflow has a higher viscosity coefficient and can provide stronger shear stress. Therefore, dust activity is frequent in winter and early spring at the Gonghe Basin.
- Dune systems can have other stable states co-existing in the semi-arid region of northern China: a vegetated stable state and a bare active state. Anthropogenic factors such as population change and increased land cultivation appear to be stronger drivers of direct desertification change, improvement or expansion of desert areas. As anthropogenic dust sources are associated with land use and ephemeral bodies of water, including grazing, farming, and industrial. Once the dunes are stabilised by vegetation, an increase in the wind cannot easily mobilise it. The presence of vegetation or snow on the surface serves to elevate surface roughness, thereby diminishing the accessibility of erodible soil sediment, shielding the ground from wind erosion, and curtailing the transport of sand particles.

O5: Mapped Frontal SDS Hotspot in Morning and Afternoon

- Morning has fewer events but a higher Frequency, and Afternoon has more events but a lower dust frequency. (i) Morning frontal system led to more dust emitted on a large scale; (iii) The dust is more readily detectable as AOD in the morning, and it may take time for dust to reach an altitude whereby it can impact AOD, 33% Frontal Dust occur after 07.00 (UTC) when Himawari-8 AOT products tend to underestimated the atmospheric aerosol load in land. (iii) Downwind Movement.

Impacts of co-incident TD from other upper wind dust sources and suspended in the local Gonghe atmosphere in the morning.

- Morning ADSs are mostly related to convective (Haze) events, and afternoon ADSs are mostly related to the breakdown of the frontal LLJ. Diurnal differences in frontal wind speed are larger and more pronounced in spring than in other seasons. Winter SDS is constrained by sediment available limitation, e.g., vegetation and snow cover. Frontal dust has an AOD signature. Quantitative dust inversions of the desert surface are required to elucidate the contribution of LLJ to total SDS fluxes.

4. Use of High-Resolution Low Earth Orbit [LEO] data for Dust Point Source [DPS] detection and derivation of Preferential Dust Source [PDS] and Land Cover/Use [LULC] Characteristics.

4.1 Introduction

Obtaining field observations of SDS from dust sources presents challenges due to the remote and harsh environments where these sources are found, as well as the dynamic and complex spatiotemporal nature of the emission process (Baddock et al., 2021; Wiggs et al., 2022). A number of researchers have attempted to constrain the drivers of SDSs and activity of dust source regions at the sub-basin scale using field and remote sensing data (e.g., Hahnenberger and Nicoll 2014; Mockford et al., 2018; Vickery et al., 2013). Recent freely available High-Resolution Remote Sensing data (HR-LEO) via Planet (e.g., Bryant and Baddock, 2021), Landsat 8/9 (Ali et al., 2022) and Sentinel 2A (Bakker et al., 2019) have significantly improved our understanding of the spatial distribution post-2014 and temporal variability of contemporary dust sources (HR-GEO, Zhang et al., 2020). For example, PlanetScope constellation remote sensing data with 3 m resolution, global, daily coverage (Planet, 2017; Baddock et al., 2021; Duan et al., 2022), Combined those new HR-LEO data provides an extraordinary opportunity to monitor aeolian SDS processes at the field (pixel) scale.

Nevertheless, many RS techniques identify incorrect dust sources due to the limitations of satellite RS including cloud effects (Boloorani et al., 2023), low spatial-temporal resolution (Boroughani et al., 2020), and dust retrieval approach (Huck et al., 2023). The RS enhancement approaches have successfully observed dust plumes, for example, Murray et al. (2016) developed Clear Sky Difference (CSD) for SEVIRI. It is important to develop new RS enhancement methods adopted on the HR-LEO data to derive Dust Point Source (DPS) accurately. The characteristics of dust particles that are important for their climate effects, such as their physical, optical, and mineralogical properties, are influenced by the local geomorphology of the dust source region (Schepanski et al., 2009). Since it is not feasible to conduct in-situ measurements at all significant dust source locations, remote sensing methods must be employed to gather comprehensive data on dust sources in the Gonghe.

Although the aeolian features and geomorphological change were mapped in the Gonghe Basin through RS and fieldwork (Luo et al., 2020; Qi et al., 2021; Baird et al., 2021), knowledge of the relative importance of each of these land surface types to the dust cycle is lacking. Studies analysing the aeolian landscapes of Gonghe have focused on the effect of parabolic dune (Luo et al., 2019a) because it was found to be the most important dust source type (Xuehua et al., 2021), but it might not provide a complete understanding of how these sources contribute to the temporal variability of SDSs. To further investigate the impact of human activities on SDSs, the land cover associated with dust sources is also examined. In this chapter, land use and land cover (referred to as 'LULC') are considered together. Linking SDS with landform types is vital for understanding what controls the nature and magnitude of SDS in space and time (Bryant, 2013).

The extent of the impact of the Gonghe Basin's SDSs on the downwind area is still uncertain, and precise research on the transmission pathway is required. NOAA HYSPLIT (Hybrid Single-Particle Lagrangian Integrated Trajectory) trajectory model is widely utilised to track dust across North China (Cao and Chen, 2022; Aili et al., 2021; Bao et al., 2023). However, outputs from this model are strongly constrained by the quality of the input, which is known as DPS (Baddock et al., 2017). Therefore, having knowledge of the specific dust source and the timing of emissions allows for the development of a long-term climatology of dust transport that better represents the actual transportation patterns.

4.1.1 Chapter Aims and Objectives

Chapter 4 Research Aim: [SUB-BASIN SCALE] Use of High-Resolution Low Earth Orbit [LEO] data for Dust Point Source [DPS] detection and derivation of Preferential Dust Source [PDS] and Land Cover/Use Characteristics.

The information and knowledge acquired in Chapters 2 and 3 were utilised to identify specific SDSs that have synergistic coverage of GEO and HR LEO data. The synergy of these two types of data is crucial to the overall narrative, as these are events that were characterised by their seasonal context and relationship to climate. Consequently, the approach used in this study is relatively well-constrained, taking into account the relative space/time bias based on GEO and LEO observations and a relatively comprehensive understanding of the regional and basin-scale dust cycle. The primary objective of this chapter is to accurately pinpoint the dust source, which will subsequently enable the derivation of potential information regarding SDS controls.

Q4.1: Where are the dust point sources [DPS] within the Gonghe Basin at the sub-basin scale?

[O4.1]: Develop a Dust Point Source [DPS] detection protocol for PlanetScope, Sentinel 2 and Landsat 8/9.

[O4.2]: Derive PDS and Land Cover/Use [LULC] Maps for the Gonghe Basin.

Q4.2: What are the properties of observed SDSs at the sub-basin scale, and what is the PDS/ LULC signature of those DPS?

[O4.3]: Use DPS data to derive PDS and LULC signatures for SDSs in the Gonghe Basin.

[O4.4]: Measure dust loadings for observed plumes emanating from the Gonghe Basin.

[O4.5]: Determine the bulk trajectory of SDSs emanating from known DPS.

4.2 Data and Method

4.2.1 Data

In Chapter 4, high-resolution (HR) LEO was used to detect SDSs and observe dust plumes from sources. Due to the early morning overpass time and relatively low temporal resolution of HR LEO, PlanetScope only identified 14 cases with clear dust plumes caused by SDSs, while Sentinel-2 detected 10 out of these 14 cases and Landsat-8 had access to 2 out of the total cases available from January 2019 to January 2023. Additionally, MODIS (moderate LEO data in Chapter 2) and Himawari-8 (GEO data in Chapter 3) observed and recorded all the mentioned SDS cases. Therefore, these cases are representative for DPS detection in the Gonghe Basin. Table 4.1 provides details on the observed start time of SDSs from Himawari-8 as well as the timing of HR LEO satellite overpasses for these specific instances. The PDS geomorphology map for the Gonghe Basin was created using soil data, desert classification, and dune-type datasets obtained from the National Tibet Plateau Data Centre. The LULC map is based on Copernicus Global Land Service data (Table 4.2).

Table 4.1 Time (UTC) of 14 SDSs observed start emission in Himawari-8 and time of HR LEO satellite (Planet, Sentinel-2 and Landsat-8) capture the SDS and data availability.

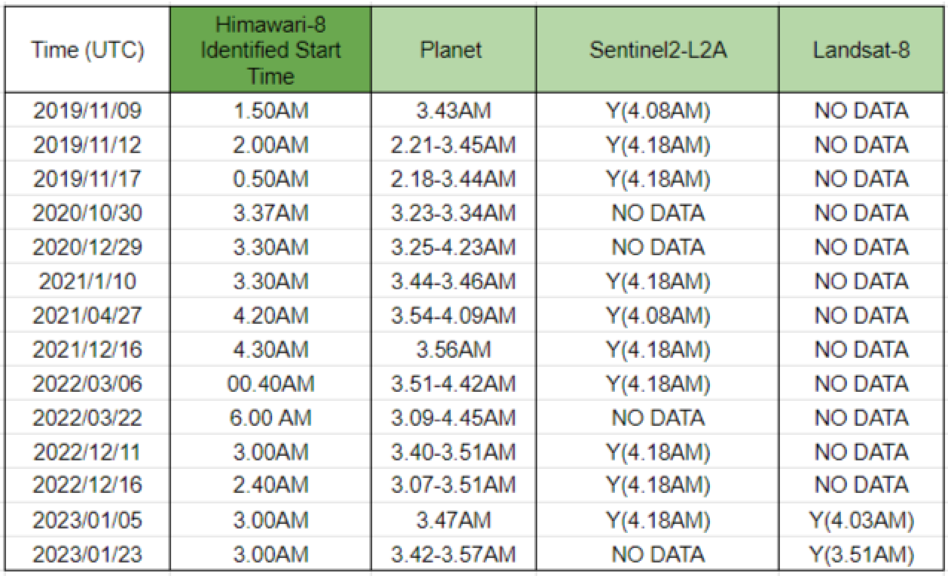

Time (UTC)	Himawari-8 Identified Start Time	Planet	Sentinel2-L2A	Landsat-8
2019/11/09	1.50AM	3.43AM	Y(4.08AM)	NO DATA
2019/11/12	2.00AM	2.21-3.45AM	Y(4.18AM)	NO DATA
2019/11/17	0.50AM	2.18-3.44AM	Y(4.18AM)	NO DATA
2020/10/30	3.37AM	3.23-3.34AM	NO DATA	NO DATA
2020/12/29	3.30AM	3.25-4.23AM	NO DATA	NO DATA
2021/1/10	3.30AM	3.44-3.46AM	Y(4.18AM)	NO DATA
2021/04/27	4.20AM	3.54-4.09AM	Y(4.08AM)	NO DATA
2021/12/16	4.30AM	3.56AM	Y(4.18AM)	NO DATA
2022/03/06	00.40AM	3.51-4.42AM	Y(4.18AM)	NO DATA
2022/03/22	6.00 AM	3.09-4.45AM	NO DATA	NO DATA
2022/12/11	3.00AM	3.40-3.51AM	Y(4.18AM)	NO DATA
2022/12/16	2.40AM	3.07-3.51AM	Y(4.18AM)	NO DATA
2023/01/05	3.00AM	3.47AM	Y(4.18AM)	Y(4.03AM)
2023/01/23	3.00AM	3.42-3.57AM	NO DATA	Y(3.51AM)

Table 4.2. Remote Sensing and Surface Data. Overpass time and the resolution (spatial; temporal) of RS are shown in the table, trade-off RS properties for better detection of SDS. HR-LEO provided maximum clarity for DPS identification and mapping PDS and LULC. Several datasets help with characteristics of PDS geomorphology, including RS, topographic, soil and geological maps and field data (e.g., Dune/desert classification) based on the surface land signature of the basin. The Global Database of Landcover is available, combined with open street map datasets and RS, to identify land use in the Gonghe Basin.

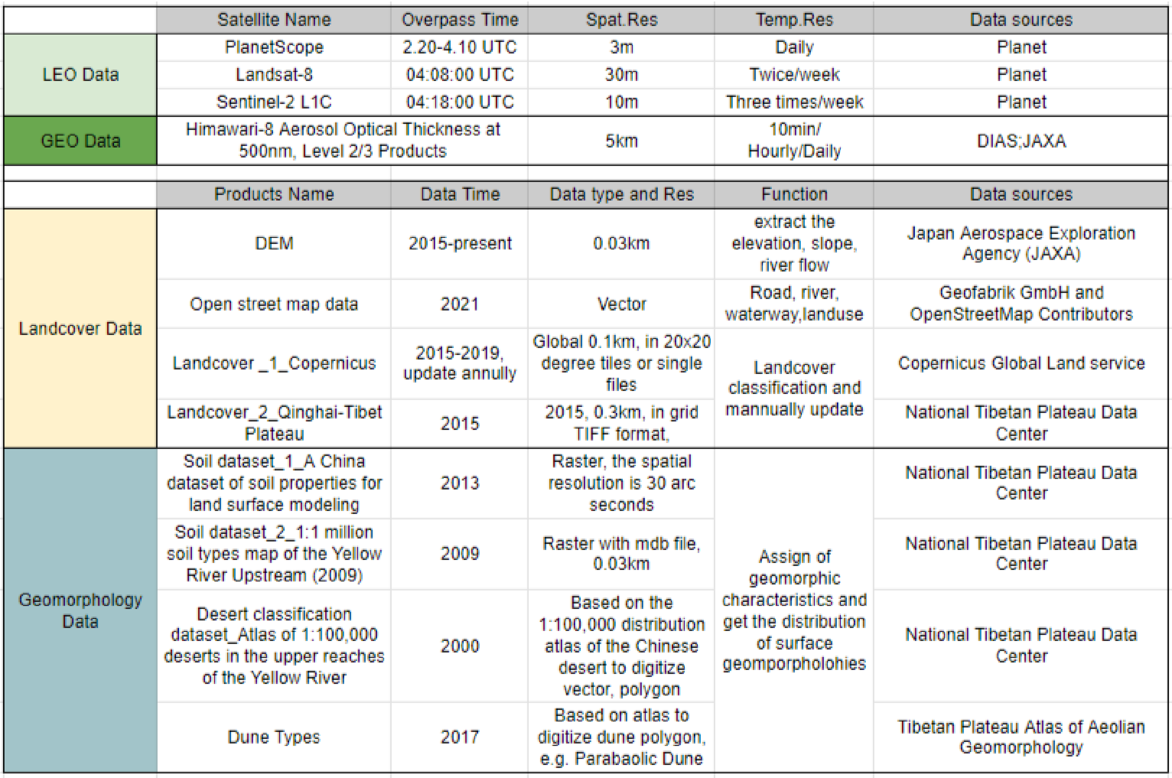

	Satellite Name	Overpass Time	Spat.Res	Temp.Res	Data sources
LEO Data	PlanetScope	2.20-4.10 UTC	3m	Daily	Planet
	Landsat-8	04:08:00 UTC	30m	Twice/week	Planet
	Sentinel-2 L1C	04:18:00 UTC	10m	Three times/week	Planet
GEO Data	Himawari-8 Aerosol Optical Thickness at 500nm, Level 2/3 Products		5km	10min/ Hourly/Daily	DIAS;JAXA
	Products Name	Data Time	Data type and Res	Function	Data sources
Landcover Data	DEM	2015-present	0.03km	extract the elevation, slope, river flow	Japan Aerospace Exploration Agency (JAXA)
	Open street map data	2021	Vector	Road, river, waterway,landuse	Geofabrik GmbH and OpenStreetMap Contributors
	Landcover _1_Copernicus	2015-2019, update annully	Global 0.1km, in 20x20 degree tiles or single files	Landcover classification and mannually update	Copernicus Global Land service
	Landcover_2_Qinghai-Tibet Plateau	2015	2015, 0.3km, in grid TIFF format,		National Tibetan Plateau Data Center
Geomorphology Data	Soil dataset_1_A China dataset of soil properties for land surface modeling	2013	Raster, the spatial resolution is 30 arc seconds	Assign of geomorphic characteristics and get the distribution of surface geomporpholohies	National Tibetan Plateau Data Center
	Soil dataset_2_1:1 million soil types map of the Yellow River Upstream (2009)	2009	Raster with mdb file, 0.03km		National Tibetan Plateau Data Center
	Desert classification dataset_Atlas of 1:100,000 deserts in the upper reaches of the Yellow River	2000	Based on the 1:100,000 distribution atlas of the Chinese desert to digitize vector, polygon		National Tibetan Plateau Data Center
	Dune Types	2017	Based on atlas to digitize dune polygon, e.g. Parabaolic Dune		Tibetan Plateau Atlas of Aeolian Geomorphology

Sentinel-2 provides high-resolution (10 m, 20 m, and 60 m) and multi-spectral coverage (via 13 bands of data in the visible, near-infrared, and short-wave infrared part of the spectrum; in Table 4.3, European Space Agency, 2015). PlanetScope was designed to be similar to Sentinel. PlanetScope data has a much higher resolution (3 m orthorectified) but only offers data in the Red (0.655 µm – comparable to Sentinel-2, band 4), Green (0.565 µm – comparable to Sentinel 2, band 3), Blue (0.49 µm comparable to Sentinel 2, band 2), and Near-Infrared (0.865 µm – comparable to Sentinel 2, band 8) wavelengths (Planet, 2017). Landsat-8 observations have a 30-metre cover in sub-tropical regions where solar elevation is greater than 5° in the 16-day repeat cycle, and it will reduce to 2 time per week after the Landsat-9 launch in 2021 (Li and Chen, 2020).

Table 4.3 Spatial resolution bands and associated wavelength of Planet (Planet, 2017), Sentinel-2 (European Space Agency, 2015) and Landsat-8 (USGS, 2023).

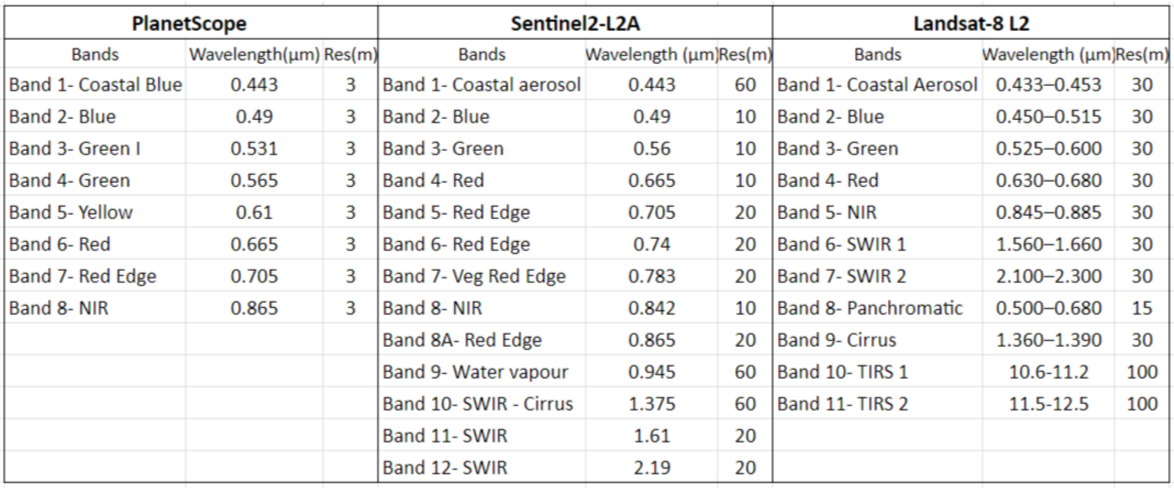

PlanetScope			**Sentinel2-L2A**			**Landsat-8 L2**		
Bands	Wavelength(µm)	Res(m)	Bands	Wavelength (µm)	Res(m)	Bands	Wavelength (µm)	Res(m)
Band 1- Coastal Blue	0.443	3	Band 1- Coastal aerosol	0.443	60	Band 1- Coastal Aerosol	0.433–0.453	30
Band 2- Blue	0.49	3	Band 2- Blue	0.49	10	Band 2- Blue	0.450–0.515	30
Band 3- Green I	0.531	3	Band 3- Green	0.56	10	Band 3- Green	0.525–0.600	30
Band 4- Green	0.565	3	Band 4- Red	0.665	10	Band 4- Red	0.630–0.680	30
Band 5- Yellow	0.61	3	Band 5- Red Edge	0.705	20	Band 5- NIR	0.845–0.885	30
Band 6- Red	0.665	3	Band 6- Red Edge	0.74	20	Band 6- SWIR 1	1.560–1.660	30
Band 7- Red Edge	0.705	3	Band 7- Veg Red Edge	0.783	20	Band 7- SWIR 2	2.100–2.300	30
Band 8- NIR	0.865	3	Band 8- NIR	0.842	10	Band 8- Panchromatic	0.500–0.680	15
			Band 8A- Red Edge	0.865	20	Band 9- Cirrus	1.360–1.390	30
			Band 9- Water vapour	0.945	60	Band 10- TIRS 1	10.6-11.2	100
			Band 10- SWIR - Cirrus	1.375	60	Band 11- TIRS 2	11.5-12.5	100
			Band 11- SWIR	1.61	20			
			Band 12- SWIR	2.19	20			

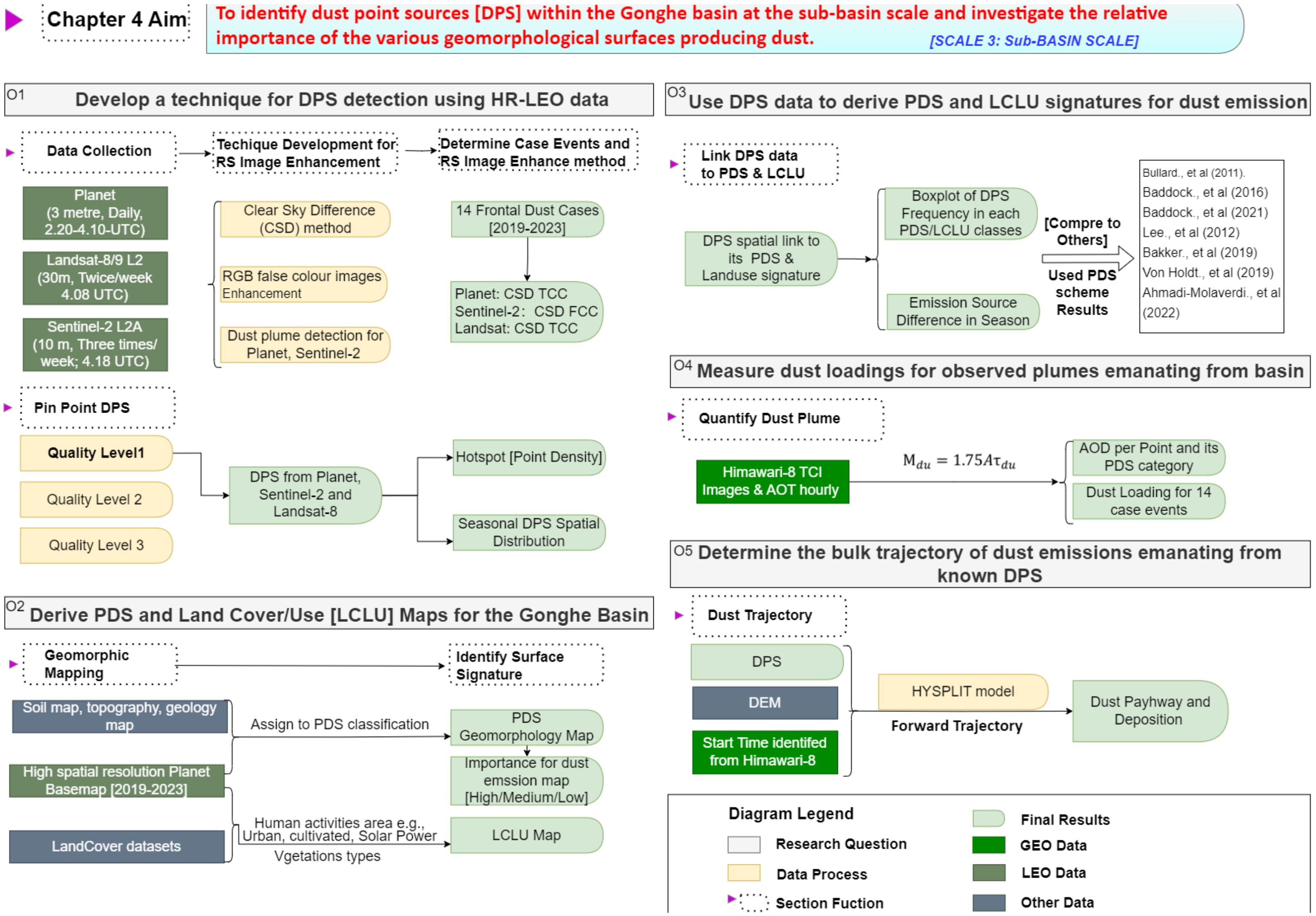

Figure 4.1. Methods and workflow that highlights specific objectives and research questions addressed in Chapter 4.

4.2.2 Remote sensing dust detection at sub-basin scale

The Chapter 4 workflow shown in Figure 4.1 matches each Objective and Result.

4.2.2.1 Remote sensing image enhancement scheme

Remote sensing image enhancement schemes were evaluated to accommodate the combined use of HR-LEO satellite sensor data to observe and detect dust plumes. To boost the detection of dust plumes, the Clear Sky Difference (CSD) pixel-based method utilised images of a dusty day minus the closest equivalent clear sky images. This approach was tested in (i) single-band mode and (ii) multi-band True-Colour Composite (TCC) and False-Colour Composite (FCC) modes. The single band mode involved a lower wavelength information requirement from the satellite sensors, utilising single band images from two separate dates (Dust Day and Clear Sky Day), and was applied to HR-LEO data (Table 4.3). The multi-band CSD TCC/FCC approach had a higher wavelength requirement, and it was developed for SEVIRI by Murray et al. (2016). Equivalent wavelengths were used (Table 4.3 and Figure 4.2) to generate a modified CSD approach for HR-LEO data.

$$\left\{\begin{array}{l} \mathrm{Red}_{8bit} = 15*255*\left(\rho_{1.6\mu m} - \rho^{csn}_{1.6\mu m}\right) \\ \mathrm{Green}_{8bit} = 15*255*\left(\rho_{0.8\mu m} - \rho^{csn}_{0.8\mu m}\right) \\ \mathrm{Blue}_{8bit} = 15*255*\left(\rho_{0.6\mu m} - \rho^{csn}_{0.6\mu m}\right) \end{array}\right\}$$

Figure 4.2 The CSD FCC dust detection rendering approach equations. Reproduced from Murray et al. (2016)

Based on Murray et al. (2016)'s work, knowing certain wavelengths is likely to work best. In this case, the single-band and multi-band CSD methods used Sentinel-2 band 11 (1.6 µm), band 7 (0.8 µm), and band 4 (0.6 µm) (Table 4.3). As Sentinel-2 band 11 has a 20 m pixel, the calculated CSD FCC-enhanced Sentinel-2 image was also set at 20 m. The Planet and Landsat-8 used the RGB bands. Planet's Clear Sky images are derived from the monthly Planet global base map corresponding to the month of each case, whereas Sentinel-2 and Landsat used an image that has no dust and cloud in the dust case month (e.g., Figure 4.3).

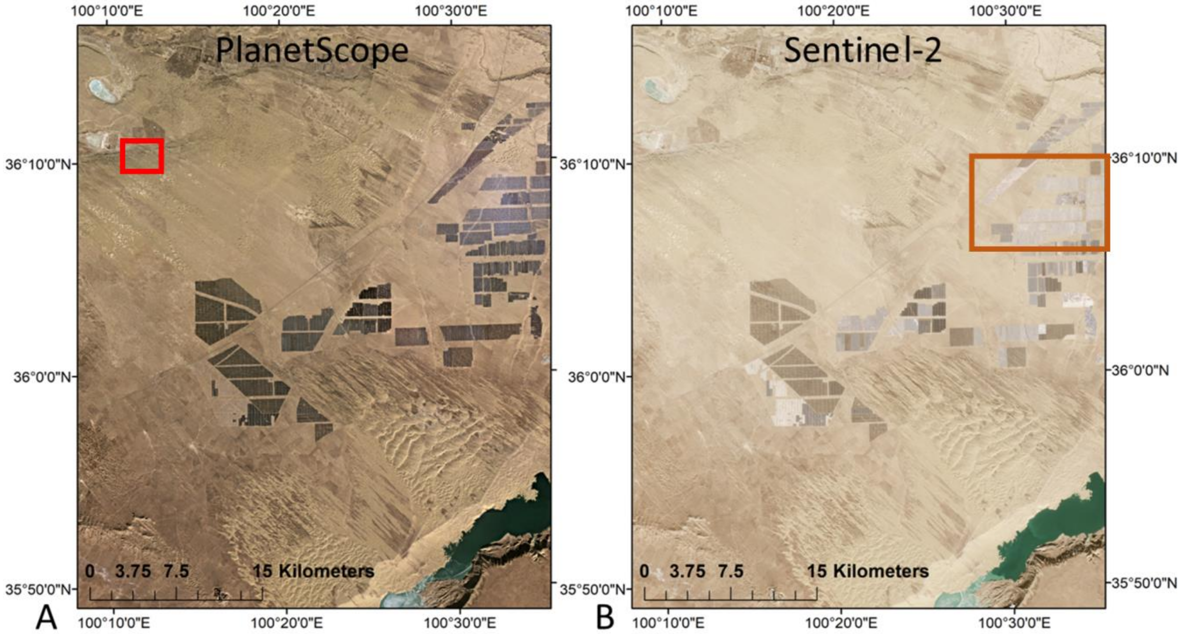

Figure 4.3 Example of Clear Sky image from PlanetScope (2023 January Monthly average Base map) and Sentinel-2 (2022 December 21st). The Red and Orange highlighted area is the boundary of the example of Figure 4.4 and 4.6, respectively.

Multiple combinations of bands were examined for optimal identification of DPS (e.g., Figure 4.4). Initial results from the CSD analyses suggest that for Sentinel 2, the most effective products were: (i) for the single-band mode, band 4, and (ii) for the multi-band mode, the CSD FCC worked even better. For PlanetScope, the results were as follows: (i) for the single-band mode, band 1, and (ii) for the multi-band mode, the TCC worked equally well. Figure 4.4 provides examples of CSD TCC for PlanetScope and three types of Sentinel-2 CSD images: (i) TCC, (ii) single band-4 CSD, and the 20 m CSD FCC for the same area. Generally, the advantage of multiband is more straightforward to locate DPS using the HR-LEO data. Thus, the muti-band composite CSD approach was chosen and utilised to pinpoint the origin of the plume, specifically, applied CSD FCC approach on Sentinel-2 and CSD TCC approach on Planet and Landsat-8 for the 14 frontal cases during 2019-2023.

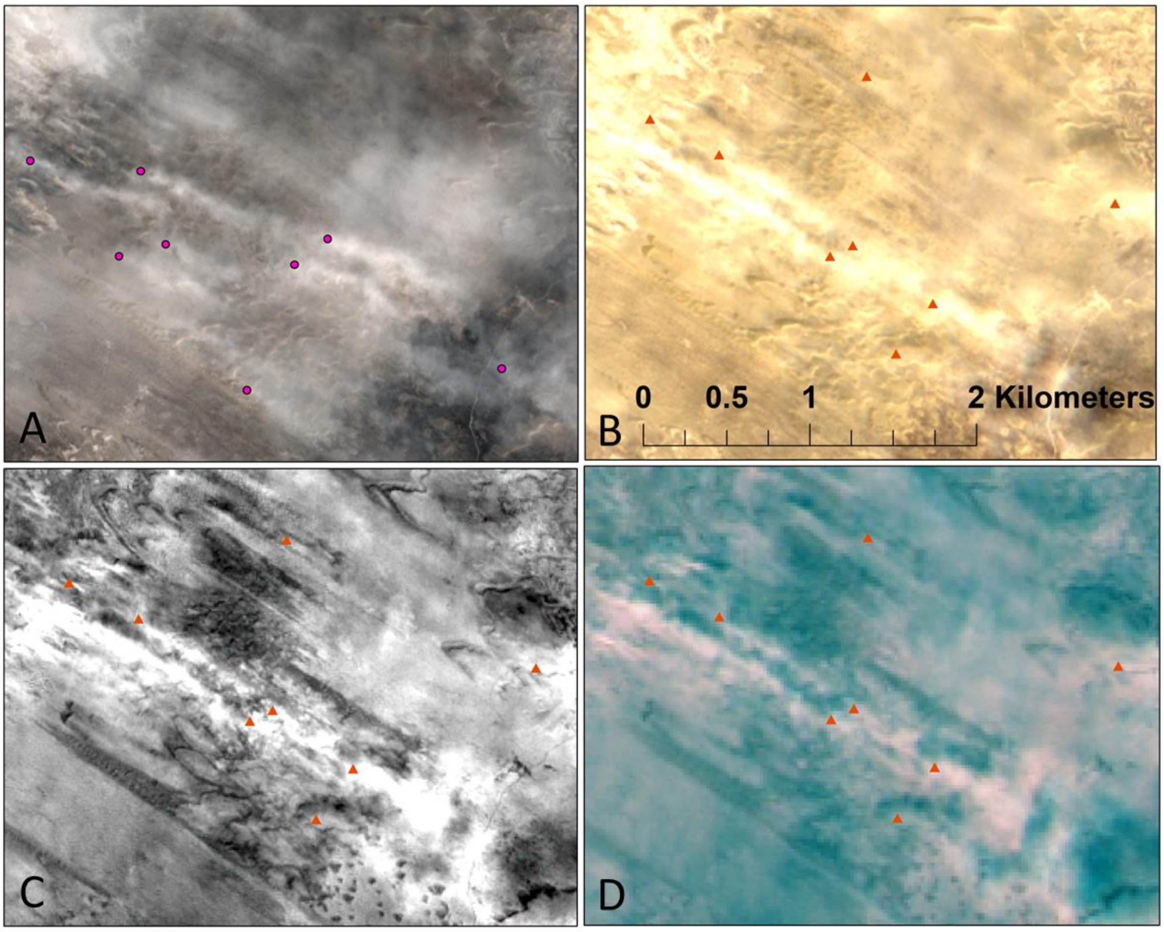

Figure 4.4 Example results for the different image enhancement methods for a small sub-scene (the relative location of this area is with a Red boundary in Figure 4.3) in the Gonghe Basin on November 17th, 2019 [one of the dust case lists in Table 4.1]. A) PlanetScope TCC; B) Sentinel-2 TCC; C) Single Band-4 CSD image from Sentinel-2; D) CSD-based FCC image from Sentinel-2 (pink= dust). The wind direction is from the W/WNW, allowing the dust pathway to be observable in the imagery and traced upwind to the NW edge of the dust plumes. The Dust Source Point (DPS) represents a detected source of emission. Round and triangular dots indicate dust sources independently detected in PlanetScope and Sentinel-2.

4.2.2.2 Applying the dust plume detection approach

A combination of Sentinel-2 (revisit period 5 days) and PlanetScope (revisit period = daily to sub-daily) were used to explore the dust point source location within the Gonghe Basin. The complete PlanetScope constellation of about 120 satellites can image approximately 60-100% of the Gonghe Basin daily, with considerable variability in basin coverage between days. Each image has a swath width of 24.6 km x 16.4 km (Planet, 2017), which means the satellite coverage varies on different days. Figure 4.5 presents these data - PlanetScope (3m resolution

Fig 4.5 A) and Sentinel-2 (10 m resolution Fig 4.5 B) True Colour Images for 17th Nov 2019 covering the Gonghe Basin. The two images both depict a SDS, but the basin coverage of the two sensors is different. Ultimately, the image enhancement scheme was applied to HR-LEO data sets to detect dust plumes.

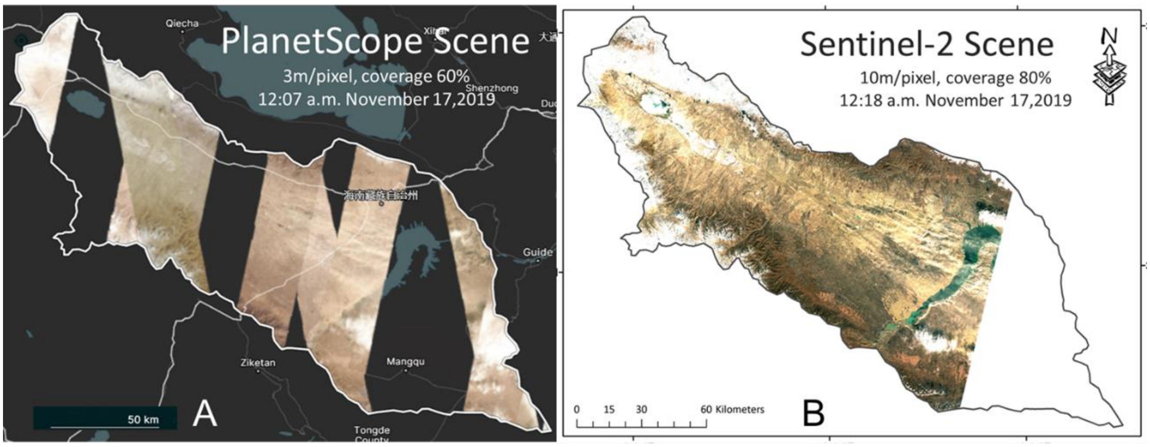

Figure 4.5 Example of Image Coverage Difference in A) PlanetScope; B) Sentinel-2 Scene for Gonghe Basin, on November 17th, 2019. Details of this SDS include the time of day, data availability (in Table 4.1), sensor's spatial and temporal resolution, overpass time (in Table 4.2), and image coverage (Table 4.4).

Although the image enhancement scheme worked well, the manual interpretation of the location of the up-wind edge of a dust plume remained subjective. As a result, a quality control (QC) flag was devised and included in the workflow to provide information regarding the relative reliability of DPS locations. For three HR-LEO Datasets, the quality tag had three levels: (i) level-1=High confidence; (ii) level-2=Medium confidence; and (iii) level-3 = Low confidence (e.g., Figure 4.6). To increase the accuracy of subjective positioning sources, for the same SDS case, DPS was independently pinpoint three times. If the plumes were found and help to trace back to the same DPS each time, labelled as QC1 which represents the dust plume that appears clear and straightforward to track to its origin source point, with a high level of confidence in accurately locating the DPS. If there was any deviation in position or inconsistency in quantity during the three instances of DPS positioning, then the point was labelled as Q2 or Q3 depending on the degree of difference. QC2 and QC3 points may have been caused by a mixture of dust plume with surface landform or transport dust plume or cloud; when tracked back to their origin DSP, the level of confidence in accuracy is considered medium to low. The number of QC1 account for about 92% of total DPS, and 6.5% of DPS were classified as QC2 and 1.5% of DPS as QC3.

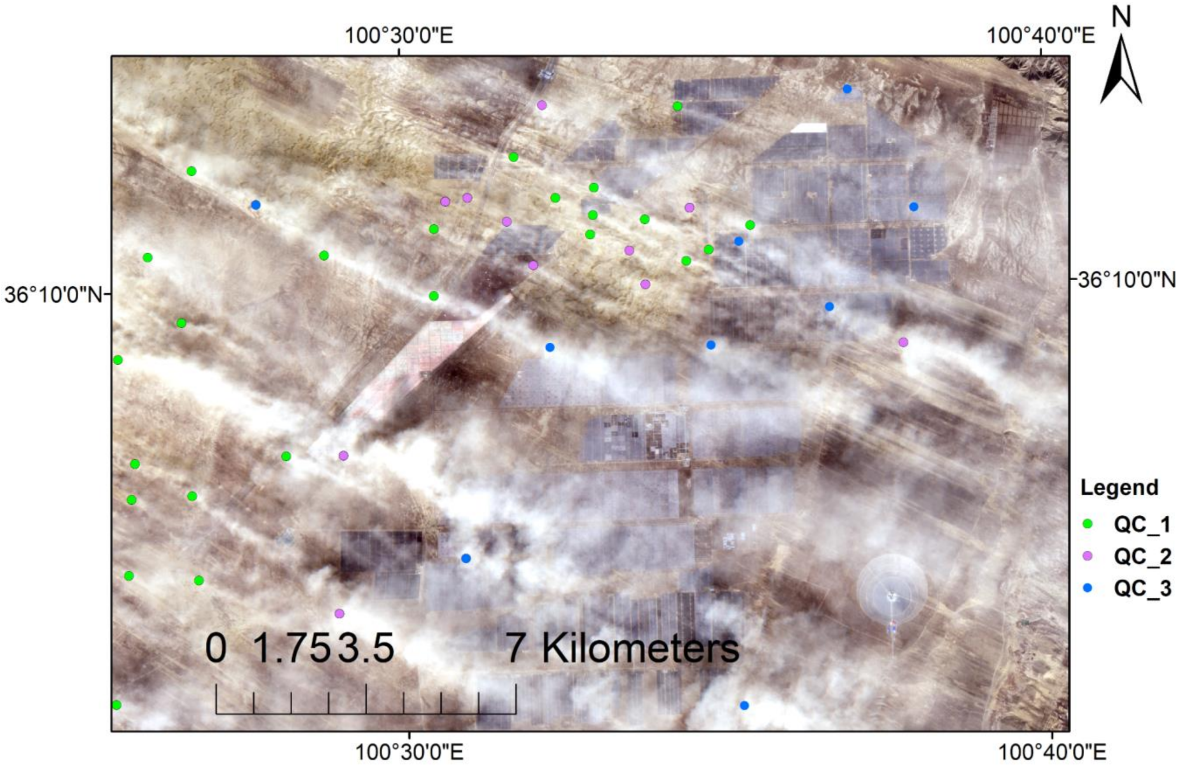

Figure 4.6 Example of three levels quality tag of DSP from Sentinel-2 in the Gonghe Basin on November 17th, 2019. The relative location of this area is highlighted with an orange boundary in Figure 4.3. The QC 1 represents the dust plume that looks clear and straightforward to track to the origin source point, with high confidence of accurately located DPS. The QC 2 and QC 3 display the dust plume mixed with landform or transport dust plume or cloud; when tracked back to the origin of DSP, the confidence of accuracy level is medium, and Low.

4.2.3 The preferential dust source scheme (PDS) and LULC

The Gonghe Basin surface landscape was characterised to appropriate geomorphological (PDS) and land-use schemes via mapping using ArcGIS software allied to published research (Bullard et al., 2011; Baddock et al., 2016; Baddock et al., 2021; Lee et al., 2012; Bakker et al., 2019; Ahmadi-Molaverdi et al., 2022; Von Holdt et al., 2019; Cui et al., 2019) and other available data (Table 4.2).

4.2.3.1 Generating a Preferential Dust Source (PDS) geomorphological scheme

The preferential dust source (PDS) scheme developed by Bullard et al. (2011), is a conceptual geomorphic scheme designed to represent the dynamics of natural dust sources and enables large-scale mapping of geomorphology in terms of key generic dust emitting surfaces. The location and extent of these surfaces were defined using satellite remote sensing, direct interpretation of high-resolution Planet Basemap images, and 30-metre elevation DEM, used to distinguish between high and low undulating terrain and the degree of erosion in alluvial systems. Soil maps provide particle size and texture, and desert maps show desert shifting/fixed status (Table 4.2).

Regarding workflow, existing geomorphological maps and desert maps were used to derive initial landform polygons (the dataset was provided by the National Tibetan Plateau Data Centre (http://data.-tpdc.ac.cn). After this, a wide range of other relevant surface conditions and parameter data were added. These include a range of factors that are known to be essential controls on SDS: (i) soil properties (e.g., surface moisture, grain size distribution, and ice cover situation); (ii) lake status (e.g., Permanent or Ephemeral Lake); (iii) aeolian surface classification, (e.g., shifting or fixed sand sheet/dunes;), and (iv) alluvial system, elevation, and vegetation coverage. Subsequently, multitemporal Planet Basemap (Image ©2023 Planet Labs PBC) was used to update the maps to include any observed landform unit. Finally, once all the above information was collated, the PDS scheme was applied to classify each polygon into the most likely category in the Gonghe Basin.

4.2.3.2 Generating a Land-use/cover [LULC] Scheme

In addition to PDS, the LULC was also mapped based on Copernicus Global Land Service (Buchorn et al., 2020), providing bio-geophysical products of the global land surface (https://land.copernic-us.vgt.vito.b-e/PDF/portal/Application.html#Home). These land cover data include 5 vegetation types, wetlands, and a range of associated data with a base 100-metre resolution. Considering human impacts on SDS in the Gonghe Basin, the urban areas, agricultural land, and solar power plants have been included. The Planet Basemap and Google Earth were employed to digitise and modify the feature polygon ranges manually.

4.2.4 Dust Point Source (DPS) Properties

4.2.4.1 Extracting landform signatures for identified dust sources

To identify the sub-basin scale dust source signature, a geospatial link was provided between dust source points and: (i) the PDS geomorphological scheme and (ii) the LULC classification map. To account for the spatial resolution differences between Planet, Sentinel-2, and Landsat-8, the 10-metre buffer was created for point sources determined by three High-resolution satellites, respectively. We used the 10-metre buffer as an Active Dust Source (ADS) to characterise its PDS and LULC signature. After calculating the area of each PDS and LULC unit in ArcGIS, dust sources identified from the Planet (841 points) and Sentinel-2 (589 points) from 2019 to 2023 were spatially joined on the maps, respectively. Also, their spatial distribution and frequency in each geomorphological class were determined. Finally, dust source emission ratios were calculated for each landform class.

4.2.4.2 Measuring Average AOD per DPS and Estimating Emitted Dust Mass per SDS

To determine the dust magnitude of the DPS and SDS event, the aerosol optical depth (AOD) was calculated for each of the DPS for the 14 SDS events during 2019-2023. The temporal resolution of MODIS was twice daily (Terra and Aqua), and the 14 SDS started between 2-4 UTM in the morning. The SDSs observed in this study spanned several hours, resulting in an average crossing time of 02:30 UTM for MODIS-Terra and 5:30 UTM for MODIS-Aqua covering 14 SDSs. Since most of the Gonghe is over bright desert surfaces, the MODIS Deep Blue (Tao et al. 2017) algorithm, a MODIS aerosol product, was used. MODIS Deep Blue, in turn, utilises measurements at blue wavelengths (412 nm and 470 nm) to analyse aerosols on bright reflective surfaces such as deserts. To compensate for the omission of temporal resolution, we simultaneously extracted the AOD of the DPS using Himawari-8 AOT 500 nm 10 min data, extracting the AOT maximum for each pixel at 0300-0500 UTM. Due to the difference in spatial resolution between the DPS data and AOD data, and to facilitate the calculation of dust mass, a 10-metre buffer was created for the DPS, and its AOD was extracted from MODIS and Himawari-8, respectively. Once the AOD of each DPS is extracted, the DPSs can be grouped by PDS landforms to estimate the total dust mass for each PDS category.

The dust column concentration equation proposed by Kaufman et al. (2005) was applied to all SDSs in this study. The dust mass was determined by examining the relationship between the DPS area and the mean aerosol optical depth (AOD) at a wavelength of 550 µm. In this equation, Mdu represents the dust mass, A represents the area of the DPS, and τdu represents the mean AOD at 550 µm. Ansmann et al. (2012) recently developed an updated version of the Kaufman equation (coefficient of 2.7), which incorporates an extinction efficiency of 0.57 and yields a coefficient of 1.75. Bakker et al. (2019) further demonstrated the successful application of the Kaufman equation in calculating the dust mass range (coefficient of 1.75 for the lower limit, coefficient of 2.7 for the upper limit) over northern Africa. The equation was applied to Himawari-8 AOD data to estimate dust mass for the 14 SDS events (Eq1, Fig 4.7).

To determine the area of a DPS circle is pi times the radius squared ($A = \pi r^2$), 'r' represents 0.03 km DPS buffer area, so the source area for each SDS equal to the number of dust times the area of a DPS circle. An average of the AOD for each event was then multiplied by the area of its dust sources and summed to obtain the total mass of material for each SDS ($A = \pi r^2 = \pi$* number of DPS* 0.03^2).

$$\mathrm{M}_{du} = 1.75 A \tau_{du}$$

[Eq.1]

Figure 4.7 *Calculating dust mass based on AOD and area (Bakker., et al. 2019, reproduced from Eq 3)*

4.2.5 Tracking DPS Transport Trajectories using Hysplit

The Hybrid Single-Particle Lagrangian Integrated Trajectory (HYSPLIT) model was developed by the US's National Oceanic and Atmospheric Administration (NOAA) Air Resources Laboratory and can be easily accessed and run through an interactive website. According to Baddock et al. (2017), HYSPLIT utilises the given Dust Source Location, altitude, and SDS start time to determine the trajectory of an air parcel, taking into account three-dimensional winds in hourly intervals for a specified period. The meteorological input driving the HYSPLIT simulations is the Global Data Assimilation System (GDAS) Archive, which 4 times per day with

1° spatial resolution to interpolate data from a variety of observing systems and instruments onto a three-dimensional grid (NOAA, 2023).

In this study, the HYSPLIT archive forward trajectory model was employed to analyse the air trajectories of dust sources from 14 dust cases in Gonghe. For each SDS case, three DPS points were selected to represent the most typical PDS dust sources as the starting points for the trajectories (e.g., Figure 4.8). The start time was consistently set to 00.00 UTC on every SDS day, and the SDS trajectories were tracked for 24 hours. While it was observed that dust from this regional area (North of the Tibetan Plateau) could be transported to Japan within 120 hours and to the Arctic within 168 hours (Wei et al., 2021), it should be noted that the accuracy of HYSPLIT trajectories diminishes as the time scale increases (Draxler et al., 2020). Conversely, shorter time scales enhance the confidence in the accuracy of the simulated trajectories. The starting height for the trajectories was set at 0 metres to model the transport of dust emitted from the surfaces of the Gonghe Basin. To observe seasonal pathway variation, a spatial analysis of the trajectory points generated by the HYSPLIT model was conducted using ArcGIS. The trajectory model generates hourly trajectory points in space, and when point connections are possible, the trajectory is treated as a continuous line. The frequency of trajectory occurrence is expressed as a percentage of the line crossing a 0.1 × 0.1° fishnet cell.

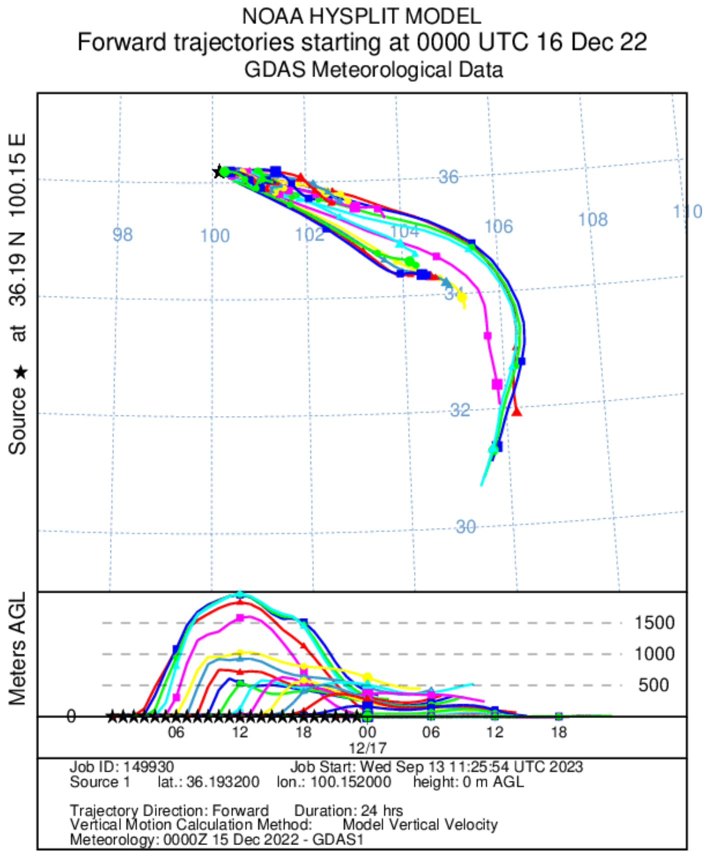

Figure 4.8 *Example of Hysplit Forward Trajectory in the Gonghe Basin on January 23rd, 2023 [one of the dust case lists in Table 4.1].* 52

4.3 Results

4.3.1 LEO Image Cadence and Basin Coverage

Within 14 Case Events, the total number of DPS mapped from Planet, Sentinel-2, and Landsat are 841, 589, and 44, respectively (Table 4.4). As Landsat is only available in 2 cases with only 33% basin coverage, it was deemed not compatible with other sensors, and therefore is reported here, but not used in subsequent r analysis. The Planet data, by comparison, has a relatively higher average basin coverage per event (82%), and this exceeds that of Sentinel-2 (76%).

Table 4.4 RS satellite converges rate and number of DPS detected for each of 14 case events by Planet, Sentinel-2, and Landsat-8 during 2019-2023.

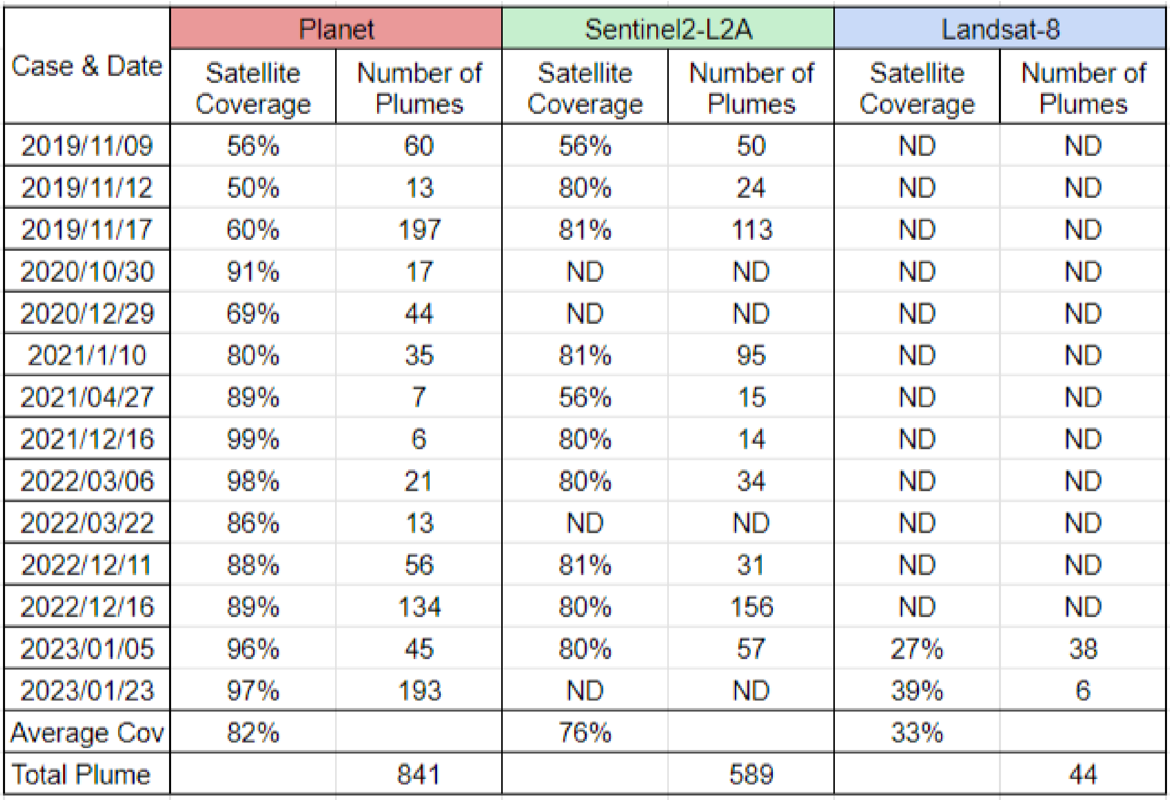

Case & Date	Planet		Sentinel2-L2A		Landsat-8	
	Satellite Coverage	Number of Plumes	Satellite Coverage	Number of Plumes	Satellite Coverage	Number of Plumes
2019/11/09	56%	60	56%	50	ND	ND
2019/11/12	50%	13	80%	24	ND	ND
2019/11/17	60%	197	81%	113	ND	ND
2020/10/30	91%	17	ND	ND	ND	ND
2020/12/29	69%	44	ND	ND	ND	ND
2021/1/10	80%	35	81%	95	ND	ND
2021/04/27	89%	7	56%	15	ND	ND
2021/12/16	99%	6	80%	14	ND	ND
2022/03/06	98%	21	80%	34	ND	ND
2022/03/22	86%	13	ND	ND	ND	ND
2022/12/11	88%	56	81%	31	ND	ND
2022/12/16	89%	134	80%	156	ND	ND
2023/01/05	96%	45	80%	57	27%	38
2023/01/23	97%	193	ND	ND	39%	6
Average Cov	82%		76%		33%	
Total Plume		841		589		44

- **DPS Maps at the Sub-Basin Scale: Planet/Sentinel/Landsat**

The manually extracted 14 case events of DPS data [Level 1 QC] from all three sensors within the Gonghe Basin are presented in Figure 4.9. Dust Source is widely distributed in the centre of Gonghe, and the locations of different sensor distributions are overall similar. Planet-derived points are located more upwind than Sentinel-derived points given dominantly westerly flow. The Landsat-identified points are more clustered because imagery only covers part of the area.

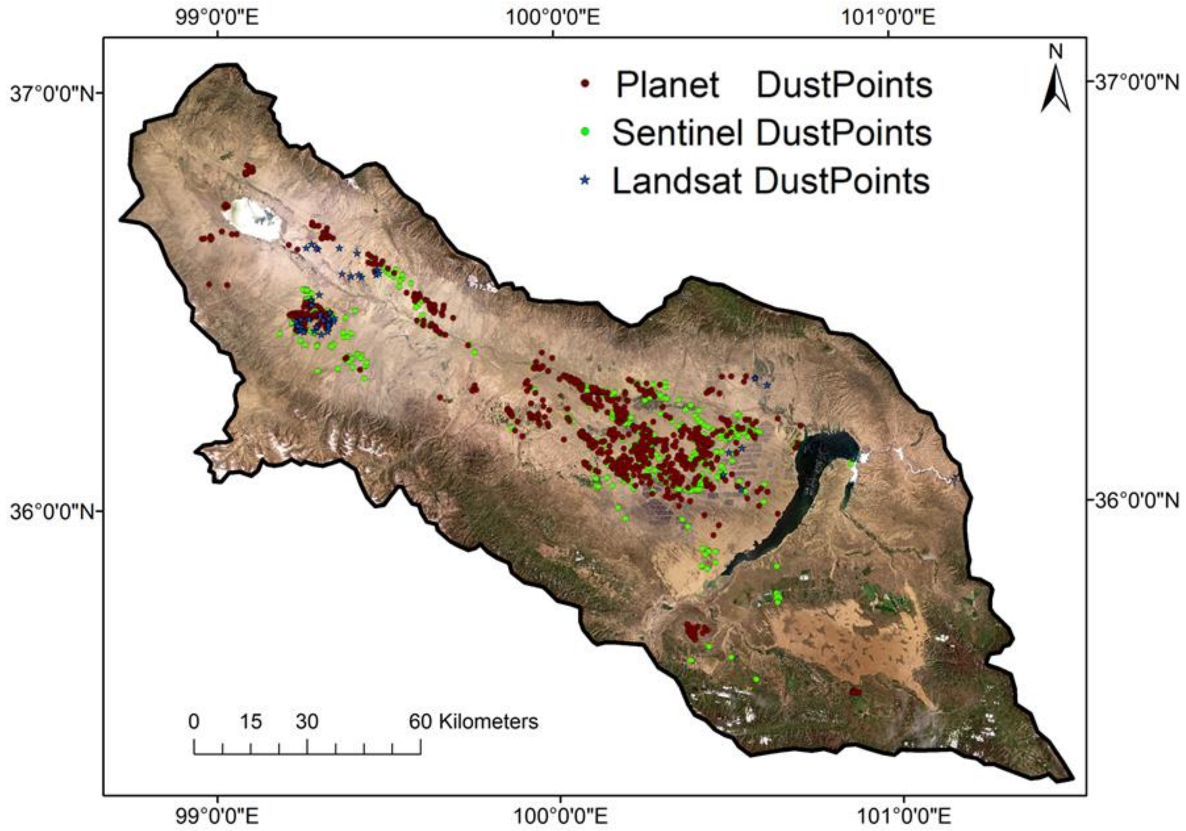

Figure 4.9 The DSP [QC1 only] distribution of 14 case events during 2019-2023. The red point represents dust points detected from the Planet, green points from Sentinel, and blue stars from Landsat. Basemap derived from Planet monthly basemap June 2023, the Gonghe Basin, China.

4.3.2 A PDS and LULC Surface Classification Scheme for the Gonge Basin

Gonghe has 8 of the 17 geomorphology classes identified by Bullard et al. (2011) (Fig 4.10). The three 'Low' emission surfaces determined according to the PDS scheme are located in the southeast of Gongh (accounting for 17% of the total area), including (1a) wet lake, (4) rocks, and (3c) alluvial deposits. High and Low-relief alluvial systems are usually adjacent, mainly distributed in Gonghe's northeast and southwest regions. There are two high-importance emission surfaces, including (1b) Ephemeral Lake occupied a relatively small area (2%) and aeolian dune (5b, 25%), e.g., Parabolic dune. Alluvial systems (2c, 3c, 3d) cover about 58% of the study area, including mountain sides, alluvial plains, and saline and alkaline landscapes. Aeolian sand systems covered 28% of the area of the GH, including sand sheets fixed by vegetation and shifting dunes.

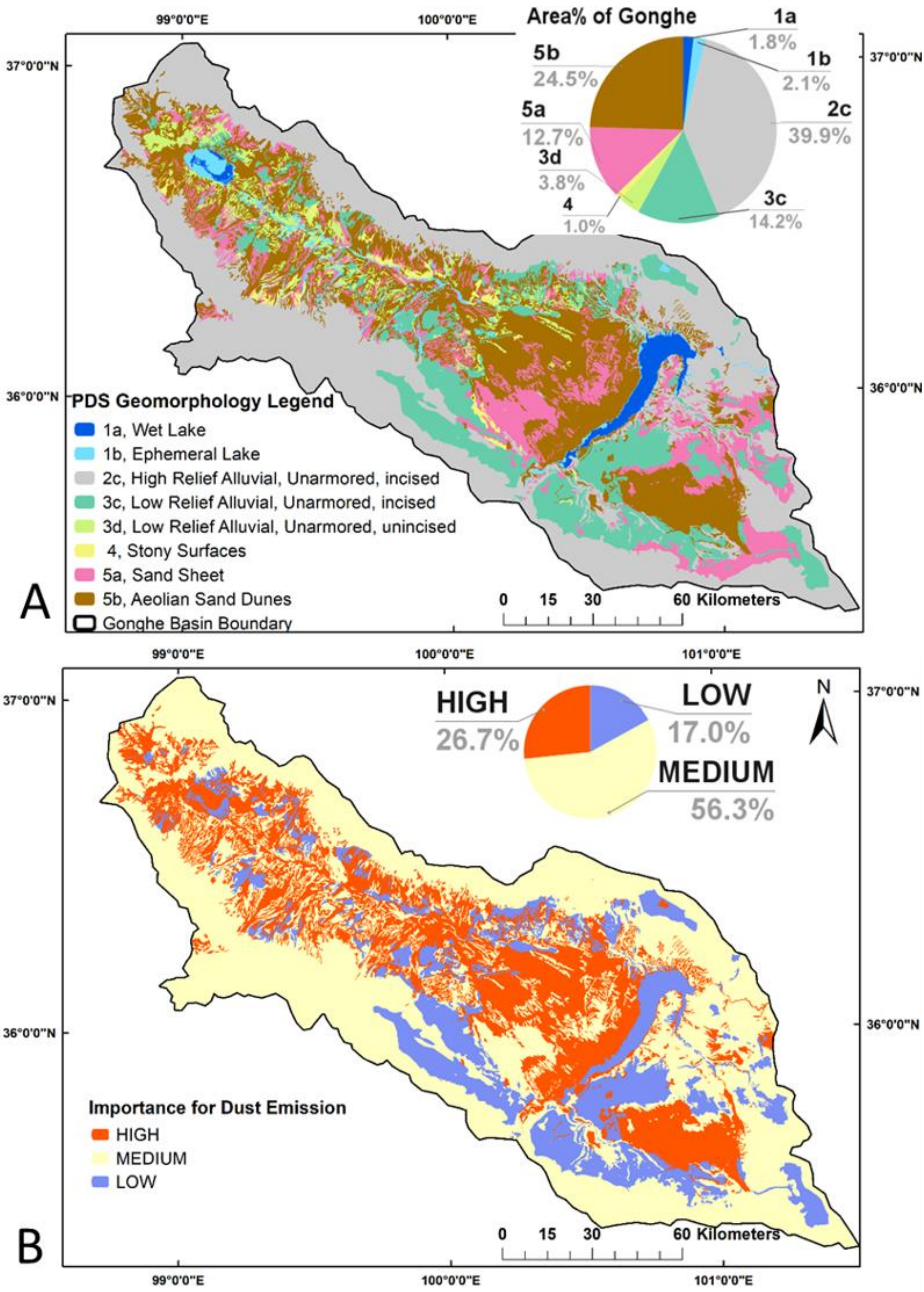

Figure 4.10 (A) Gonghe Basin distribution of surface PDS (Preferential Dust Source) geomorphologies; (B) their relative importance for SDS (Sand and Dust Storms).

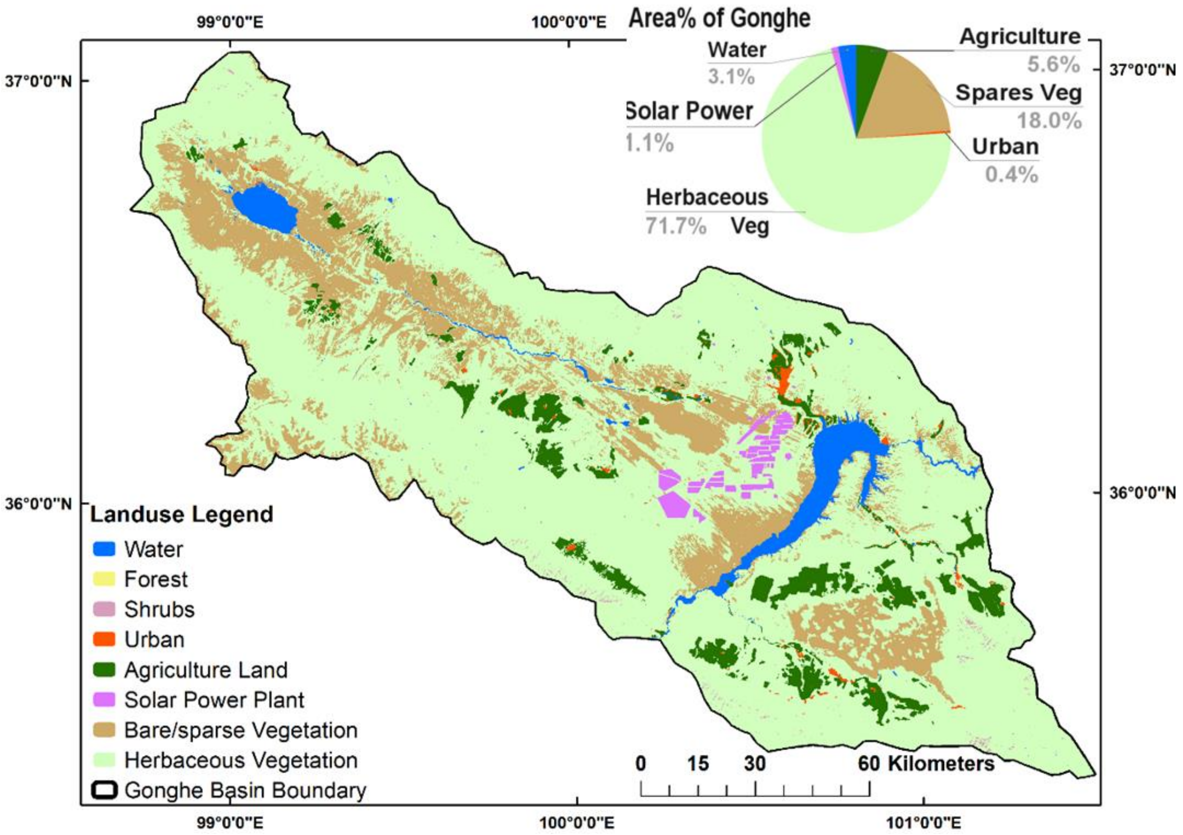

Figure 4.11 Gonghe Basin distribution of surface LULC (Land Use and Land Cover).

Gonghe is located in semi-arid areas, with herbaceous vegetation (72%) being the main land cover, and together with bare/sparse vegetation (18%) distributed in the central area of the Basin, it constitutes 90% of the Gonghe area (Fig 4.11). The water area is 3.11%, with Forests and Shrubs accounting for the most minor proportion. Human activities affect areas including 0.44% urban areas, 5.57% arable land, and 1.06% solar power stations.

4.3.3 Dust Points Sources and their PDS/LULC signature

4.3.3.1 Overview of the 14 case studies

The distribution of dust sources on the surfaces of different landforms shows (Table 4.5, and Figure 4.12) that although Sand Dune (5b) is only a quarter of the study area, 5b contribute 63.3% of the DPS identifying by [Planet] & 69.4% by [Sentinel]. In contrast, only 0.4% of the

DPS [Planet] and 1.2% [Sentinel] originated from High relief alluvial (2c), and no dust emitted from Wet Lake (1a). 1a and 2c, two PDS low emission category surfaces covering nearly half (42%) of the GH. It should be noted that in alluvial systems, category 3c has the highest proportion of SDS 17.5% [Planet] & 8.1% [Sentinel], while the stone desert system (4) has very few dust points (1.2%-2%) with its small area.

Table 4.5 Surface area covered by PDS and LULC defined category and its area (km^2) and the proportion of the Gonghe area. The frequency (%) of DPSs detected by Planet and Sentinel-2 is observed from those surfaces.

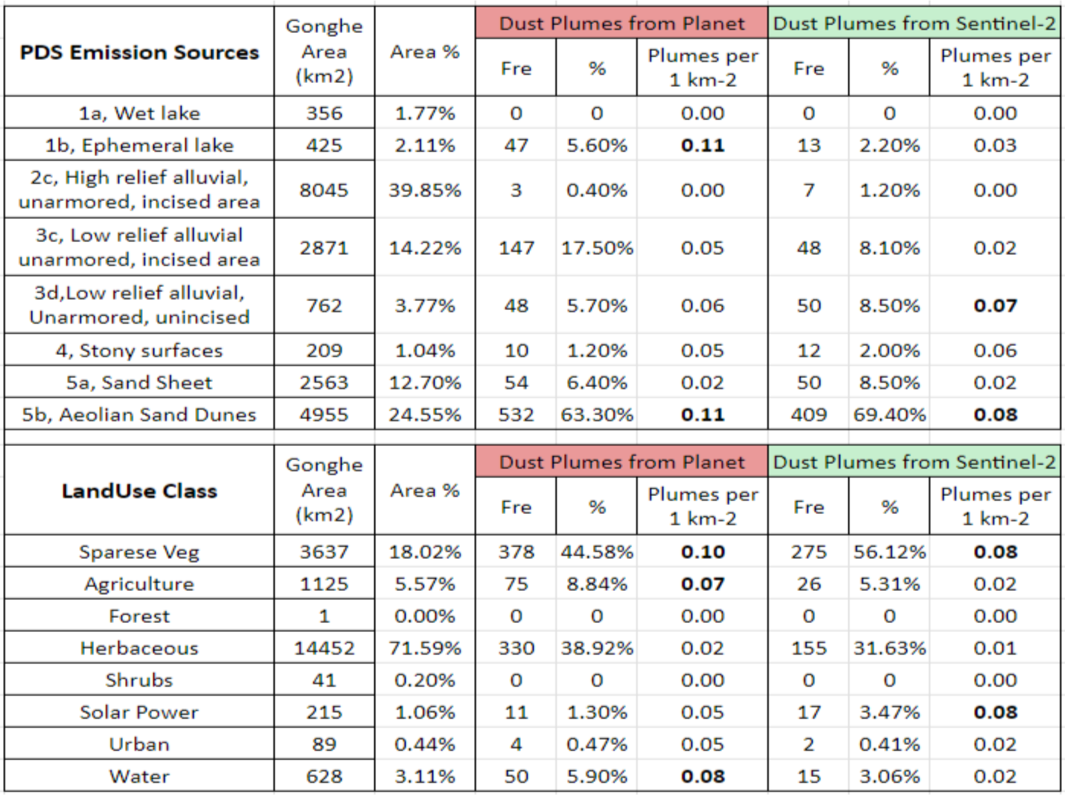

PDS Emission Sources	Gonghe Area (km2)	Area %	Dust Plumes from Planet			Dust Plumes from Sentinel-2		
			Fre	%	Plumes per 1 km-2	Fre	%	Plumes per 1 km-2
1a, Wet lake	356	1.77%	0	0	0.00	0	0	0.00
1b, Ephemeral lake	425	2.11%	47	5.60%	**0.11**	13	2.20%	0.03
2c, High relief alluvial, unarmored, incised area	8045	39.85%	3	0.40%	0.00	7	1.20%	0.00
3c, Low relief alluvial unarmored, incised area	2871	14.22%	147	17.50%	0.05	48	8.10%	0.02
3d,Low relief alluvial, Unarmored, unincised	762	3.77%	48	5.70%	0.06	50	8.50%	**0.07**
4, Stony surfaces	209	1.04%	10	1.20%	0.05	12	2.00%	0.06
5a, Sand Sheet	2563	12.70%	54	6.40%	0.02	50	8.50%	0.02
5b, Aeolian Sand Dunes	4955	24.55%	532	63.30%	**0.11**	409	69.40%	**0.08**

LandUse Class	Gonghe Area (km2)	Area %	Dust Plumes from Planet			Dust Plumes from Sentinel-2		
			Fre	%	Plumes per 1 km-2	Fre	%	Plumes per 1 km-2
Sparese Veg	3637	18.02%	378	44.58%	**0.10**	275	56.12%	**0.08**
Agriculture	1125	5.57%	75	8.84%	**0.07**	26	5.31%	0.02
Forest	1	0.00%	0	0	0.00	0	0	0.00
Herbaceous	14452	71.59%	330	38.92%	0.02	155	31.63%	0.01
Shrubs	41	0.20%	0	0	0.00	0	0	0.00
Solar Power	215	1.06%	11	1.30%	0.05	17	3.47%	**0.08**
Urban	89	0.44%	4	0.47%	0.05	2	0.41%	0.02
Water	628	3.11%	50	5.90%	**0.08**	15	3.06%	0.02

To evaluate the importance of PDS class on emission, we have calculated the number of DPS per km^2 from each geomorphic class in the Gonghe. The number of DPS per km^2 is the highest for ephemeral lakes (1b, 0.11) and sand dunes (5b, 0.11), which cover less than 27% of the area and account for about 70% of the DPSs. Followed by classes 3d (0.06), 3c (0.05). Although the number of DPS per km^2 of class 3c is lower than that of class 3d, the number of DPS in class 3c is much higher than that of classes 3d and 5a [Planet], and the high coverage area of 3c averages the rate value. The number of DPS per km^2 is less than 0.02 for PDS type 2c, and 5a, indicating that they emit much less relative to their area.

The distribution of identified dust sources indicates that most DPSs originate from a specific location susceptible to SDS. The distribution of dust sources across land use classes showed that 45% of dust points observed by [Planet] and 56% by [Sentinel] from bare/sparse vegetation areas, and 39% of dust points [Planet] and 32% [Sentinel] contributed by herbaceous. Agricultural land contributes 9% [Planet] and 5.3% [Sentinel] of the dust source, and urban and solar power contribute 2-4%. Bare/sparse had a higher frequency of dust sources than other land covers, followed by herbaceous and agricultural, respectively. Regarding the number of DPS per km^2, Planet identifies bare/sparse vegetation >water >agriculture; Sentinel identifies Solar power >Sparse area has most SDS.

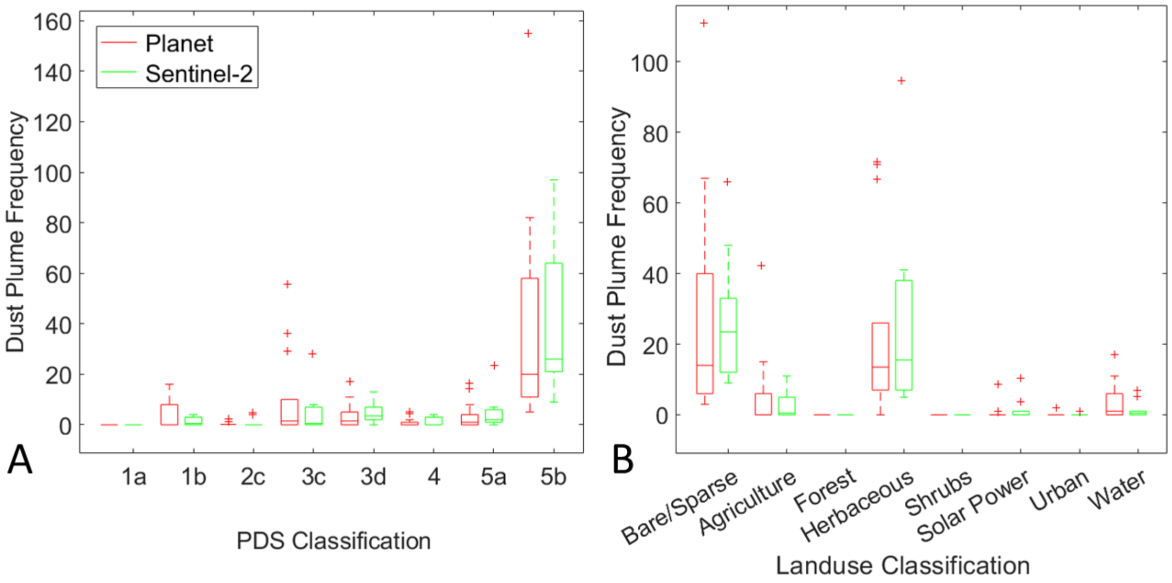

Figure 4.12 Comparison of DPS (Dust Point Source) signatures derived from Planet (Red) and Sentinel-2 (Green) from 14 cases selected during 2019-2023. The apparent dust signature for (A)PDS (Preferential Dust Source) Geomorphology and (B) LULC (Land Use and Land Cover) are presented.

4.3.3.2 DPS Seasonality for specific PDS Classes

Only 14 frontal SDSs cases were identified from PlanetScope imagery, indicating a limited dataset. It is acknowledged that the data may be skewed, thereby potentially stretching the validity of seasonal assertions derived from the DPS. Nonetheless, Figure 4.15 provides insights into the interplay between the spatial distribution of dust sources, geomorphological characteristics, and seasonal variations within the Gonghe Basin.

Sand Dune (5b) contribute the highest dust emission frequency in the three seasons in PDS scheme and is especially active in autumn cases (Fig 4.13). Comparing spring and autumn, In Winter, the alluvial system (3c, 3d) becomes vital for SDS, which matches the LULC scheme as an agricultural land activation in winter [DJF]. Ephemeral Lake (1b) is sensitive in autumn and winter.

Seasonal changes in PDS emission categories are also reflected in spatial changes (Fig 4.14). Winter has a slightly different spatial distribution pattern than other dust seasons. The northwest of the basin area is mainly active in winter, and the middle of the basin area is active in 3 seasons. Dust sources are not uniformly distributed throughout the basin, but most of the dust sources come from these two important areas of the Gonghe, which have more 1b, 3c, and 5b [PDS] than other areas, and are also areas of LULC influenced by human activity (Fig 4.13 F). These landforms are considered to be the most important SDS source types. The northwest area has more diverse dust sources, including Lake, Low-Relief (LR) alluvial, and aeolian dune, while a single dominant landform, the aeolian deposit, mainly influences the middle area of the basin. The most robust inter-seasonal variability of dust is observed in the northwest regions, where the dust distribution is more susceptible to dust particle availability.

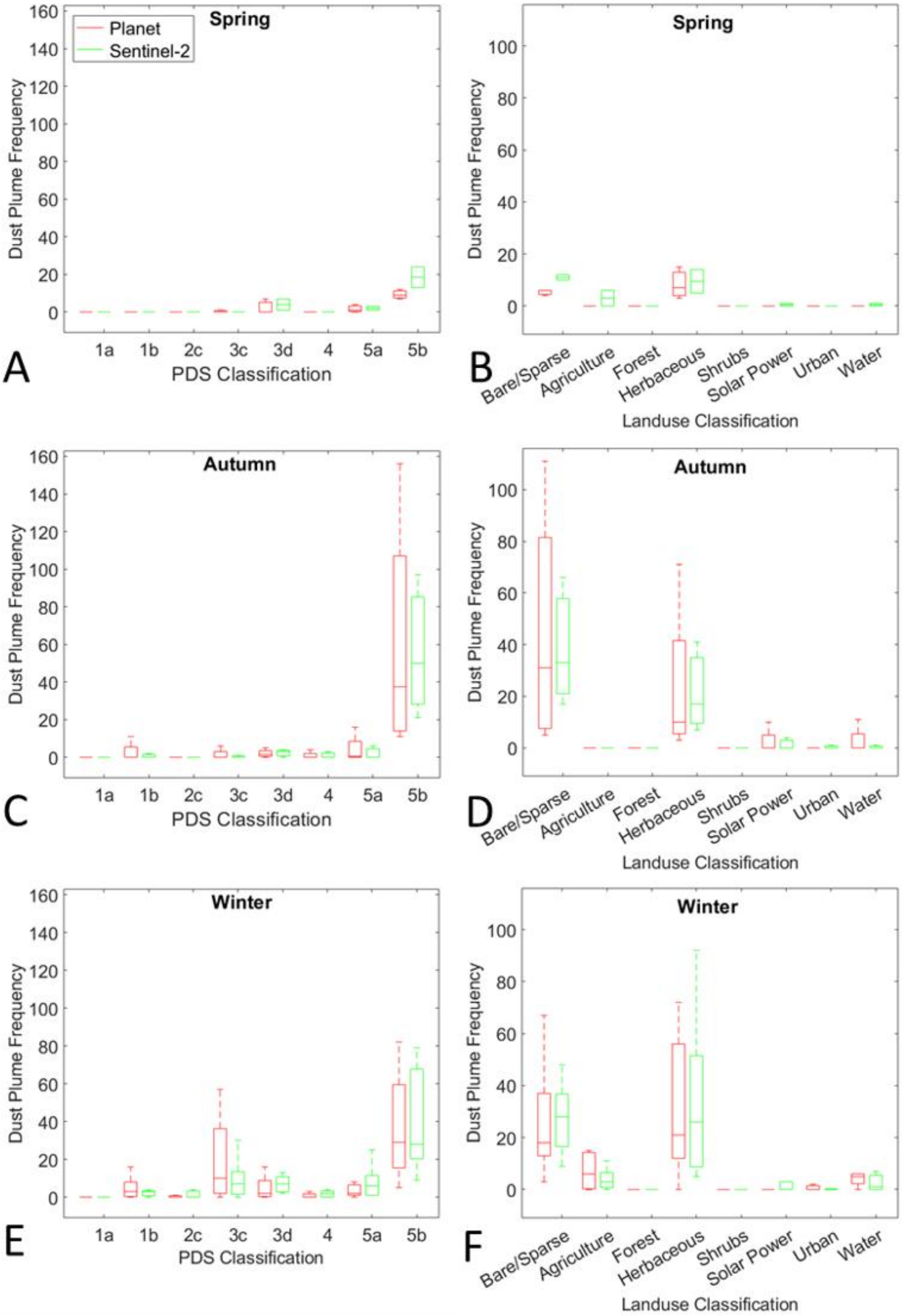

Figure 4.13 DPS frequency boxplot by PDS (Preferential Dust Source) and LULC (Land Use and Land Cover) class in the Gonghe Basin (2019-2023) in spring, autumn, and winter.

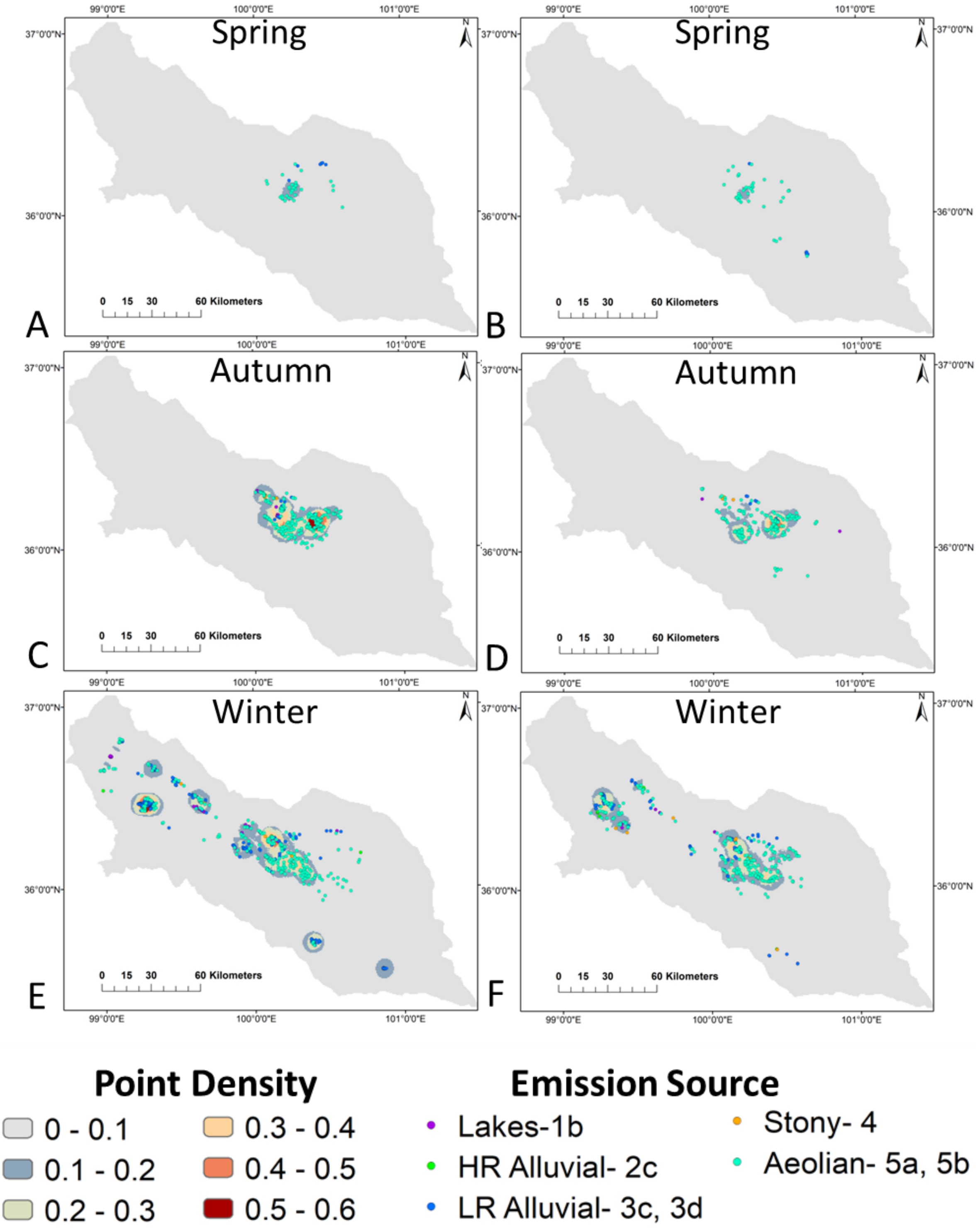

Figure 4.14 PDS (Preferential Dust Source) Geomorphology of the Gonghe dust sources of 14 cases during 2019-2023 in spring, autumn, and winter dust seasons from PlanetScope (Left) and Sentinel-2 (Right). Basemap is a 600m resolution point density map in that season. Coloured dots represent individual dust point sources, with the colour signifying the geomorphic category of the dust point source.

4.3.4 Dust Loadings for Specific PDS Categories

Overall, the Ephemeral Lake and aeolian sand surface (1b, 5a, and 5b) contribute to the top 3 high-intensity dust (high AOD values, Fig 4.15 D). Sentinel-derived dust points' AOD (Green Box) is higher than from Planet (Red Box). Winter is similar to the overall dust intensity distribution (Figure 4.15 C); In Autumn, dust emits from 5a, 5b, and 1b and has the highest AOD range from 0.5-2.5 (Figure 4.15 B), much higher than in another season. In Spring, plume clusters from the aeolian dust source and 5b intensity are the highest (Figure 4.15 A).

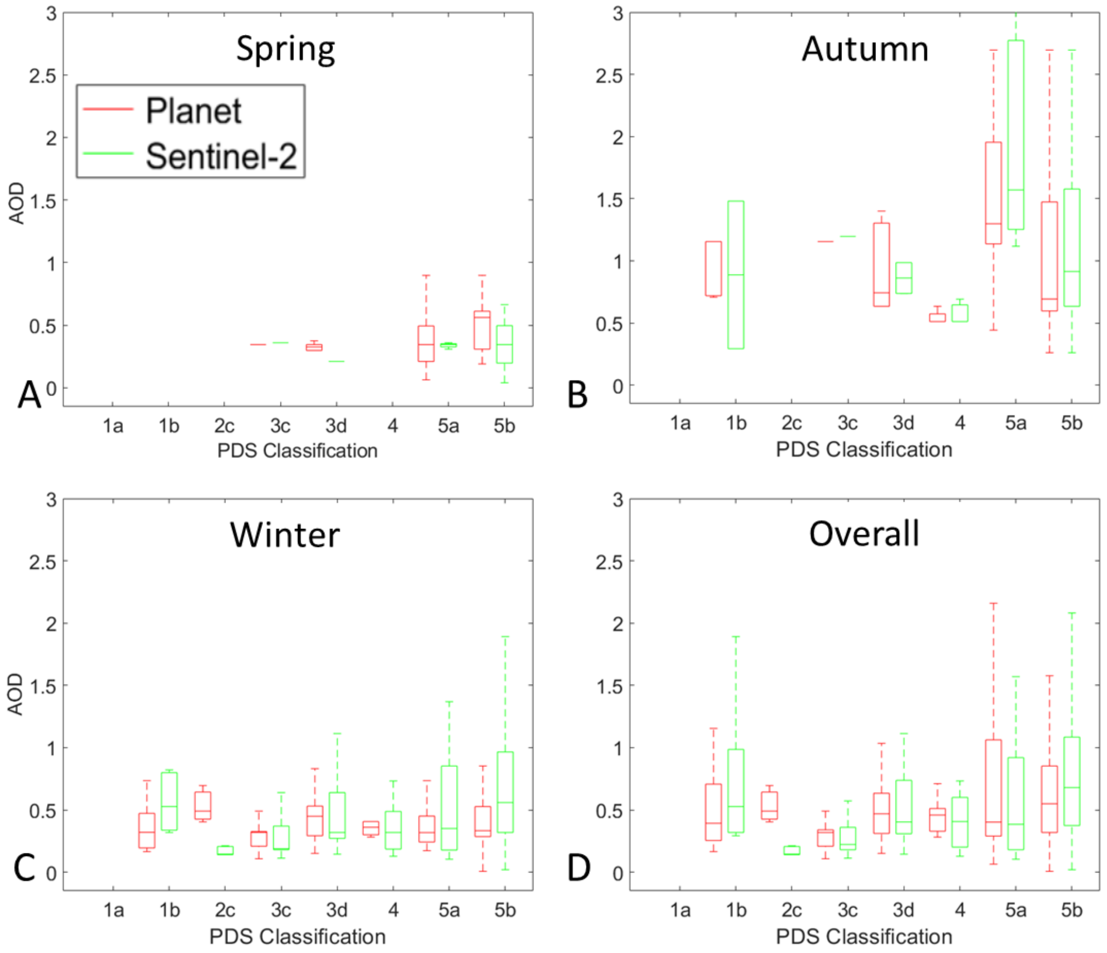

Figure 4.15 Planet and Sentinel detected DPS (Dust Point Source) corresponding to Himawari-8 derived AOD by PDS (Preferential Dust Source) class in the Gonghe Basin (2019-2023) in spring (A), autumn (B), winter (C), and Overall (D).

The number of DPS for each PDS category was then combined with its corresponding AOD value to derive the total amount of dust loading for each PDS category (Table 4.6). Dust from aeolian sources accounts for approximately 84.7% of the total dust mass, while low relief alluvial deposition accounts for 1.9%, Ephemeral Lake about 2.6%, and from other surfaces (stony, high relief alluvial) accounts for 0.8%.

For the fourteen case SDSs caused by pre/post frontal systems, the morning SDS start time (between 1-4 UTM), its DUP, AOD, and dust mass for each case are detailed in Table 4.6 below. The total dust mass for 14 SDSs is about 0.196-0.302 Tg, of which the four most prominent dust cases accounted for 42.3% (Table 4.6). In Autumn, 4 SDSs produced significantly dust mass (44.7%); 7 cases produced 35.3% of the total dust mass in winter; and 4 SDSs generated about 20% of total dust mass in spring.

Table 4.6 Daily DUP and means AOD from MODIS-Terra, MODIS-Aqua, Himawar-8 for each of 14 case events and its Dust mass. Teragram (Tg) = 1 × 10−12 grams (g).

Time	DUP (m3s3)	Number of DPS (Planet)	MODIS-Terra	MODIS-Aqua	Himwarai-8 AOT_mean	Dust Mass (Tg)
2019/11/09	841	60	ND	0.337	0.525	0.017 - 0.027
2019/11/12	1067	13	0.021	ND	0.831	0.006 - 0.009
2019/11/17	1543	197	0.512	0.259	0.669	0.072 - 0.112
2020/10/30	350	17	0.091	0.078	0.692	0.006 - 0.010
2020/12/29	1413	44	0.054	0.211	0.264	0.006 - 0.010
2021/1/10	1640	35	0.089	0.218	0.476	0.009 - 0.014
2021/04/27	1473	7	0.093	0.348	0.330	0.001 - 0.002
2021/12/16	106	6	0.090	0.101	0.236	0.0007 - 0.001
2022/03/06	1459	21	0.134	0.198	0.264	0.003 - 0.005
2022/03/22	1368	13	0.267	0.364	0.618	0.004 - 0.007
2022/12/11	880	56	0.323	0.249	0.392	0.012 - 0.019
2022/12/16	1496	134	0.113	0.176	0.341	0.025 - 0.039
2023/01/05	1175	45	0.066	0.182	0.184	0.005 -0.007
2023/01/23	1944	193	0.105	0.102	0.253	0.027 -0.041
Total		841				0.196 - 0.302

4.3.5 Transport Pathways

There are evident seasonal variations in the propagation height and distance of the dust transport path, while the direction remains consistent (Figure 4.16). The longest transmission distance of suspended dust particles occurs during winter, followed by spring and autumn. In autumn, the dust transport trajectory has a height below 1000 m (detail see Appendix M, N and O), resulting in a shorter travel distance. During spring, the dust transmission height reaches 2500 m, with a 24-hour transmission distance extending as far as ChongQing (about 1050 km). The transmission distance in winter is similar to that in spring, with a height ranging from 500 to 2000 m. Dust aerosol emission from Gonghe has the potential post-24h to impact on downwind cities, including Gansu, XiAn and Chongqing (See base map in Fig 4.16). The southeastern transportation route is evident during three seasons, with autumn [SON] being the most active period. Despite the relatively low transportation distance and height during autumn [SON], these are the days with the highest dust mass value (Table 4.6). In spring and winter, the range of dust pathways from the Gonghe is similar. However, the dust pathway in winter is more dispersed across different SDS cases (Appendix O), resulting in a lower frequency of trajectory lines in winter.

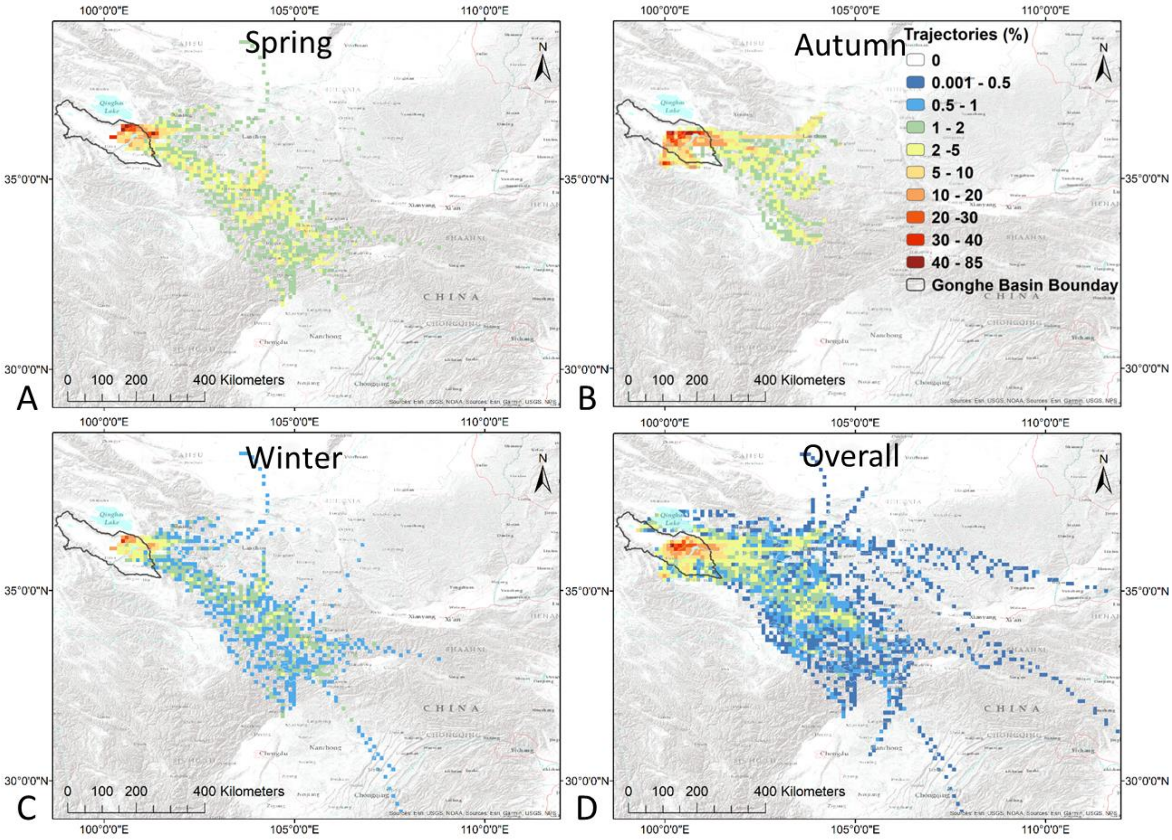

Figure 4.16 Trajectory line density (% of trajectories per 0.1° × 0.1° cell) for 24 h simulations run at a 0 m start height from Gonghe Basin for 14 DSD 2019-2023 in spring (A) Spring [MAM]; (B) Autumn [SON]; (C) Winter [DJF]; and (D) Overall. See Fig. 4.14 for trajectory HR-LEO detected DPS start points.

4.4 Discussion

4.4.1 SDS and Dust Sources Evaluation using RS data

Here, we evaluated a combined dataset of LEO and GEO Remote Sensing data for SDS detection and the mapping of identifying Dust Point Source (DPS). Himawari-8 10-minute data were able to provide SDS detection for daytime in the Gonghe Basin. Planet and Sentinel-2 observe the SDS only in the morning [02.00 - 04.00 UTC]. A combined PlanetScope and Sentinel-2 approach is advisable to detect dust source locations at the sub-basin scale. Both have positives. The Planet sensor can be generated daily with an average 82% basin coverage. Sentinel-2 has a three times/week revisit with 76% basin coverage.

Generally, DPS locations for Sentinel-2 and PlanetScope broadly are coincident, but there are systematic differences within the Gonghe. These are mainly manifested in the following ways: (1) Planet points for the same source are located upwind of Sentinel-2 points (Figure 4.9). As the driving wind typically originates from the northwest, the upwind movement means that PlanetScope points generally shift northwest. (2) different/unique sources were detected in each image. Based on those cases, we can suggest three possible reasons for the difference: (a) PlanetScope (02.20 - 04.00 UTC) overpass time is earlier than Sentinel-2 (04.18 UTC), so there is a chance that some locations will stop/start emitting dust in this period; (b) the superior spatial resolution of Planet 3 m imagery may simply identify smaller sources that are not apparent in Sentinel-2 data; (3) Sentinel-2 uses the CSD FCC image enhancement method which can lead to superior detection for some dust sources than the version of CSD applied to PlanetScope. Murray et al. (2016) indicate that CSD image rendering methods improved the ability to detect DPSs and improved ability to resolve and pinpoint DPS. The 10-metre Landsat data works well on pinpoint dust points, with only two event cases. Still, Landsat limits of 33% basin converge and a relatively low temporal resolution (2 times/week) makes it hard to discover the full story of Gonghe. Landsat data suggest that a higher temporal resolution and coverage is essential for catching emission processes. Thus, there are trade-offs when using either Sentinel-2 or PlanetScope data, and factors such as (i) time/space sample, (ii) spectral resolution, (iii) enhancement methods, and (iv) data coverage all remain critical to the detection of dust sources at the sub-basin scale. Combining the two datasets balances these trade-offs and provides a useful aggregate dust source data set for those SDSs.

CubeSat observed dust source distribution is similar to the Himawari-8 Fo-AOT derived ADS area. The ADS area includes Sand Dunes, Ephemeral Lake, and farmland located in the middle of the Gonghe Basin, and the edge of the mountain area is of low importance for SDS. During dust emission, CubeSat can pinpoint the upwind origin of individual dust plumes to precise emission surfaces and small-scale geomorphological settings for discovering details of the emission process. This capability provides insight into the spatial heterogeneity of processes and emissions far beyond what MODIS medium-resolution sensing or GEO Himawari-8 reveals. The SDS potential of 1b Chaka Lake needs further investigation. Ephemeral lake rarely produces obvious plumes visible on LEO satellite imagery (only observed in 2 cases from Planet), but in the Hotspot Map generated by GEO Himawari-8 AOT, 1b was identified as a major dust source, emitting dust continuously during the daytime. The continuous 10-min GEO (Himawari-8) data capability of observing the SDS process in the daytime achieved insight into the temporal heterogeneity of emissions far beyond that revealed by the LEO satellite, increasing the possibility of the observed SDSs process. The advantage of using Himawari-8 TCI to observe dust plumes is that even a short duration or small (Disturbance SDS) dust activation can be captured. GEO AOT products are particularly effective in detecting constantly emitting dust sources, such as ephemeral lakes like Chaka Lake, haze, and intense SDSs like Haboob. However, GEO data has limitations when it comes to detecting DPS. CubeSat data address this drawback, as the 3 to 10-metre resolution of CubeSats allows for precise identification of the upwind origin of individual dust plumes and provides detailed information about the emission process within small-scale geomorphological settings.

High resolution RS observes at the sub-basin (Pixel) scale, directly linking the SDSs process, approaching comparability with field observations; at the regional or basin scale, we must infer the process. Chapter 2 highlights some challenges associated with MODIS detection SDSs and link with control factors at the regional scale. Himawari-8 has demonstrated the contribution of high temporal frequency remote sensing in this regard (Shi et al., 2023); Baddock et al. (2021) validated the temporal and spatial DPS observational capabilities of CubeSat data with a case study of an SDS in the Chihuahuan Desert, Mexico. To directly link the SDS process, Chapter 4 combines high spatial resolution CubeSat images with high temporal resolution Himawari-8. Temporally, Himawari-8 observed the timing of SDS since its start at a sub-daily scale in the daytime; Spatially, CubeSat data was used to pinpoint locations of SDS at field-scale.

When estimating SDS's dust mass using AOD and the Area of DPS, the results are influenced by the type of RS sensor-derived AOD, aerosol size, refractive index, backscattering, and extinction coefficients. Dust mass could significantly vary in different SDSs, for example, in a dust event on 17th November 2019 which was the largest SDS among the 14 cases, with a large range of dust plumes occurrence and the highest AOD value, contributing dust loading value of 0.072-0.112 Tg was 5-10 times higher than in other SDSs (Table 4.6).

4.4.2 PDS and Land Cover/Use Characterisation for the Gonghe Basin, based on Frontal SDS from 2019-2022

4.4.2.1 PDS Characterisation in the Gonghe Basin

The PDS scheme uses sedimentology and soil properties, along with key constraints such as sediment supply and availability, to determine different potentials for SDSs (Ahmadi-Molaverdi et al., 2022). The PDS system is divided into lakes, high-relief alluvial, low-relief alluvial, stony surfaces, and aeolian surfaces, and has been evaluated at several dust source regions using remote sensing images (e.g., Bullard et al., 2011; Lee et al., 2012; von Holdt et al., 2019; Cui et al., 2019). According to Bullard et al. (2011), some geomorphological components are more susceptible to wind erosion and likely to be dust sources than others. For example, Baddock et al. (2016) used MODIS Deep Blue Products to determine the actual importance ranking at the Chihuahuan Desert and compared it to the Bullard predicted importance rankings of each PDS surface type for SDSs. Most surface types were consistent with observed features, demonstrating the importance of geomorphic controls on emissions.

Table 4.7 Percentage of DPSs observed from 5 active source regions divided by PDS geomorphological scheme

PDS Gemophological		Chihuahua Desert (Bullard et al., 2011)	Lake Eyre Basin (Bullard et al., 2011)	Ilam province (Ahmadi-Molaverdi et al., 2022).	Llano Estacado (Lee et al., 2012)	Nambi Desert (von Holdt et al., 2019)	Gonghe Basin	
ID	Emission Sources	Dust plumes %	Dust plumes %	Dust plumes %	Dust plumes %	Dust plumes %	% by Planet	% by Sentinel-2
Lakes								
1a	Wet	0			0	42.9	0	0
1b	Ephemeral	29.5	11		2.9		5.6	2.2
1c	Dry – consolidated							
1d	Dry – non consolidated	18.4						
High Relief Alluvial Systems								
2a	Armored, incised			24		51.1		
2b	Armored, unincised		0.6					
2c	Unarmored, incised	0		43			0.4	1.2
2d	Unarmored, unincised	20.7			2.6			
Low Relief Alluvial Systems								
3a	Armored – incised							
3b	Armored - unincised							
3c	Unarmored – incised	0		16	0		17.5	8.1
3d	Unarmored– unincised	12.0	16.5	15	6.4		5.7	8.5
Stony surface								
4	Stony surfaces	0.5	3.8			1	1.2	2
Aeolian								
5a	Sand Sheet	1.8	5.7		78.7	3.9	6.4	8.5
5b	Aeolian sand dunes	13.8	57.6	1	5.0		63.3	69.4
6	Loess				4.5			
7	Low emission surfaces	3.2	4.9	1	0			

The summary percentages for DPS distributions in the PDS scheme from 4 active dust sources have been compiled in Table 4.7 to compare with this case study. Generally, the temporary lake and aeolian dune PDS categories appear in all regions and have relatively high emission scores. Bullard et al. (2011) propose that these two classes have medium to high importance for SDS globally. However, in each case, the dominant PDS emission type noted in each region differs significantly.

Ephemeral lakes (Class 1b) are the dominant PDS class in the Chihuahuan desert, accounting for 29.5% of DPSs (Bullard et al., 2011, Table 4.7). Alluvial systems are the highest PDS class in the Namib Desert (43%, by von Holdt et al., 2019). The remaining regions have all identified the aeolian system as the dominant PDS class, accounting for over 65% of points sources in each case. Sand sheets (Class 5a) play a significant role in the Llano Estacado region (78.7%, by Lee et al., 2012), and aeolian dunes (Class 5b) account for nearly 57.6% of DPSs in Lake Eyre Basin (by Bullard et al., 2011, Table 4.7).

Many fieldwork and satellite data analyses have highlighted ephemeral lakes as important sources of dust (Bryant, 2013). Based on these data and the dynamics of sedimentation and sediment balance at these features, the PDS scheme classifies ephemeral lakes as the 'High' important for SDSs (Bullard et al., 2011). This prediction is confirmed in the Gonghe Himawari-8 Hotsopt map, as the ephemeral lake classification area (Chaka Lake) is associated with the highest average frequency in the long-term dust record (Zone1). Ephemeral Lake includes the Chaka Salt Lake and the semi-dry river connected to the Longyangxixa Reservoir. An extensive network of water channels forms in the Gonghe Basin, contributing nearly 1.3% of the dust source. Alluvial plains are located in the southwest and northeast of the channel network and are widely distributed, with farmland extending in a narrow band, with 8.84% of the dust sources in the region originating from cultivated areas. The High-Relief (HR) Alluvial is on two sides of the Gonge, and like the LR alluvial, the HR alluvial is divided into the water channel, observing two DPSs.

In the PDS scheme, the importance of dunes for SDSs varies from low to high depending on factors such as dune type, composition, history, and location (Baddock et al., 2016). The primary source of uncertainty is the classification of dunes, which may be low-emission sources if dunes are young and/or active/vegetated; high emission sources if dunes are aged and/or stable but have experienced recent disturbances (Bullard et al., 2011). Parabolic dune is formed by winds blowing out the centre of the dune, leaving just a rim on the outside in "U" shaped dunes usually stabilised by vegetation (Luo et al., 2019b). Blowout formation often marks the reactivation of previously fixed parabolic dunes and is recognised as a direct response of beaches and inland, dry, arid landscapes to climate change and human activities (Barchyn and Hugenholtz, 2012). Gonghe blowouts mainly occur on the north shore area of the Longyangxia Reservoir (Luo et al., 2019b). Sediment characteristics, freeze-thaw processes, wind/water erosion, and human impacts all play an essential role in initiating and expanding mega-blowouts (Luo et al., 2019a). The occurrence of mega-well blowouts primarily took place within the palaeodunes situated on the Yellow River terrace. Field data collected by Luo et al. (2019a) suggests that these palaeodunes possess a thin vegetation cover and a loosely consolidated sublayer composed of sandy material. When the top surface layer is disrupted, a significant quantity of loose sandy sediment becomes exposed, thus increasing the susceptibility to wind erosion. Various factors, including drought, overgrazing, modern transportation activities (such as vehicle movement), and cycles of freezing and thawing, have the potential to disrupt the delicate vegetated surface of the Gonghe region in the QTP, and exacerbate the occurrence of blowouts and wind-driven SDS. By contrast, the southern Longyangxia Reservoir Dune in the Gonghe is a stable dune area.

Also, it is important to examine the composition of the dust sources to estimate the land erodibility of the different geomorphology types. Currently, active dunes are the predominant sources of dust in the Sahara, primarily due to their extensive distribution in areas characterised by high-speed winds and their susceptibility to erosion. Notably, research by Bristow et al. (2009) identified sand dunes composed of diatomite pellets in the Bodélé Depression (BD) of Chad as a significant contributor to dust emissions. Additionally, Crouvi et al. (2012) demonstrated that quartz-rich dunes in the vicinity also play a role in dust production, and act as agents for the dispersion of fine deposits from dry lakes. Aeolian abrasion emerges as a crucial process in the formation of fine dust particles within active dune environments (Crouvi, et al., 2012).

It is worth noting that sand dunes are not a typical dust source landform in China. Cui et al. (2019) conduct fieldwork and note that their results broadly concur with the PDS scheme

(Bullard et al., 2011), and they quantify aeolian SDS potential in northern China using a portable wind tunnel. Their study site found that sparse grasslands and coppice dunes (vegetated dunes) emitted five times more dust particles than free dunes (Cui et al., 2019). In other regions of China, Wang et al., (2006) indicated that Gobi (stony surfaces) were responsible for most of the recorded SDSs (e.g., from the Kunlun, Qilian, and Helan mountains), and Wang et al. (2015) ranked dust susceptibility in the following coppice dunes > dunes > stony surfaces > grasslands. Thus, we highlighted some divergence from this consensus within the Gonghe Basin that aeolian dunes produce proportionately more DPSs than other surface types.

Dust sources with moderate importance for emissions are of limited sediment supply, and they are vulnerable to switch between periods of intense dust activity driven by sediment supply and periods of low concentrations. This "switching" dynamic leads to large variations in SDSs and is reflected in significant changes in the number of DPSs in ephemeral lakes and low-relief unarmoured alluvial surfaces (3c and 3d) at the Gonghe during winter. However, seasonal variations in SDSs may also be caused by fluctuations in transport capacity. For active aeolian surfaces, e.g., blowout, SDSs begin when winds speed over dust uplift potential. SDSs from HR alluvial systems (e.g., 2c) are very low and significantly different from LR (3c, 3d) systems. High vegetation cover in some areas is negatively correlated with the frequency of dust occurrence, and this area includes high-elevation mountains consisting of hard limestone. In high-latitude environments, dramatic temporal changes in sediment availability have been identified as key factors controlling dust activity (Baddock et al., 2017; Bullard et al., 2016). Gonghe, located in the high-altitude Tibet Plateau, also shows similar characteristics.

4.4.2.2 LULC Characteristics and Possible Human Impacts

The relative emission of PDS landform types in the study area is informative but does not completely explain the spatial variability of dust sources. Lee et al. (2012) conducted a study to examine the correlation between dust sources and human-induced alterations of landscapes by expanding the utilisation of surface classification methods. Pastures and agricultural lands modified from alluvial systems are the most important sources of SDSs in Ilam Province, Iran (Ahmadi-Molaverdi et al., 2022). Similarly, due to anthropogenic disturbance, a relatively large amount of DPS is generated by a small portion of the land surface within the alluvial surface in the Gonghe. By considering both PDS and LULC, it was discovered that cultivated land covers approximately 40% of the 3c, with half of the dust sources located in these cultivated areas. Moreover, the number of DPSs per square kilometre (0.07) in this region is significantly higher compared to the 3c (0.05). In comparison to other areas, the number of DPSs per square kilometre in the Gonghe alluvial region (0.054) is two orders of magnitude greater than the non-anthropogenically degraded sands of the Chihuahuan Desert in the United States (0.0004) and notably higher than the human-influenced Llano Estacado (0.008) located in Northwestern Texas and eastern New Mexico.

SDSs originate from landscape features rich in fluvial deposits (fine-grained sediments), and the low density of vegetation and bare area increases the potential for SDSs (Engelstaedter et al., 2003). Agricultural activities disrupt the topsoil, exposing many fine silt particles to wind erosion. Particularly in the post-harvest autumn and winter, when farmland lacks vegetation at Gonghe. Webb and Strong (2011) confirmed that soil surface disturbance by agricultural practices reduces the stability of soils against wind erosion and largely increases the availability of fine particles for SDSs. In Gonghe, the PDS scheme low relief alluvial 3c class should modify to the ‘Medium’ important for SDSs due to human-active impact.

In terms of wind, dust uplift wind speed will likely occur from October to May in the Gonghe [detail in Chapter 2]. In terms of temperature, the temperature range in the GH basin is similar in spring and autumn, -3 to 6℃, and in winter, -14 to -6 ℃. Rainfall is concentrated in May to September, peaking in July, with other months having less than 20 mm. Consequently, the period of SDS occurrence coincides with the dry season and aligns with the post-harvest phase of crops. Most crops, especially maize, are largely harvested by September, leaving most fields bare. The combination of strong winter winds and the absence of vegetation makes agricultural fields in these areas a critical point for dust generation. It explains why alluvial will emission in winter and present spatial source differences. Ahmadi-Molaverdi et al. (2022) suggest that when the sand layer in China is anthropogenically modified by agriculture, its dust emission rate and wind erosion are much higher than other surface types. The impact of land surface agricultural modification on dust susceptibility is widely recognised globally (Hooper and Marx, 2018; Wiggs and Holmes, 2011; Weiss et al., 2013). An example can be seen in the SEVIRI record of major dust sources in South Africa, which predominantly appear to be anthropogenic in nature and are influenced by land cover and management (Eckardt et al., 2020). Agriculturally disturbed sand beds in western Texas and eastern New Mexico have been identified as a major source of SDSs (Lee et al., 2012).

The bare land area dominates the overall SDS from the Gonghe, corresponding to the aeolian surface of the PDS, followed by a relatively large DPS derived from anthropogenic areas, including the city, agriculture, and solar power areas. Apart from the Alluvial System, anthropogenic changes in LULC also affect the emission rates of other landform types. Cultivation, vehicle, and livestock disturbance of surface, and impacts on the underground water table line and the area of ephemeral lakes. These Bare/Sparse areas are also artificially managed by grazing and desertification projects, a government program to fix sand and plant shrubs using straw checkerboards widely used for wind erosion control (Zhang et al., 2018). However, in all but the most extreme droughts, they maintain a patchy vegetative cover, making them less susceptible to erosion than bare surfaces, especially during the dry and windy seasons (Dong et al., 2007). The Gonghe land surface has been extensively modified by agriculture, the Solar Power Planet programme and the grass-checker sand fixation project, and thus, the wind erodibility of the study area is primarily moderated by human disturbance, unlike the more 'original' dust sources discussed by Bullard et al. (2011). Anthropogenic influences on dust edge emissions similar to the Gonghe include western Ilam Province, Iran (Ahmadi-Molaverdi et al., 2022), the post-Soviet Central Asia (Xi and Sokolik, 2016), and Southern Africa (Ginoux et al., 2012). In Northern China, Du et al. (2018) estimated that about 3.7% of SDSs originate from anthropogenically modified land. DPSs originate from human-disturbed land, e.g., in the southern High Plains, intensive agriculture on wind-sand-derived soils, including regular ploughing and harvesting of the leading cotton crop cover before periods of the strongest winds, markedly increases the wind-sand layer emission rates. In contrast, in the Taklamakan Desert, where there is little human activity, the dust source is mainly from dune surface (Jin and He, 2023); In Ala Shan Plateau, SDS from the Gobi surfaces, code 4 in the PDS scheme as stony (Wang et al., 2012).

4.4.3 Dust Transport Pathway from the Gonghe Basin

The trajectory analysis of the Dust Source Point (DSP) in Gonghe, based on observations from 14 SDS cases, revealed distinct seasonal emission patterns (Figure 4.16). The study emphasised the significance of atmospheric and topographic conditions in influencing dust transport. In particular, the SDS trajectory of the Frontal System causing SDS was found to follow a southeast direction within 24 hours. This trajectory was associated with strong near-surface winds from the northwest, driven by westward or frontal winds as a counterclockwise cyclonic system passed beneath the basin from west to east. However, Cao and Chen (2022) discovered that certain dust aerosols over the QTP also underwent long-distance transport to northeastern East Asia despite the prevailing northwest winds. The forward trajectory model originating from 72-168 hours indicated that Gonghe dust followed a path toward northeastern East Asia and reached the Japanese and Greenland glaciers. Wei et al. (2021) confirmed this pathway using Hf-Nd-Sr isotope tracking, in combination with ground instruments and MODIS satellite observations and explained that the pathway was attributed to the northward movement of high-altitude westerly. Moreover, the unique topography of the QTP facilitated the ascent of dust aerosols to the upper troposphere through strong upward motion, as highlighted by Tan et al. (2021). Yuan et al. (2019) further emphasised the role of the QTP in lifting dust aerosols to higher levels through the thermodynamics of the region. This enabled dust to be transported over longer distances in the middle and upper troposphere, thereby extending the lifespan of dust. The potential transport distance of dust particles increased with the starting height (Aili et al., 2021). Additionally, Xu et al. (2020) utilised CALIPSO observations to demonstrate that the maximum lifting height of dust from the QTP occurred in spring. The emission and transportation of dust not only impacted air quality and the biogeochemical cycles in downwind areas but also posed a serious threat to human health (Wei et al., 2022). SDSs were found to significantly deteriorate air quality and increase the concentrations of PM 2.5 and PM 10, and inhalation of these particles could lead to respiratory and cardiovascular issues (Basith et al., 2022).

4.5 Conclusion

Q4.1: Where is the dust point sources [DPS] within the Gonghe Basin at the sub-basin scale, and What is the PDS/ LULC signature of those DPS?

[O4.1] Develop a Dust Point Source [DPS] detection protocol for PlanetScope, Sentinel 2 and Landsat 8/9

- This chapter uses a new RS image CSD enhancement approach to generate DPS from HR-LEO satellites. The multiple-band composite approach was helpful in aiding DPS detectability.
- There is a close agreement between Sentinel-2 and Planet detectability. However, data volumes for the former are slightly higher than the latter. In addition, Planet images are better at detecting DPSs, as its 3-metre resolution allows markedly better plume determination at the plot scale.
- There are trade-offs when using either Planet or Sentinel-2 data, and factors such as (i) time/space sample, (ii) spectral resolution, (iii) enhancement methods, and (iv) data coverage all remain critical to the detection of dust sources at the sub-basin scale.
- The 14 frontal SDSs used here were detected by the HR-LEO satellites in the morning [02.00 - 04.30 UTC] during 2019-2023. It should be noted that the 14 cases also were recorded in the MODIS-Terra, MODIS-Aqua (Section 2.3.1; Figure 2.7), VIIRS, and Himawari-8 (highlighted in Appendix J).
- Using a combined PlanetScope, Sentinel-2, and Landsat 8/9 datasets is advisable. High-resolution LEO images allow for precise identification of the upwind origin of individual dust plumes and provide detailed information about the emission process within the sub-basin scale. Using the synthetic HR-LEO datasets expands the overpass time window, which increases the chance of observing the basin and detecting DPSs.

[O4.2] Deriving PDS and Land Cover/Use [LULC] Maps for the Gonghe Basin

I have applied the Bullard et al. (2011) PDS method across the Gonghe Basin to produce the geomorphology map and digitised LULC map in 2023.

Chapter 4 - Use of LEO data for DPS detection and derivation of PDS and LULC

Question 4.2: What are the properties of observed SDSs at the sub-basin scale?

[O4.3] Use DPS data to derive PDS and LULC signatures for SDSs in the Gonghe Basin.

- Gonghe Basin has 8 types of PDS geomorphology, with Sand Dune (5b) being the main dust source, followed by Ephemeral Lake (1b). Additionally, unconsolidated low-relief alluvial surfaces (3c, 3d) and sand sheets (5a) have a moderate potential for SDSs. In contrast, Wet lakes (1a), high-relief alluvial (2c), and stony surfaces (4) are less likely to produce dust. Approximately 69.7% of the DPS is derived from Aeolian deposits (5a, 5b), compared to 23.2% originating from alluvial deposits (2c, 3c, and 3d) and 5.6% from ephemeral lakes (1a). Nevertheless, dunes are not a typical dust source landform in China. Gonghe contains Parabolic dune consisting of a thin vegetation-covered top surface layer and a poorly cemented sandy sublayer. Once the dune's surface is destroyed, a large amount of loose sandy sediment is available with high wind erosion capacity.
- However, PDS does not fully explain the spatial variability of dust sources in the study area. Combined with PDS and LULC, cultivated land contributes 50% of DPS from the 3c and accounts for 40% area of 3c. SDSs originate from landscape features rich in fluvial deposits (fine-grained sediments), and soil surface disturbance by agricultural practices most likely reduces the stability of soils against wind erosion and largely increases the availability of fine particles for SDS, particularly in the post-harvest autumn and winter months. This perhaps explains why alluvial surfaces are flagged in winter, and present ADS locations vary spatially in different seasons.

[O4.4] Measure dust loadings for plumes emanating from the Gonghe Basin

- The overall dust mass in the study (for the 14 Frontal SDS cases) was estimated to range 0.196-0.302 Tg. Most of this dust (approximately 84.7%) originated from Aeolian PDS classes (PDS class: 5a and 5b). LR alluvial (PDS class: 3c and 3d) deposition accounted for 1.9 % of the total dust mass, while Ephemeral Lake (PDS class: 1b) contributed about 2.6 %. Dust from other surfaces, such as stony (PDS class: 4) and HR alluvial (PDS class: 2c), made up 0.8 % of the total. In terms of seasonal distribution, during winter, 7 cases were responsible for 35.3% of the total dust mass. In contrast, during Autumn, 4 SDS generated a significantly higher amount of dust (44.7%), which was approximately twice the amount produced by the 4 SDS cases in Spring (20%).

[O4.5] Determining the trajectory of SDSs emanating from DPS

- The HYSPLIT forward model was utilised to analyse the dust transport characteristics of Gonghe in three different seasons based on detected DPS. Results indicate noticeable variations in the height and distance of dust transport paths across seasons, although the direction remains consistent. Detailed analysis of air trajectory density reveals that spring and winter are the seasons with the longest dust transport distances. In autumn, trajectory distances are relatively shorter, and the height remains below 1000 m, although the dust loading level is the highest during this season.
- In both spring and winter, the dust pathways from Gonghe exhibit similar characteristics, with a height ranging from 2000-2500 m. However, the dust pathway in winter shows a more dispersed direction, resulting in a lower frequency of trajectory lines compared to spring. Over 24 hours, the transportation channel extends southeastward, impacting regions such as Gansu, XiAn, and Chongqing in China. Under favourable atmospheric conditions, dust from Gonghe can propagate northeastward over long distances for an extended period (48-168 hours), reaching places like Japan and Greenland.

5. Discussion

The thesis aim is to "Understanding controls on dust emission using remote sensing in the Gonghe Basin, China" (Section 1.7). In this chapter, I will discuss the extent to which I have achieved this aim based on the material presented in Chapters 2-4 and will examine the broader implications of this research. First, I will evaluate the progress made in Sand and Dust Storms (SDS) detection using available remote sensing data and discuss the RS methodological contribution of my work (Section 5.1). Second, I will discuss the implications of my findings to our understanding of SDSs from the Gonghe Basin and beyond (Section 5.2). In each case, I will compare (i) observed Gonghe Basin dust sources and processes to those recorded in other parts of China and globally, (ii) PDS dust emission chronologies and highlight the implications of understanding how aeolian processes (specifically dune celerity/ motion) can drive the dust cycle. Finally, recommendations for future research are outlined and elaborated (Section 5.3).

5.1 How does remote sensing detection of dust emission change as a function of spatial and temporal scale?

A key aspect of this thesis is the development of methods for SDS that operate across Regional, Basin and Sub-Basin scales using Remote Sensing (RS) data. Satellite data are now widely used to detect SDS in the atmosphere (Yu et al., 2015; Bakker et al., 2019; She et al., 2018). Low Earth Orbit (LEO, e.g., Baddock et al., 2009) or Geostationary Earth Orbits (GEO, e.g., Schepanski et al., 2009) provide different time/space opportunities to observe and quantitatively record SDS. It is clear that the increased range of platforms and sensors used to monitor SDS in the past 20 years has directly led to new insights into atmospheric SDS processes (Tie Dai, 2019), identification of dust source locations (Nobakht, et al., 2021), and quantification of global aerosol burdens (Colarco et al., 2010). However, each of these leaps in understanding highlights significant challenges in observing SDS without some level of operational bias (e.g., time of overpass relative to SDS occurrence) or omission (e.g., impacts of cloud or night-time). Here, I take advantage of an opportunity to use all newly available data and products from GEO and LEO sensors to refine the scale of observed temporal and spatial heterogeneity of SDS in the Gonghe Basin, and to identify any inherent observational bias.

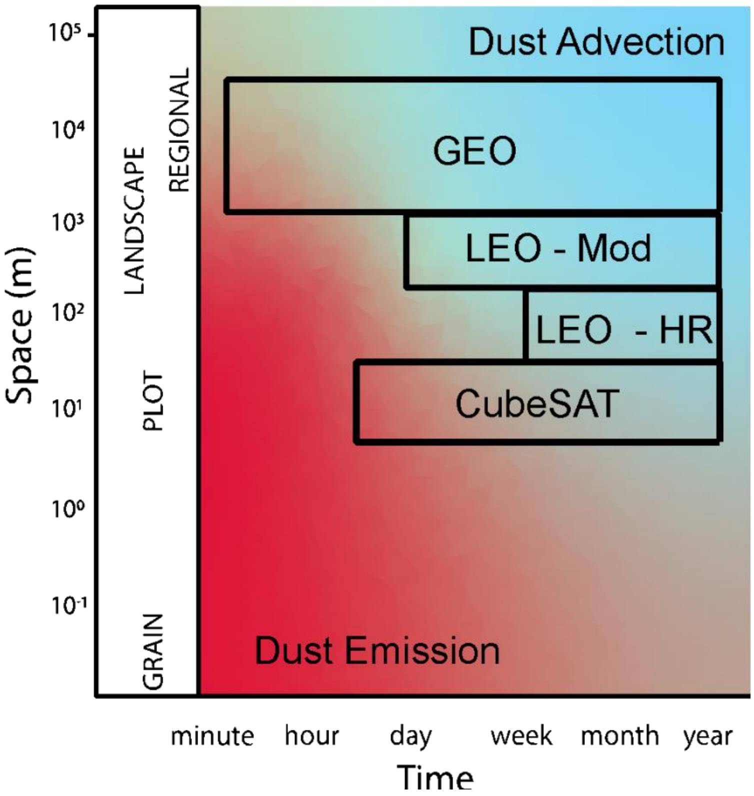

Figure 5.1 Time and spatial scales of dust emission and dust advection, related to the monitoring/detection capabilities of existing satellite systems: GEO, LEO-Mod (Moderate Spatial Resolution), LEO-HR (High Spatial Resolution) and CubeSAT.

For the available RS archive, comprehensive coverage of a range of datasets is available for each year. The datasets used here include GEO (e.g., Himawari-8) 10-minute, LEO (e.g., MODIS Terra and Aqua) daily, LEO-HR (e.g., Sentinel-2 and Landsat 8/9) 2-3 times/weekly, and CubeSat daily/sub-daily. Regarding SDS detection, show that GEO datasets provide the most complete record of SDS events at the basin scales. GEO data, especially collected at 10-minute intervals, are more likely to provide close observations of SDS. However, when deriving DPS for specific SDS, GEO data have insufficient spatial resolution to locate them at a scale appropriate to geomorphological/PDS units. To do this we must utilise LEO data, but it is important to understand the climatological and diurnal context of the SDS from GEO data before embarking on this step. Thus, GEO data are essential in determining the start time of SDS during the daytime. However, a key recommendation here is to adopt a hybrid approach through the use of a workflow of synergistic GEO and LEO data, to provide a comprehensive and climatologically constrained timeline for SDS and DPS data; as the use of LEO data alone for DPS mapping can provide an extremely biassed and unrepresentative estimation of SDS emission sites, events and controls. Figure 5.1 emphasises that only certain types of data will get close to the time/scale of emission, enabling precise identification of dust sources. GEO data works well in terms of time resolution but can only provide a crude assessment at the basin scale. Once the climatology of SDSs is known LEO-MOD), it becomes possible to search for LEO-HR and CubeSat data to obtain more detailed information.

In this section, I will discuss how an integrated or synergistic approach to RS data use can aid understanding of source activity at the sub-basin scale, and I (i) summarise the strengths and limitations of each sensor, (ii) discuss how the challenges of RS detect Dust Hazards: Cloud, Detection, Space/Time, and (iv) highlight where the methodological contributions of this thesis can be utilised elsewhere in the future. Specifically, Moderate spatial Resolution Low Earth Orbit (MR-LEO, e.g., MODIS and VIIRS) are used in Chapter 2, High Temporal Resolution Geostationary Orbit (GEO, e.g., Himawari-8) is applied in Chapter 3, and LEO-HR (e.g., Landsat-8, Sentinel-2), and CubeSAT (PlanetScope) are utilised in chapter 4.

5.1.1 What aspects of the dust cycle are most likely to be observed by moderate resolution LEO data [e.g., MODIS, Sentinel-3, MERIS, etc]?

Moderate-resolution (MR) LEO has been successfully used to monitor SDSs at a regional scale (Murray et al., 2016). For example, Taramelli et al. (2013) used MODIS to map potential dust sources and combine NDVI to assess land cover discrimination. Wang et al. (2022) discovered the spatial distribution of dust intensity through MODIS Aerosol Optical Depth (AOD) products. The MODIS aerosol products can also be used to derive the Angstrom index (α), which allows aerosol particle size estimation (Kaskaoutis et al., 2011). These data have been used to distinguish between coarse mode particles (dust) and fine mode particles (Gharibzadeh et al., 2018).

Using MODIS Deep blue DOD time-series data, I investigated Dust Storm Day (DSD) and dust cycle on a monthly and annual basis during 2000-2022 (Section 2.3). The existing AOD threshold to extract dust approach is widely used globally (Proestakis et al., 2018; Pu and Ginoux, 2018; Jafari and Malekian, 2015). The AOD detection method is influenced by cloud coverage (Rogozovsky et al., 2021), the spatial and temporal discreteness of the events (Li et al., 2021a), dust altitude (Huck, Bryant, and King, 2023) and dust loading (Li et al., 2021b). Also, the AOD threshold for defining SDS that distinguishes dust from non-dust has proven problematic. Thresholds vary by region, season, and in some cases individual SDS (Nobakht et al., 2021). The fact that LEO sensors' overpass times allow for the observation of dust in transport (e.g., dust advection) rather than close to the source detected all the SDS from the ground, like observing the dust emission from sources(Huck et al., 2023).

5.1.2 What does GEO data add to our understanding of dust activation, and what can we determine regarding a diurnal, seasonal and annual dust cycle?

LEO sensors present a challenge for exploring dust source locations, in contrast to GEO, which is an effective method for identifying dust source regions (e.g., SEVIRI, Hennen et al., 2019); Himawari-8, Shang et al., 2018). GEO has a higher frequency of observations compared to LEO. The AOD of the new Himawari-8 satellite instrument has been assimilated into a dust simulation model over East Asia (Jin et al., 2019). Himawari-8 has continuous images with a temporal resolution of 10 minutes and a spatial resolution of 2 kilometres to capture the previously unrecognised life cycle, generation, evolution, and outflow of Gonghe's SDS (Tie Dai, 2019). This advanced GEO can monitor East Asian SDS that typically have significant spatial and temporal variability (Jin et al., 2019).

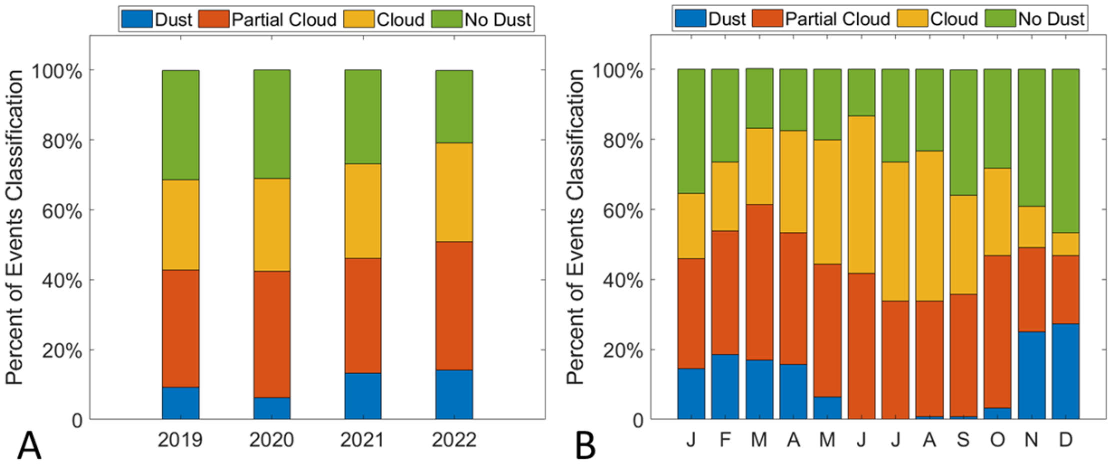

Figure 5.2 GEO Himawari-8 Events Classification(A) Percentage of 4 types of events in 2019-2022 separately; (B) Percentage of 4 types of events in different times of year during 2019-2022 in the Gonghe Basin, China. [reused from Figure 3.6]

This is particularly important for classifying SDS based on climatological and meteorological characteristics of SDS events. Four types of climatology system-lead SDS were identified at the Gonghe Basin, including Haboob, Dust Advection (Haze/floating dust) **[TD]**, Pre/post-

Frontal, and Local Disturbance **[LD].** Two Dust types (Haze and frontal) associated with cold fronts are the primary mechanisms for GH transport and ejected dust.

A significant limitation of RS detections of SDSs is Clouds. Although Mod-LEO MODIS cloud data have been used to investigate intra-seasonal variations in QTP cloudiness, LEO satellites have limited temporal resolution (Shang et al., 2018). The terrain over the QTP is complex, with large mountainous regions covered by snow and ice, which satellites may misinterpret as clouds (Hutchison et al., 2012). Several inherent and identifiable spatial and temporal biases are associated with high-latitude dust using LEO sensors, including understanding the influence of clouds on SDSs and dust source detection (e.g., Baddock et al., 2009). Neither LEO nor GEO satellites are able to provide accurate cloud discrimination and existing cloud-screening of RS results in fewer samples of SDSs. For example, Huck et al., (2023) found that relative to ground observations, the AERONET cloud-screening algorithm may remove as much as 97 % of known SDSs (3% detection). Thus, there needs to be more direct observations from satellites over the QTP to determine the extent and seasonal variability of cloud obscuration and how it affects the identification of SDSs. Therefore, based on the Himawari-8 TCI time-serious image, I performed observational analyses to calculate the proportions of Partial Dust (PC), Cloud (C), No Dust (N), and Dust (N) from 2019 to 2022 (Fig 5.2). The cloud influence limits the Himawari-8 observational time window to be restricted to 40% of the year.

Although lots of research detects dust sources using GEO or LEO datasets, only a few studies compare with other LEO satellite dust detectability (Zhang, 2019). I compared the relative detection rates of mod-LEO and GEO. Where the cloud is not apparent, the continuous and short interval of GEO (Himawari-8) data also demonstrates an ability to provide a complete view of the daytime SDS process. In contrast, the Mod-LEO (MODIS) data is limited by 2 times per day and overpass period between 10.30 to 13.30 local time, resulting in a much lower sample and detection rate. For Gonghe, the observation time was reduced from the GEO 00.00 - 10.00 UTC to Mod-LEO 02.30 - 06.30 UTC, resulting in a 34.6 % reduction in the total number of DSD of Mod-LEO for the year. Events recorded using HR-LEO (02.30 - 04.30 UTC) observations were a further 39.3% less than those recorded using Mod-LEO data. The observations of LEO are severely underestimated. This conclusion is supported by the study of Tie Dai (2019), that Himawari-8 hourly AOT was superior to those using Mod-LEO observations.

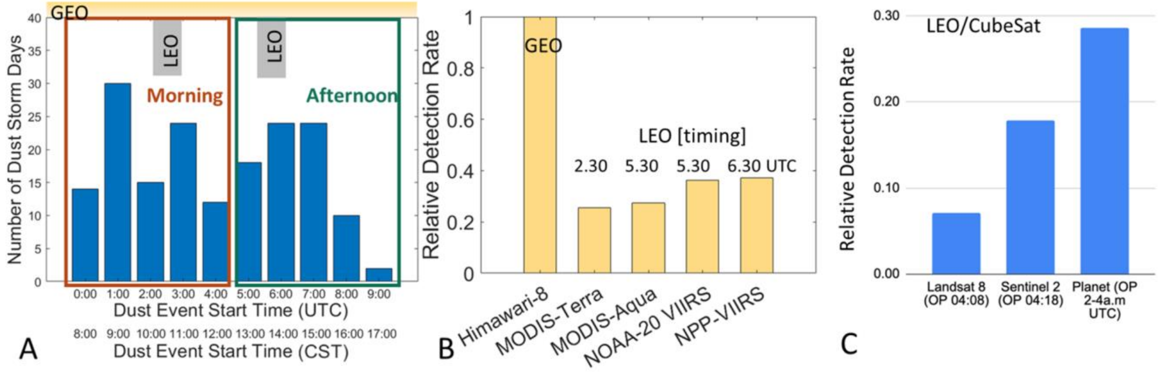

Figure 5.3 (A) Number of DSD start at different times of day (UTC, CST), in relation to GEO and Mod-LEO observation time window; (B) SDS relative detection rate of Himawari-8; MODIS-Terra, MODIS-Aqua, NOAA-20 VIIRS and NPP-VIIRS and its overpass time. (C) SDS relative detection rate of HR-LEO (Landsat-8 and Sentinel-2) and CubeSat (Planet) and its overpass time UTC. [Figure 5.2 A and B reused from Figure 3.5 A and B]

Comparing Mod-LEO and GEO data reveals the annual cycle of SDS frequencies derived, with DSD occurring from November to May. The monthly frequency of SDSs increases significantly as the temporal resolution increases and the time close to the high DUP (in the afternoon). The total number of DSDs detected is GEO > MODIS Aqua > MODIS Terra. Area averaged AOD for DSD derived from Mod-LEO data is generally higher than via GEO data. DUP is higher for DSD events derived from GEO datasets, with peaks in spring and winter. MODIS-Aqua has the highest DUP in November and December.

More importantly, the number of DSD detected from different sensors varies significantly from different seasons. Mod-LEO shows SDS activity across the Gonghe peaks in the spring [MAM], while GEO shows that SDS peaks in the winter [DJF]. Three datasets record nearly no SDSs from June to September. Higher DSD was observed from GEO than Mod-LEO in November-February (Fig 5.3, low cloud). The similarity of the results, except for winter, can also be attributed to increased cloud cover (Shang et al., 2018). SDSs associated with increased cloudiness (e.g., from an active frontal system) pose challenges for RS analysis of dust. Firstly, meteorological clouds can obscure the image's dust when it is directly above the basin, resulting in missed events (Knippertz and Todd, 2012). When Frontal systems lead to high wind speeds (Yu et al., 2021), dust transport to the southeast along the basin might be blocked by clouds (Schepanski, 2012).

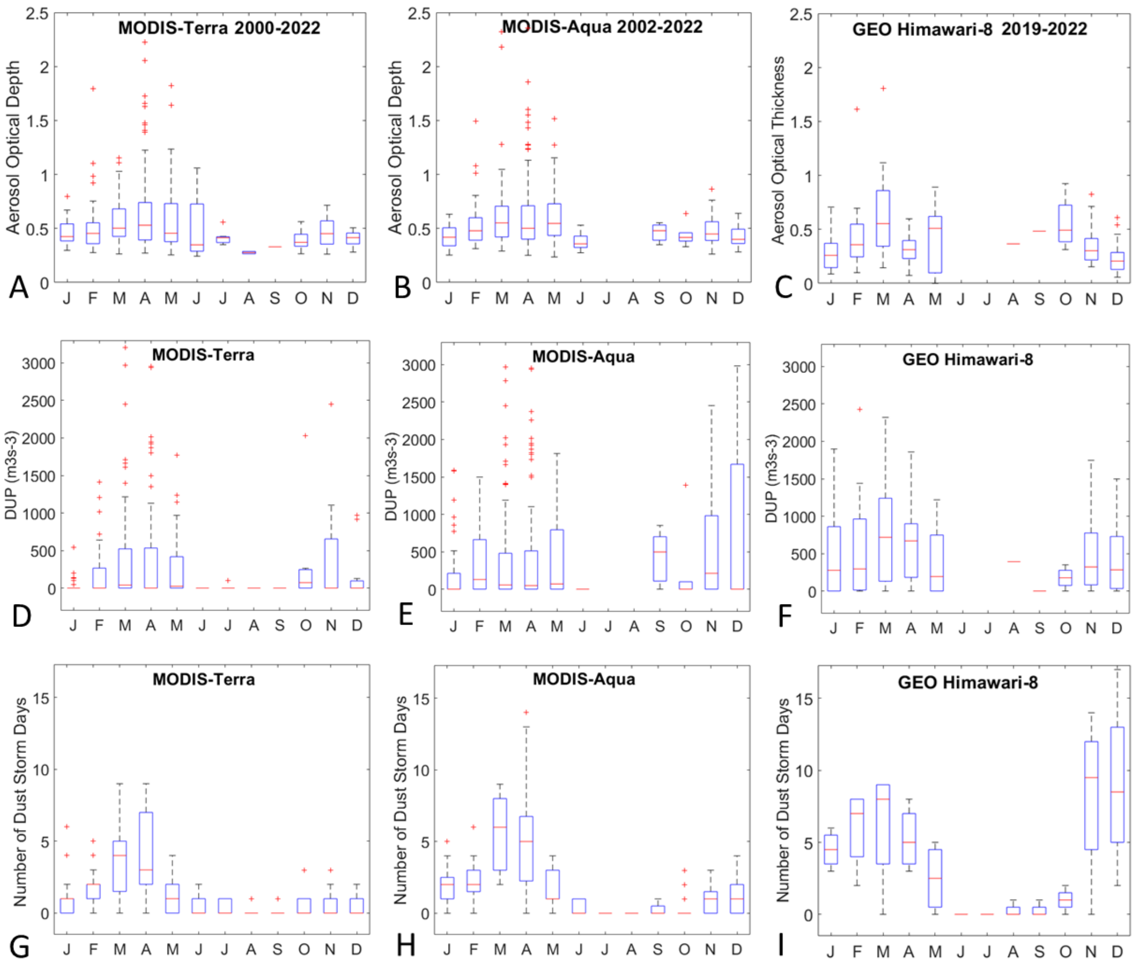

Figure 5.4 Annual Cycle of Dust relates factors. The first two columns are the LEO dataset (2000-2022), showing MODIS-Terra and Aqua, respectively, and the third column is the GEO dataset (2019-2022). The first row is the AOD, the second is the Dust Uplift Potential (DUP), and the third row is the number of Dust Storm Days (DSD).

Dust mobilisation is forced by meteorological processes varying in time or following diurnal cycles (Nobakht et al., 2021). GEO Himawari-8 VIS data can be used effectively for SDS observation but are best utilised for direct integration with meteorological data to link SDS observations to climate phenomena at an appropriate time-scale (hourly, sub-daily). It was proved in this thesis that various dust mechanisms influence wind intensity and peak timing (Figure 5.5 B), influencing SDS timing (Figure 5.5 A). In other dust source regions, such as the Sahara Desert (Schepanski et al., 2007; 2009) and the Middle East (Hennen et al., 2019), SDSs often occur after sunrise and the end of the nighttime inversion. Himawari-8 TCI is advantageous for observing dust plumes, especially for short durations or small dust activation events. Using Himawari-8 to build sub-daily (10 hour/10 min) dust detection in the

Gonghe basin, I found that the peak frequency of SDS is between 13.00 and 15.00 CST. Compared with the Middle East (6:00 and 12:00), Gonghe SDSs are much later. In Northwest China, similarly, He et al. (2020) confirmed that SDS occurs suddenly in tens of minutes during the late afternoon. Here, the wind speed gradually increases from 0.00 (CST), peaks at 15.00 or 16.00 (CST), and then gradually decreases during the night. SDSs occurring in the morning are more likely to be recorded in LEO and GEO. Afternoon has higher DUP and more DSD (Fig 5.5 B and C). Even when we account for the impact of the cloud, the actual ground DSD is still underestimated by RS (both GEO and Mod-LEO). Cloud is more likely to form in QTP in the afternoon (Shang et al., 2018), constraining the GEO's observations.

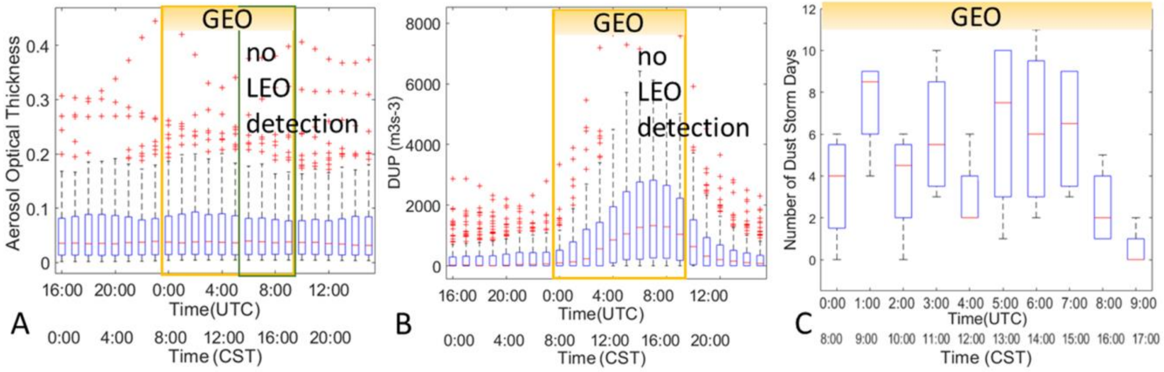

Figure 5.5 (A) Himawari-8 detected DSD's 24-hour Dust Extinction AOT from Merra-2 Reanalysis data; (B) Himawari-8 detected DSD's 24-hour DUP from Merra-2 Reanalysis data; (C) Number of Himawari-8 detected DSD start time sub-daily distribution, from 2019 to 2022 in the Gonghe Basin, China. [Figure 5.4 A reused from Appendix K, A part]

Dust Source Hotspots were detected for frontal-caused SDS using the existing AOD thresholds approach by Himawari-8. To locate the dust source accurately, the AOD image should coincide with the moment of emission or be closest in time to the moment of emission. Schepanski et al. (2012) suggested the advantages of using a manual method to select images is more appropriate for generating detail and helping to find the timing for optimal detection. Although Himawari-8 demonstrated that it could accurately record the time of dust generation, the dust mask screening method only deterministically produces many dust observations (Jin et al., 2019). Kahn et al. (2009) suggested that AOD values are a product of atmospheric SDS and dispersion, not always coinciding with the dust source's location. Himawari-8 AOD products are effective in detecting and quantifying emissions from constantly emitting dust sources but have limitations for detecting DPSs. Therefore, high spatial resolution data are crucial for locating accurate dust sources.

5.1.3 What component of the dust cycle can we detect using data with high space/time resolutions [e.g., Landsat/Sentinel-2/Planet/Himawari-8]

Baddock et al. (2021) demonstrated that dust point source [DPS] details could be captured using PlanetScope and DPS data can be aggregated and visualised. CubeSat data (e.g., Planet) addresses aspects of this limitation by providing precise identification of the upwind origin of SDS, and detailed information about emission processes in small-scale geomorphological settings. Observing dust at the emission source is critical, as its geomorphology varies between different source regions and determines the importance of the emissions and the factors that control emissions. Accurately simulating the dispersion of dust requires knowledge of the location of dust sources (Iraji et al., 2021), and knowing dust particles' properties helps improve dust in climate models (Bohlmann et al., 2018). A combination of HR-LEO (Sentinel-2 and Landsat-8/9) and CubeSat is the best data to capture for SDS activity at a scale appropriate to PDS schemes but operates at a very low sample rate (often less than 10 % of all detectable SDS are represented in these data). Using the synthetic HR-LEO datasets expands the overpass time window, which increases the chance of observing the basin and detecting DPS. Therefore, based on the Pre/Post-Frontal SDS identified by Himawari-8, I found 14 of the corresponding cases near the HR-LEO/CubeSat overpass time [02.00 – 04.30 UTC].

My research has found that dust sources identified using GEO and synthetic HR-LEO data have broadly similar spatial patterns and surface characteristics (Fig 5.6). A large part of the recorded SDS "hot spots" is concentrated in the 'Source B' area in spring and Autumn, while the spatial coverage of dust sources in winter is relatively broad in 'Source A/B/C/D'. Frequency occurrence of AOT (Fo-AOT) from Himawari-8 on the left side of Fig 5.6, the yellow and red grid cells represent that over 50% of the time the site is captured with SDS, and the AOD value of the Pixel is >0.2 threshold, so it is recorded as present of dust (reused from Figure 3.14). FO-AOT in spring is 10.9%, 8.6% in Autumn, and 25% in Winter. Also, when mapping the Active Dust Source (ADS) area, seasonality is going to be missed, that also quite biased.

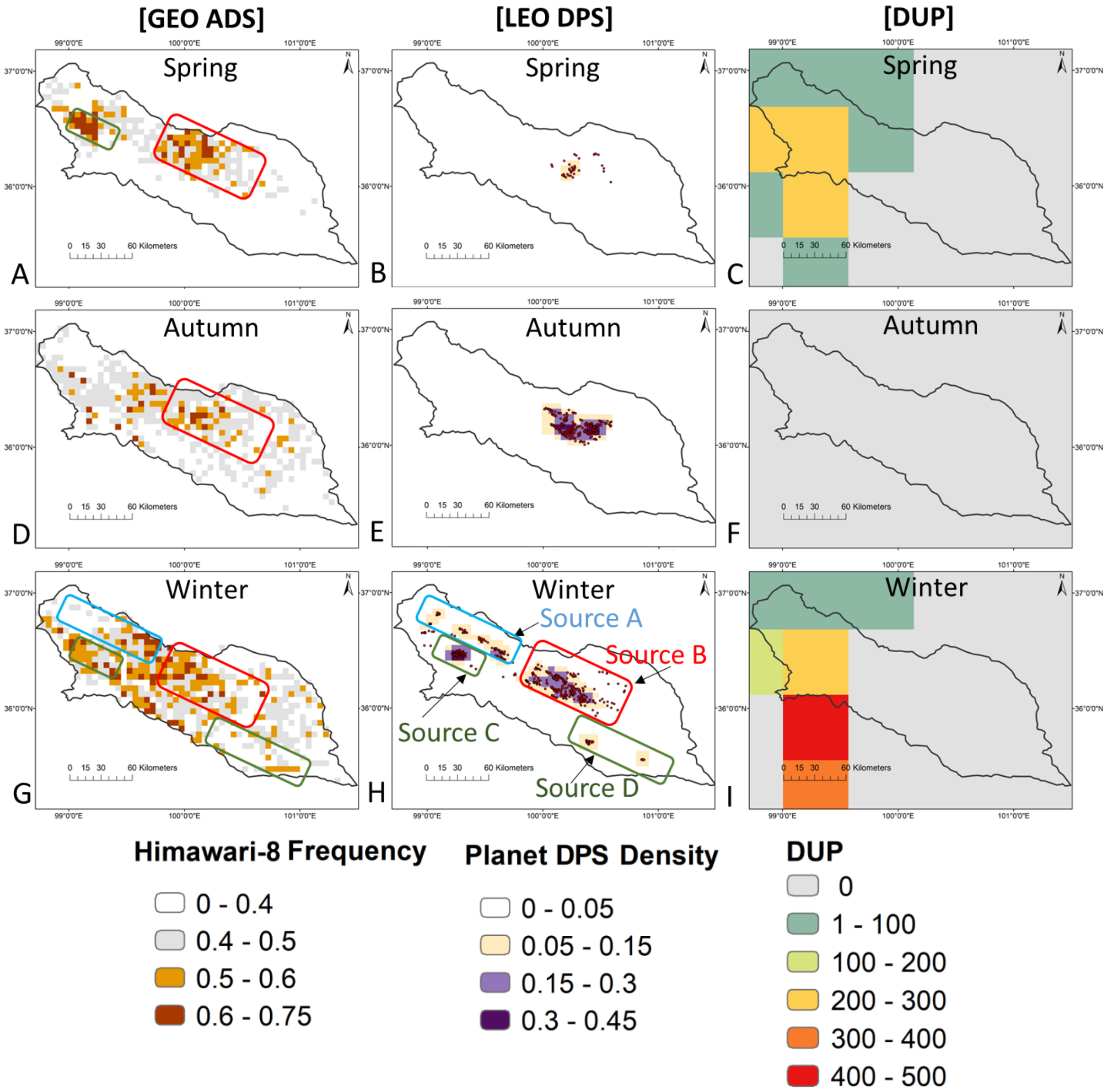

Figure 5.6 Seasonal difference of source area from GEO (Left) and HR-LEO (Middle) with pixel size 5km and seasonal difference of DUP (Right) in the Gonghe basin 2019-2023. Frequency Occurrence of AOT (Fo-AOT): Frontal Dust detected by Himawari-8 AOT (Left) data and Dust Point Source (DPS) density: 14 frontal dust cases captured by Planet (Middle) and visually pinpointed to the source area. Threshold Wind Velocity (TWV) is 6 ms^{-1}, *Where wind speed is lower than TWV,* then the DUP =0 in that area (Based on equation 2 in Chapter 2).

To compare the GEO (Himawari-8) and synthetic HR-LEO datasets, HR-LEO (Planet) derived point density is represented by 5 km grid cells to compare the GEO and HR-LEO datasets. The high-frequency area of the HR-LEO (middle of Figure 5.6 which reanalysis from Figure 4.9) are generally more concentrated than GEO (left side of Figure 5.6), and these emission 'hot spots' only account for 1.2% of the area of Gonghe in Spring, 7.7% in Autumn, 16.1% in Winter. Still, almost all DPSs are included. Hotspots are mainly composed of three landform types in the Gonghe Basin. (i) Aeolian sand dune and sand sheet. These areas generate many DPSs, formed by the emission of multiple discrete dust sources, mainly distributed in ‘Source B’ (Red Rectangle), which is formed by historical dust activity; (ii) Ephemeral lakes mainly located in ‘Source A’ (Blue); (iii) Alluvial deposit, which mainly contains cultivated areas affected by human activities and distributed in ‘Source C’ and D (Green) activation in winter.

The spatial location differences of dust sources observed by GEO and HR-LEO sensors are caused by three key factors. These three factors are (i) Detection method, (ii) Downwind Movement, and (iii) RS observation timing.

I applied different dust source detection approaches based on the RS’s Spatial-Temporal characteristics in Chapters 3 and 4. Using Planet's high-spatial-resolution images, manually pinpointing helps accurately track back to the plume source. Still, Planet can only observe the instantaneous emissions that occur at 02.00 - 04.00 UTC in the morning. The high temporal resolution of Himawari-8 includes TCI and AOD products, in which TCI allows us to observe the SDS emission process and determine the start time. However, identifying dust sources from the GEO TCI with low spatial resolution is too subjective and inaccurate. Thus, combined with Himawari-8 AOD products, Dust is screened through the threshold to quantify the dust source objectively. There is a time gap between Himawari-8 TCI recognition of dust and AOD detecting dust, causing some SDSs to be missing from AOD detection. Dust plumes can be observed in TCI from 08.00 to 09.00 UTC in the afternoon, but there is no AOD data available due to SDS not reaching the height that AOD products can recognise before daytime. The trajectory (Section 4.4.5) results suggested that the spread height of dust in the morning is higher than in the afternoon, so capturing AOD (dust) in the morning is more accessible. Also, AOT only works with a certain degree of sunlight. Too early or late in the daytime has no AOD data available. Chappell et al. (2023) revealed little spatial relationship between DOD (=AOD) frequency and satellite-observed DPS, with differences up to 2 orders of magnitude.

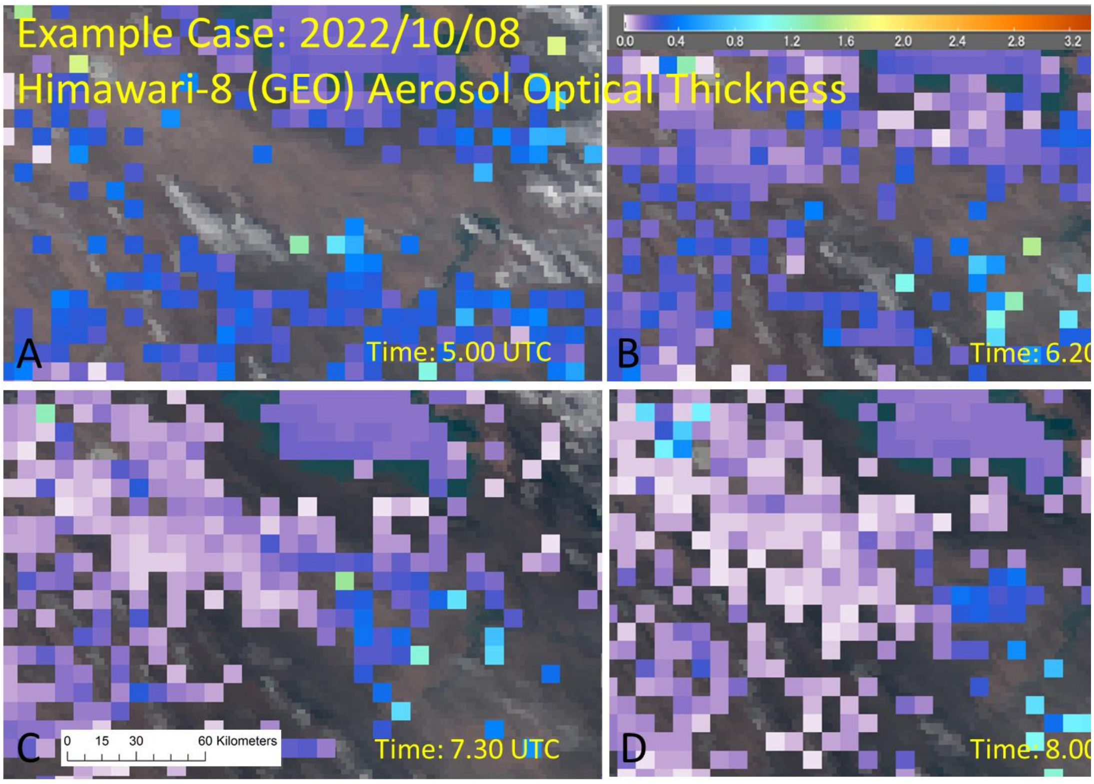

Figure 5.7 An example case of GEO (Himawari-8) satellite Aerosol Optical Thickness (AOT) products in different times of 2022/10/08. Time: (A) 05.00 UTC; (B) 06.20 UTC; (C)07.30 UTC; (D) 08.00 UTC. [Reused from Appendix H]

The spatial offset caused by the movement of dust downwind is evident and related to the timing of sensor-captured SDS. Northwestern winds dominate the Gonghe Basin, so dust particles are transported south-eastward. Figure 5.7 shows the downwind movement of dust retrieved by Himawari-8 AOD during 05.00 - 08.00 UTC since dust starts emitted, which indicates that Himawari-8 could capture SDS from the source but also capture plume transport downwind, causing some misdetection of DPS location. This perhaps explains why Himawari-8 detected an extra hotspot area than Planet in winter (Figure 5.6 G). Similarly, Nobakht et al. (2021) found that the DPS did not always correlate with high atmospheric optical depth (AOD) in the southern Taklimakan, where few DPS were detected despite the high AOD values using MODIS data, and they attributed it to dust transport from the upwind sources. Actually, Nobakht et al. (2021) frequency of occurrence of the DOD (FO-DOD) map includes the Gonghe Basin at the edge of Figure 5.8, and the FO-DOD of Gonghe is about 20%, but no DPS was pointed out. However, given what I know from Gonghe, it is very likely that Nobakht et al. (2021) are missing key components. Although they identified Gonghe as a dust source, MODIS with lower temporal resolution affect accurate source distribution, also those small DPS (on a regional scale) are missed.

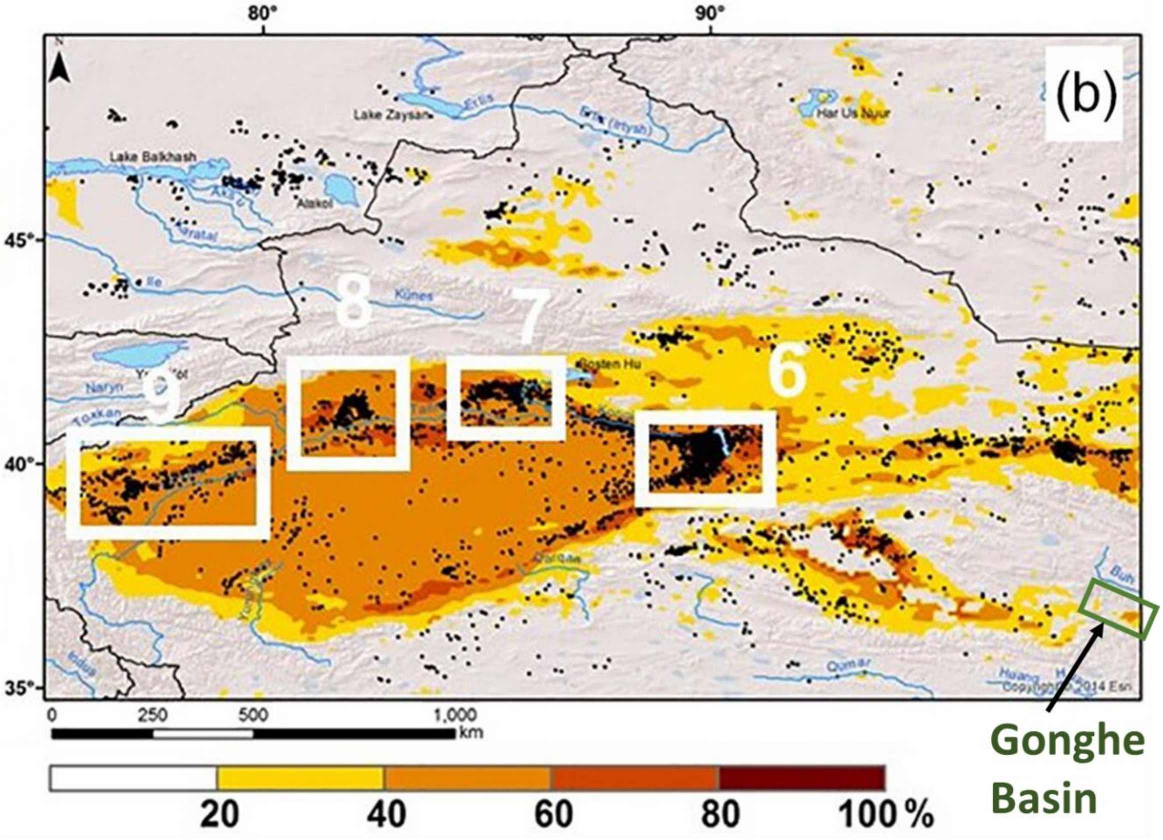

Figure 5.8 Locations of DPS (black dots) in the Northwest of China. The summer and spring frequency of occurrence of DOD (FO-DOD) are used as background. The white box highlights the dust sources: 6-Lake Lop Nur; 7-the Konqi alluvial fan; 8-the Aksu and Muzart; 9-the Yarkand and Green Box highlight the Gonghe Basin. (Reproduced from Nobakht et al., 2021; Fig.3B).

RS data that do not capture the onset of SDSs miss capturing some discrete sources. Typically, higher spatial resolution data can identify more details and thus distinguish more individual plumes, e.g., Planet found more DPS than Sentinel-2 (Figure 5.9). However, there are some notable exceptions: (i) Although Landsat-8's coverage rate and spatial resolution are lower than Planet and Sentinel-2, Landsat-8 happened to capture several small DPS that Sentinel-2 and Planet did not observe. (ii) Dust source C area was detected in Himawari-8, but it was not observed emission in Planet, resulting from Planet's low sample (only 2 cases) in Spring 2019-2023. Frontal dust occurs more frequently in the afternoon than in the morning. Still, Planet only captures SDS in the morning, usually in the early emission phase, which is easy to track back, but the number of observed DPS is also low. These two examples highlight the limitations of HR-LEO; discrete sources can be missed if not captured at the time of emission. Many studies recognised SDSs as a small-scale stochastic process (Shao et al., 2011; Kok et al., 2014; Bullard, 2010).

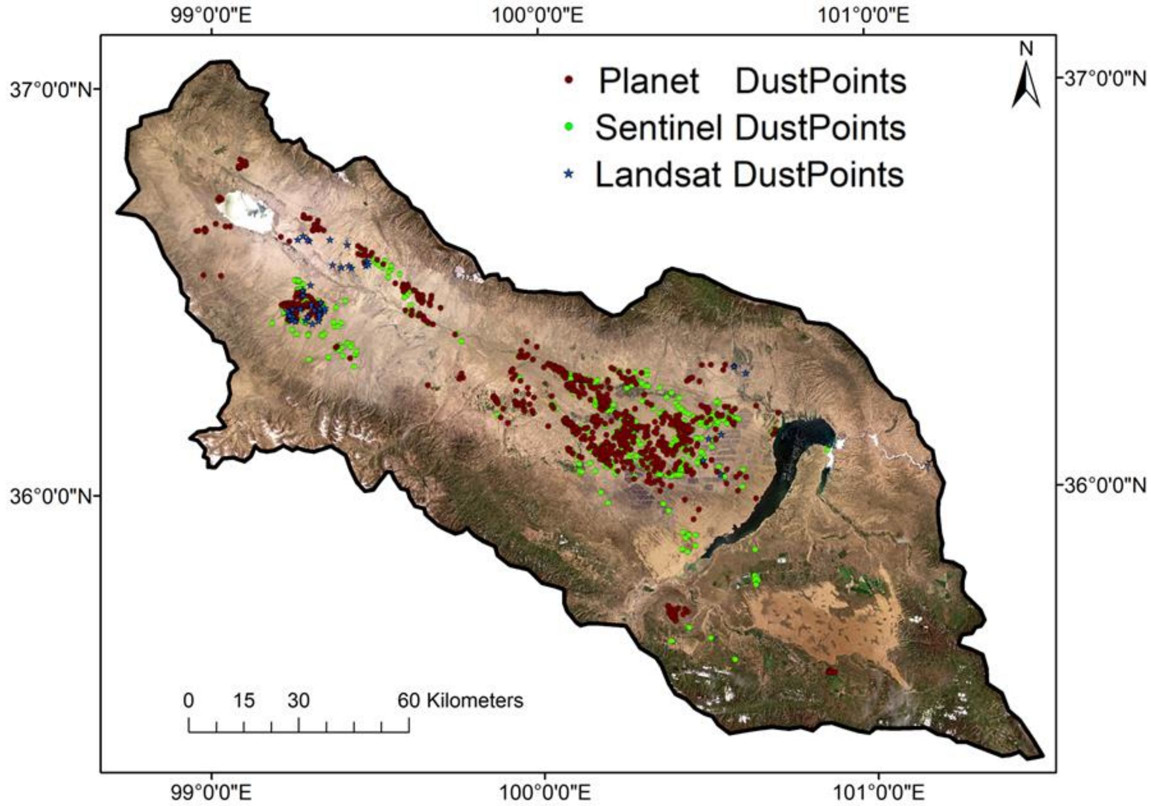

Figure 5.9 The DSP [QC1 only] distribution of 14 case events during 2019-2023. The red point represents dust points detected from the Planet, green points from Sentinel, and blue stars from Landsat. Basemap derived from Planet monthly basemap June 2023, the Gonghe Basin, China. [Reused from Figure 4.9]

In this study, subjective interpretations were made in selecting the time of day for the AOD image that best represented the dust source in GEO, manually tracking the plume, and locating the DSP position in HR-LEO, with a low likelihood of accurately replicating the results. Lavi Bekin et al. (2020) used MSG-SEVIRI dust RGB data to map dust sources in Northern Africa. Their visual comparison with RS images suggested that visually interpreting dust sources can be considered reliable.

5.2 Wider importance of SDS observed in the Gonghe Basin

The central motivation of this paper is to understand SDS control. While the content of Chapters 2-4 focuse on how dust sources can be characterised using remote sensing, it is helpful to consider that my results have broader implications for facilitating improved modelling and more effective dune management/mitigation. Here, I first discuss the emission characteristics of geomorphological features within the basin, comparing other sources in China and globally. Secondly, I consider the importance of environmental conditions, discussing how SDS and aeolian landforms respond to climate impact in Quaternary and the 21st century. Finally, I examine human-induced changes to the environment, focusing on the farmland, solar power plants, and sand dunes in Gonghe and how desertification management projects and economic policy have a two-way effect on the emission potential of these land surfaces.

5.2.1 How do Gonghe Basin SDS data compare to other dust sources in China and globally?

Characterising the relative importance of the emission of different landforms is an essential step towards regional/global erosivity mapping and specifying dust sources in regional/global models (Parajuli and Zender 2017). I applied the Bullard (2011) Preferential Dust Sources (PDS) scheme in the Gonghe Basin and examined the relationship between landscape and SDSs over the seasonal cycle, demonstrating the spatial and temporal heterogeneity of emissions. For most geomorphology types, SDSs are highest in winter and lowest in spring based on planet-derived DPSs (Chapter 4). The Aeolian Sand dune (5a, 5b) is the dominant dust source in three seasons (winter, spring, and autumn), followed by Low-Relief (LR)-Alluvial and Ephemeral Lake the seasonal variation in their emission potential was more pronounced. The LR-Alluvial system (3c, 3d) becomes vital for SDS in winter, which can be explained by the land-use scheme, as agricultural land erosion is possible in winter. Ephemeral Lake (1b) is sensitive in autumn and winter, while HR-Alluvial (2c), stone pavement (4), and Wet lakes (1a) are characterised by low emissions (Figure 4.11). Cui et al. (2019) applied the PDS scheme in northern China's Tengger Desert and Mu Us Sandy Land. The ranking of emission potentials is based on PI-SWERL: disturbed surfaces> sparse grasslands and coppice dunes>wadis>interdunes and dunes. This ranking is different from the Gonghe, which revealed that sand dune is not the typical dust source in China.

Many studies have shown that the primary dust source in arid regions of China is the 'Gobi' desert (Bird et al., 2015; Chen et al. (2017)) and alluvial deposits adjacent to the Gobi desert (Wang et al., 2006; Ahmadi-Molaverdi et al., 2022), whereas sandy deserts with relatively high vegetation cover or extensively covered by mobile sand are not a major source of sand and dust (Wang et al., 2008). Figure 5.10 shows that the Gobi region distribution includes the southern Tarim Basin, the Alaxa Plateau, and southern Mongolia. These erodible particles are deposited by intermittent flooding in the mountains, while weathering and wind erosion processes acting on the rough parts of the Gobi/Dune surface also produce fine particles (Niu et al., (2019). Shifting dunes are also not a major source of dust, and after prolonged periods of intense wind erosion, the well-sorted nature of sand dunes often prevents them from being considered a major source of dust (PM_{50} that particle <50 μm in diameter usually < 4%, Wang et al., 2005). The SDSs potential is lower in other sandy desert areas, such as northern Gurbantunggut and eastern Taklamakan, where surfaces with dense gravel or high vegetation cover inhibit SDSs (Wang et al., 2008).

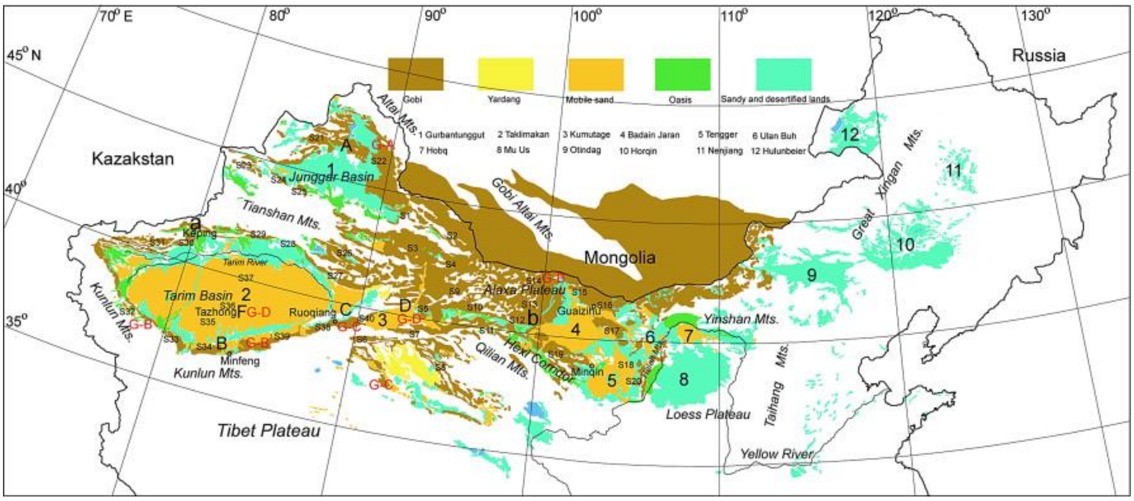

Figure 5.10 Geomorphology of Northern China and Mongolia, showing the distribution of sandy and Gobi deserts. The numbers 1 to 12 indicate major sandy deserts; G-A to G-D identify the four major Gobi. Gonghe was classified as a sandy desert (Reproduced from Wang et al., 2008, Figure 2*).*

However, recent studies have shown that sand dunes can sometimes be a main dust source. (i) In the absence of vegetation, dune systems produce a large proportion of fine dust by removing iron oxide and clay coatings of dust grains during saltation (Bullard and White., 2005; Swet et al., 2019). (ii) Coppice dunes stabilised by vegetation contain abundant erodible particles much higher than in ephemeral lake systems and have very high SDS potential. Once coppice dunes are anthropogenically disturbed, such as overgrazing and groundwater depletion, they may become a major source of dust (Sweeney et al., 2016). (iii) The basin has a long history of aeolian activity and abundant sand sources, e.g., Gonghe Basin (Detail in Section 5.2.2). Sand Dunes have a relatively high proportion of fine particles (clays and silts) in the Gonghe Basin, producing sustained and high-intensity emissions under strong Wind. Zhang et al. (2022) confirmed that fine-grained wind-formed sediments in the northeastern Tibetan Plateau are ideal sites for SDSs. Furthermore, Blowout development can lead to the reactivation of palaeodunes (Luo et al., 2018), which consistently produce fine particles, emphasising the importance of sediment supply in controlling SDSs.

Many arid and semi-arid regions have permanent and ephemeral river systems that occur in many arid and semi-arid regions (Powell, 2009). Fluvial systems play an important role in areas dominated by wind and sand, and they act as agents of wind-sand landscape formation in many arid and semi-arid regions (Davidson et al., 2011). Contemporary drying of lakes is particularly prevalent due to the over-abstraction of water for irrigation, poor water management, and the observed warming of the climate (Liu et al., 2019). The ephemeral lake was recognised as a prominent dust source in many regions (Kandakji et al., 2020; Ginoux et al., 2012; Hennen et al., 2019) and a major source in a wide range of areas, including Lake Urmia in a northwestern Iran (Boroughani et al., 2019), in Xinjiang, China (Liu et al., 2021). Nobakht et al. (2021) found that SDSs in the Taklamakan region are mainly associated with river systems and alluvial deposits. Ephemeral erodibility is closely related to the availability of water resources in this arid region. Dust sources are concentrated along the Tarim and its tributaries and east of Lake Lop Nur, where it dried up. In the Gonghe, Ephemeral Lake is the second high-potential SDS source. For example, since October, the Low precipitation has decreased water levels, leading to Chaka lakes' drying up, becoming active dust sources in Autumn and Winter.

Changes in the availability of erodible sediment cause alluvial deposit seasonal changes in emissions. On monthly or seasonal scales, soil erodibility is primarily controlled by sediment availability rather than sediment supply (Cui et al., 2019). Dynamic changes in soil moisture, vegetation conditions, and soil surface crusting strongly impact SDSs (Webb and Strong 2011). Bullard et al. (2011) suggested that farmland SDSs exhibit strong seasonality associated with farming and irrigation. LR-Alluvial distributes most of the vegetation and cultivated land in Gonghe, and vegetation cover variation is a major contributor to the seasonality of alluvial emissions. Another example of alluvial fans used in agriculture is the Taklimakan, and SDSs occur mainly on farmland edges and abandoned or degraded farmland (Nobakht et al., 2021). Despite the cultivated area being smaller, these areas can be strong sources of dust due to human disturbance, which reduces the stability of soils against wind erosion and largely increases the availability of fine particles for SDSs. The sediment availability is limited by emissions attenuation over time.

The limitation of the PDS scheme is that it requires specific inputs to map the landscape, which does not apply to all areas, and its crucial requirement is to identify and create surface classes or geomorphological units, which can easily be subjective. The PDS scheme exhibits a limited scope as it only encompasses seven classes. However, it fails to consider the influence of human impact on surfaces and cannot account for the complexity and older deposits. Moreover, it does not effectively transfer to different contexts. Hence, the PDS scheme may need to be revised when classifying land surfaces in China.

5.2.1 What are the implications for aeolian processes (dunes in the Gonghe Basin) driving the dust cycle?

Research on desertification during the geological history of the Gonghe Basin focuses on the evolution of landforms, sedimentary strata (Qiang et al., 2016), the history of aeolian activity (Dong et al., 2017) and its driving mechanism (Jia et al., 2023), which is significant for understanding the control factors of SDS. The extensive development of sand dunes in the Gonghe Basin is based on the abundant supply of dust sediments formed by transforming alluvial and lake sediments from the Early and Middle Pleistocene (Xu et al., 1982). The oldest formation history of aeolian sand in the Gonghe Basin is 33.5±2.1 ka BP (Qiang et al., 2013). In the early and middle Holocene, affected by the westerlies, the basin had a predominantly arid climate and developed sand dune fields. Dune was fixed in the late Holocene, under the influence of the Asian summer monsoon-caused humid climate background (Liu et al., 2020).

Currently, the aeolian landform materials in the Gonghe Basin are derived from the erosion of sediments, lake materials, and the weathering of exposed and semi-exposed gravels. The main inland river in the Gonghe Basin is the Shazhuyu River, and the main outflow river in the area is the Yellow River. The rivers erode surface materials and carry large amounts of sand, creating a stable and abundant sand source in the flat and wide valley. Northwest winds produced a large amount of fine sediment development of aeolian sand dune landform of about 4955 km^2 (Table 4.4). The aeolian sand landform is distributed in a belt along the river valley in the highland plains and Yellow River terraces (Dong et al., 2017). Depending on the distance from the water body, there is an alternating pattern of shifting dunes and fixed and semi-fixed dunes with sparse vegetation. Qi et al. (2021) confirmed that the migration direction of shifting dunes in the Gonghe Basin has mostly been consistent with the wind direction in the past 30 years, mainly in the low-relief area in the centre of the basin and on the windward slopes of the foothills, migrating toward the northwest. Direct risks brought by sand dune movement include sand dune encroachment on farm buildings, risks of filling the Longyangxia Dam reservoir and erosion of solar power plants in the downwind area (Baird, 2021). The height of the Tibetan Plateau (>1000m) is very conducive to the transportation of dust materials to the deposition area (Zhang et al., 2022). Dust sources in the TP blowing to the downwind area have also been identified as the primary loess sources (Wang et al., 2008).

Since the Tibetan Plateau is located between these different climate systems, climate change has various impacts on the Tibetan Plateau (Chen et al., 2021). The Gonghe Basin is affected by the Asian monsoon circulation and the mid-latitude westerly circulation, resulting in wet summers and dry winters (Liu et al., 2020). In Chapter 2, I found that the frequency of SDSs is related to climate conditions such as wind speed, snow cover, and vegetation. The Gonghe Basin became warmer and drier between 2000-2022. Wind speed, relative humidity, and DOD decreased, while NDVI, rainfall, soil moisture, and temperature gradually increased. Precipitation and temperature promote the increase in vegetation coverage, accompanied by an increase in surface soil moisture. Rising temperatures weaken the temperature gradient on the Tibetan Plateau and reduce wind speeds. Improved dust availability and reduced the transport wind capacity, reducing aeolian activity. Overall, these changing trends have been beneficial in reducing the frequency of SDSs in the Gonghe Basin in the past two decades.

Wind speed is positively correlated to dust occurrence. Dust activity and wind speed showed a clear diurnal pattern and seasonal cycle, with low frequency in the morning and higher in the afternoon, with higher values from November to April in the Gonghe Basin (Chapters 2 and 3 results). Strong winds transport cold and dry air masses to the Gonghe Basin in winter and Spring. According to the findings by Dörwald et al. (2023), the impact of the Westerlies during the spring and winter seasons leads to a heightened intensity of the DP. Conversely, during summer and autumn, the winds of the East Asian Summer Monsoon (EASM) originating from the southeast contribute to a weakening of the Resultant Drift Potential (RDP) while not reversing the prevailing wind direction, which generally flows from the northwest. The overall trend of the basin is consistent with the prevailing wind direction, which is conducive to invading prevailing winds. Although the basic processes controlling aeolian emissions at high latitudes are essentially the same as in temperate regions, there are additional processes that are specific to or enhanced in cold regions, including low temperatures, humidity, strong winds, and permafrost (Bullard et al., 2016), all of which influence the timing of SDSs (Bullard et al., 2013). The higher altitude leads to low air density and temperature, which strongly changes the airflow characteristics and the resulting wind and sand movement (Dong et al., 2017). Winds in cold environments transport sediments more efficiently than winds in warm environments. Cold air is denser and more turbulent than warm air and can exert a greater drag on particles (Bullard et al., 2016). In addition, at a given wind speed, increasing altitude when the air density is lower, the saltation jump height is higher than at low altitudes (Han et al., 2014).

Furthermore, it has long been recognised that soil moisture availability (e.g., alternating wetting and drying, freeze-thaw cycles) plays an important role in regulating aggregate stability (Cui et al., 2019; Webb and Strong, 2011). In the semi-arid Gonghe Basin, occasional heavy snowfalls lead to no SDS in that month (such as in November 2020). Therefore, I suggested that snow cover is the key factor in controlling SDSs in winter.

5.2.3 How Human-Induced Change Impacts Desertification and SDS?

The frequency and location of SDS are also closely related to human impacts such as grazing, farming, dune stabilisation and greening. Table 4.4 shows that agricultural areas and solar power plants are considered medium erodible areas, indicating the presence of potential for anthropogenic dust in the Gonghe region. The successive introduction and implementation of economic promotion policies and ecological environment projects have a two-way effect on desertification changes (Xu, Luo, and Chen 2021).

The development of desertification is attributed to the unreasonable and intensive use of land by economic promotion policies in the context of population explosion (Shao et al., 2023). In the primary stage of social development, especially in developing countries, population and economic growth are always accompanied by the destruction of the ecological environment (Lu et al., 2017). Since the 21st century, many economic policies have been implemented in China, such as the Great Western Development Strategy in 2000 and the New Rural Development Strategy in 2004 (Li et al., 2015). These policies impact land use changes, converting large amounts of grassland, sand sheet, and unused land into artificial surfaces, including towns, cultivated land, and roads. In addition, the cancellation of agricultural taxes in 2005 and the reform of the system of collective rights and land transfer in 2008 promoted agricultural development (Qi, 2016), causing local economic development while further intensifying desertification, e.g., Mu Us Sandy Land in North China, (Xie, Lu, and Feng 2022). In the Gonghe Basin, Yan et al. (2009) explored the dramatic increase in livestock numbers since the mid-20th century and attempted to reclaim farmland in the semi-arid basin in the late 1980s have led to severe desertification processes; Meng et al. (2016) suggested the total population of the Gonghe Basin in 2013 was 212,700, with an average annual growth rate of approximately 4.13%, and an urbanisation rate of 41.62%; Dörwald et al. (2023) confirmed the agricultural area increased by 23.7% from 1968 to 2022 (from 636 km^2 to 787 km^2). Overall, anthropogenic factors include population and economic growth, overgrazing, over reclamation and road expansion (Niu et al., 2023), and poorly managed land induces desertification and subsequent dune migration and emission (Xie, Lu, and Feng, 2022).

Ecological protection projects help control the development of desertification to a certain extent, reducing SDSs. A series of environmental protection policies have been introduced, including the widely implemented Three-North Shelterbelt Project (Li et al., 2012), the Natural Forest Conservation Program (Cao et al., 2010), Desert Prevention and Transformation in 2001 and the Grazing Forbidden Project in 2012 (Liu et al., 2008). The straw checkerboard barrier is a common measure to fix dune migration and is widely used to protect infrastructure (e.g., railway) in North China (Wang, Qu, and Niu 2020). Zhang et al. (2023) evaluated the impact of an ecological restoration program in South China karst. Conversion of farmland to forest successfully relieved farmers from low-productivity land, and it played a positive role in greening and reduced disturbance during the restoration process. However, ecological quality is generally negatively related to economic development. In Gonghe, the construction of the Solar Power Station has impacted the local climate, such as an increase in daytime temperatures and an increase in nearby humidity, creating favourable conditions for vegetation growth (Wu et al., 2020). This will increase sand surface stickiness, making it less likely to be ejected by wind, potentially reducing the frequency of sandstorms (Lu, 2013). For example, the dry steppe is the main dust source in Balkhash-Junggar and has a higher threshold friction velocity than any other subregion (Xi and Sokolik, 2015). Nevertheless, the water supply in a semi-arid Gonghe region characterised by total precipitation (<300 mm/year, Chapter 2) is insufficient to satisfy the water requirements for afforestation and crop cultivation in most areas.

Human activities, particularly the utilisation of surface water and groundwater for irrigation purposes, have the potential to cause water redistribution within the soil profile and alter the dynamics of moisture exchange between soil layers and aquifers (Long et al., 2015), especially for the Gonghe, where the water resource carrying capacity is low (Meng et al., 2016). The total water area of lakes in the Gonghe Basin decreased significantly from the 1950s to the 1980s, mainly due to the basin experiencing an intensive stage of agricultural development in the past few decades (Wu et al., 2016). The cultivated area is 632 km^2, of which the irrigated farmland area is 238 km^2 (Meng et al., 2016). A large portion of the runoff from reservoirs along the Shazhuyu River and its tributaries is redistributed to irrigate farmland. Besides, Groundwater from the Qiabuqia River Valley is used for daily residential and industrial water use. This resulted in lakes shrinking and causing half of the wetlands to dry up and degrade into saline-alkali lands (classified as 3d in the PDS scheme; Li et al 2017). Famiglietti (2014) discussed the global groundwater crisis, shedding light on the unsustainable pumping rates of groundwater in various regions, such as the North China Plain, Australia's Canning Basin, and the High Plains and Central Valley aquifers in the United States. These areas, which are in close proximity to agricultural regions, play a pivotal role in sustaining high agricultural productivity.

Wu et al. (2016) suggested that changes in lake areas have mainly been controlled by precipitation and temperature since 1990 in the Gonghe Basin. As the temperature increased slightly, a slight drying trend occurred, and some lake areas decreased sharply before remaining relatively stable. Zhang et al., (2019) support this opinion, with accelerated warming in the Tibetan Plateau from 1970 to 2018 leading to a multitude of consequences, including glacier melting, permafrost degradation, increased precipitation, and the expansion of lakes. On the other hand, there is evidence of a widespread decline in global lake water storage for 53% of these water bodies over the period 1992–2020 (Yao et al., 2023).

The Gonghe Basin is a relatively complex setting for a dust source. Firstly, its geographical location means that it is situated within the local advected and transport dust zone for upwind dust sources [e.g., Qaidam Basin, Taklimakan Desert]. Secondly, its location between the Asian Summer Monsoon (EASM) and the Westerlies climate systems influences the climate in the Gonghe Basin in various seasons: leading to wet summers and dry winters and evidence of fluctuation on decadal timescales. Thirdly, a long history of aeolian activity has led to the formation of diverse landforms, with areas of accessible and partially anchored sand dunes emerging as the predominant source areas. Lastly, it is essential to note that Gonghe experiences both natural and human impacts (Wu et al., 2016; Dörwald et al., 2023), further shaping its complex dust source characteristics. The main drivers of sand and dust control are climate factors, unsustainable human activities, and inappropriate policy measures. Accurately understanding the location and spatial-temporal heterogeneity of dust sources can help improve the efficiency of active dune management (Hennen et al., 2019) and reduce SDSs from high-PDS surfaces (Guo et al., 2019). Ecological restoration and economic development are negatively correlated (Zhang et al., 2023), and balancing both while considering the carrying capacity of regional natural resources (such as water resources) remains challenging.

5.3 Recommendations for future research

This thesis has made a significant contribution to our understanding of what controls emissions from a remote sensing perspective. There are several aspects of future research that I have suggested: (i) Investigate future RS design on the increase in space/time

/wavelength resolution of satellite record of Earth's land surface to improve the breadth and depth of actionable information freely available for research; (ii) Further field-work helped to build a comprehensive SDS story. Enhanced Remote Sensing data (e.g., Landsat Next) is helpful in identifying sources of SDS at high resolution, followed by ground-based measurements and improved characterisation of candidate surfaces in dust modelling, thereby allowing better estimates of SDS.

[O1] Calibration and validation of maps of dust sources for this basin derived from Remote Sensing data.

- Allow improved identification of candidate geomorphological surfaces that emit dust (e.g., active dunes, blowouts, nebkhas, dry/ephemeral lakes, irrigated agriculture and alluvial surfaces). Revised PDS scheme which includes Land Cover/Use (LULC). Sentinel-2 will support the operational generation of products such as the mapping of land cover, land use, change detection, and geophysical variables with coverage of the earth's land surface from -56° to +83° latitude (Krebs and Gunter, 2023).
- When classifying dust event types, except visually observing the phenological and meteorological characteristics of SDSs, secondary data should be brought in, such as observed rapid temperature drops could have been used to define haboobs, etc (Miller, et al., 2008).
- Underpin future research from the forthcoming Earth Surface Mineral Dust Source Investigation (EMIT) instrument on the International Space Station (ISS). The goal of the EMIT mission is to map where the dust originates and estimate its composition so that scientists can better understand how it affects the planet (NASA, 2023). The data collected by EMIT will underpin future research on the mineral composition of arid land dust source regions and its impact on climate. This research will help scientists better understand the role of mineral dust in the radiative forcing of the atmosphere and its impact on climate change (NASA, 2023).
- Enhancement of Satellite's spatial/temporal/spectral resolutions. Landsat Next signifies a significant advancement in measurement capabilities and will be

launched in late 2030 (Landsat Science, 2023). It is poised to gather 26 bands at a temporal revisit rate of 6 days, which is 15 more bands than what Landsat 8/9 offers with its 16-day repeat interval. Among these new bands, five possess comparable spatial (10-20 metre) and spectral attributes to those found in the Sentinel-2 mission, thereby facilitating improved data synergy and fusion. Additionally, there are 10 new spectral bands specifically designed to support various applications, including crop production and soil conservation (e.g., crop residues), climate and snow dynamics research (e.g., snow grain size and albedo), as well as mineral mapping based on thermal emissivity.

[O2] Surface sediment characterisation at each confirmed SDS source and use a PiSWIRL to determine the likely emission thresholds for SDS.

- It would be useful to generate shear velocity thresholds and relative PM dust flux (e.g., Raffaele, Bruno, and Wiggs, 2018) for all the PDS and DPS locations contained in this thesis However, it would be useful to build in a temporal component to cover the range of months in which SDS are apparent in each class.
- Assess other surface factors that affect erodibility, such as salt crusts, vegetation cover, microbiology crust and dune stability (e.g., Cui et al., 2019; Nauman et al., 2023; Katra, 2020; Nauman et al., 2023). The existence of those surface factors can increase soil stability and reduce erodibility by increasing soil cohesion and reducing soil porosity. Analyses of the surface samples were used to identify the significant factors controlling erodibility (Von Holdt et al., 2019). The accuracy in determining surface properties also constrains the performance of the models because it determines the threshold friction velocity for a surface (Parajuli et al., 2014). For example, incorporating information on vegetation cover and microbiology crust can help reduce the uncertainty in SDS estimates.

6. Conclusions

The aim of this PhD thesis has been to improve our understanding of controls on SDS from remote sensing in the Gonghe Basin, China. Given the remote and harsh nature of this location, synergistic remote sensing data are used with implement existing and novel methodologies to study SDS at greater spatial and temporal scales than previously accomplished. Specifically, it has focused on addressing the gaps surrounding the process and drivers of SDS and the nature of dust-emitting surfaces, identifying the season and interannual chronology, observing SDS activation timing and mechanism, and tracking Dust Source Point (DSP) from geomorphology and land use landforms. Below is a summary of the main findings of each empirical chapter.

Chapter 2 Aim: A season and interannual chronology and drivers of SDS in the Gonghe Basin [2000-2022] - [REGIONAL SCALE]

To initially detect SDS in the Gonghe Basin, a long-time series of MODIS [2000-2022, Terra/Aqua AOD, AE and DOD) data were used. Existing threshold-based methods were utilised and subsequently assessed. Data were used to detect and quantify SDS occurrence [as Dust Storm Days; DSD], MODIS [2000-2022, Terra/Aqua AOD, AE, DOD). Analysis revealed peak SDS seasons in DJF [average DOD = 0.293 in Terra; 0.32 in Aqua]and MAM [average DOD =0.332 in Terra; 0.385 in Aqua]. Typically, we recorded 19 DSD year^{-1} and the wind speed in DSD is about 6.3 ms^{-1}, higher than that in the non-DSD 3.2 ms^{-1}. Comparison of these data with reanalysis data (Merra-2) and contextual data (e.g., NDVI, snow cover, etc.) shows how SDS occurrence and intensity are strongly influenced by vegetation cover and DUP by controlling sediment availability [in DJF] and transport capability [in MAM]. Regional climate drivers, Westerlies [DJF] and East Asian Summer Monsoon (EASM) [JJA] have a weak positive influence on SDS occurrence. The frequency of SDS has declined over the last two decades, related to the reduction trend in wind speed, although a warming trend. Relative humidity shows a decreasing trend, while NDVI, rainfall, soil wetness, and temperature gradually increase. The Gonghe Basin is expected to witness a decreased occurrence of SDS in the future.

Chapter 3 Aim: Understanding controls on SDS in the Gonghe Basin using GEO data [2019-2022] - [BASIN SCALE]

Sub-daily assessment of SDS/DSD observed by MODIS was undertaken between 2019-2022 using GEO-stationary Himawari-8 data (VIS and AOT). This allowed derivation of SDS start time, duration, and prevailing DUP. The results show that cloud effects limit the observing time window of [10 minutes] Himawari-8 by 40% of the year. SDS mainly happened from November to May. Winter [DJF] has the lowest cloud cover and the highest number of DSD detections from Himawari-8, indicating that RS-detected dust loading in this region is still underestimated. Further, we find that MODIS [Terra/Aqua] overpass times [02.30 - 05.30 UTC] missed the peak DUP [08.00 UTC] and SDS start time [05:00 - 10.00 UTC], highlighting significant bias in recorded MODIS DSD, where 34.6% of SDS start between 05.30 - 10.00 UTC. The continuous and short interval of GEO data demonstrates the ability to provide a complete view of the SDS process in the daytime (00.00 – 10.00 UTC). GEO achieved insight into the temporal heterogeneity of emissions far beyond that revealed by the LEO satellite, increasing temporal resolution on the frequency of observed SDS.

Himawari-8 allows work at the scale of meteorological observations, thereby linking dust observations to climate phenomena. Dust activity in Gonghe attributed to four key types of SDS: Haboob [4.6 %], Haze [38.2 %], Pre/Post Frontal systems [47.4 %], and unidentified processes [9.8 %]. Haze and Frontal systems were found to be the main meteorological drivers of dust transport and emissions in the Gonghe. The wind speed of SDS shows a clear diurnal cycle. The wind speed gradually increases from 16.00 (UTC), peaks at 07.00 or 08.00 (UTC), and then gradually decreases during the night. Higher active dust source frequencies in the morning are mostly related to convective (Haze), while in the afternoon are more related to the breakdown of the Frontal Low-Level Jet (LLJ).

Chapter 4 Aim: Use of High-Resolution Low Earth Orbit [LEO] data for Dust Point Source [DPS] detection and derivation of Preferential Dust Source [PDS] and Land Cover/Use Characteristics. [SUB-BASIN SCALE]

Using a subset of observed SDS events, a new image enhancement workflow for high-resolution Sentinel-2 and PlanetScope imagery is presented to optimise the mapping of dust point sources (DPS) locations in the Gonghe Basin. These SDS events were then used to populate a Preferential Dust Source (PDS; Bullard et al. (2011)) geomorphic scheme to characterise the land surface signature of SDS in the Gonghe Basin, linking plumes to specific surface landforms. We find that approximately 70% of the DPS for the 14 events were emitted from aeolian dunes (PDS class: 5a and 5b), compared to 23.2% originating from alluvial deposits (PDS class: 2c, 3c, and 3d) and 5.6% from ephemeral lakes (PDS class: 1b). Also, considering human impact, cultivated land accounts for 40% of low-relief alluvial (PDS class: 3c), contributing half of the dust sources, and is active in winter, indicating the seasonal variation of dust sources. Nevertheless, dunes are not a typical dust source landform in China. Gonghe contains blowout dunes, once the dune's surface is destroyed, a large amount of coarse sediment with the saltation process causes the fine dust in the terrain to eject from the surface. The total dust mass was estimated for 14 SDSs is about 0.196-0.302 Tg. Most of the dust, approximately 84.7%, originated from aeolian dune. The forward HYSPLIT forward model revealed that Spring [MAM] and winter [DJF] are the seasons with the longest dust transport distances. However, autumn [SON] has the highest dust loading level and consistent transport direction. The Gonghe Basin is therefore a unique dust source region that has an implicit link between sand transport and SDS, and HYSPLIT trajectories suggest a large down-wind zone of deposition, post-24h impact on the downwind cities (e.g., Gansu, Xian).

- *Significance of Remote Sensing Data Selection for SDS Analysis*

From this thesis, RS data have their contributions to the exploration of different stages of SDS due to their different data characteristics. Integrated multiple RS can complement each other's shortcomings and provide the possibility for further understanding of SDSs. Combining AOD products from GEO and LEO satellite sensors can produce more comprehensive results. However, AOD products from satellite sensors are insufficient due to limited spatial/temporal coverage and cloud presence, hampering aerosol detection. Thus, it is necessary to combine HR LEO with visual pinpoint to identify the SDS location accurately.

Moderate Resolution LEO data have a lower detection rate than GEO data, but higher spatial resolution, and are capable of identifying a viable time-series DSD on a monthly/yearly basis; albeit with the expectation that a proportion of these events will be observed in transport rather than at source. GEO Himawari-8 VIS data can be used effectively for SDS observation, but are best utilised for direct integration with meteorological data to link SDS observations to climate phenomena at an appropriate time-scale (hourly, sub-daily). The continuous and short interval of GEO (Himawari-8) data also demonstrates an ability to provide a complete view of the daytime SDS process. Himawari-8 TCI is advantageous for observing dust plumes, even for short durations or small dust activation events. Himawari-8 AOD products are effective in detecting and quantifying emissions from constantly emitting dust sources but have limitations for detecting DPSs. CubeSat data (e.g., Planet) addresses aspects of this limitation by providing precise identification of the upwind origin of SDS, and detailed information about emission processes in small-scale geomorphological settings. A combination of HR-LEO and CubeSat is the best data to capture for SDSs activity at a scale appropriate to PDS schemes, but operates at a very low sample rate (often less than 10 % of all detectable SDS are represented in these data). Using the synthetic HR-LEO datasets expands the overpass time window, which increases the chance of observing the basin and detecting DPSs.

- *Dust Emission Controls*

The results of all three empirical chapters were then combined to explain the controls of SDS at the Gonghe Basin. (i) Regional scale, it was determined that the occurrence of dust during the winter and spring seasons is governed by limitations in wind capacity and the availability of sediment, such as vegetation, snow cover, and frozen sediment availability. In the Gonghe Basin specifically, the presence of Quaternary aeolian deposits and a robust fluvial system provide a sufficient supply of erodible fine sediment, thereby eliminating supply. (ii) Basin-scale, the presence of strong wind speeds emerges as the primary driver of SDSs. SDS shows a clear diurnal cycle that coincides with the diurnal cycle of wind. During winter and early spring, the Tibet Plateau experiences lower temperatures and higher air pressure compared to other months, resulting in higher air density and wind speeds. Higher-density airflow has a higher viscosity coefficient and can provide stronger shear stress. Consequently, dust activity is more prevalent during winter and early spring in the Gonghe Basin. (iii) Sub-basin Scale, dust is emitted from specific landforms. Aeolian deposits are the main dust source and are active except in summer. As for the alluvial system, the availability of sediment is limited by the wet/dry/frozen condition of the lake. Cultivated land experiences dust activity in the post-harvest crop period (winter), with sediment availability restricted by vegetation.

- *Implications of this thesis*

The most significant output from this thesis is using synergistic remote sensing to observe the process and drivers of SDS. This is the first dataset of its kind, and represents a leap in scale of processing controlling the location and activity of dust source regions at the sub-basin scale compared to previous SDS studies. SDS observations derived from LEO data with simultaneous observations made by GEO satellite data overcome sample bias: overpass time, spatial, and cloud existence. RS capture surface erodibility heterogeneity and link (in space and time) to the climate mechanisms driving the SDS at the sub-basin scale. The dust source and activation frequency detection method I have developed (Chapter 3) represents a significant step forward in monitoring capability. By implementing Bullard et al. (2009, 2008) proposed preferential dust source (PDS) geomorphic classification method and considering human impact applied LULC mapping, I have linked SDS observations with PDS and LULC landform scheme to quantify factors that may control the nature and magnitude of SDS, which could directly be relevant to modelling studies for accurate estimates of dust aerosol effects. This information is significant for the overall understanding of dust sources in China.

References

Adachi et al., (2007). Dust transport along a cold front: A case study of a cyclone observed on 19-20 April 2000 in Northeast Asia. Journal of Japan Society for Atmospheric Environment/Taiki Kankyo Gakkaishi, 42(6), 327-338.

Adebiyi and Kok (2020). 'Climate models miss most of the coarse dust in the atmosphere', Science Advances, 6(15), p. eaaz9507. Available at: https://doi.org/10.1126/sciadv.aaz9507.

Adebiyi et al., (2023). 'A review of coarse mineral dust in the Earth system', Aeolian Research, 60, p. 100849.

Ahmad et al., (2006) 'Aerosol index from TOMS and OMI measurements', 86th AMS Annual Meeting, 10.

Ahmadi-Molaverdi et al., (2022). Geomorphological and spatial analysis of dust sources in Ilam Province, Iran. Sedimentary Geology, 436, 106168.

Aili et al., (2021). A cluster analysis of forward trajectory to identify the transport pathway of salt-dust particles from dried bottom of Aral Sea, Central Asia. Atmosphere, 12(6), 764.

Aili, Oanh and Abuduwaili, (2016). 'Variation trends of dust storms in relation to meteorological conditions and anthropogenic impacts in the northeast edge of the Taklimakan Desert, China', Open Journal of Air Pollution, 5(4), pp. 127–143.

Ali et al., (2022). Assessment of Aeolian Activity in the Bodélé Depression, Chad: A Dense Spatiotemporal Time Series From Landsat-8 and Sentinel-2 Data. Frontiers in Environmental Science, 9, 808802.

Allen et al., (2015). Dust detection from ground-based observations in the summer global dust maximum: Results from Fennec 2011 and 2012 and implications for modeling and field observations. Journal of Geophysical Research: Atmospheres, 120(3), pp.897-916.

An et al., (2012) 'Interplay between the Westerlies and Asian monsoon recorded in Lake Qinghai sediments since 32 ka', Scientific Reports, 2, pp. 1–7. doi: 10.1038/srep00619.

An et al., (2018). Temporal and spatial variations in sand and dust storm events in East Asia from 2007 to 2016: Relationships with surface conditions and climate change. Science of The Total Environment, 633, 452-462.

Anderson et al., (2005) 'Testing the MODIS satellite retrieval of aerosol fine-mode fraction', Journal of Geophysical Research: Atmospheres, 110(D18).

Anisimov et al., (2018). Observations and cloud-resolving modeling of Haboob dust storms over the Arabian Peninsula. Journal of Geophysical Research: Atmospheres, 123(21), 12-147.

Anoruo (2022) 'Monsoon-seasonal validation of MODIS aerosol optical depth and characterisation using AERONET observation retrieve over Italy', Environmental Research. Elsevier Inc., 204(PB), p. 111985. doi: 10.1016/j.envres.2021.111985.

References

Ansmann et al., (2012). Profiling of fine and coarse particle mass: case studies of Saharan dust and Eyjafjallajökull/Grimsvötn volcanic plumes. Atmospheric Chemistry and Physics, 12(20), 9399-9415.

Ausati and Amanollahi (2016) 'Assessing the accuracy of ANFIS, EEMD-GRNN, PCR, and MLR models in predicting PM2. 5', Atmospheric environment, 142, pp. 465–474.

Azorin-Molina et al. (2016) 'Trends of daily peak wind gusts in Spain and Portugal, 1961--2014', Journal of Geophysical Research: Atmospheres. Wiley Online Library, 121(3), pp. 1059–1078.

Badarinath et al., (2007) 'Aerosol climatology: dependence of the Angstrom exponent on wavelength over four AERONET sites', Atmospheric Chemistry and Physics Discussions, 7(3), pp. 7347–7397. doi: 10.5194/acpd-7-7347-2007.

Baddock et al., (2009) 'Dust source identification using MODIS: A comparison of techniques applied to the Lake Eyre Basin, Australia', Remote Sensing of Environment, pp. 1511–1528. Available at: https://doi.org/10.1016/j.rse.2009.03.002.

Baddock et al., (2015). Drivers of Australian dust: A case study of frontal winds and dust dynamics in the lower Lake Eyre Basin. Earth Surface Processes and Landforms, 40(14), 1982-1988.

Baddock et al., (2016) 'Do MODIS-defined dust sources have a geomorphological signature?', Geophysical Research Letters, pp. 2606–2613. doi: 10.1002/2015GL067327.

Baddock et al., (2017). Pathways of high-latitude dust in the North Atlantic. Earth and Planetary Science Letters, 459, 170-182.

Baddock et al., (2021) 'Understanding dust sources through remote sensing: Making a case for CubeSats', Journal of Arid Environments. Elsevier Ltd, 184(June 2020), p. 104335. doi: 10.1016/j.jaridenv.2020.104335.

Baird (2021). Dune Sands: Quantifying Celerity, Reactivation Morphometrics, and Provenance (Doctoral dissertation, UCL (University College London)).

Bakker et al., (2019) 'Evaluating the Relative Importance of Northern African Mineral Dust Sources Using Remote Sensing', Atmospheric Chemistry and Physics Discussions, (April), pp. 1–17. doi: 10.5194/acp-2019-253.

Banks et al., (2019). The sensitivity of the colour of dust in MSG-SEVIRI Desert Dust infrared composite imagery to surface and atmospheric conditions. Atmospheric Chemistry and Physics, 19(10), 6893-6911.

Bao et al., (2021) 'Impacts of Underlying Surface on the Dusty Weather in Central Inner Mongolian Steppe, China', Earth and Space Science, 8(9), pp. 1–17. doi: 10.1029/2021EA001672.

Bao et al., (2023). The Transport Path and Vertical Structure of Dust Storms in East Asia and the Impacts on Cities in Northern China. Remote Sensing, 15(12), 3183.

Barchyn and Hugenholtz (2012). Predicting vegetation-stabilized dune field morphology. Geophysical Research Letters, 39(17).

References

Basith et al., (2022). The impact of fine particulate matter 2.5 on the cardiovascular system: A review of the invisible killer. Nanomaterials, 12(15), 2656.

Bergametti et al., (2017). Dust uplift potential in the Central Sahel: an analysis based on 10 years of meteorological measurements at high temporal resolution. Journal of Geophysical Research: Atmospheres, 122(22), 12-433.

Bi et al., (2017). 'Measurement of scattering and absorption properties of dust aerosol in a Gobi farmland region of northwestern China-a potential anthropogenic influence', Atmos. Chem. Phys, 17, pp. 7775–7792. Available at: https://doi.org/10.5194/acp-17-7775-2017.

Bibi, Alam and Bibi (2016) 'In-depth discrimination of aerosol types using multiple clustering techniques over four locations in Indo-Gangetic plains', Atmospheric Research. Elsevier, 181, pp. 106–114.

Bird et al., (2015). Quaternary dust source variation across the Chinese Loess Plateau. Palaeogeography, Palaeoclimatology, Palaeoecology, 435, 254-264.

Bohlmann et al., (2018). Ship-borne aerosol profiling with lidar over the Atlantic Ocean: from pure marine conditions to complex dust–smoke mixtures. Atmospheric Chemistry and Physics, 18(13), 9661-9679.

Boloorani et al., (2020) 'Identification of dust sources using long term satellite and climatic data: A case study of Tigris and Euphrates basin', Atmospheric Environment, 224(December 2019), p. 117299. Available at: https://doi.org/10.1016/j.atmosenv.2020.117299.

Boloorani et al., (2021) 'Water bodies changes in Tigris and Euphrates basin has impacted dust storms phenomena', Aeolian Research. Elsevier, 50, p. 100698.

Boloorani et al., (2023). Visual interpretation of satellite imagery for hotspot dust sources identification. Remote Sensing Applications: Society and Environment, 29, 100888.

Boroughani et al (2019). Desiccating Lake Urmia: a new dust source of regional importance. IEEE Geoscience and Remote Sensing Letters, 17(9), 1483-1487.

Boroughani et al., (2020). Application of remote sensing techniques and machine learning algorithms in dust source detection and dust source susceptibility mapping. Ecological Informatics, 56, 101059.

Brey et al., (2020) 'Estimating the Spread in Future Fine Dust Concentrations in the Southwest United States', Journal of Geophysical Research: Atmospheres, 125(21), pp. 1–12. Available at: https://doi.org/10.1029/2019JD031735.

Bristow, et al., (2009), Deflation in the dustiestplace on Earth: The Bodélé Depression, Chad, Geomorphology,105,50–58,doi:10.1016/j.geomorph.2007.12.014

Bryant (2013) 'Recent advances in our understanding of dust source emission processes', Progress in Physical Geography, pp. 397–421. doi: 10.1177/0309133313479391.

Bryant et al., (2007) 'Dust emission response to climate in southern Africa', Journal of Geophysical Research Atmospheres. doi: 10.1029/2005JD007025.

References

Buchhorn et al., (2020). Copernicus global land service: Land cover 100m: collection 3: epoch 2019: Globe. Version V3. 0.1.

Bullard and White (2005). Dust production and the release of iron oxides resulting from the aeolian abrasion of natural dune sands. Earth Surface Processes and Landforms: The Journal of the British Geomorphological Research Group, 30(1), 95-106.

Bullard et al., (2008). Sub-basin scale dust source geomorphology detected using MODIS. Geophysical Research Letters, 35(15).

Bullard et al., (2011). Preferential dust sources: A geomorphological classification designed for use in global dust-cycle models. Journal of Geophysical Research: Earth Surface, 116(F4).

Bullard et al., (2016). High-latitude dust in the Earth system. Reviews of Geophysics, 54(2), pp.447-485.

Cao and Chen (2022). The Tibetan Plateau as dust aerosol transit station in middle troposphere over northern East Asia: A case study. Atmospheric Research, 280, 106416.

Cao et al., (2010). Impacts of the Natural Forest Conservation Program on the livelihoods of residents of Northwestern China: Perceptions of residents affected by the program. Ecological Economics, 69(7), 1454-1462.

Cao et al., (2018). "Characterizing sand and dust storms (SDS) intensity in China based on meteorological data." Sustainability 10.7 (2018): 2372.

Caton Harrison et al., (2021). Satellite-derived characteristics of Saharan cold pool outflows during boreal summer. Journal of Geophysical Research: Atmospheres, 126(3), e2020JD033387.

Chappell et al., (2010). Estimating aerodynamic resistance of rough surfaces using angular reflectance. Remote Sensing of Environment, 114(7), 1462-1470.

Chappell et al., (2023). Elucidating hidden and enduring weaknesses in dust emission modelling. Journal of Geophysical Research: Atmospheres, e2023JD038584.

Chappell, Adrian, et al. (2023). Satellites reveal Earth's seasonally shifting dust emission sources. Science of the Total Environment, 883, 163452.

Chen and Dong (2018) ‘Wind Regime and dune field patterns in the Gonghe Bain, Qinghai, China’, journal of desert research, pp. 492–499.

Chen et al., (2007), Nd and Sr isotopic characteristics of Chinese deserts: Implications for the provenances of Asian dust, Geochim. Cosmochim. Acta, 71, 3904–3914, doi:10.1016/j.gca.2007.04.033.

Chen et al., (2013) ‘A 2000-year dust storm record from Lake Sugan in the dust source area of arid China’, Journal of Geophysical Research Atmospheres, 118(5), pp. 2149–2160. doi: 10.1002/jgrd.50140.

References

Chen et al., (2013). Modeling the transport and radiative forcing of Taklimakan dust over the Tibetan Plateau: A case study in the summer of 2006. Journal of Geophysical Research: Atmospheres, 118(2), 797-812.

Chen et al., (2017). Comparison of dust emissions, transport, and deposition between the Taklimakan Desert and Gobi Desert from 2007 to 2011. Science China Earth Sciences, 60, 1338-1355.

Chen et al., (2021). Formation of a low-level barrier jet and its modulation by dust radiative forcing over the Hexi Corridor in Central China on March 17, 2010. Quarterly Journal of the Royal Meteorological Society, 147(736), 1873-1891.

Chen et al., (2021). Increasing summer precipitation in arid Central Asia linked to the weakening of the East Asian summer monsoon in the recent decades. International Journal of Climatology, 41(2), 1024-1038.

Chen et al., (2023). A super dust storm enhanced by radiative feedback. npj Climate and Atmospheric Science, 6(1), 90.

Chen, F. et al. (2019) ‘Westerlies Asia and monsoonal Asia: Spatiotemporal differences in climate change and possible mechanisms on decadal to sub-orbital timescales’, Earth-Science Reviews. Elsevier, 192(March), pp. 337–354. doi: 10.1016/j.earscirev.2019.03.005.

Chen, P., et al., 2023. Water availability in China's oases decreased between 1987 and 2017. Earth's Future, 11(4), p.e2022EF003340.

Cheng, T. et al. (2006) ‘Aerosol properties and radiative forcing in Hunshan Dake desert, northern China’, Atmospheric Environment. Elsevier, 40(12), pp. 2169–2179.

Chris Deziel, (2018), From Website: Nature, How Does Elevation Affect Weather?[online]. [Viewed 03 June 2023]. Available from: https://sciencing.com/elevation-affect-weather-4630.html

Colarco et al., (2010). Online simulations of global aerosol distributions in the NASA GEOS-4 model and comparisons to satellite and ground-based aerosol optical depth. Journal of Geophysical Research: Atmospheres, 115(D14).

Collins et al., (2011). Development and evaluation of an Earth-System model–HadGEM2. Geoscientific Model Development, 4(4), pp.1051-1075.

Comrie and Glueck (2007) ‘Assessment of Climate--Coccidioidomycosis Model: Model Sensitivity for Assessing Climatologic Effects on the Risk of Acquiring Coccidioidomycosis’, Annals of the New York Academy of Sciences, 1111(1), pp. 83–95.

Cooley, Ryan, and Smith (2021). Human alteration of global surface water storage variability. Nature, 591(7848), 78-81.

Cowie et al., (2014). A climatology of dust emission events from northern Africa using long-term surface observations. Atmospheric Chemistry and Physics, 14(16), 8579-8597.

Crouvi, et al., (2012). Multiple dust sources in the Sahara Desert: The importance of sand dunes. *Geophysical Research Letters*, *39*(13).

References

Csavina et al., (2014) ‘Effect of wind speed and relative humidity on atmospheric dust concentrations in semi-arid climates’, Science of the Total Environment. Elsevier, 487, pp. 82–90.

CubeSats, (2023). European Space Agency. https://www.esa.int/Enabling_Support/Preparing_for_the_Future/Discovery_and_Preparation/CubeSats [Access date: 25/08/2023]

Cui et al., (2019) ‘Quantifying the effect of geomorphology on aeolian dust emission potential in northern China’, Earth Surface Processes and Landforms, 2884(August), pp. 2872–2884. doi: 10.1002/esp.4714.

Cui, A. et al. (2021) ‘Tibetan Plateau Precipitation Modulated by the Periodically Coupled Westerlies and Asian Monsoon’, Geophysical Research Letters, 48(7), pp. 1–10. doi: 10.1029/2020GL091543.

Cui, X. et al. (2018) ‘Spatial and temporal variation of the near-surface wind environment in the dune fields of northern China’, International Journal of Climatology, 38(5), pp. 2333–2351. doi: 10.1002/joc.5338.

Dai, Zhao and Chen (2018) ‘Climate change and drought: a precipitation and evaporation perspective’, Current Climate Change Reports. Springer, 4(3), pp. 301–312.

Davidson et al., (2011). From river to rock record: The preservation of fluvial sediments and their subsequent interpretation. SEPM Society for Sedimentary Geology.

DIAS (2023), Data Integration and Analysis System (DIAS)[online]. [Viewed 20 December 2022]. Available from:https://diasjp.net/en/guide/

Ding, Zhao and Dong, (2010), In Chinese. Aeolian sand physics. doi:10.1016/j.geomorph.2007.12.014

Dong et al., (1993). Desertification and controls in the Gonghe Basin, Qinghai Province, pp. 10–25, Science Press, Beijing (in Chinese).

Dong et al., (2007). "Wind tunnel test on effect of controlling windand deposited sand of geogrid sand-barrier. Sci." Soil Water Conserv 5.1, 35-39.

Dong et al., (2009) ‘Geomorphological hierarchies for complex mega-dunes and their implications for mega-dune evolution in the Badain Jaran Desert’, Geomorphology. Elsevier B.V., 106(3–4), pp. 180–185. doi: 10.1016/j.geomorph.2008.10.015.

Dong et al., (2017a). Tibetan Plateau Atlas of Aeolian Geomorphology. Maps Press of Xi’an, Xi’an, pp. 116, in Chinese with English abstract.

Dong et al., (2017b). ‘High-Altitude Aeolian Research on the Tibetan Plateau’, Reviews of Geophysics, pp. 864–901. doi: 10.1002/2017RG000585.

Dong, H. et al. (2010) ‘Impacts of environmental change and human activity on microbial ecosystems on the Tibetan Plateau, NW China’, GSA Today, 20(6), pp. 4–10. doi: 10.1130/GSATG75A.1.

References

Dörwald et al., (2023). ‘Dune movement under climatic changes on the north-eastern Tibetan Plateau as recorded by long-term satellite observation versus ERA-5 reanalysis’, Earth Surface Processes and Landforms [Preprint].

Draxler et al., (2020). HYSPLIT user's guide, Version 5-Last Revision: April 2020.

Du et al., (2018). "Modelling of sand/dust emission in Northern China from 2001 to 2014." Geoderma 330, 162-176.

Du et al., (2022). Modeling dust emission in alpine regions with low air temperature and low air pressure–A case study on the Qinghai-Tibetan Plateau (QTP). Geoderma, 422, 115930.

Duan et al., (2022). "High-resolution planetscope imagery and machine learning for estimating suspended particulate matter in the Ebinur Lake, Xinjiang, China." IEEE Journal of Selected Topics in Applied Earth Observations and Remote Sensing 16, 1019-1032.

Duniway et al., (2019) ‘Wind erosion and dust from US drylands: a review of causes, consequences, and solutions in a changing world’, Ecosphere, 10(3). doi: 10.1002/ecs2.2650.

Dyke (2004) ‘An outline of North American deglaciation with emphasis on central and northern Canada’, Developments in quaternary sciences. Elsevier, 2, pp. 373–424.

East and Sankey (2020). Geomorphic and sedimentary effects of modern climate change: current and anticipated future conditions in the western United States. Reviews of Geophysics, 58(4), e2019RG000692.

Eckardt et al., (2020). "South Africa’s agricultural dust sources and events from MSG SEVIRI." Aeolian Research 47, 100637.

Engelstaedter et al., (2003). "Controls of dust emissions by vegetation and topographic depressions: An evaluation using dust storm frequency data." Geophysical Research Letters 30.6.

European Space Agency (ESA), (2015). Sentinel Online. Sentinel-2 User Handbook. [Viewed 19 January 2020]. Available from: https://sentinel.esa.int/documents/247904/685211/Sentinel-2_User_Handbook

Famiglietti (2014). The global groundwater crisis. Nature Climate Change, 4(11), 945-948.

Fang et al., (2004). Dust storms and loess accumulation on the Tibetan Plateau: a case study of dust event on 4 March 2003 in Lhasa. Chinese Science Bulletin, 49, 953-960.

Feng and Li (2019) ‘The environmental evolution of the Gonghe Basin since the 12 ka revealed by magnetic susceptibility’, Journal of Stratigraphy, 43(1), pp. 101–108.

Feng et al., (2008) ‘Land Desertification Dynamic Analysis Based on Remote Sensing in Guinan County of Qinhai Province’, Remote Sensing Technology and Application, 23(6), pp. 633-638.

Feng et al., (2023). Warmth Favored Dust Activities on the Northeastern Qinghai-Tibet Plateau. Geophysical Research Letters, 50(11), e2023GL103781.

References

Feuerstein and Schepanski (2018). Identification of dust sources in a Saharan dust hot-spot and their implementation in a dust-emission model. Remote Sensing, 11(1), 4.

Fiedler et al., (2013). Climatology of nocturnal low-level jets over North Africa and implications for modeling mineral dust emission. Journal of Geophysical Research: Atmospheres, 118(12), 6100-6121.

Fiedler, et al., (2016). A process-based evaluation of dust-emitting winds in the CMIP5 simulation of HadGEM2-ES. Climate Dynamics, 46, 1107-1130.

Filonchyk (2022). Characteristics of the severe March 2021 Gobi Desert dust storm and its impact on air pollution in China. Chemosphere, 287, 132219.

Foroutan et al., (2017). Development and evaluation of a physics-based windblown dust emission scheme implemented in the C MAQ modeling system. Journal of Advances in Modeling Earth Systems, 9(1), 585-608.

Galloza et al. (2018) 'Exploring dust emission responses to land cover change using an ecological land classification', Aeolian Research, 32(August 2017), pp. 141–153. doi: 10.1016/j.aeolia.2018.03.001.

Gao et al., (1993). A preliminary study on the evolution of the desert in the north-western margin of the Chinese monsoon region during the Holocene. (in Chinese). China science, 23(2), pp. 202-208

Gao et al., (2019) 'Wind regime for long-ridge yardangs in the Qaidam Basin, Northwest China', Journal of Arid Land, 11(5), pp. 701–712. doi: 10.1007/s40333-019-0108-4.

Gao et al., (2022). NDVI-based vegetation dynamics and their responses to climate change and human activities from 1982 to 2020: A case study in the Mu Us Sandy Land, China. Ecological Indicators, 137, 108745.

Gasso et al., (2010) A combined observational and modelling approach to study modern dust transport from the Patagonia desert to East Antarc- tica. AtmosphericChemistryandPhysics 10: 8287–8303.

Ge et al., (2016). Potential transport pathways of dust emanating from the playa of Ebinur Lake, Xinjiang, in arid northwest China. Atmospheric Research, 178, 196-206.

Gharibzadeh et al., (2018) 'Characterization of aerosol optical properties using multiple clustering techniques over Zanjan, Iran, during 2010–2013', Applied Optics, 57(11), p. 2881. doi: 10.1364/ao.57.002881.

Gherboudj et al., (2017) 'Identifying natural dust source regions over the Middle-East and North-Africa: Estimation of dust emission potential', Earth-Science Reviews. Elsevier B.V., 165, pp. 342–355. doi: 10.1016/j.earscirev.2016.12.010.

Gill (1996). Eolian sediments generated by anthropogenic disturbance of playas: human impacts on the geomorphic system and geomorphic impacts on the human system. Geomorphology, 17(1-3), 207-228.

References

Ginoux et al., (2001), Sources and distribution of dust aerosols with the GOCART model, J. Geophys. Res., 106, 20,255–20,273, doi:10.1029/ 2000JD000053.

Ginoux et al., (2012). Global-scale attribution of anthropogenic and natural dust sources and their emission rates based on MODIS Deep Blue aerosol products. Reviews of Geophysics, 50(3).

Ginoux, Garbuzov and Hsu (2010) 'Identification of anthropogenic and natural dust sources using moderate resolution imaging spectroradiometer (MODIS) deep blue level 2 data', Journal of Geophysical Research Atmospheres, 115(5), pp. 1–10. doi: 10.1029/2009JD012398.

Gkikas et al., (2021) 'ModIs Dust AeroSol (MIDAS): A global fine-resolution dust optical depth data set', Atmospheric Measurement Techniques. Copernicus GmbH, 14(1), pp. 309–334. doi: 10.5194/amt-14-309-2021.

Go et al., (2022). Inferring iron-oxide species content in atmospheric mineral dust from DSCOVR EPIC observations. Atmospheric Chemistry and Physics, 22(2), 1395-1423.

Goudie (2014) 'Desert dust and human health disorders', Environment International, pp. 101–113. doi: 10.1016/j.envint.2013.10.011.

Gu et al.,(2021). An overview of triggering mechanisms and characteristics of local strong sandstorms in China and haboobs. Atmosphere, 12(6), 752.

Guan et al., (2017) 'Dust storms in northern China: long-term spatiotemporal characteristics and climate controls', Journal of Climate. American Meteorological Society, 30(17), pp. 6683–6700.

Gui et al., (2022) 'Record-breaking dust loading during two mega dust storm events over northern China in March 2021: aerosol optical and radiative properties and meteorological drivers', Atmospheric Chemistry and Physics, 22(12), pp. 7905–7932. Available at: https://doi.org/10.5194/acp-22-7905-2022.

Guo, et al (2019). High-altitude and long-range transport of aerosols causing regional severe haze during extreme dust storms explains why afforestation does not prevent storms. Environmental Chemistry Letters, 17, 1333-1340.

Hahnenberger, and Nicoll (2014). Geomorphic and land cover identification of dust sources in the eastern Great Basin of Utah, USA. Geomorphology, 204, 657-672.

Han et al., (2008) 'Shifts of dust source regions over central Asia and the Tibetan Plateau: Connections with the Arctic oscillation and the westerly jet', Atmospheric Environment, 42(10), pp. 2358–2368. doi: 10.1016/j.atmosenv.2007.12.025.

Han et al., (2009). Suppression of precipitation by dust particles originated in the Tibetan Plateau. Atmospheric Environment, 43(3), 568–574.

Han et al., (2015). Desertification assessments in the Hexi corridor of northern China's Gansu Province by remote sensing. Natural Hazards, 75, 2715-2731.

References

Han,et al (2014). The effect of air density on sand transport structures and the adobe abrasion profile: a field wind-tunnel experiment over a wide range of altitude. Boundary-layer meteorology, 150, 299-317.

Hassan et al., (2023). Impacts of spatial heterogeneity of anthropogenic aerosol emissions in a regionally-refined global aerosol-climate model. EGUsphere, 2023, 1-37.

Haustein et al., (2015). Testing the performance of state-of-the-art dust- emission schemes using DO4Models field data. Geoscientific Model Development Discussion, 7, 5739–5789.

Hayasaki et al., (2006). Interannual variation of cold frontal activity in spring in Mongolia. Journal of the Meteorological Society of Japan. Ser. II, 84(3), pp.463-475.

He et al., (2020). RANS simulation of local strong sandstorms induced by a cold pool with vorticity. Atmosphere, 11(4), 321.

Heinold et al., (2013). The role of deep convection and nocturnal low-level jets for dust emission in summertime West Africa: Estimates from convection-permitting simulations. Journal of Geophysical Research: Atmospheres, 118(10), 4385-4400.

Hennen (2017). Identifying mineral dust emission sources in the Middle East using remote sensing techniques (Doctoral dissertation, University of Reading).

Hennen et al., (2019). An assessment of SEVIRI imagery at various temporal resolutions and the effect on accurate dust emission mapping. Remote Sensing, 11(8), 918.

Hermida et al., (2018). "Characterization of synoptic patterns causing dust outbreaks that affect the Arabian Peninsula." Atmospheric Research 199: 29-39.

Hong-Bo (2012). Numerical simulation of the heavy rainfall in the Yangtze-Huai River Basin during summer 2003 using the WRF model. Atmospheric and Oceanic Science Letters, 5(1), 20-25.

Hooper and Marx (2018). A global doubling of dust emissions during the Anthropocene?. Global and Planetary Change, 169, 70-91.

Hsu et al., (2004). Aerosol properties over bright-reflecting source regions. IEEE Transactions on Geoscience and Remote Sensing, 42(3), pp.557-569.

Hu and Mitsuta (1997). Micrometeorological characteristics and local triggering mechanism of strong dust storm. Sci. Atmos. Sin. 21, 581–589. (In Chinese)

Huang et al. (2013) ‘Interannual precipitation variations in the mid-latitude Asia and their association with large-scale atmospheric circulation’, Chinese Science Bulletin, 58(32), pp. 3962–3968. doi: 10.1007/s11434-013-5970-4.

Huang et al., (2023). Single-scattering properties of ellipsoidal dust aerosols constrained by measured dust shape distributions. Atmospheric Chemistry and Physics, 23(4), 2557-2577.

Huang et al., (2020). Climate models and remote sensing retrievals neglect substantial desert dust asphericity. Geophysical Research Letters, 47(6), e2019GL086592.

References

Huck et al., (2023). The (mis) identification of high-latitude dust events using remote sensing methods in the Yukon, Canada: a sub-daily variability analysis. Atmospheric Chemistry and Physics, 23(11), 6299-6318.

Hutchison et al., (2012). The use of global synthetic data for pre-launch tuning of the VIIRS cloud mask algorithm. International Journal of Remote Sensing, 33(5), 1400-1423.

Iraji et al (2021). Determining the source of dust storms with use of coupling WRF and HYSPLIT models: A case study of Yazd province in central desert of Iran. Dynamics of Atmospheres and Oceans, 93, 101197.

Jia et al., (2015). Source and transportation of summer dust over the Tibetan Plateau. Atmospheric Environment, 123, pp.210-219.

Jia et al., (2022). Chinese Interstadials 14–17 recorded in a precisely U-Th dated stalagmite from the northern edge of the Asian summer monsoon during the MIS 4/3 boundary. Palaeogeography, Palaeoclimatology, Palaeoecology, 607, 111265.

Jia, et al (2023). The Changes of Desertification and Its Driving Factors in the Gonghe Basin of North China over the Past 10 Years. Land, 12(5), 998.

Jia, W. et al. (2022) ‘Highly resolved $δ$13C and trace element ratios of precisely dated stalagmite from northwestern China: Hydroclimate reconstruction during the last two millennia’, Quaternary Science Reviews. Elsevier, p. 107473.

Jiang et al., (2023). Extreme-wind events in China in the past 50 years and their impacts on sandstorm variations. Frontiers in Earth Science, 10, 1058275.

Jianjun (2017) ‘Analysis and countermeasures on desertified land and sandified land in Guinan County of Qinghai Province’, FOREST RESOURCES WANAGEMENT, (2), p. 12.

Jin and He (2023). "On the Association between Fine Dust Concentrations from Sand Dunes and Environmental Factors in the Taklimakan Desert." Remote Sensing 15.7, 1719.

Jin, J., et al (2020). Source backtracking for dust storm emission inversion using an adjoint method: case study of Northeast China. Atmospheric Chemistry and Physics, 20(23), 15207-15225.

Jinbing et al., (2019). Dust emission inversion using himawari-8 AODs over east Asia: an extreme dust event in may 2017. Journal of Advances in Modeling Earth Systems, 11(2), pp.446-467.

Jing, et al. (2017). Integrated analysis of dust transport and budget in a severe Asian dust event. Aerosol and Air Quality Research, 17(10), 2390-2400.

Jugder et al., (2011). Spatial and temporal variations of dust concentrations in the Gobi Desert of Mongolia. Global and Planetary Change, 78(1-2), 14-22.

Kahn et al (2009). MISR aerosol product attributes and statistical comparisons with MODIS. IEEE Transactions on Geoscience and Remote Sensing, 47(12), 4095-4114.

References

Kandakji, et al (2020). Identifying and characterizing dust point sources in the southwestern United States using remote sensing and GIS. Geomorphology, 353, 107019.

Kang et al., (2016). Long-term trends of dust events over Tibetan Plateau during 1961–2010. Atmospheric Environment, 125, 188-198.

Karami, Sara, et al., (2021). Evaluation of nine operational models in forecasting different types of synoptic dust events in the Middle East. Geosciences, 11(11), 458.

Kaskaoutis et al., (2011) 'Extremely large anthropogenic-aerosol contribution to total aerosol load over the Bay of Bengal during winter season', Atmospheric Chemistry and Physics. Copernicus GmbH, 11(14), pp. 7097–7117.

Katra (2020). Soil erosion by wind and dust emission in semi-arid soils due to agricultural activities. Agronomy, 10(1), 89.

Kaufman, et al., (2005). Dust transport and deposition observed from the Terra-Moderate Resolution Imaging Spectroradiometer (MODIS) spacecraft over the Atlantic Ocean. Journal of Geophysical Research: Atmospheres, 110(D10).

Kim et al., (2017). Role of surface wind and vegetation cover in multi-decadal variations of dust emission in the Sahara and Sahel. Atmospheric Environment, 148, pp.282-296.

Kjeldsen et al., (2014). Mapping erodibility in dust source regions based on geomorphology, meteorology, and remote sensing. Journal of Geophysical Research: Earth Surface, 119(6), 1310–1321. 754 https://doi.org/10.1002/2013JF003034.Received

Knippertz (2014). Meteorological aspects of dust storms. Mineral dust: A key player in the earth system, 121-147.

Knippertz and Todd (2012). Mineral dust aerosols over the Sahara: Meteorological controls on emission and transport and implications for modeling. Reviews of Geophysics, 50(1).

Kok at al (2014). An improved dust emission model with insights into the global dust cycle's climate sensitivity. Atmospheric Chemistry & Physics, 14(5).

Kok et al., (2018). Global and regional importance of the direct dust-climate feedback. Nature Communications, 9(1), 241.

Kok et al., (2020) 'Improved representation of the global dust cycle using observational constraints on dust properties and abundance - supplement', Atmospheric Chemistry and Physics Discussions, (November), pp. 1–45.

Kok et al., (2021a). Contribution of the world's main dust source regions to the global cycle of desert dust. Atmospheric Chemistry and Physics, 21(10), pp.8169-8193.

Kok et al., (2021b). Improved representation of the global dust cycle using observational constraints on dust properties and abundance. Atmospheric Chemistry and Physics, 21(10), pp.8127-8167.

Kok et al., (2023). Mineral dust aerosol impacts on global climate and climate change. Nature Reviews Earth & Environment, 4(2), pp.71-86.

References

Krasnov, Katra and Friger (2016) ‘Increase in dust storm related PM10 concentrations: A time series analysis of 2001--2015’, Environmental pollution, 213, pp. 36–42.

Krebs and Gunter (2023). “Sentinel 2A, 2B, 2C, 2D”. Gunter's Space Page. Retrieved September 25, from https://space.skyrocket.de/doc_sdat/sentinel-2.htm

Kumar et al. (2014) ‘Long-term (2003-2013) climatological trends and variations in aerosol optical parameters retrieved from MODIS over three stations in South Africa’, Atmospheric Environment. Elsevier Ltd, 95, pp. 400–408. doi: 10.1016/j.atmosenv.2014.07.001.

Kurosaki and Mikami (2004) ‘Effect of snow cover on threshold wind velocity of dust outbreak’, Geophysical Research Letters, 31(3), pp. 1–5. doi: 10.1029/2003GL018632.

Lancaster (2022). Response of Aeolian Processes and Landforms to Climate Change and Variability.

Landsat Science, (2023). A New and Revolutionary Landsat Mission, from https://landsat.gsfc.nasa.gov/satellites/landsat-next/ [Access date: 09/09/2023]

Laurent et al., (2005) ‘Simulation of the mineral dust emission frequencies from desert areas of China and Mongolia using an aerodynamic roughness length map derived from the POLDER/ADEOS 1 surface products’, Journal of Geophysical Research D: Atmospheres, 110(18), pp. 1–21. doi: 10.1029/2004JD005013.

Lavi Bekin et al (2020). Areal extent of dust emission events and source geomorphology in Northern Africa from MSG-SEVIRI data. Remote Sensing, 12(17), 2775.

Lee and Kim (2012) ‘Roles of surface wind, NDVI and snow cover in the recent changes in Asian dust storm occurrence frequency’, Atmospheric Environment. Elsevier Ltd, 59(June 2002), pp. 366–375. doi: 10.1016/j.atmosenv.2012.05.022.

Lee et al., (2012). Geomorphic and land cover characteristics of aeolian dust sources in West Texas and eastern New Mexico, USA. Aeolian Research, 3(4), 459-466.

Lehmkuhl et al., (2021). Loess landscapes of Europe–Mapping, geomorphology, and zonal differentiation. Earth-Science Reviews, 215, 103496.

Lei and Wang (2014). Observed characteristics of dust storm events over the western United States using meteorological, satellite, and air quality measurements. Atmospheric Chemistry and Physics, 14(15), 7847-7857.

Lensky and Rosenfeld (2008). Clouds-aerosols-precipitation satellite analysis tool (CAPSAT). Atmospheric Chemistry and Physics, 8(22), 6739-6753.

Leung et al., (2023). A new process-based and scale-aware desert dust emission scheme for global climate models–Part I: Description and evaluation against inverse modeling emissions. Atmospheric Chemistry and Physics, 23(11), 6487-6523.

Li and Chen (2020) ‘Global Revisit Interval Analysis of Landsat-8 -9 aLund Sentinel-2A -2B Data for Terrestrial Monitoring’, Sensors (Basel, Switzerland), 20(22). doi: 10.3390/s20226631.

References

Li and Chen (2023). Dust impacts on Mongolian cyclone and cold front in East Asia: a case study during 18–22 March 2010. Frontiers in Environmental Science, 11, p.627.

Li et al., (2021a). Aerosol optical depth (AOD): spatial and temporal variations and association with meteorological covariates in Taklimakan desert, China. PeerJ, 9, e10542.

Li et al., (2021b). Spatio-temporal changes of AOD in Xinjiang of China from 2000 to 2019: Which factor is more influential, natural factor or human factor?. Plos one, 16(8), e0253942.

Li, et al (2012). An overview of the “Three-North” Shelterbelt project in China. Forestry Studies in China, 14, 70-79.

Li, et al (2015). Remote sensing monitoring recent rapid increase of coal mining activity of an important energy base in northern China, a case study of Mu Us Sandy Land. Resources, Conservation and Recycling, 94, 129-135.

Li, J. et al. (2022) ‘Predominant type of dust storms that influences air quality over northern China and future projections’, Earth’s Future. Wiley Online Library, 10(6), p. e2022EF002649.

Li, Q. et al. (2020) ‘Analysis of Predictability of Local Rainstorm in Qinghai during August 19-20, 2019’, Meteorological and Environmental Research, 11(5), pp. 157–166.

Li, Wang, and Yan (2017). Assessing the role of policies on land-use/cover change from 1965 to 2015 in the Mu Us Sandy Land, northern China. Sustainability, 9(7), 1164.

Li, X. et al. (2016) ‘Causes and processes of sandy desertification in Guinan County, Qinghai–Tibet Plateau’, Environmental Earth Sciences, 75(8), pp. 1–12. Available at: https://doi.org/10.1007/s12665-016-5481-0.

Li, Y., et al (2019). Influence of Thermal Effects on Qinghai-Tibet Plateau on Air Quality in Typical Regions of China in Winter. Atmosphere, 11(1), 50.

Li, Z. et al. (2018) ‘Observed surface wind speed declining induced by urbanization in East China’, Climate dynamics. Springer, 50(3), pp. 735–749.

Liou, K.-N. (2002) An introduction to atmospheric radiation. Vol. 84. Elsevier, 2002.

Liu and Liu (2015) ‘Climatology of dust storms in northern China and Mongolia: Results from MODIS observations during 2000–2010’, Journal of Geographical Sciences, 25(11), pp. 1298–1306. doi: 10.1007/s11442-015-1235-2.

Liu et al., (2013) ‘Holocene climatic change revealed by aeolian deposits from the Gonghe Basin, northeastern Qinghai-Tibetan Plateau’, Quaternary International. Elsevier Ltd and INQUA, 296, pp. 231–240. doi: 10.1016/j.quaint.2012.05.003.

Liu et al., (2014). Advances in low-level jet research and future prospects. Journal of Meteorological Research, 28(1), 57-75.

Liu et al., (2020) ‘Holocene Moisture Variation Recorded by Aeolian Sand-Palaeosol Sequences of the Gonghe Basin, Northeastern Qinghai-Tibetan Plateau, China’, Acta Geologica Sinica, 94(3), pp. 668–681. doi: 10.1111/1755-6724.14541.

References

Liu et al., (2021). Effects of natural and anthropogenic factors and their interactions on dust events in Northern China. Catena, 196, 104919.

Liu et al., (2022). Stronger winds increase the sand-dust storm risk in northern China. Environmental Science: Atmospheres, 2(6), 1259-1262.

Liu J Y., et al (2021) Evolution of sandy desertification in North China from 2010 to 2018 [J]. Geological Survey of China, 2021, 8(6):25-34 (in Chineses)

Liu, et al (2008). Ecological and socioeconomic effects of China's policies for ecosystem services. Proceedings of the National academy of Sciences, 105(28), 9477-9482.

Liu, et al (2019). Recent lake area changes in Central Asia. Scientific reports, 9(1), 16277.

Liu, et al (2021). Characteristics of dust aerosols and identification of dust sources in Xinjiang, China. Atmospheric Environment, 262, 118651.

Liu, J. et al. (2021) 'Characteristics of dust aerosols and identification of dust sources in Xinjiang, China', Atmospheric Environment. Elsevier Ltd, 262(July), p. 118651. doi: 10.1016/j.atmosenv.2021.118651.

Liu, X. and Xin, L. (2021) 'China's deserts greening and response to climate variability and human activities', PLoS ONE, 16(8 August), pp. 1–20. doi: 10.1371/journal.pone.0256462.

Liu, X. et al. (2012) 'Luminescence chronology of aeolian deposits from the Qinghai Lake area in the Northeastern Qinghai-Tibetan Plateau and its palaeoenvironmental implications', Quaternary Geochronology. Elsevier, 10, pp. 37–43.

Liu, X. et al. (2018) 'Palaeoenvironmental implication of grain-size compositions of terrace deposits on the western Chinese Loess Plateau', Aeolian research. Elsevier, 32, pp. 202–209.

Liu, Y. et al. (2020) 'Dust storm susceptibility on different land surface types in arid and semiarid regions of northern China', Atmospheric Research, 243(April). doi: 10.1016/j.atmosres.2020.105031.

Livingstone I, Warren A. (1996). Aeolian Geomorphology: An Introduction. Longman Singapore Publishers: Singapore

Long et al., (2015). Deriving scaling factors using a global hydrological model to restore GRACE total water storage changes for China's Yangtze River Basin. Remote Sensing of Environment, 168, 177-193.

Lou et al., (2016) 'Impacts of the East Asian Monsoon on springtime dust concentrations over China', pp. 8137–8152. doi: 10.1002/2016JD024758.Received.

Lu and Shao (2001). Toward quantitative prediction of dust storms: an integrated wind erosion modelling system and its applications. Environmental Modelling & Software, 16(3), 233-249.

Lu, (2013). The Environmental Effect Analysis of PV Power Plant Construction in Desert Gobbi-take Dongdongtan Million Kiloweatt Solar Power Demonstration Base, Jiuquan City as An Example (Doctoral dissertation, Lanzhou University).

References

Lu, et al (2017). The dynamic relationship between environmental pollution, economic development and public health: Evidence from China. Journal of Cleaner Production, 166, 134-147.

Lu, H. Y. et al. (2013) ‘Chinese deserts and sand fields in Last Glacial Maximum and Holocene Optimum’, Chinese Science Bulletin, 58(23), pp. 2775–2783. doi: 10.1007/s11434-013-5919-7.

Luo et al., (2019a). Mega-blowouts in Qinghai–Tibet Plateau: Morphology, distribution and initiation. Earth Surface Processes and Landforms, 44(2), pp.449-458.

Luo et al., (2019b). Historical evolution and controls on mega-blowouts in northeastern Qinghai-Tibetan Plateau, China. Geomorphology, 329, pp.17-31.

Luo et al., (2020). Optimization of UAVs-SfM data collection in aeolian landform morphodynamics: a case study from the Gonghe Basin, China. Earth Surface Processes and Landforms, 45(13), 3293-3312.

Lyapustin, A. et al. (2014) ‘Scientific impact of MODIS C5 calibration degradation and C6+ improvements’, Atmospheric Measurement Techniques, 7(12), pp. 4353–4365.

Madhavan, Sun and Xiong (2021). Sensor calibration impacts on dust detection based on MODIS and VIIRS thermal emissive bands. Advances in Space Research, 67(10), 3059-3071.

Mahowald et al., (2005) ‘Atmospheric global dust cycle and iron inputs to the ocean’, Global Biogeochemical Cycles, 19(4). doi: 10.1029/2004GB002402.

Mahowald, et al. (2014) ‘The size distribution of desert dust aerosols and its impact on the Earth system’, Aeolian Research. Elsevier B.V., 15, pp. 53–71. doi: 10.1016/j.aeolia.2013.09.002.

Mahowald, et al. (2003) ‘Ephemeral lakes and desert dust sources’, Geophysical Research Letters, 30(2), pp. 30–33. doi: 10.1029/2002GL016041.

Mann et al., (2010) ‘Description and evaluation of GLOMAP-mode: A modal global aerosol microphysics model for the UKCA composition-climate model’. Geoscientific Model Development 3: 519–551.

Maring, et al. (2003) ‘Mineral dust aerosol size distribution change during atmospheric transport’, Journal of Geophysical Research: Atmospheres. Wiley Online Library, 108(D19).

Mark (1969) Archaic classification of barbiturates, Clinical Pharmacology and Therapeutics. doi: 10.1002/cpt1969103287.

Marsham, et al. (2011) ‘The importance of the representation of deep convection for modeled dust-generating winds over West Africa during summer’, Geophysical Research Letters, 38(16), pp. 2–7. doi: 10.1029/2011GL048368.

Mason, et al. (2009) ‘Dune mobility and aridity at the desert margin of northern China at a time of peak monsoon strength’, Geology. Geological Society of America, 37(10), pp. 947–950.

References

Meinander, Outi, et al. (2022). Newly identified climatically and environmentally significant high-latitude dust sources. Atmospheric Chemistry and Physics, 22(17), 11889-11930.

Mekhilef, et al (2011). A review on solar energy use in industries. Renewable and sustainable energy reviews, 15(4), 1777-1790.

Meng et al., (2020). Impact of South Asian monsoon on summer dust weather occurrence over the Tarim basin in Northwest China. Environmental Research Communications, 2(10), 105001.

MENG, et al (2016). Evaluation of water resources carrying capacity of Gonghe Basin based on fuzzy comprehensive evaluation method. Journal of Groundwater Science and Engineering Vol, 4(2).

Miao et al., (2016) 'Functional degradation of the water-sediment regulation scheme in the lower Yellow River: Spatial and temporal analyses', Science of the Total Environment. Elsevier B.V., 551–552, pp. 16–22. doi: 10.1016/j.scitotenv.2016.02.006.

Miao, Ni and Borthwick (2010) 'Recent changes of water discharge and sediment load in the Yellow River basin, China', Progress in Physical Geography, 34(4), pp. 541–561. doi: 10.1177/0309133310369434.

Miao, et al(2016). Human activity accelerating the rapid desertification of the Mu Us Sandy Lands, North China. Scientific Reports, 6(1), 23003.

Micklin (2007). The Aral sea disaster. Annu. Rev. Earth Planet. Sci., 35, 47-72.

Middleton and Goudie (2001) 'Saharan dust: Sources and trajectories', Transactions of the Institute of British Geographers, 26(2), pp. 165–181. doi: 10.1111/1475-5661.00013.

Middleton, (2019) 'Variability and trends in dust storm frequency on decadal timescales: Climatic drivers and human impacts', Geosciences (Switzerland), 9(6). doi: 10.3390/geosciences9060261.

Miller, (2016). S.D., US Secretary of Navy. System and method for atmospheric parameter enhancement. U.S. Patent 9,383,478.

Miller, et al., (2008). Haboob dust storms of the southern Arabian Peninsula. *Journal of Geophysical Research: Atmospheres*, *113*(D1).

Mockford., Bullard., and Thorsteinsson, (2018). The dynamic effects of sediment availability on the relationship between wind speed and dust concentration. Earth Surface Processes and Landforms, 43(11), 2484-2492.

Modarres, (2021) 'Dust storm frequency change in relation to climate drivers', International Journal of Climatology, 41(S1), pp. E187–E199. doi: 10.1002/joc.6675.

Moridnejad et al., (2015) 'A new inventory for middle east dust source points', Environmental Monitoring and Assessment, 187(9). doi: 10.1007/s10661-015-4806-x.

Muhs et al., (2014). Identifying sources of aeolian mineral dust: Present and past. Mineral dust: A key player in the earth system, 51-74.

References

Muneer, Gueymard and Kambezidis (2004) ‘3-Hourly Horizontal Irradiation and Illuminance. Solar Radiation and Daylight Models’. Oxford: Butterworth-Heinemann.

Murray, et al (2016). Enhancing weak transient signals in SEVIRI false color imagery: Application to dust source detection in southern Africa. Journal of Geophysical Research: Atmospheres, 121(17), 10-199.

Myhre (2009) ‘Consistency between satellite-derived and modeled estimates of the direct aerosol effect’, Science. American Association for the Advancement of Science, 325(5937), pp. 187–190.

Naeger, et al (2015). Monitoring and tracking the trans-Pacific transport of aerosols using multi-satellite aerosol optical depth retrievals. Atmospheric Measurement Techniques Discussions, 8(10).

Namdari, et al. (2018) ‘Impacts of climate and synoptic fluctuations on dust storm activity over the Middle East’, Atmospheric environment. Elsevier, 173, pp. 265–276.

NASA, (2022). A Focus on Mineral Dust, Science Objective. from https://earth.jpl.nasa.gov/emit/science/objectives/ [Access date: 25/09/2023]

NASA, (2023). ISS: EMIT (Earth surface Mineral dust source InvesTigation). from https://www.eoportal.org/satellite-missions/iss-emit#eop-quick-facts-section [Access date: 24/09/2023]

Nauman et al., (2023). Synergistic soil, land use, and climate influences on wind erosion on the Colorado Plateau: Implications for management. Science of The Total Environment, 164605.

Niu, et al (2019). Quantifying provenance of reservoir sediment using multiple composite fingerprints in an arid region experiencing both wind and water erosion. Geomorphology, 332, 112-121.

Niu, et al (2023). High-Altitude Aeolian Desertification and Sand Dunes on the Tibetan Plateau, China. In Sand Dunes of the Northern Hemisphere (pp. 179-194). CRC Press.

NOAA (2022), Joint Polar Satellite System[online]. [Viewed 21 November 2022]. Available from: https://www.nesdis.noaa.gov/current-satellite-missions/currently-flying/joint-polar-satellite-system

NOAA, (2023). Global Data Assimilation System (GDAS1) Archive Information. https://www.ready.noaa.gov/gdas1.php [Web access: 2023/08/24]

Nobakht et al (2021). New inventory of dust emission sources in Central Asia and northwestern China derived from MODIS imagery using dust enhancement technique. Journal of Geophysical Research: Atmospheres, 126(4), e2020JD033382.

Omar, et al. (2005) ‘Development of global aerosol models using cluster analysis of Aerosol Robotic Network (AERONET) measurements’, Journal of Geophysical Research D: Atmospheres, 110(10), pp. 1–14. doi: 10.1029/2004JD004874.

References

Orsolini et al., (2019). Evaluation of snow depth and snow cover over the Tibetan Plateau in global reanalyses using in situ and satellite remote sensing observations. Cryosphere, 13(8), 2221–2239. https://doi.org/10.5194/tc-13-2221-2019

Parajuli and Zender (2017). Connecting geomorphology to dust emission through high-resolution mapping of global land cover and sediment supply. Aeolian Research, 27, 47-65.

Parajuli, et al., (2014). Mapping erodibility in dust source regions based on geomorphology, meteorology, and remote sensing. Journal of Geophysical Research: Earth Surface, 119(9), 1977-1994.

Pathak et al., (2012) 'Seasonal heterogeneity in aerosol types over Dibrugarh-North-Eastern India', Atmospheric Environment, 47(June 2014), pp. 307–315. doi: 10.1016/j.atmosenv.2011.10.061.

Pearce and Walker (2005) 'Frequency and magnitude biases in the d Fryberger T model , with implications for characterizing geomorphically effective winds', 68, pp. 39–55. doi: 10.1016/j.geomorph.2004.09.030.

Pi et al., (2017). Atmospheric dust events in central Asia: Relationship to wind, soil type, and land use. Journal of Geophysical Research: Atmospheres, 122(12), 6652-6671.

Piao, et al. (2014) 'Evidence for a weakening relationship between interannual temperature variability and northern vegetation activity', Nature communications. Nature Publishing Group, 5(1), pp. 1–7.

Piedra and Moosmüller., (2017). Optical losses of photovoltaic cells due to aerosol deposition: Role of particle refractive index and size. Solar Energy, 155, pp.637-646.

Piedra, and Moosmüller (2017). Optical losses of photovoltaic cells due to aerosol deposition: Role of particle refractive index and size. Solar Energy, 155, pp.637-646.

Powell (2009). Dryland rivers: processes and forms. In Geomorphology of desert environments (pp. 333-373). Dordrecht: Springer Netherlands.

Proestakis and Amiridis et al. (2018) 'Nine-year spatial and temporal evolution of desert dust aerosols over South and East Asia as revealed by CALIOP', Atmospheric Chemistry and Physics, 18(2), pp. 1337–1362. doi: 10.5194/acp-18-1337-2018.

Prospero et al., (2002). Environmental characterization of global sources of atmospheric soil dust identified with the Nimbus 7 Total Ozone Mapping Spectrometer (TOMS) absorbing aerosol product, Rev. Geophys., 40(1), 1002, doi:10.1029/2000RG000095.

Prospero et al., (2010). African dust deposition to Florida: temporal and spatial variability and comparison to models, J. Geophys. Res., 115, D13304, doi:10.1029/2009JD012773, 2010.

Pu and Ginoux (2016). The impact of the Pacific Decadal Oscillation on springtime dust activity in Syria. Atmospheric Chemistry and Physics, 16(21), 13431-13448.

Pu and Ginoux (2018). How reliable are CMIP5 models in simulating dust optical depth?. Atmospheric Chemistry and Physics, 18(16), 12491-12510.

References

Pye. (2015). Aeolian dust and dust deposits. Elsevier.

Qi et al., (2021). "Variations in aeolian landform patterns in the Gonghe Basin over the last 30 years." Journal of Mountain Science 18.8, 2034-2047.

Qi, (2016). Study on the Conservation of Chinese Agricultural Land Resources. In 2016 5th International Conference on Social Science, Education and Humanities Research (SSEHR 2016) (pp. 1356-1359). Atlantis Press.

Qi, et al., (2021). Variations in aeolian landform patterns in the Gonghe Basin over the last 30 years. Journal of Mountain Science, 18(8), 2034-2047.

Qiang et al. (2010) 'Aeolian deposits at the southeastern margin of the Tengger Desert (China): Implications for surface wind strength in the Asian dust source area over the past 20,000 years', Palaeogeography, Palaeoclimatology, Palaeoecology. Elsevier B.V., 286(1–2), pp. 66–80. doi: 10.1016/j.palaeo.2009.12.005.

Qiang et al. (2014) 'Holocene record of eolian activity from Genggahai Lake, northeastern Qinghai-Tibetan Plateau, China', Geophysical Research Letters, 41(2), pp. 589–595. doi: 10.1002/2013GL058806.

Qiang et al. (2017) 'A 16-ka oxygen-isotope record from Genggahai Lake on the northeastern Qinghai-Tibetan Plateau: Hydroclimatic evolution and changes in atmospheric circulation', Quaternary Science Reviews. Elsevier Ltd, 162, pp. 72–87. doi: 10.1016/j.quascirev.2017.03.004.

Qiang et al., (2007). Impacts of wind velocity on sand and dust deposition during dust storm as inferred from a series of observations in the northeastern Qinghai–Tibetan Plateau, China. Powder Technology, 175(2), pp.82-89.

Qiang et al., (2013) 'Late Quaternary aeolian activity in Gonghe Basin, northeastern Qinghai-Tibetan Plateau, China', Quaternary Research (United States), 79(3), pp. 403–412. doi: 10.1016/j.yqres.2013.03.003.

Qiang et al., (2016). Late Pleistocene and Holocene aeolian sedimentation in Gonghe Basin, northeastern Qinghai-Tibetan Plateau: Variability, processes, and climatic implications. Quaternary Science Reviews, 132, pp.57-73.

Qianrong Ma (2021). Changes in cloud amount over the Tibetan Plateau and impacts of large-scale circulation. Atmospheric Research, 249, 105332.

Qin et al. (2018) 'Characteristic and driving factors of aerosol optical depth over Mainland China during 1980-2017', Remote Sensing, 10(7), pp. 1–25. doi: 10.3390/rs10071064.

Qu et al., (2006). Asian dust storm monitoring combining Terra and Aqua MODIS SRB measurements. IEEE Geoscience and remote sensing letters, 3(4), 484-486.

Raffaele, Bruno, and Wiggs (2018). Uncertainty propagation in aeolian processes: From threshold shear velocity to sand transport rate. Geomorphology, 301, 28-38.

Raman et al., (2014). Revisiting haboobs in the southwestern United States: An observational case study of the 5 July 2011 Phoenix dust storm. Atmospheric Environment, 89, 179-188.

References

Ravi et al., (2011) ‘Aeolian processes and the biosphere’, Reviews of Geophysics, 49(3), pp. 1–45. doi: 10.1029/2010RG000328.

Rogozovsky et al., (2021). Impact of aerosol layering, complex aerosol mixing, and cloud coverage on high-resolution MAIAC aerosol optical depth measurements: Fusion of lidar, AERONET, satellite, and ground-based measurements. Atmospheric Environment, 247, 118163.

Roustaei et al. (2021) ‘Investigating Lagged Cross-correlation between Wind Erosion and Drought in Southern Iran’s arid regions Investigating Lagged Cross-correlation between Wind Erosion and Drought in Southern Iran’s arid regions’, Desert Ecosystem Engineering Journal, 3(2), pp. 29–42.

Sagintayev et al., (2012) ‘A remote sensing contribution to hydrologic modelling in arid and inaccessible watersheds, Pishin Lora basin, Pakistan’, Hydrological Processes, 26(1), pp. 85–99. doi: 10.1002/hyp.8114.

Saidou Chaibou et al., (2020). Dust radiative forcing and its impact on surface energy budget over West Africa. Scientific reports, 10(1), 12236.

Schepanski (2018) ‘Transport of mineral dust and its impact on climate’, Geosciences (Switzerland), 8(5). doi: 10.3390/geosciences8050151.

Schepanski et al., (2007). A new Saharan dust source activation frequency map derived from MSG-SEVIRI IR-channels. Geophysical Research Letters, 34(18).

Schepanski et al., (2009). Meteorological processes forcing Saharan dust emission inferred from MSG-SEVIRI observations of subdaily dust source activation and numerical models. Journal of geophysical research: atmospheres, 114(D10).

Schepanski et al., (2012), Comparison of satellite based observations of Saharan dust source areas, Remote Sens. Environ., 123,90–97, doi:10.1016/j.rse.2012.03.019.

Schiemann, Lüthi, and Schär (2009). Seasonality and interannual variability of the westerly jet in the Tibetan Plateau region. Journal of climate, 22(11), 2940-2957.

Schuster, Dubovik and Holben (2006) ‘Angstrom exponent and bimodal aerosol size distributions’, Journal of Geophysical Research: Atmospheres. Wiley Online Library, 111(D7).

Shang et al., (2018). Diurnal cycle and seasonal variation of cloud cover over the Tibetan Plateau as determined from Himawari-8 new-generation geostationary satellite data. Scientific reports, 8(1), 1105.

Shao and Dong, (2006). A review on East Asian dust storm climate, modelling and monitoring. Global and Planetary Change, 52(1-4), pp.1-22.

Shao et al., (2002). Numerical prediction of northeast Asian dust storms using an integrated wind erosion modeling system. Journal of Geophysical Research: Atmospheres, 107(D24), pp.AAC-21.

Shao et al., (2003). "Real-time numerical prediction of northeast Asian dust storms using an integrated modeling system." J. Geophys. Res 108.4691: 10-1029.

References

Shao et al., (2011) ‘Dust cycle: An emerging core theme in Earth system science’, Aeolian Research. Elsevier B.V., 2(4), pp. 181–204. doi: 10.1016/j.aeolia.2011.02.001.

Shao, et al (2023). Environmental sensitivity assessment of land desertification in the Hexi Corridor, China. Catena, 220, 106728.

She et al. (2018) ‘Dust detection and intensity estimation using Himawari-8/AHI observation’, Remote Sensing, 10(4), pp. 1–20. Available at: https://doi.org/10.3390/rs10040490.

Shi et al., (2015) ‘Wind speed change regionalization in China (1961--2012)’, Advances in Climate Change Research. Elsevier, 6(2), pp. 151–158.

Shi et al., (2020). Developing a dust storm detection method combining Support Vector Machine and satellite data in typical dust regions of Asia. Advances in Space Research, 65(4), pp.1263-1278.

Shi et al., (2023). "Dust Detection Over East Asia From Multispectral and Multi-Temporal Himawari-8/AHI Thermal Infrared Observations." Earth and Space Science 10.2, e2022EA002738.

Shi, et al., (2021). Drivers to dust emissions over dust belt from 1980 to 2018 and their variation in two global warming phases. *Science of The Total Environment*, *767*, 144860.

Shi, M., et al. (2016). Quantifying the impacts of landscape heterogeneity and model resolution on dust emissions in the Arabian Peninsula. Environmental Modelling & Software, 78, 106–119.

Shuying, Defu and Shenren (1982) ‘Aeolian sand deposits in the Gonghe Basin, Qinghai province’, Journal of Desert Research, 2(3), pp. 1–8.

Sinclair and LeGrand (2019). Reproducibility assessment and uncertainty quantification in subjective dust source mapping. Aeolian research, 40, 42-52.

Soi Ahn (2021). Composite Aerosol Optical Depth Mapping over Northeast Asia from GEO-LEO Satellite Observations. Remote Sensing, 13(6), 1096.

Stauch et al. (2018) ‘Environmental changes during the late Pleistocene and the Holocene in the Gonghe Basin, north-eastern Tibetan Plateau’, Palaeogeography, Palaeoclimatology, Palaeoecology. Elsevier B.V., 509, pp. 144–155. doi: 10.1016/j.palaeo.2016.12.032.

Sun, Zhang and Liu (2001). Spatial and temporal characteristics of dust storms in China and its surrounding regions, 1960–1999: Relations to source area and climate. Journal of Geophysical Research: Atmospheres, 106(D10), 10325-10333.

Sweeney et al., (2011) ‘Quantifying dust emissions from desert landforms, eastern Mojave Desert, USA’, Geomorphology. Elsevier B.V., 135(1–2), pp. 21–34. doi: 10.1016/j.geomorph.2011.07.022.

Sweeney, et al (2016). Sand dunes as potential sources of dust in northern China. Science China Earth Sciences, 59, 760-769.

References

Swet, ei al (2019). Can active sands generate dust particles by wind-induced processes?. Earth and Planetary Science Letters, 506, 371-380.

Takemura et al., (2005). Simulation of climate response to aerosol direct and indirect effects with aerosol transport-radiation model. Journal of Geophysical Research: Atmospheres, 110(D2).

Tan et al., (2021). Impact of massive topography on the dust cycle surrounding the Tibetan Plateau. Atmospheric Environment, 264, 118703.

Tanaka et al., (2011) 'The effects of snow cover and soil moisture on Asian dust: I. A numerical sensitivity study', Sola. Meteorological Society of Japan, 7(Special_Edition), pp. 36–39.

Tao (2014) 'Aeolian desertification and its control in Northern China', International Soil and Water Conservation Research. Elsevier, 2(4), pp. 34–41.

Tao, et al. (2017). Evaluation of MODIS Deep Blue aerosol algorithm in desert region of East Asia: Ground validation and intercomparison. Journal of Geophysical Research: Atmospheres, 122(19), 10-357.

Taramelli et al., (2013). Spatial and temporal dust source variability in northern China identified using advanced remote sensing analysis. Earth Surface Processes and Landforms, 38(8), 793-809.

Taylor et al., (2012). An overview of CMIP5 and the experiment design. Bulletin of the American meteorological Society, 93(4), pp.485-498.

Terradellas, Nickovic, and Zhang (2015). Airborne dust: a hazard to human health, environment and society. Boletín-Organización Meteorológica Mundial, 64(2), 44-48.

Tetsuya TAKEMI (2005). Explicit simulations of convective-scale transport of mineral dust in severe convective weather. 気象集誌. 第 2 輯, 83, 187-203.

Tian, et al., (2020). Recovery of Early Holocene paleowind direction from the Gonghe Basin in northeastern Tibetan Plateau and its implications for provenance of Chinese loess (in Chinese with English abstract). Quaternary Scienec,40 (1), 95-104.

Tie Dai, (2019). Hourly aerosol assimilation of Himawari-8 AOT using the four-dimensional local ensemble transform Kalman filter. Journal of Advances in Modeling Earth Systems, 11(3), 680-711.

Tindan, et al. (2023). Understanding day–night differences in dust aerosols over the dust belt of North Africa, the Middle East, and Asia. Atmospheric Chemistry and Physics, 23(9), 5435-5466.

Tortini et al., (2020). Satellite-based remote sensing data set of global surface water storage change from 1992 to 2018. Earth System Science Data, 12(2), 1141-1151.

Tramutoli, et al., (2010), July. A Robust Satellite Technique (RST) for dust storm detection and monitoring: The case of 2009 Australian event. In 2010 IEEE International Geoscience and Remote Sensing Symposium (pp. 1707-1709). IEEE.

References

USGS, (2023). What are the band designations for the Landsat satellites?. https://www.usgs.gov/faqs/what-are-band-designations-landsat-satellites. [Web access: 2023/06/24]

Vautard, R. et al. (2010) ‘Northern Hemisphere atmospheric stilling partly attributed to an increase in surface roughness’, Nature geoscience. Nature Publishing Group, 3(11), pp. 756–761.

Vickery et al., (2013) ‘A sub-basin scale dust plume source frequency inventory for southern Africa, 2005-2008’, Geophysical Research Letters, 40(19), pp. 5274–5279. doi: 10.1002/grl.50968.

Vimpere, et al (2021). Continental interior parabolic dunes as a potential proxy for past climates. Global and Planetary Change, 206, 103622.

Von Holdt et al., (2017) ‘Landsat identifies aeolian dust emission dynamics at the landform scale’, Remote Sensing of Environment, pp. 229–243. doi: 10.1016/j.rse.2017.06.010.

Von Holdt et al., (2019). Assessing landscape dust emission potential using combined ground-based measurements and remote sensing data. Journal of Geophysical Research: Earth Surface, 124(5), 1080-1098.

Vukovic, A., et al (2014). Numerical simulation of" an American haboob". Atmospheric Chemistry and Physics, 14(7), 3211-3230.

Walker, A. (2010) ‘Natural ventilation’, Whole Building Design Guide: A Program of the National Institute of Building Sciences.

Wang et al (2005). Surface sample collection and dust source analysis in northwestern China. Catena, 59(1), 35-53.

Wang et al (2008). Dust sources in arid and semiarid China and southern Mongolia: Impacts of geomorphological setting and surface materials. Geomorphology, 97(3-4), 583-600.

Wang et al. (2015). ‘Horizontal wind erosion flux and potential dust emission in arid and semiarid regions of China: A major source area for East Asia dust storms’, Catena. Elsevier B.V., 133, pp. 373–384. doi: 10.1016/j.catena.2015.06.011.

Wang et al., (2005). Regional characteristics of three kinds of dust storm events in China. Atmospheric Environment, 39(3), 509-520.

Wang et al., (2011) "The significance of Gobi desert surfaces for dust emissions in China: an experimental study." Environmental Earth Sciences 64, 1039-1050.

Wang et al., (2020) ‘Spatiotemporal variation of NDVI in the vegetation growing season in the source region of the Yellow River, China’, ISPRS International Journal of Geo-Information, 9(4), p. 282.

Wang et al., (2020). Evaluation of Himawari-8 version 2.0 aerosol products against AERONET ground-based measurements over central and northern China. Atmospheric Environment, 224, 117357.

References

Wang et al., (2022). Hybrid Methods' Integration for Remote Sensing Monitoring and Process Analysis of Dust Storm Based on Multi-Source Data. Atmosphere, 14(1), 3.

Wang, et al (2006). Control of dust emissions by geomorphic conditions, wind environments and land use in northern China: An examination based on dust storm frequency from 1960 to 2003. Geomorphology, 81(3-4), 292-308.

Wang, Gao and Yu (2019) 'Quantifying trends of land change in Qinghai-Tibet Plateau during 2001-2015', Remote Sensing, 11(20), pp. 1–21. doi: 10.3390/rs11202435.

Wang, Qu and Niu (2020). Comparative study of the shelter efficacy of straw checkerboard barriers and rocky checkerboard barriers in a wind tunnel. Aeolian Research, 43, 100575.

Wang, et al(2021). Identifying a transport mechanism of dust aerosols over South Asia to the Tibetan Plateau: A case study. Science of the Total Environment, 758, 143714.

Wang, et al. (2018) 'Spatial and temporal evolution of natural and anthropogenic dust events over northern China', Scientific Reports. Springer US, 8(1), pp. 1–9. doi: 10.1038/s41598-018-20382-5.

Wang, et al (2012). "Characteristics of the Gobi desert and their significance for dust emissions in the Ala Shan Plateau (Central Asia): an experimental study." Journal of arid environments 81, 35-46.

Wang, et al (2020). Why are there more summer afternoon low clouds over the Tibetan Plateau compared to eastern China?. Geophysical Research Letters, 47(23), e2020GL089665.

Wang, et al. (2017) 'Atmospheric moisture budget and its regulation on the variability of summer precipitation over the tibetan plateau', Journal of Geophysical Research, 122(2), pp. 614–630. doi: 10.1002/2016JD025515.

Wang, Zhang and Draxler (2009) 'TrajStat: GIS-based software that uses various trajectory statistical analysis methods to identify potential sources from long-term air pollution measurement data', Environmental Modelling \& Software. Elsevier, 24(8), pp. 938–939.

Wang, Zhou and Dong (2006) 'Control of dust emissions by geomorphic conditions, wind environments and land use in northern China: An examination based on dust storm frequency from 1960 to 2003', Geomorphology, 81(3–4), pp. 292–308. doi: 10.1016/j.geomorph.2006.04.015.

Washington et al., (2003), Dust-storm source areas determined by the Total Ozone Monitoring Spectrometer and surface observations, Ann. Assoc. Am. Geogr., 93, 297–313, doi:10.1111/1467-8306.9302003.

Webb and Pierre (2018). Quantifying anthropogenic dust emissions. Earth's Future, 6(2), pp.286-295.

Webb and Strong (2011). Soil erodibility dynamics and its representation for wind erosion and dust emission models. Aeolian Research, 3(2), 165-179.

References

Webb et al., (2019) ‘Reducing Sampling Uncertainty in Aeolian Research to Improve Change Detection’, Journal of Geophysical Research: Earth Surface, 124(6), pp. 1366–1377. doi: 10.1029/2019JF005042.

Wei et al., (2021). Hf–Nd–Sr Isotopic Composition of the Tibetan Plateau Dust as a Fingerprint for Regional to Hemispherical Transport. Environmental Science & Technology, 55(14), 10121-10132.

Wei et al., (2022). Grain-size composition of the surface sediments in Chinese deserts and the associated dust emission. Catena, 219, 106615.

Weiss, Lee, et al (2013). "Mapping key agricultural sources of dust emissions within the Lake Simcoe airshed." Inland Waters 3.2, 153-166.

Wenrui Yao, (2020). Can MERRA-2 reanalysis data reproduce the three-dimensional evolution characteristics of a typical dust process in East Asia? A case study of the dust event in May 2017. Remote Sensing, 12(6), 902.

Wiggs and Holmes (2011). Dynamic controls on wind erosion and dust generation on west-central Free State agricultural land, South Africa. Earth Surface Processes and Landforms, 36(6), 827-838.

Wiggs et al., (2022). Quantifying mechanisms of aeolian dust emission: Field measurements at Etosha Pan, Namibia. Journal of Geophysical Research: Earth Surface, 127(8), e2022JF006675.

Wu et al., (2016). Effects of climate change and human activity on lake shrinkage in Gonghe Basin of northeastern Tibetan Plateau during the past 60 years. Journal of Arid Land, 8, 479-491.

Wu et al., (2018). Initial assessment of radiometric performance of N20 VIIRS reflective solar bands using vicarious approaches. In Earth Observing Missions and Sensors: Development, Implementation, and Characterization V (Vol. 10781, pp. 142-153). SPIE.

Wu et al., (2020). Observational study on the impact of large-scale photovoltaic development in deserts on local air temperature and humidity. Sustainability, 12(8), 3403.

Wu et al., (2022). Drivers of recent decline in dust activity over East Asia. Nature Communications, 13(1), 7105.

Wu, Lin and Liu (2020). ‘Global dust cycle and uncertainty in CMIP5 models’, Atmospheric Chemistry and Physics Discussions, 5, pp. 1–52. doi: 10.5194/acp-2020-179.

Xi and Sokolik (2015). Seasonal dynamics of threshold friction velocity and dust emission in Central Asia. Journal of Geophysical Research: Atmospheres, 120(4), 1536-1564.

Xi and Sokolik (2016). Quantifying the anthropogenic dust emission from agricultural land use and desiccation of the Aral Sea in Central Asia. Journal of Geophysical Research: Atmospheres, 121(20), 12-270.

Xiao et al., (2002). Holocene climate changes over the desert/loess transition of north-central China. Earth and Planetary Science Letter 197, 11–18.

References

Xie, Lu, and Feng (2022). Effects of climate change and human activities on aeolian desertification reversal in mu us Sandy land, China. Sustainability, 14(3), 1669.

Xingqi et al., (2008) ‘Evolution of Chaka Salt Lake in NW China in response to climatic change during the Latest Pleistocene-Holocene’, Quaternary Science Reviews, 27(7–8), pp. 867–879. doi: 10.1016/j.quascirev.2007.12.006.

Xu et al., (2020). Critical transitions in Chinese dunes during the past 12,000 years. Science Advances, 6(9), p.eaay8020.

Xu et al., (1982). Aeolian sand deposits in Gonghe Basin (in Chinese with English abstract). Journal of Desert Research, 2, 1–8.

Xu et al., (1984). A discussion on the development of landforms and evolution of environments in the Gonghe Basin. Journal of Lanzhou University, 20(1), 146-157.

Xu et al., (2006). Steady decline of east Asian monsoon winds, 1969–2000: Evidence from direct ground measurements of wind speed. Journal of Geophysical Research: Atmospheres, 111(D24).

Xu et al., (2015). Vegetated dune morphodynamics during recent stabilization of the Mu Us dune field, north-central China. Geomorphology, 228, pp.486-503.

Xu et al., (2020). Distribution and transport characteristics of dust aerosol over Tibetan Plateau and Taklimakan Desert in China using MERRA-2 and CALIPSO data. Atmospheric environment, 237, 117670.

Xu et al., (2022). Holocene aeolian activity recorded by mountain paleosols, Gonghe Basin, Northeast Qinghai-Tibet Plateau. Frontiers in Earth Science, 10, 832993.

Xu et al., (2023). Identifying spatio-temporal climatic characteristics and events of the South-Asian aerosol pollution transport to the Tibetan Plateau. Atmospheric Research, 286, 106683.

Xu, Luo, and Chen (2021). The aeolian desertification process and driving mechanism of Qinghai Lake basin from 2004 to 2019. In E3S Web of Conferences (Vol. 308, p. 02025). EDP Sciences.

Xue et al., (2013). Evaluation of aeolian desertification from 1975 to 2010 and its causes in northwest Shanxi Province, China. Global and Planetary Change, 107, 102-108.

Xuehua et al (2021). "Form-flow Feedback within Blowouts at Different Developing Stages in the Gonghe Basin, Qinghai Province." Advances in Earth Science 36.1 , 95.

Yan et al (2009). Assessment of aeolian desertification trends from 1975's to 2005's in the watershed of the Longyangxia Reservoir in the upper reaches of China's Yellow River. Geomorphology, 112(3-4), 205-211.

Yang et al., (2011). Quaternary environmental changes in the drylands of China–a critical review. Quaternary Science Reviews, 30(23-24), 3219-3233.

References

Yang et al., (2012). OSL chronology and possible forcing mechanisms of dune evolution in the Horqin dune field in northern China since the Last Glacial Maximum. Quaternary Research 78, 185–196.

Yang et al., (2019). Spatiotemporal variation characteristics of ecosystem service losses in the agro-pastoral ecotone of Northern China. International Journal of Environmental Research and Public Health, 16(7), 1199.

Yang et al., (2021). Distinct effects of winter monsoon and westerly circulation on dust aerosol transport over East Asia. Theoretical and Applied Climatology, 144, 1031-1042.

Yang, et al., (2006). Microparticle content records of the Dunde ice core and dust storms in northwestern China. Journal of Asian Earth Sciences, 27(2), pp.223-229.

Yang, et al., (2022). Upper troposphere dust belt formation processes vary seasonally and spatially in the Northern Hemisphere. *Communications Earth & Environment*, *3*(1), 24.
Yao et al., (2023). Satellites reveal widespread decline in global lake water storage. Science, 380(6646), 743-749.

Yin et al., (2022). 'Why super sandstorm 2021 in North China?', National science review. Oxford University Press, 9(3), p. nwab165.

Ying et al., (2023). "Mechanisms of dust source accumulation and synoptic disturbance triggering the 2023 spring sandstorm in northern China." Trans Atmos Sci 46.3: 321-331.

You et al., (2010) 'Decreasing wind speed and weakening latitudinal surface pressure gradients in the Tibetan Plateau', Climate Research, 42(1), pp. 57–64.

Yu et al., (2015) 'Investigation of aerosol optical depth (AOD) and Ångström exponent over the desert region of Northwestern China based on measurements from the China aerosol remote sensing network (CARSNET)', Aerosol and Air Quality Research, 15(5), pp. 2024–2036. Available at: https://doi.org/10.4209/aaqr.2014.12.0326.

Yu et al., (2021). A global analysis of diurnal variability in dust and dust mixture using CATS observations. Atmospheric Chemistry and Physics, 21(3), 1427-1447.

Yu, et al., (2015). 'Investigation of aerosol optical depth (AOD) and Ångström exponent over the desert region of Northwestern China based on measurements from the China aerosol remote sensing network (CARSNET)', Aerosol and Air Quality Research, 15(5), pp. 2024–2036. doi: 10.4209/aaqr.2014.12.0326.

Yu and Lai (2014). 'Holocene climate change inferred from stratigraphy and OSL chronology of aeolian sediments in the Qaidam Basin, northeastern Qinghai--Tibetan Plateau', Quaternary Research. Cambridge University Press, 81(3), pp. 488–499.

Yu, Y. et al. (2015) 'Climatic controls on the interannual to decadal variability in Saudi Arabian dust activity: Toward the development of a seasonal dust prediction model', Journal of Geophysical Research: Atmospheres, 120(5), pp. 1739–1758.

Yuan et al., (2019). Influence of dynamic and thermal forcing on the meridional transport of Taklimakan Desert dust in spring and summer. Journal of Climate, 32(3), 749-767.

References

Yu-han, Q.I. (2021). ‘Variations in aeolian landform patterns in the Gonghe Basin over the last 30 years’, 18, pp. 2034–2047.

Yumimoto and Takemura (2015). ‘Long-term inverse modeling of Asian dust: Interannual variations of its emission, transport, deposition, and radiative forcing’, Journal of Geophysical Research: Atmospheres. Wiley Online Library, 120(4), pp. 1582–1607.

Yumimoto et al (2019). Dust vortex in the Taklimakan Desert by himawari-8 high frequency and resolution observation. Scientific reports, 9(1), 1209.

Zeng et al. (2018). ‘Response of dune mobility and pedogenesis to fluctuations in monsoon precipitation and human activity in the Hulunbuir dune field, northeastern China, since the last deglaciation’, Global and Planetary Change. Elsevier, 168, pp. 1–14.

Zeng et al., (2011). Magnetostratigraphy of loess in northeastern China and paleoclimatic changes (in Chinese). Chin Sci Bull, 56: 2267–2275

Zeng, Feng, and Gao (2003). Desert formation and evolution in Qaidam Basin since the last glacial epoch. Acta Geogr. Sin. 3, 452–457, in Chinese with English abstract.

Zhang and Li (2003). Research status of sand-dust storm observation and classification standard. J. Desert Res. 2003, 23, 586–591. (In Chinese)

Zhang et al., (2022). Diagnostic Analysis of Dynamic Characteristics of a Strong Sandstorm Weather Process in Eastern Hexi Corridor[J].Climate Change Research Express, 11(01): 98-108. https://doi.org/10.12677/CCRL.2022.111011 (in Chinese)

Zhang et al., (2020). "Aeolian dust in Central Asia: Spatial distribution and temporal variability." Atmospheric Environment 238, 117734.

Zhang, Chen and Xie (2019). Tibetan Plateau's lake level and volume changes from NASA's ICESat/ICESat-2 and Landsat Missions. Geophysical Research Letters, 46(22), 13107-13118.

Zhang, et al (2016). Multiple afforestation programs accelerate the greenness in the ‘Three North’region of China from 1982 to 2013. Ecological Indicators, 61, 404-412.

Zhang, et al (2018). "Effect of straw checkerboards on wind proofing, sand fixation, and ecological restoration in shifting sandy land." International journal of environmental research and public health 15.10, 2184.

Zhang, et al (2022). Not all gravel deserts in northern China are sources of regionally deposited dust. Atmospheric Environment, 273, 118984.

Zhang, et al (2023). ‘Impact of ecological restoration on ecosystem service trade-offs: Insight from karst desertification control’, Land Degradation \& Development [Preprint].

Zhang, et al., (2019) ‘Impact of near-surface wind speed variability on wind erosion in the eastern agro-pastoral transitional zone of Northern China, 1982--2016’, Agricultural and Forest Meteorology. Elsevier, 271, pp. 102–115.

Zhang, et al., (2008) ‘Experiment on dust flux during duststorm periods over desert area’, Acta Meteorol. Sin. Citeseer, 22(2), pp. 239–247.

References

Zhang, et al., (2018) 'Response of wind erosion dynamics to climate change and human activity in Inner Mongolia, China during 1990 to 2015', Science of the Total Environment. Elsevier, 639, pp. 1038–1050.

Zhang, et al., (2007) 'Evaluation of grassland dynamics in the northern-tibet plateau of china using remote sensing and climate data', Sensors, 7(12), pp. 3312–3328. doi: 10.3390/s7123312.

Zhang, et al., (2017) 'Comparison of wind erosion based on measurements and SWEEP simulation: A case study in Kangbao County, Hebei Province, China', Soil and Tillage Research. Elsevier, 165, pp. 169–180.

Zhang, (2019). General comparison of FY-4A/AGRI with other GEO/LEO instruments and its potential and challenges in non-meteorological applications. Frontiers in Earth Science, 6, 224.

Zhang, Xu, and Zhang (2019). Assessment of Himawari-8 AHI aerosol optical depth over land. Remote Sensing, 11(9), 1108.

Zhang, et al., (2017). Extensive and drastically different alpine lake changes on Asia's high plateaus during the past four decades. Geophysical Research Letters, 44(1), 252-260.

Zhang, et al. (2019) 'Increase in surface friction dominates the observed surface wind speed decline during 1973--2014 in the northern hemisphere lands', Journal of Climate, 32(21), pp. 7421–7435.

Zhao et al., (2006) 'A simulated climatology of Asian dust aerosol and its trans-Pacific transport. Part II: interannual variability and climate connections', J Clim, 19(1), p. 104122Gong.

Zhao et al., (2010). Holocene millennial-scale climate variations documented by multiple lake-level proxies in sediment cores from Hurleg Lake, Northwest China. Journal of Paleolimnology 44, 995–1008

Zhou et al., (2019) 'Dust uplift potential in the Taklimakan Desert: an analysis based on different wind speed measurement intervals', Theoretical and Applied Climatology. Theoretical and Applied Climatology, 137(1–2), pp. 1449–1456. doi: 10.1007/s00704-018-2678-z.

Zhou et al., (2020). Dust aerosol retrieval over the oceans with the MODIS/VIIRS Dark-Target algorithm: 1. Dust detection. Earth and Space Science, 7(10), e2020EA001221.

Zongyan et al., (2018). Wind Regime and Dune Field Patterns in the Gonghe Basin, Qinghai, China. Journal of Desert Research, 38(3), pp.492-499.

Zou and Zhai (2004) 'Relationship between vegetation coverage and spring dust storms over northern China', Journal of Geophysical Research: Atmospheres, 109(3), pp. 1–9. doi: 10.1029/2003jd003913.

Appendices

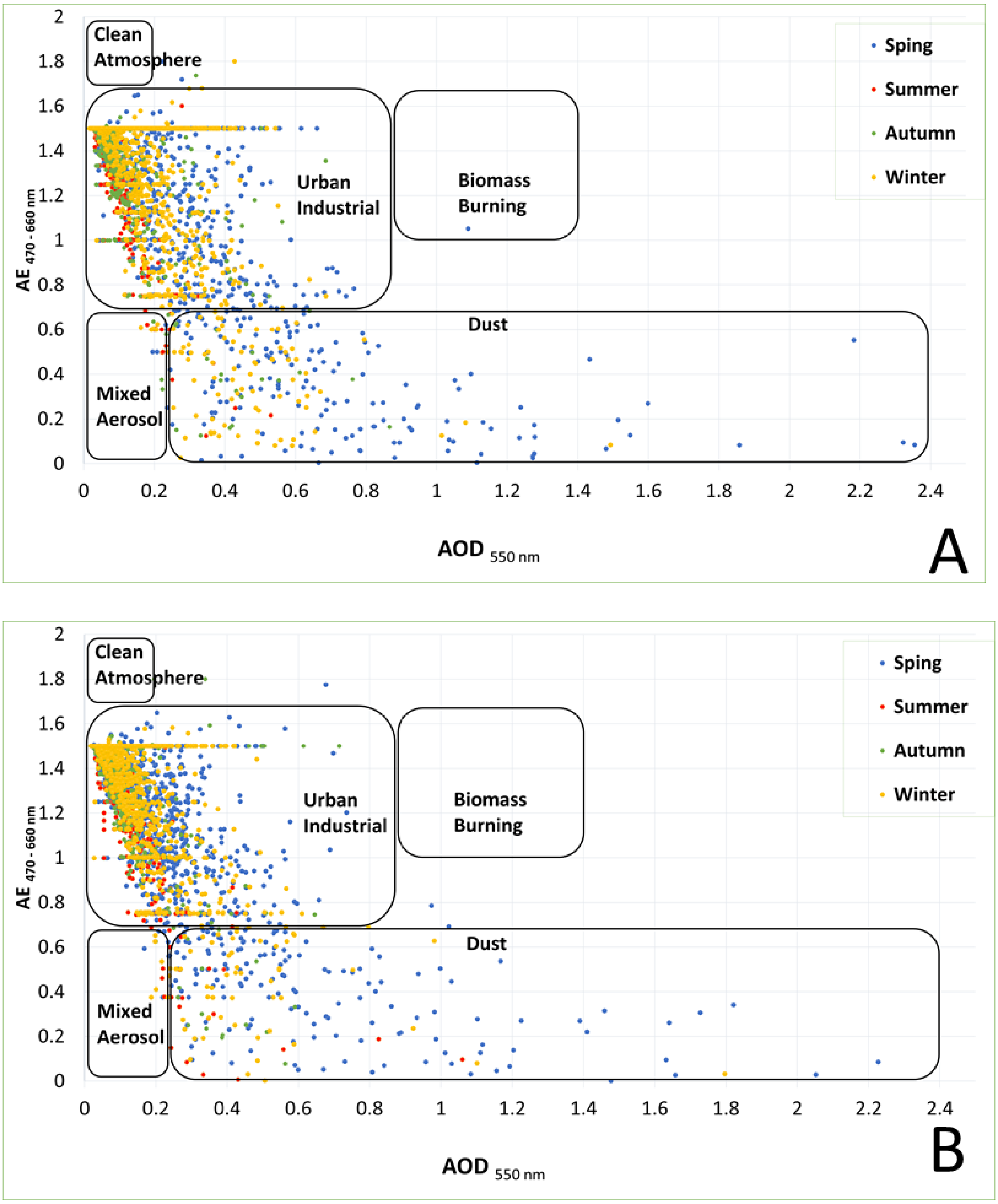

Appendix A. Seasonal scatter plot of AOD 550 nm versus AE 470–660 nm over the Gonghe Basin 2000–2022, *and data from A) MODIS-Terra; B) MODIS-Aqua. The four colour legends represent the 4 seasons; blue is spring; red is summer; green is autumn. and orange is winter.*

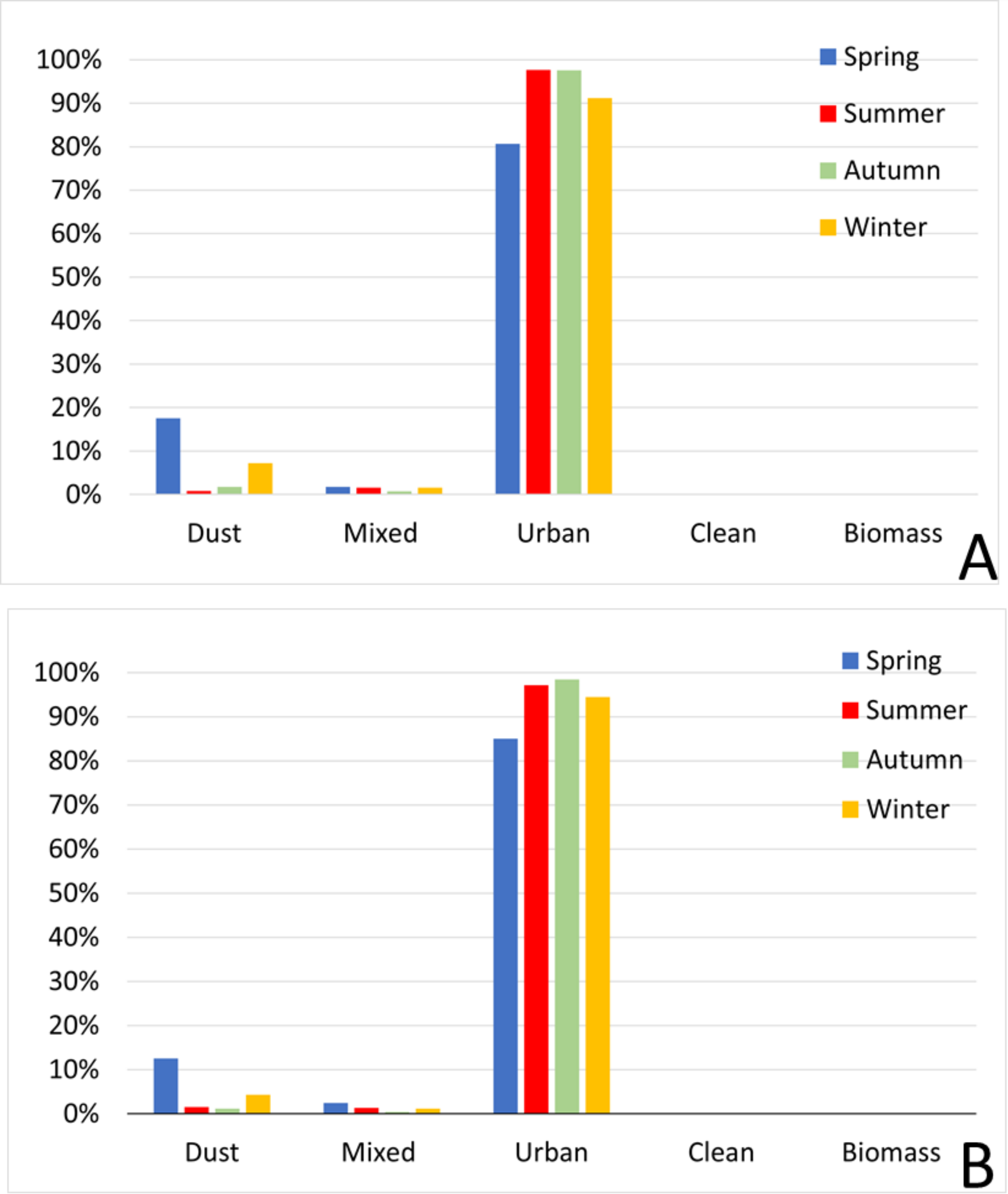

Appendix B. Seasonal contribution of each type of aerosols according to the scattered plot of AOD550nm versus AE 470–660nm over the Gonghe Basin 2000–2022, and data from A) MODIS-Terra; B) MODIS-Aqua. Dust is identified by K2011 methods.

Appendix C. Cumulative occurrence of the different wind speed classes above TWV from 1980 -2022 at the Gonghe Basin and their contribution to DUP.

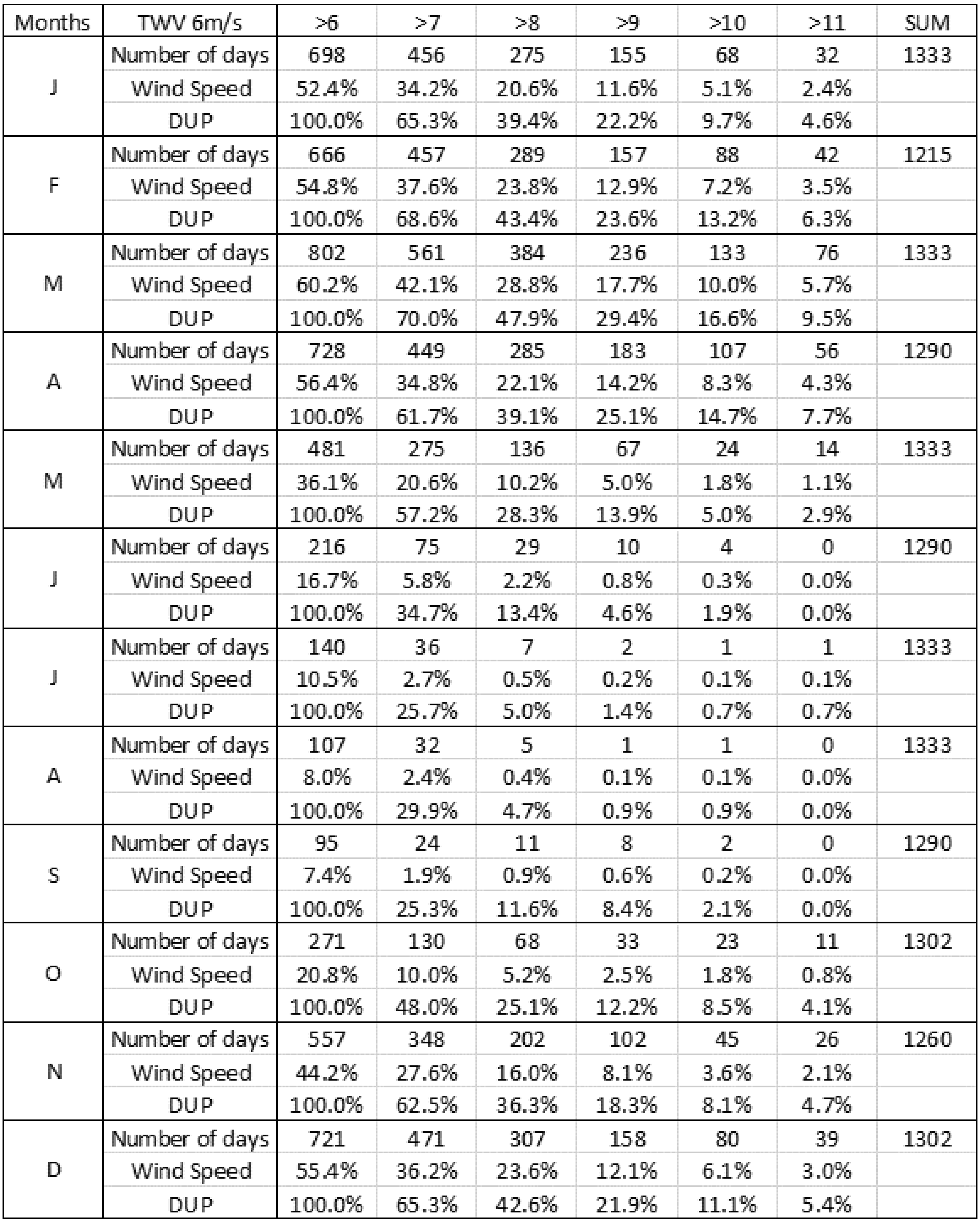

Months	TWV 6m/s	>6	>7	>8	>9	>10	>11	SUM
J	Number of days	698	456	275	155	68	32	1333
	Wind Speed	52.4%	34.2%	20.6%	11.6%	5.1%	2.4%	
	DUP	100.0%	65.3%	39.4%	22.2%	9.7%	4.6%	
F	Number of days	666	457	289	157	88	42	1215
	Wind Speed	54.8%	37.6%	23.8%	12.9%	7.2%	3.5%	
	DUP	100.0%	68.6%	43.4%	23.6%	13.2%	6.3%	
M	Number of days	802	561	384	236	133	76	1333
	Wind Speed	60.2%	42.1%	28.8%	17.7%	10.0%	5.7%	
	DUP	100.0%	70.0%	47.9%	29.4%	16.6%	9.5%	
A	Number of days	728	449	285	183	107	56	1290
	Wind Speed	56.4%	34.8%	22.1%	14.2%	8.3%	4.3%	
	DUP	100.0%	61.7%	39.1%	25.1%	14.7%	7.7%	
M	Number of days	481	275	136	67	24	14	1333
	Wind Speed	36.1%	20.6%	10.2%	5.0%	1.8%	1.1%	
	DUP	100.0%	57.2%	28.3%	13.9%	5.0%	2.9%	
J	Number of days	216	75	29	10	4	0	1290
	Wind Speed	16.7%	5.8%	2.2%	0.8%	0.3%	0.0%	
	DUP	100.0%	34.7%	13.4%	4.6%	1.9%	0.0%	
J	Number of days	140	36	7	2	1	1	1333
	Wind Speed	10.5%	2.7%	0.5%	0.2%	0.1%	0.1%	
	DUP	100.0%	25.7%	5.0%	1.4%	0.7%	0.7%	
A	Number of days	107	32	5	1	1	0	1333
	Wind Speed	8.0%	2.4%	0.4%	0.1%	0.1%	0.0%	
	DUP	100.0%	29.9%	4.7%	0.9%	0.9%	0.0%	
S	Number of days	95	24	11	8	2	0	1290
	Wind Speed	7.4%	1.9%	0.9%	0.6%	0.2%	0.0%	
	DUP	100.0%	25.3%	11.6%	8.4%	2.1%	0.0%	
O	Number of days	271	130	68	33	23	11	1302
	Wind Speed	20.8%	10.0%	5.2%	2.5%	1.8%	0.8%	
	DUP	100.0%	48.0%	25.1%	12.2%	8.5%	4.1%	
N	Number of days	557	348	202	102	45	26	1260
	Wind Speed	44.2%	27.6%	16.0%	8.1%	3.6%	2.1%	
	DUP	100.0%	62.5%	36.3%	18.3%	8.1%	4.7%	
D	Number of days	721	471	307	158	80	39	1302
	Wind Speed	55.4%	36.2%	23.6%	12.1%	6.1%	3.0%	
	DUP	100.0%	65.3%	42.6%	21.9%	11.1%	5.4%	

Appendix D. Correlation between DSD' AOD, AE and DUP for each month, the yellow highlight means statistically significant (p<0.05), and the grey box does not have enough data to calculate the correlation.

DUP Correlation		J	F	M	A	M	J	J	A	S	O	N	D
P2021-Terra	AOD	-0.009	-0.008	0.105	0.184	0.010		-0.093			0.148	0.061	-0.227
	AE	0.273	0.226	0.037	-0.084	-0.038		-0.103			$.719^{*}$	0.093	0.067
P2021-Aqua	AOD	$.193^{*}$	0.141	0.113	$.239^{**}$	$.349^{**}$	-0.108			0.606	0.278	0.278	$.275^{*}$
	AE	-0.084	$-.194^{*}$	-0.085	$-.232^{**}$	$-.380^{**}$	0.078			-0.051	0.089	0.089	-0.198
K2011-Terra	AOD	$.484^{*}$	0.004	0.115	$.260^{*}$	0.174		-0.182			0.405	0.343	-0.243
	AE	0.133	0.262	0.009	-0.072	0.052		0.203			0.257	0.537	$.770^{*}$
K2011-Aqua	AOD	0.286	0.187	0.066	$.242^{*}$	0.129					$.934^{*}$	0.551	0.173
	AE	0.172	$.338^{*}$	-0.043	-0.088	-0.058					0.672	-0.261	$.518^{*}$
P&G2016-Terra	AOD	-0.009	-0.008	0.105	0.184	0.010		-0.093			0.148	0.061	-0.227
	AE	0.273	0.226	0.037	-0.084	-0.038		-0.103			$.719^{*}$	0.093	0.067
P&G2016-Aqua	AOD	0.274	0.112	-0.032	0.156	0.105				0.049	$.889^{*}$	$.554^{*}$	0.216
	AE	0.201	0.098	$.217^{*}$	-0.032	-0.121				0.291	0.388	-0.317	0.225

The AOD value of DSD identified from the three methods has a moderate positive correlation with the DUP. The yellow highlight represents statistically significant months (p<0.05), indicating that higher DUP causes higher AOD which means more dust loading on the ground. A strong positive relationship between AOD and DUP was found from P&G2016-Aqua in October. The influence of DUP on dust loading varies in different months, November, March, and April (r=0.3) are higher than December to February (r=0.2). Other climate factors may play a significant role during the winter period control dust emission.

Based on the P2021 and K2011 dust definition datasets, a weak negative correlation was found between AE and DUP from November to May (Appendix D). With DUP rise, the AOD value increases and decreases AE, which indicates higher DUP leading to coarse dust particles emitted from the basin, suggesting the dust blows derived from the basin. However, a moderate positive AE and DUP correlation was found from both P2021 and P&G2016 dust datasets in December and March. Increased DUP raises AE value, considering the basin might have transported dust (fine dust aerosol) during the winter period which matches the results in Figure 2.10 E&F&G&H the average AE value is about 1. Increased DUP raises AE value, considering the basin might have transported dust by high-speed winds.

Appendices

Appendix E. Anomaly correlation between climate factors and Dust, the orange highlight is statistically significant correlation results.

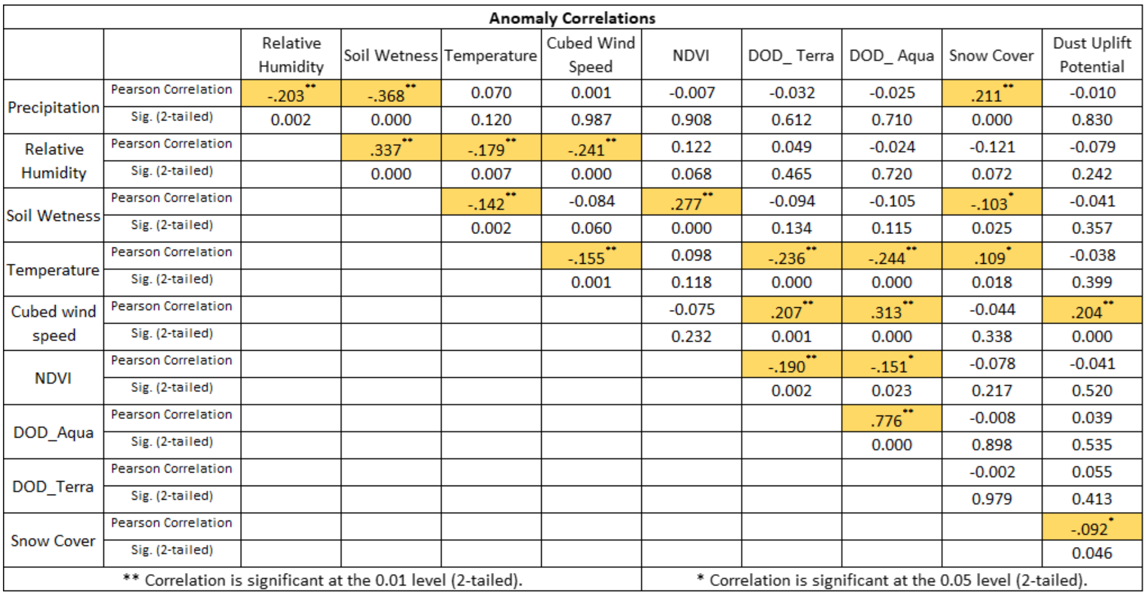

Anomaly Correlations										
		Relative Humidity	Soil Wetness	Temperature	Cubed Wind Speed	NDVI	DOD_ Terra	DOD_ Aqua	Snow Cover	Dust Uplift Potential
Precipitation	Pearson Correlation	-.203**	-.368**	0.070	0.001	-0.007	-0.032	-0.025	.211**	-0.010
	Sig. (2-tailed)	0.002	0.000	0.120	0.987	0.908	0.612	0.710	0.000	0.830
Relative Humidity	Pearson Correlation		.337**	-.179**	-.241**	0.122	0.049	-0.024	-0.121	-0.079
	Sig. (2-tailed)		0.000	0.007	0.000	0.068	0.465	0.720	0.072	0.242
Soil Wetness	Pearson Correlation			-.142**	-0.084	.277**	-0.094	-0.105	-.103*	-0.041
	Sig. (2-tailed)			0.002	0.060	0.000	0.134	0.115	0.025	0.357
Temperature	Pearson Correlation				-.155**	0.098	-.236**	-.244**	.109*	-0.038
	Sig. (2-tailed)				0.001	0.118	0.000	0.000	0.018	0.399
Cubed wind speed	Pearson Correlation					-0.075	.207**	.313**	-0.044	.204**
	Sig. (2-tailed)					0.232	0.001	0.000	0.338	0.000
NDVI	Pearson Correlation						-.190**	-.151*	-0.078	-0.041
	Sig. (2-tailed)						0.002	0.023	0.217	0.520
DOD_Aqua	Pearson Correlation							.776**	-0.008	0.039
	Sig. (2-tailed)							0.000	0.898	0.535
DOD_Terra	Pearson Correlation								-0.002	0.055
	Sig. (2-tailed)								0.979	0.413
Snow Cover	Pearson Correlation									-.092*
	Sig. (2-tailed)									0.046
** Correlation is significant at the 0.01 level (2-tailed).						* Correlation is significant at the 0.05 level (2-tailed).				

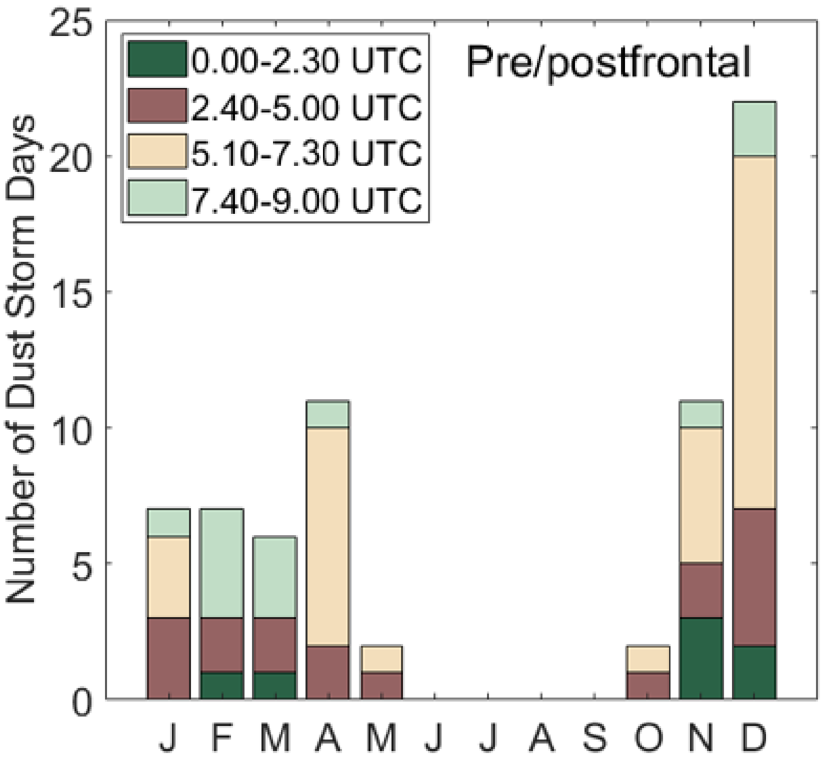

Appendix F. The number of DSD from Pre/Postfrontal cased SDS start time (UTM) vs 12 months*, during 2019-2022, at the Gonghe Basin, China.*

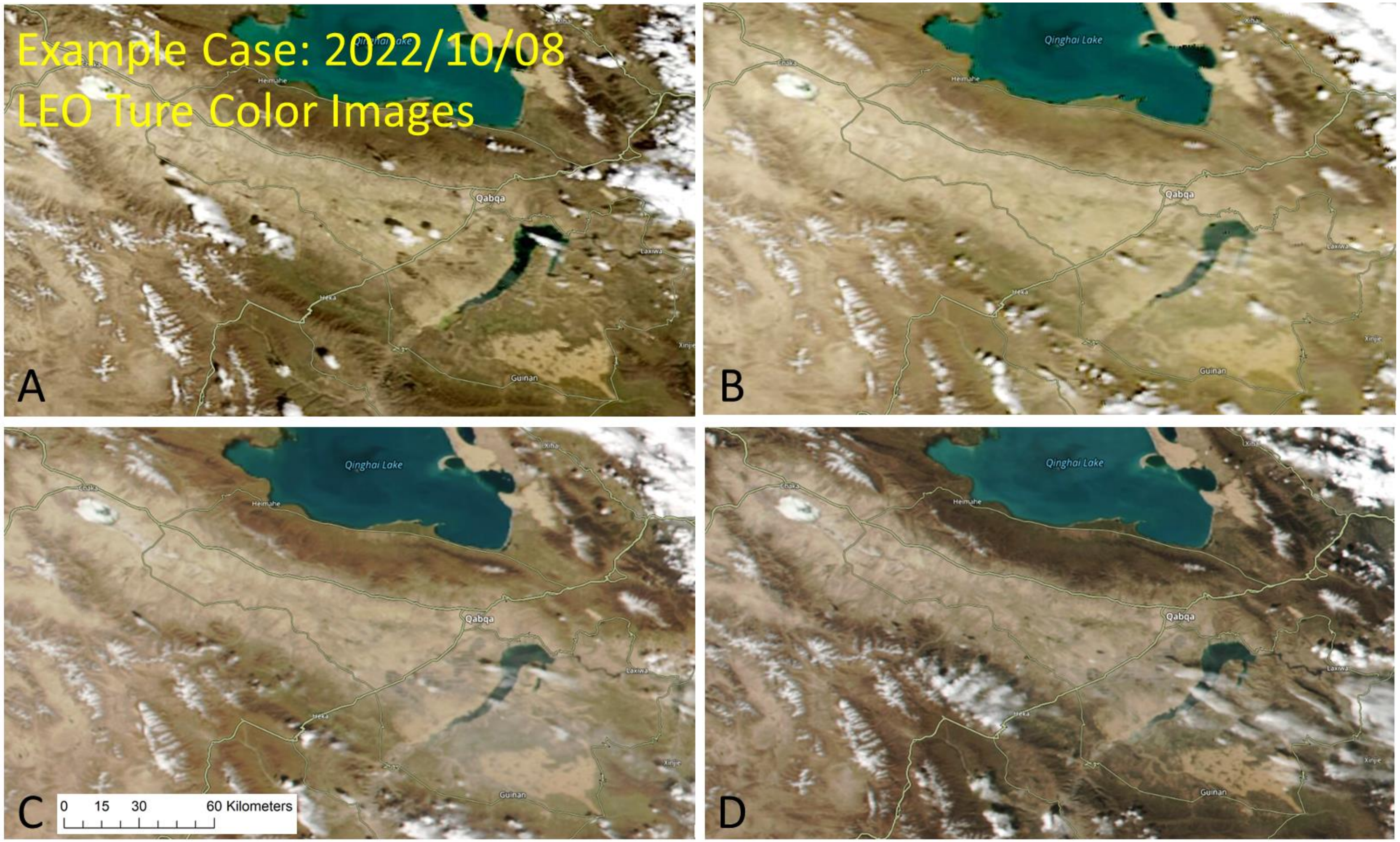

Appendix G. An example case of LEO satellite True Colour Image. *(A) MODIS-Terra; (B) MODIS-Aqua; (C)NOAA-20 VIIRS; (D) Suomi NPP-VIIRS on 2022/10/08.*

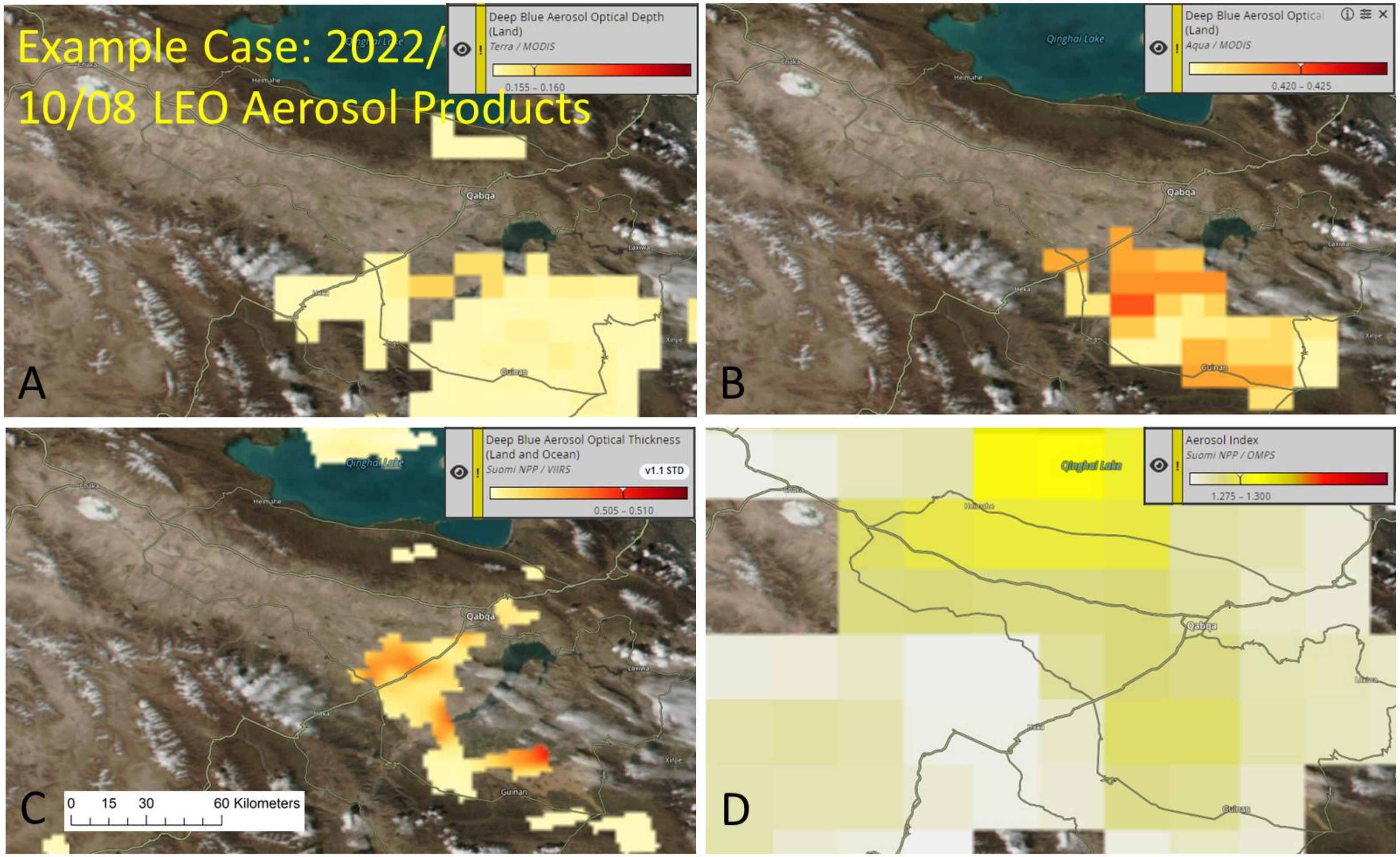

Appendix H. An example case of LEO satellite Aerosol Products. *(A) MODIS-Terra Aerosol Optical Depth (AOD); (B)MODIS-Aqua Aerosol Optical Depth (AOD); (C) Suomi NPP-VIIRS Aerosol Optical Thickness (AOT); (D) Suomi NPP-OMPS Aerosol Index (AI) on 2022/10/08.*

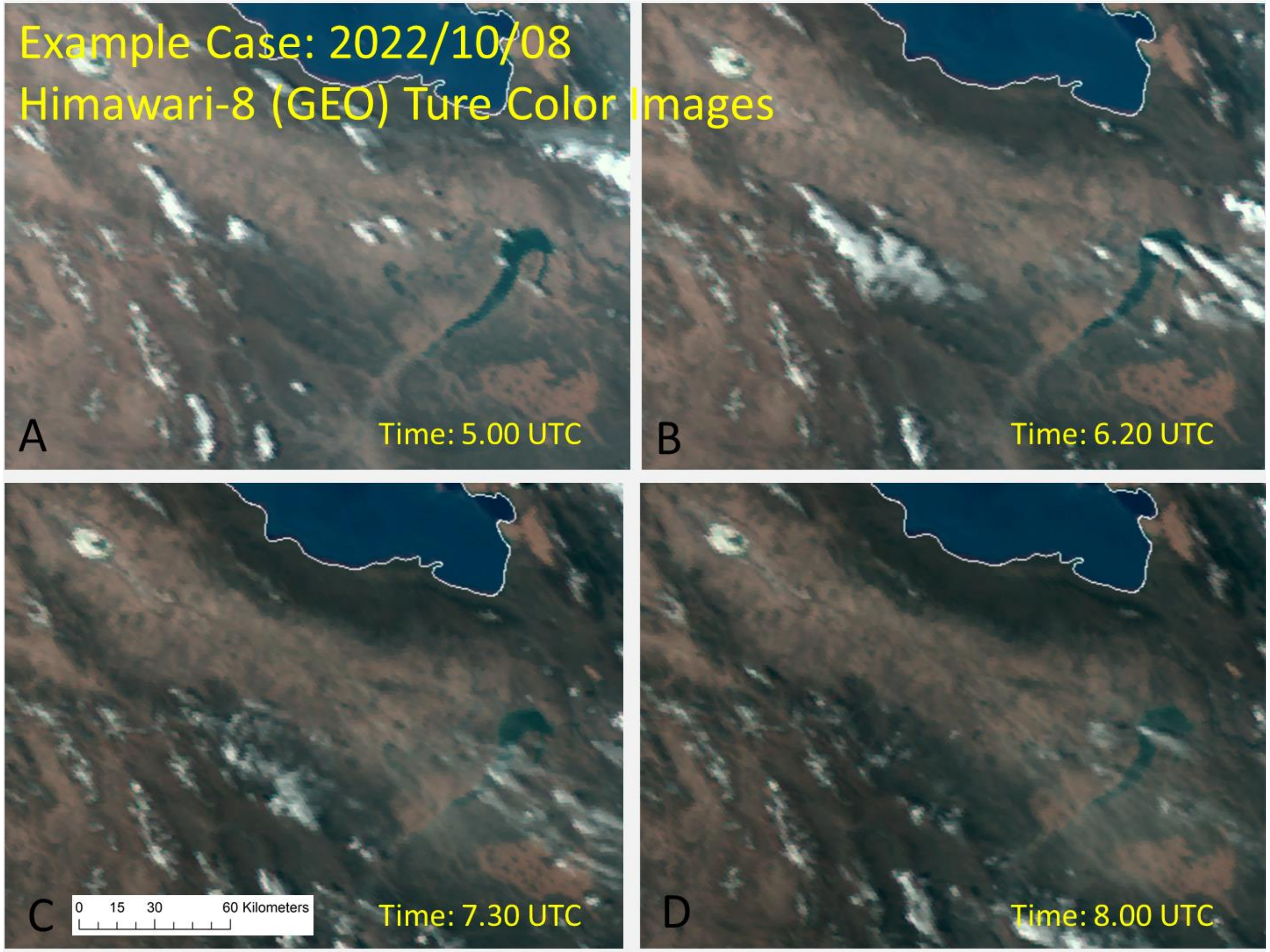

Appendix I. An example case of GEO (Himawari-8) satellite True Colour Image (TCI) in different time of 2022/10/08. *Time: (A) 05.00 UTC; (B) 06.20 UTC; (C) 07.30 UTC; (D) 08.00 UTC.*

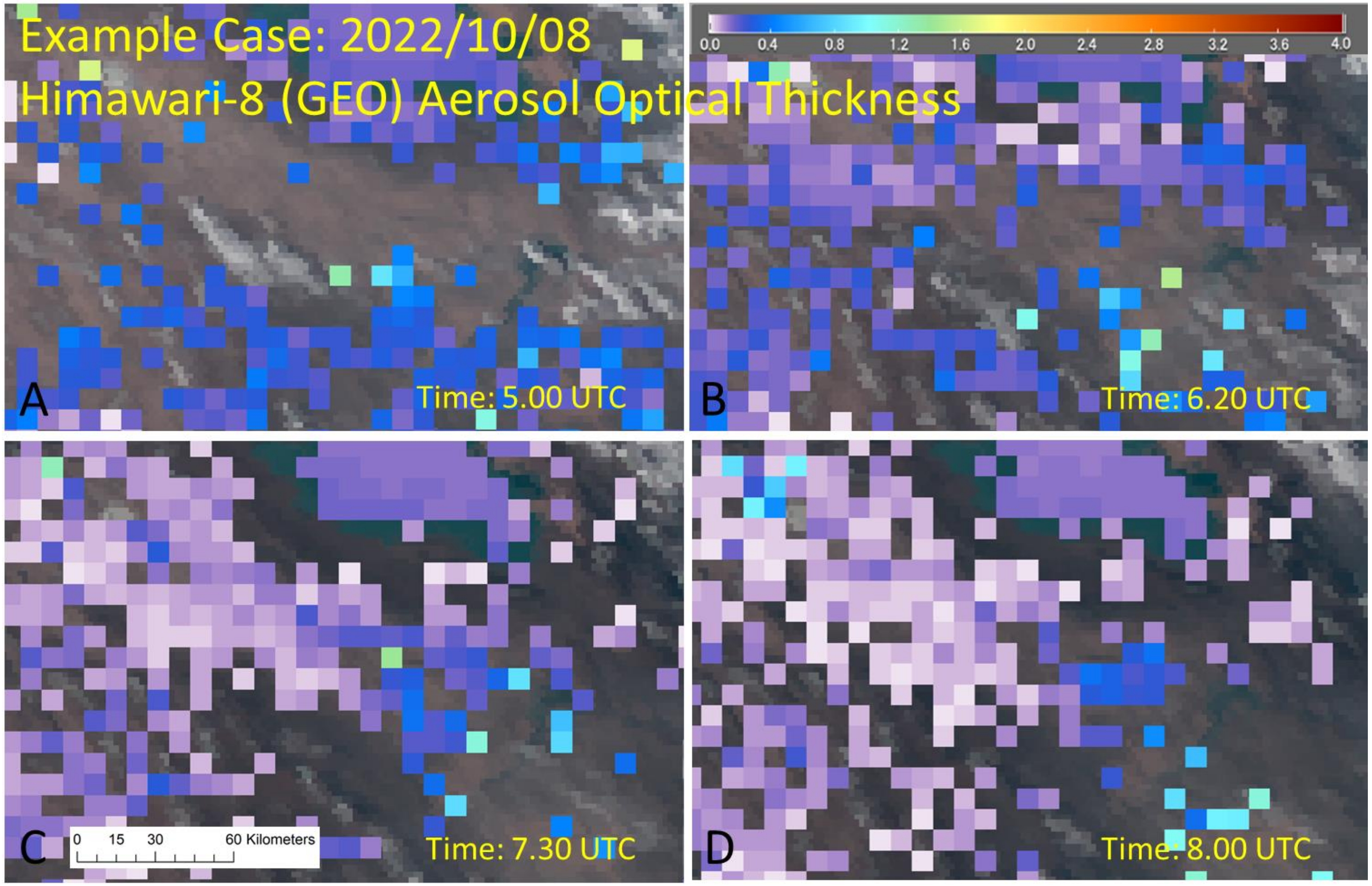

Appendix1. An example case of GEO(Himawari-8) satellite Aerosol Optical Thickness (AOT) products in different time of 2022/10/08. *Time: (A) 05.00 UTC; (B) 06.20 UTC; (C) 07.30 UTC; (D) 08.00 UTC.*

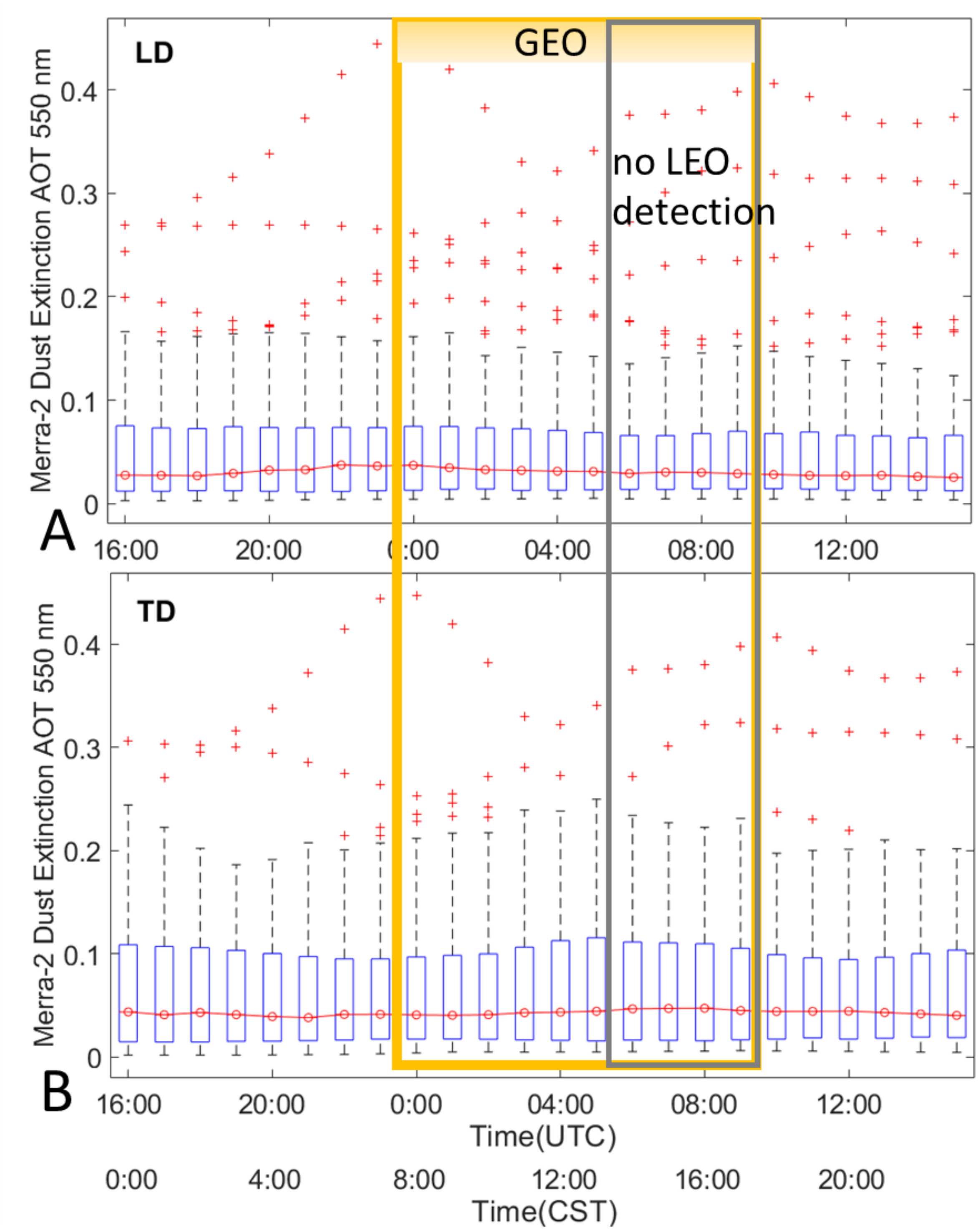

Appendix 2 Merra-2 hourly Dust Extinction AOT 550 nm dataset. *A) LD date 24-hour (00.00-23.00 CST) AOT and its median value line (red); B) TD date 24-hour AOT boxplot, 2019-2022*

Appendix L. DSD events detail information during 2019-2022. The Red Highlighed DSD was also captured by PlanetScope satellite and analysis in Chapter 4 and added two extra DSD in 2023 in the bottom.

Date	SDS	Start Time (UTC)	End Time (UTC)	Duration (minutes)	Type of Dust	Mechanism
11-Jan-2019	Y	3.30AM	9.30AM	360	LD	Disturbance
21-Jan-19	Y	3.00AM	9.30AM	390	LD	Disturbance
22-Jan-19	Y	3.00AM	9.30AM	390	LD	Disturbance
31-Jan-19	Y	1.40AM	9.30AM	470	TD	Haze
7-Feb-19	Y	1.40AM	9.30AM	470	TD	Haze
10-Feb-19	Y	3.40AM	9.30AM	350	TD	Haze
14-Feb-19	Y	3.40AM	9.30AM	350	LD	Frontal
14-Feb-19	Y	1.00AM	9.30AM	510	TD	Haze
17-Feb-19	Y	2.20AM	9.30AM	450	TD	Haze
18-Feb-19	Y	2.00AM	9.30AM	450	LD	Frontal
17-Mar-19	Y	1.30AM	10.30AM	540	TD	Haze
20-Mar-19	Y	1.40AM	10.30AM	490	TD	Haze
23-Mar-19	Y	1.00AM	10.30AM	570	TD	Haze
24-Mar-19	Y	6.30AM	10.30AM	240	LD	Frontal
24-Mar-19	Y	0.40AM	10.30AM	550	TD	Haze
27-Mar-19	Y	8.00AM	10.30AM	150	LD	Frontal
29-Mar-19	Y	6.00AM	10.30AM	270	LD	Frontal
9-Apr-19	Y	7.00AM	10.30AM	210	LD	Frontal
9-Apr-19	Y	0.40AM	10.30AM	550	TD	Haze
10-Apr-19	Y	4.40AM	10.30AM	310	LD	Frontal
12-Apr-19	Y	0.40AM	10.30AM	550	TD	Haze
15-Apr-19	Y	1.40AM	4.50AM	190	LD	Disturbance
24-Apr-19	Y	0.40AM	9.00AM	500	LD	Frontal
25-Apr-19	Y	4.00AM	10.30AM	360	LD	Disturbance
27-Apr-19	Y	3.00AM	9.00AM	360	LD	Disturbance
8-May-19	Y	1.30AM	10.30AM	540	TD	Haze
9-Nov-19	Y	1.50AM	9.00AM	470	LD	Frontal
11-Nov-19	Y	7.00AM	9.00AM	120	LD	Frontal
12-Nov-19	Y	2.00AM	9.00AM	420	LD	Frontal
13-Nov-19	Y	0.50AM	9.00AM	490	TD	Haze
16-Nov-19	Y	7.40AM	9.00AM	80	LD	Frontal
17-Nov-19	Y	0.50AM	9.00AM	490	LD	Frontal
26-Nov-19	Y	2.00AM	9.00AM	420	TD	Haze
27-Nov-19	Y	2.00AM	9.00AM	420	TD	Haze
29-Nov-19	Y	5.30AM	9.00AM	210	TD	Haze
17-Dec-19	Y	3.30AM	9.00AM	330	TD	Haze
25-Dec-19	Y	2.00AM	9.00AM	420	LD	Frontal
3-Jan-20	Y	4.40AM	9.40AM	300	TD	Haze
14-Jan-20	Y	4.00AM	6.40AM	160	TD	Haze
15-Jan-20	Y	1.30AM	9.00 AM	450	TD	Haze
2-Feb-20	Y	2.50AM	7.00 AM	250	TD	Haze
13-Feb-20	Y	8.40AM	10.20AM	100	LD	Frontal

14-Feb-20	Y	6.00AM	10.20AM	260	LD	Frontal
16-Feb-20	Y	2.10AM	10.20AM	490	TD	Haze
17-Feb-20	Y	1.40AM	10.20AM	520	TD	Haze
20-Feb-20	Y	6.20AM	10.20AM	240	LD	Frontal
20-Feb-20	Y	3.40AM	10.20AM	380	TD	Haze
29-Feb-20	Y	2.10AM	10.20AM	490	TD	Haze
11-Apr-20	Y	7.20AM	10.20AM	180	TD	Haboob
11-Apr-20	Y	1.20AM	10.20AM	540	TD	Haze
18-Apr-20	Y	6.40AM	12.00AM	320	LD	Frontal
22-Sep-20	Y	2.30AM	10.30AM	480	TD	Haze
6-Oct-20	Y	7.20AM	10.30AM	190	LD	Frontal
30-Oct-20	Y	3.37AM	11.30AM	480	LD	Frontal
14-Dec-20	Y	2.10AM	9.10AM	420	TD	Haze
16-Dec-20	Y	7.40AM	9.10AM	90	TD	Haze
20-Dec-20	Y	6.20AM	9.10AM	170	LD	Frontal
23-Dec-20	Y	8.00AM	9.10AM	70	LD	Frontal
25-Dec-20	Y	1.30AM	9.10AM	460	TD	Haze
28-Dec-20	Y	8.00AM	9.10AM	70	LD	Frontal
29-Dec-20	Y	3.30AM	9.10AM	340	LD	Frontal
31-Dec-20	Y	7.00AM	9.10AM	130	LD	Frontal
5-Jan-21	Y	3.30AM	10.00 AM	390	LD	Frontal
10-Jan-21	Y	3.30AM	10.00 AM	390	LD	Frontal
11-Jan-21	Y	6.40AM	9.50AM	190	LD	Frontal
17-Jan-21	Y	7.00AM	9.50AM	170	LD	Frontal
27-Jan-21	Y	5.00AM	10.00 AM	300	LD	Frontal
31-Jan-21	Y	8.00AM	10.00 AM	120	LD	Frontal
24-Feb-21	Y	1.00AM	4.00AM	180	TD	Haze
27-Feb-21	Y	3.30AM	10.20AM	410	TD	Haboob
16-Mar-21	Y	1.20AM	10.30 AM	550	TD	Haze
17-Mar-21	Y	1.20AM	10.30 AM	550	TD	Haze
18-Mar-21	Y	1.20AM	10.30 AM	550	TD	Haze
19-Mar-21	Y	4.10AM	8.00 AM	230	LD	Frontal
19-Mar-21	Y	0.30AM	8.00 AM	450	TD	Haze
20-Mar-21	Y	1.20AM	10.30 AM	550	TD	Haze
21-Mar-21	Y	1.20AM	10.30 AM	550	TD	Haze
25-Mar-21	Y	0.40AM	9.00AM	500	TD	Haboob
28-Mar-21	Y	9.30AM	12.00AM	120	LD	Frontal
11-Apr-21	Y	7.00AM	12.00 AM	300	LD	Frontal
25-Apr-21	Y	7.30AM	12.00AM	270	TD	Haze
26-Apr-21	Y	7.50AM	12.00AM	250	LD	Frontal
27-Apr-21	Y	4.20AM	12.00AM	460	LD	Frontal
28-Apr-21	Y	6.30AM	12.00AM	330	LD	Frontal
29-Apr-21	Y	6.40AM	12.00AM	320	LD	Frontal
3-May-21	Y	3.40AM	12.00AM	500	LD	Frontal
3-May-21	Y	3.00AM	12.00AM	540	TD	Haboob
4-May-21	Y	9.00AM	12.00AM	180	TD	Haboob
4-May-21	Y	0.30AM	10.30AM	600	TD	Haze
5-May-21	Y	5.40AM	12.00AM	380	LD	Frontal
23-Aug-21	Y	7.20AM	12.00AM	280	TD	Haze
13-Oct-21	Y	4.30AM	10.40AM	370	TD	Haze

6-Nov-21	Y	6.10AM	9.30AM	200	LD	Frontal
9-Nov-21	Y	7.00AM	9.00AM	120	LD	Disturbance
11-Nov-21	Y	5.00AM	9.00AM	240	LD	Frontal
11-Nov-21	Y	1.30AM	9.00AM	450	TD	Haze
14-Nov-21	Y	6.30AM	9.00AM	150	LD	Frontal
15-Nov-21	Y	1.30AM	7.00AM	330	TD	Haze
17-Nov-21	Y	4.30AM	9.00AM	270	LD	Disturbance
20-Nov-21	Y	3.20AM	9.00AM	340	LD	Frontal
21-Nov-21	Y	3.00AM	9.00AM	360	LD	Disturbance
22-Nov-21	Y	4.30AM	9.00AM	270	TD	Haze
23-Nov-21	Y	5.00AM	9.00AM	240	LD	Disturbance
28-Nov-21	Y	7.50AM	9.00AM	70	LD	Frontal
29-Nov-21	Y	3.00AM	9.00AM	360	LD	Disturbance
29-Nov-21	Y	1.30AM	9.00AM	450	TD	Haze
1-Dec-21	Y	6.30AM	9.00AM	150	LD	Frontal
4-Dec-21	Y	6.00AM	9.00AM	180	LD	Frontal
11-Dec-21	Y	6.00AM	9.00AM	180	LD	Frontal
16-Dec-21	Y	4.30AM	9.00AM	270	LD	Frontal
24-Dec-21	Y	5.40AM	9.00AM	200	LD	Disturbance
26-Dec-21	Y	3.00AM	9.00AM	360	TD	Haze
27-Dec-21	Y	3.00AM	9.00AM	360	TD	Haze
28-Dec-21	Y	7.00AM	9.00AM	120	LD	Disturbance
31-Dec-21	Y	7.20AM	9.00AM	100	LD	Frontal
9-Jan-22	Y	8.00AM	9.20AM	80	TD	Haze
21-Jan-22	Y	1.30 AM	9.20 AM	470	TD	Haze
24-Jan-22	Y	1.30 AM	9.20 AM	470	TD	Haze
29-Jan-22	Y	5.30 AM	9.30 AM	240	TD	Haze
30-Jan-22	Y	6.00 AM	9.30 AM	210	LD	Frontal
14-Feb-22	Y	6.30 AM	10.00 AM	210	LD	Frontal
16-Feb-22	Y	8.50AM	10.00AM	70	LD	Frontal
18-Feb-22	Y	7.20 AM	10.00 AM	160	LD	Frontal
19-Feb-22	Y	8.40 AM	10.00 AM	80	LD	Frontal
23-Feb-22	Y	7.30 AM	10.00 AM	150	LD	Frontal
25-Feb-22	Y	8.30 AM	10.00 AM	90	LD	Frontal
28-Feb-22	Y	3.00AM	10.00 AM	420	LD	Frontal
28-Feb-22	Y	1.30 AM	10.00 AM	510	TD	Haze
3-Mar-22	Y	7.00 AM	10.00 AM	180	LD	Frontal
4-Mar-22	Y	5.40AM	10.00AM	260	TD	Haze
6-Mar-22	Y	0.40AM	10.00AM	560	LD	Frontal
12-Mar-22	Y	8.50 AM	10.20 AM	90	LD	Frontal
18-Mar-22	Y	4.10 AM	10.20 AM	360	LD	Frontal
18-Mar-22	Y	0.30AM	10.20 AM	590	TD	Haze
22-Mar-22	Y	6.00 AM	10.20 AM	260	LD	Frontal
22-Mar-22	Y	0.30AM	10.20 AM	590	TD	Haze
27-Mar-22	Y	3.10AM	9.00AM	350	TD	Haze
8-Apr-22	Y	5.40AM	11.50AM	370	LD	Frontal
12-Apr-22	Y	7.00AM	11.50AM	290	LD	Frontal
17-Apr-22	Y	6.00AM	11.50AM	350	LD	Frontal
28-Apr-22	Y	0.40AM	6.00AM	320	TD	Haze
2-May-22	Y	5.00AM	12.00PM	420	LD	Disturbance

3-May-22	Y	5.40AM	12.00PM	360	LD	Disturbance
7-May-22	Y	0.40AM	9.00AM	500	TD	Haboob
14-May-22	Y	5.10 AM	9.00AM	230	TD	Haze
8-Oct-22	Y	5.30 AM	11.00AM	330	LD	Frontal
2-Nov-22	Y	1.30AM	9.00AM	450	TD	Haze
18-Nov-22	Y	1.10AM	8.50AM	460	TD	Haze
23-Nov-22	Y	7.00AM	8.50AM	110	LD	Disturbance
24-Nov-22	Y	6.00AM	8.50AM	170	TD	Haboob
25-Nov-22	Y	6.00AM	8.50AM	170	LD	Frontal
27-Nov-22	Y	7.10AM	8.50AM	100	TD	Haze
28-Nov-22	Y	4.00AM	8.50AM	290	LD	Frontal
28-Nov-22	Y	1.30AM	8.50AM	440	TD	Haze
29-Nov-22	Y	1.30AM	8.50AM	440	TD	Haze
30-Nov-22	Y	6.00AM	8.50AM	170	LD	Frontal
1-Dec-22	Y	5.30AM	8.50AM	200	LD	Frontal
3-Dec-22	Y	2.30AM	8.50AM	240	TD	Haze
4-Dec-22	Y	7.00AM	8.50AM	110	LD	Frontal
4-Dec-22	Y	1.30AM	8.50AM	440	TD	Haze
10-Dec-22	Y	2.30AM	8.50AM	380	TD	Haze
11-Dec-22	Y	3.00AM	8.50AM	350	LD	Frontal
12-Dec-22	Y	6.00AM	8.50AM	170	LD	Frontal
13-Dec-22	Y	5.40AM	8.50AM	190	LD	Frontal
15-Dec-22		6.40AM	8.50AM	130	LD	Frontal
15-Dec-22	Y	5.40AM	8.50AM	190	TD	Haboob
16-Dec-22	Y	2.40AM	8.50AM	370	LD	Frontal
19-Dec-22	Y	6.20AM	8.50AM	150	LD	Frontal
20-Dec-22	Y	2.30AM	8.50AM	380	LD	Frontal
22-Dec-22	Y	7.00AM	8.50AM	110	LD	Frontal
26-Dec-22	Y	7.00AM	8.50AM	110	LD	Frontal
27-Dec-22	Y	3.10AM	8.50AM	340	LD	Disturbance
28-Dec-22	Y	6.30AM	8.50AM	140	LD	Frontal
05-Jan-23	Y	3.00AM	9.10AM	250	LD	Frontal
23-Jan-23	Y	3.00AM	9.40AM	280	LD	Frontal

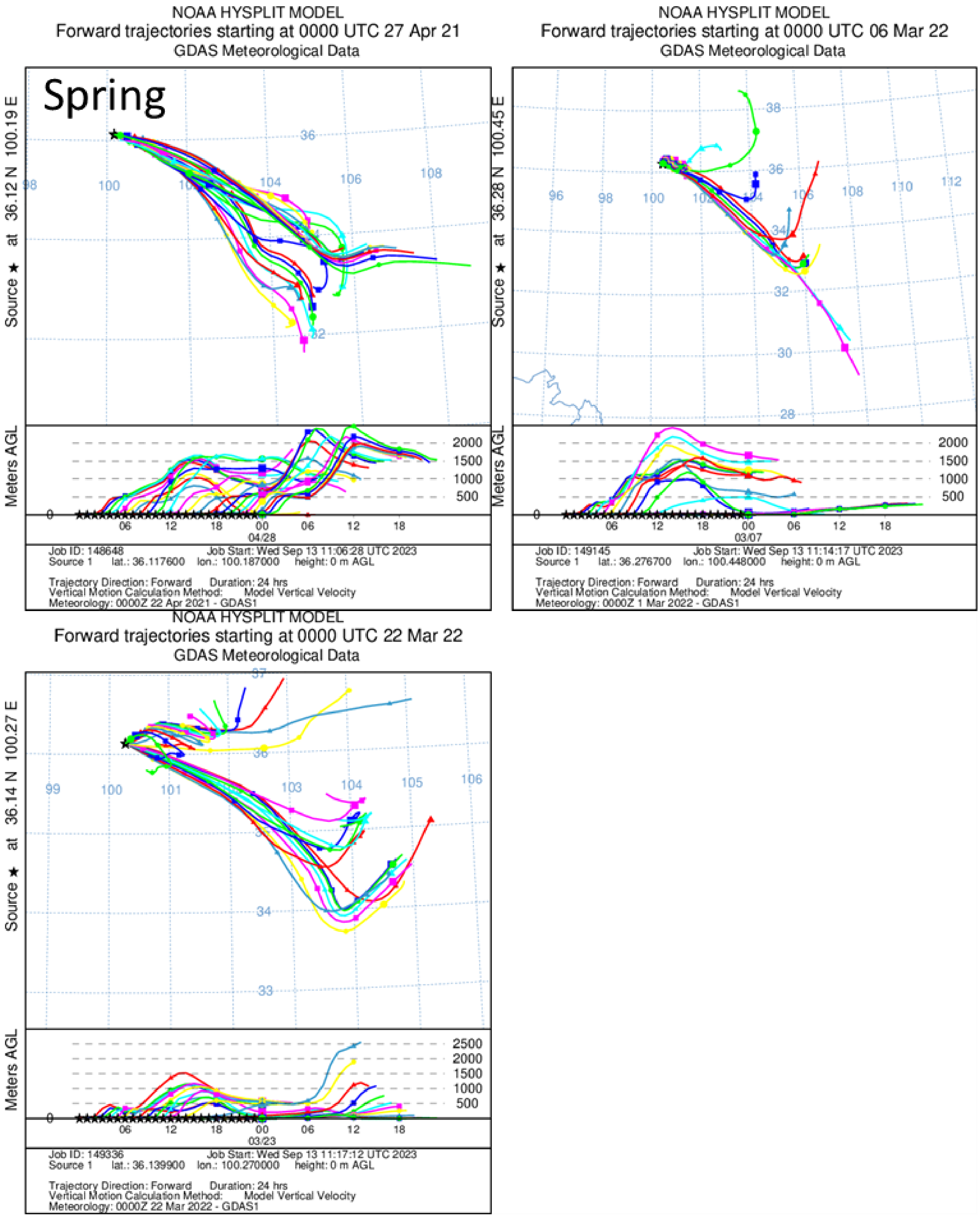

Appendix M. Trajectory pathway and height from Spring [MAM] cases in 2019-2023 in the Gonghe Basin, China.

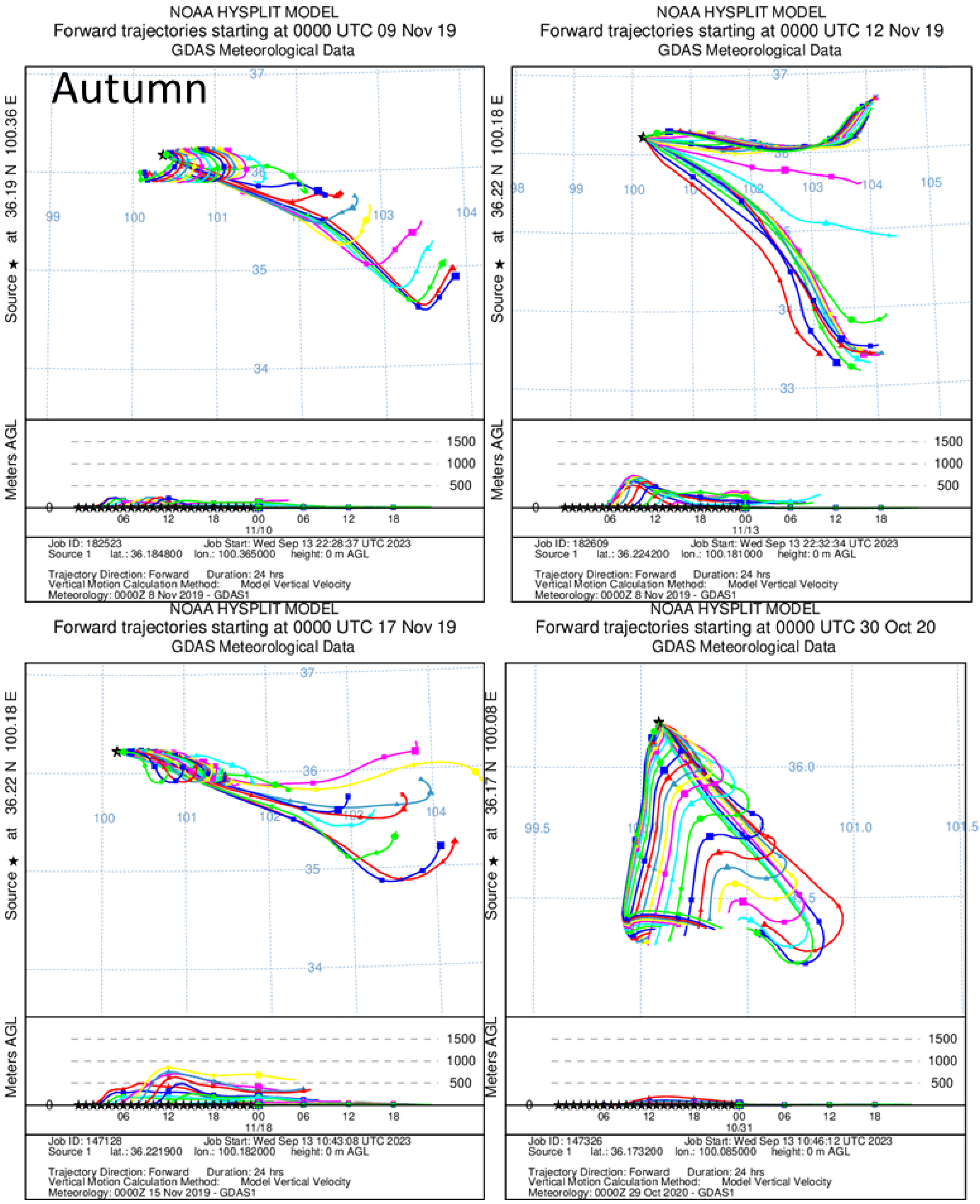

Appendix N. Trajectory pathway and height from Autumn [SON] cases in 2019-2023 in the Gonghe Basin, China.

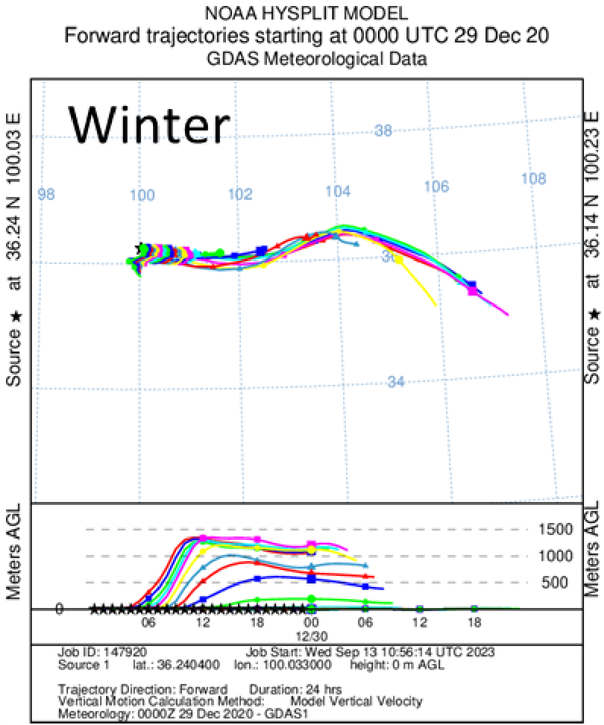
NOAA HYSPLIT MODEL
Forward trajectories starting at 0000 UTC 29 Dec 20
GDAS Meteorological Data
Winter
Source ★ at 36.24 N 100.03 E
98
100
102
104
106
108
38
36
34
Meters AGL
1500
1000
500
0
06
12
18
00
06
12
18
12/30
Job ID: 147920 Job Start: Wed Sep 13 10:56:14 UTC 2023
Source 1 lat.: 36.240400 lon.: 100.033000 height: 0 m AGL
Trajectory Direction: Forward Duration: 24 hrs
Vertical Motion Calculation Method: Model Vertical Velocity
Meteorology: 0000Z 29 Dec 2020 - GDAS1

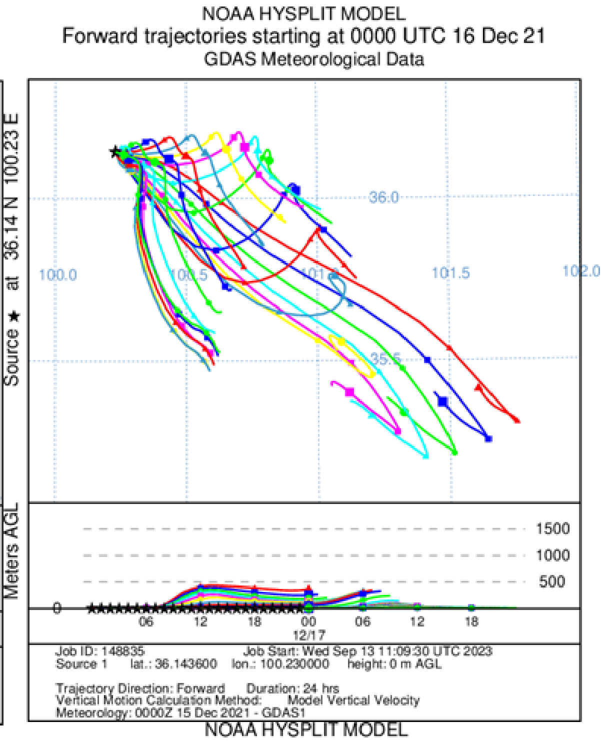
NOAA HYSPLIT MODEL
Forward trajectories starting at 0000 UTC 16 Dec 21
GDAS Meteorological Data
Source ★ at 36.14 N 100.23 E
100.0
100.5
101.0
101.5
102.0
36.0
35.5
Meters AGL
1500
1000
500
0
06
12
18
00
06
12
18
12/17
Job ID: 148835 Job Start: Wed Sep 13 11:09:30 UTC 2023
Source 1 lat.: 36.143600 lon.: 100.230000 height: 0 m AGL
Trajectory Direction: Forward Duration: 24 hrs
Vertical Motion Calculation Method: Model Vertical Velocity
Meteorology: 0000Z 15 Dec 2021 - GDAS1

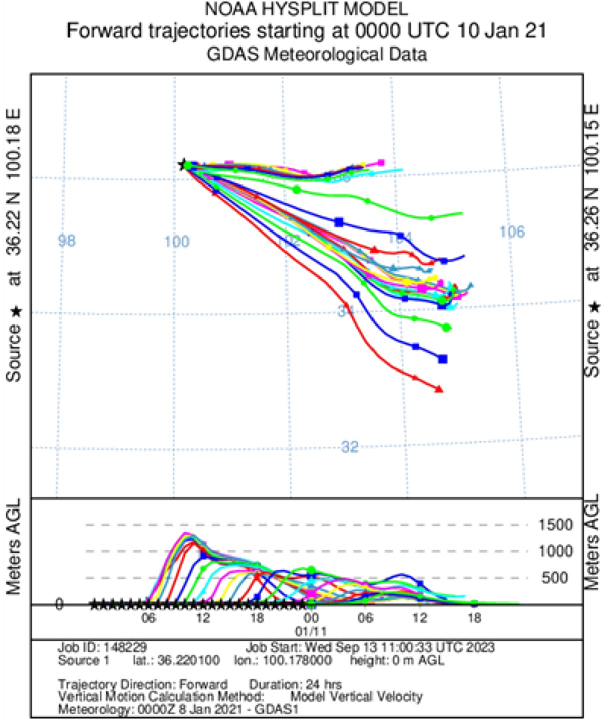
NOAA HYSPLIT MODEL
Forward trajectories starting at 0000 UTC 10 Jan 21
GDAS Meteorological Data
Source ★ at 36.22 N 100.18 E
98
100
102
104
106
34
32
Meters AGL
1500
1000
500
0
06
12
18
00
06
12
18
01/11
Job ID: 148229 Job Start: Wed Sep 13 11:00:33 UTC 2023
Source 1 lat.: 36.220100 lon.: 100.178000 height: 0 m AGL
Trajectory Direction: Forward Duration: 24 hrs
Vertical Motion Calculation Method: Model Vertical Velocity
Meteorology: 0000Z 8 Jan 2021 - GDAS1

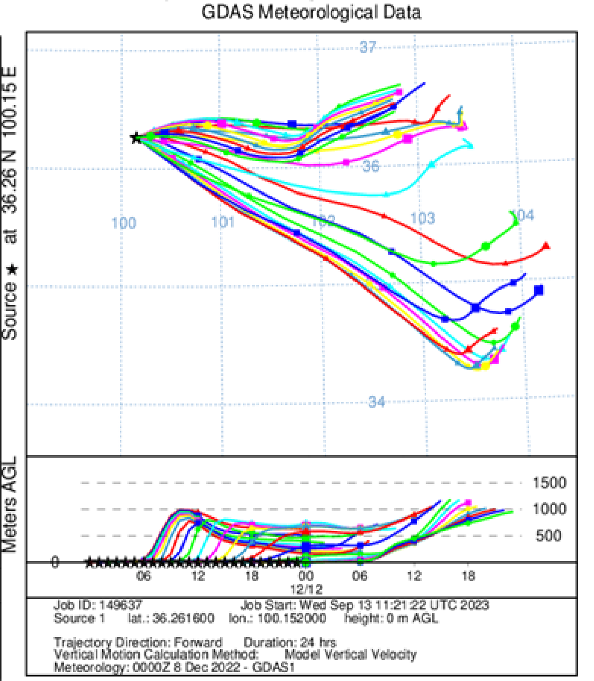
NOAA HYSPLIT MODEL
Forward trajectories starting at 0000 UTC 11 Dec 22
GDAS Meteorological Data
Source ★ at 36.26 N 100.15 E
37
36
34
100
101
102
103
104
Meters AGL
1500
1000
500
0
06
12
18
00
06
12
18
12/12
Job ID: 149637 Job Start: Wed Sep 13 11:21:22 UTC 2023
Source 1 lat.: 36.261600 lon.: 100.152000 height: 0 m AGL
Trajectory Direction: Forward Duration: 24 hrs
Vertical Motion Calculation Method: Model Vertical Velocity
Meteorology: 0000Z 8 Dec 2022 - GDAS1

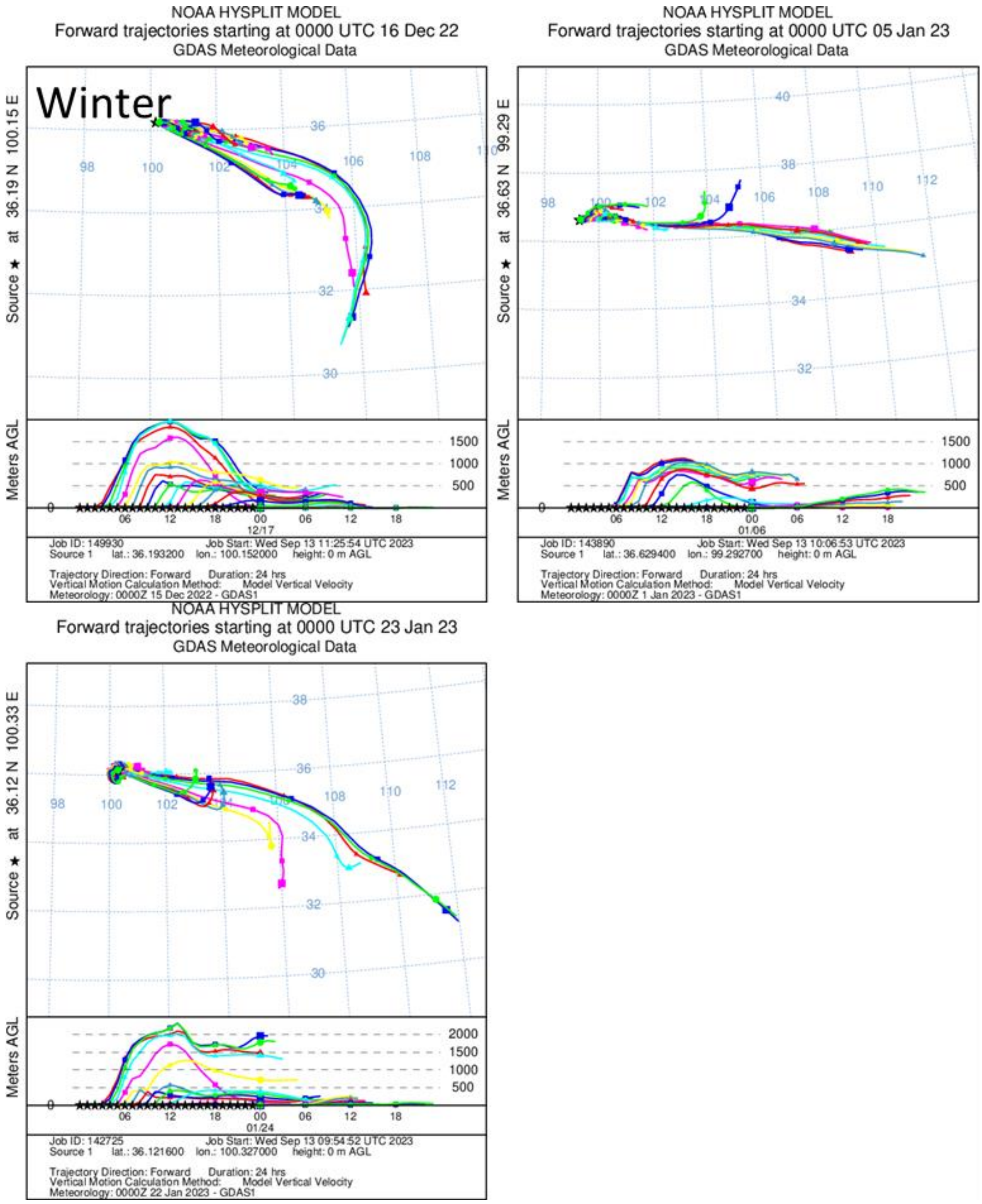

Appendix O. Trajectory pathway and height from Winter [DJF] cases in 2019-2023 in the Gonghe Basin, China.